Vietnam Ministry of Science and Technology

P-ISSN 2525-2461 • E-ISSN 2615-9937

# Vietnam Journal of Science, Technology and Engineering

MARCH 2024 • VOLUME 66 NUMBER 1

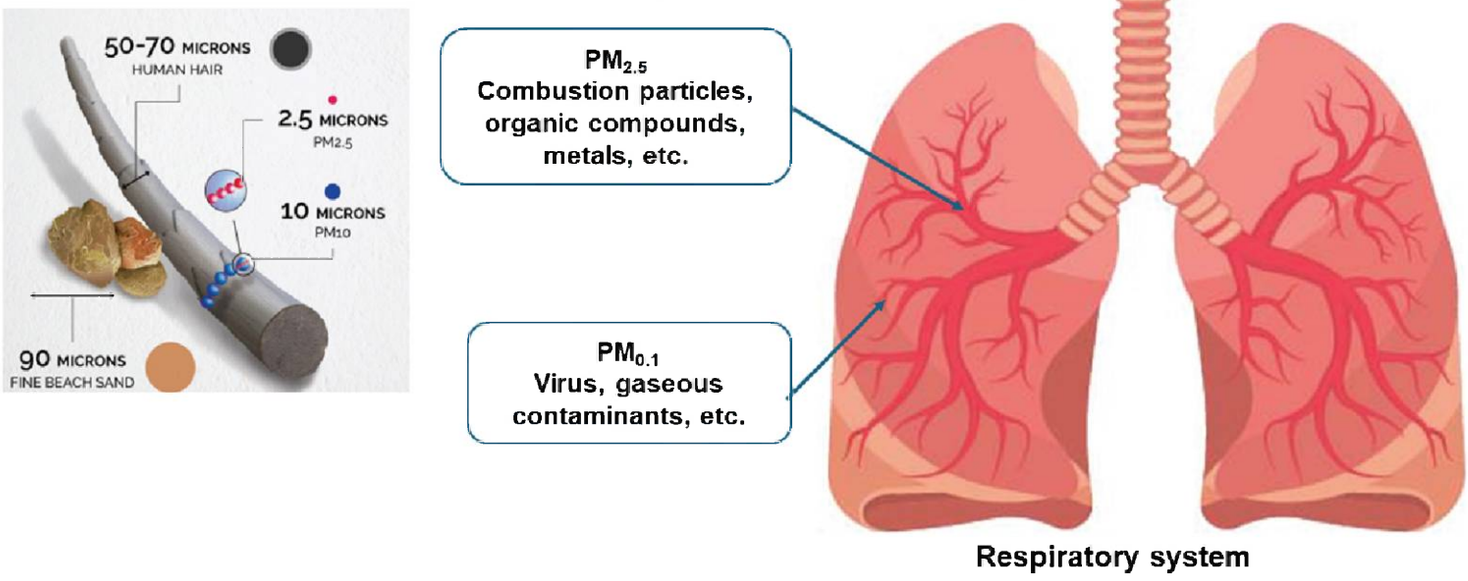


## Environmental and health impacts of air pollution: A mini-review

VIETNAM JOURNAL OF SCIENCE, TECHNOLOGY AND ENGINEERING * MARCH 2024 * VOLUME 66 NUMBER 1

vietnamscience.vn or vietnamscience.vjst.vn

*Vietnam Journal of Science, Technology and Engineering (VJSTE)* **is a quarterly double-blind peer-reviewed academic journal. VJSTE publishes research articles and review articles in all areas of science, technology and engineering with the focus on the physical sciences, life sciences and environmental sciences including the following topics:**

- **Physical Sciences**
- **Agriculture**
- **Medicine**
- **Pharmacology**
- **Biology**
- **Biotechnology**
- **Biomedical Applications**
- **Ecology**
- **Climatology**
- **Environmental Science.**

## CLASSIFICATION SCHEME

1. **Mathematics and Computer Science**
   - **1.1. Mathematics**
   - **1.2. Computer Science**
   - **1.3. Computational Science**
2. **Physical Sciences**
   - **2.1. Physics**
   - **2.2. Chemistry**
   - **2.3. Engineering**
3. **Life Sciences**
   - **3.1. Agriculture**
   - **3.2. Medicine**
   - **3.3. Pharmacology**
   - **3.4. Biology**
   - **3.5. Biotechnology**
   - **3.6. Biomedical Applications**
4. **Earth Sciences**
   - **4.1. Geography**
   - **4.2. Geology**
   - **4.3. Geophysics**
   - **4.4. Oceanography**
5. **Environmental Sciences**
   - **5.1. Ecology**
   - **5.2. Climatology**
   - **5.3. Environmental Science**

# CONTENTS

MARCH 2024 • VOLUME 66 NUMBER 1



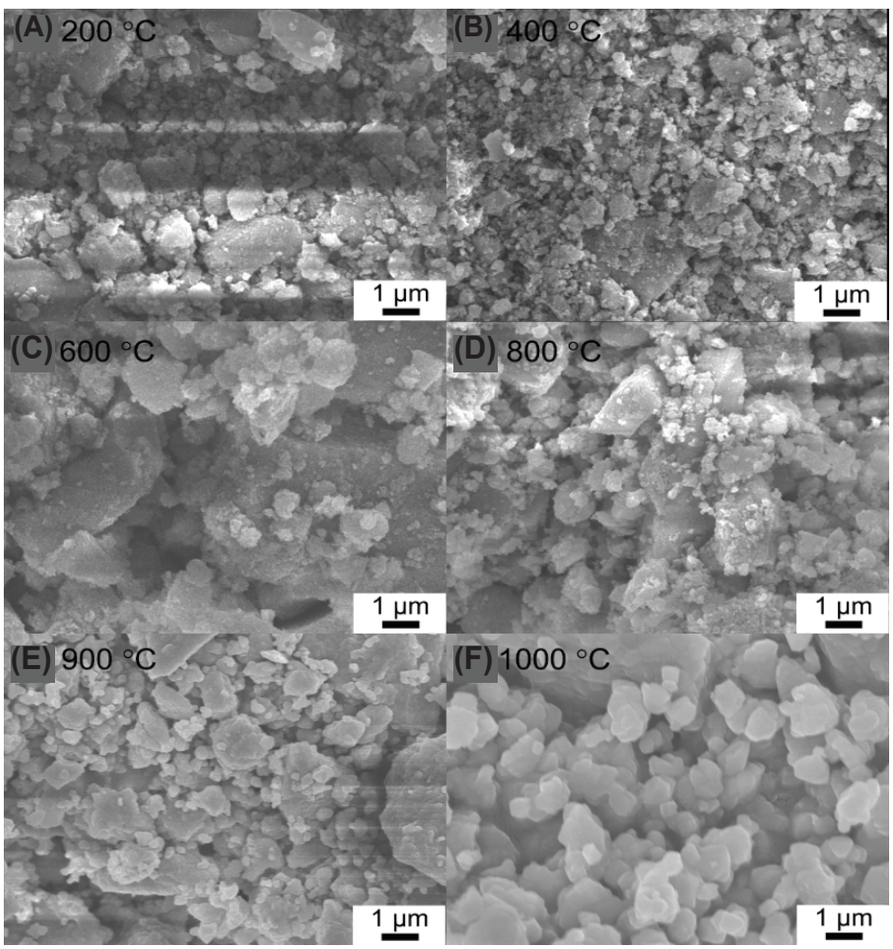


## PHYSICAL SCIENCES

# CONTENTS

MARCH 2024 • VOLUME 66 NUMBER 1

## LIFE SCIENCES



## ENVIRONMENTAL SCIENCES



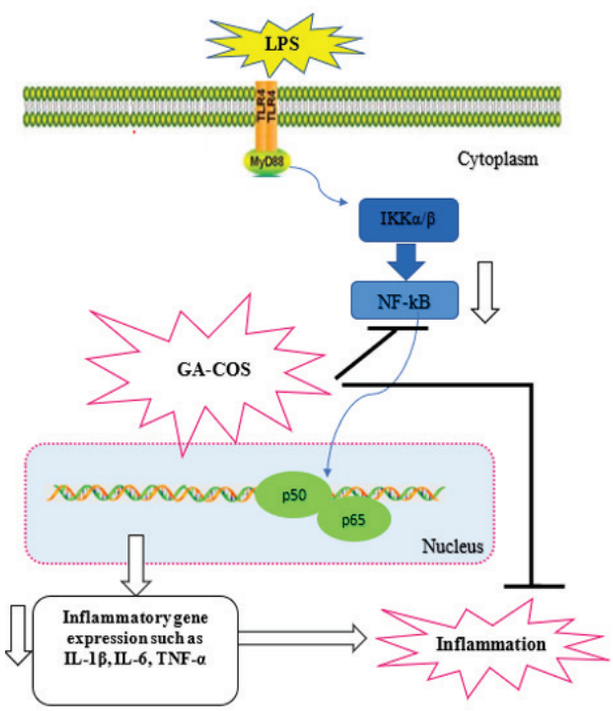

# Effects of humidity and temperature on quality factor of micro-beam resonators in atmospheric pressure and gas rarefaction

**Nguyen Chi Cuong[1*], Trinh Xuan Thang[1], Lam Minh Thinh[1], Vuong Dinh Duy Phuc[1], Phan Minh Truong[2], Truong Huu Ly[1], Ngo Vo Ke Thanh[1], Le Quoc Cuong[1]**

*[1]Research Laboratories of Saigon High-Tech Park, Lot I3, N2 Street, Saigon High-Tech Park, Tan Phu Ward, District 9, Ho Chi Minh City, Vietnam*
*[2]Institute for Computational Science and Technology, SBI Building, Quang Trung Software City, Tan Chanh Hiep Ward, District 12, Ho Chi Minh City, Vietnam*

Received 10 March 2023; revised 1 June 2023; accepted 18 July 2023

***Abstract:***

**At atmospheric pressure ($p$=101325 Pa), the effects of humidity and temperature on moist air become important when discussing the quality factor of micro-cantilever and micro-bridge resonators. The squeeze film damping (SFD) problem, the dominant damping source for micro-beam resonators, is modelled using the modified molecular gas lubrication (MMGL) equation with finite element modelling (FEM) in the eigenvalue problem. The MMGL equation is modified with the effective viscosity of moist air ($\mu_{eff}$) to account for the effects of humidity and temperature. Other damping sources, such as thermoelastic damping (TED) and the support loss of micro-beam resonators, are also calculated. The quality factor of micro-beam resonators is then discussed over a wide range of temperatures and relative humidity levels at atmospheric pressure and gas rarefaction. The results show that the quality factor of micro-cantilever and micro-bridge resonators increases as both humidity and temperature rise in atmospheric pressure and gas rarefaction. Furthermore, the quality factor of a micro-bridge resonator with changes in humidity and temperature is significantly higher than that of a micro-cantilever resonator in atmospheric pressure and gas rarefaction.**

***Keywords:*** **micro-beam resonators, quality factor, relative humidity, squeeze film damping, temperature.**

***Classification numbers:*** **2.1, 2.3**

## 1. Introduction

Micro-beam resonators [1] are utilised in many Micro-Electro-Mechanical Systems (MEMS) sensor applications for environmental monitoring [e.g., temperature ($T$), humidity ($RH$), pollutant gases] [2, 3]. The advantages of temperature and humidity MEMS sensors based on MEMS technology include a wide detection range, rapid resonant response, and high precision. However, in moist air, the detection of temperature and water vapour plays a pivotal role in many MEMS sensor applications for environmental monitoring [4].

In MEMS resonators, the quality factor is the primary outcome when micro-beam resonators operate at atmospheric pressure. External SFD is one of the significant damping sources of MEMS resonators as airflow is squeezed in the gap spacing between a micro-beam and its surrounding substrate [5]. In addition, TED [6-9] and support loss [10] are other damping sources for micro-beam resonators. For micro-beam structures of resonators, three kinds of damping sources - SFD, TED, and support loss - which are more dominant than other damping sources, have been considered to accurately evaluate the quality factor of micro-beam resonators [11]. At atmospheric pressure, the quality factor of micro-beam resonators is highly influenced by the effects of temperature ($T$) and humidity ($RH$) due to the increased viscous damping of moist air. Thus, the effects of temperature and relative humidity are crucial to discuss when aiming to improve the quality factor of micro-beam resonators since the transverse vibration of micro-beam resonators is significantly resisted by the SFD.

*Corresponding author: Email: cuong.nguyenchi@shtplabs.org

In gas rarefaction, atmospheric pressure ($p$=101325 Pa) is introduced into a narrow air gap spacing ($h_0$). Then, slip flow occurs on the micro-beam and substrate surfaces. Hence, the effect of gas rarefaction becomes significant on the dynamic performance of MEMS resonators, even at atmospheric pressure and ultra-thin gap spacing [11, 12]. To account for the effects of temperature and relative humidity in atmospheric pressure and gas rarefaction, the effective viscosity of moist air ($\mu_{eff}=\mu/Q_p$), which is defined as the ratio of the Poiseuille flow rate ($Q_p$) [13] and the dynamic viscosity ($\mu$) [14] of moist air, modifying the MMGL equation for the SFD problem. As a result, the influences of temperature and relative humidity on the quality factor of micro-beam resonators can be addressed in both atmospheric pressure and gas rarefaction. Existing literature has examined the effects of temperature and relative humidity on the quality factors of MEMS resonators under atmospheric pressure [15-19]. Consequently, the quality factor of micro-cantilevers is heavily influenced by temperature and relative humidity in the atmospheric environment. However, the effects of temperature and relative humidity of moist air on the quality factor of micro-bridge resonators in atmospheric pressure and gas rarefaction have not yet been considered.

In this article, the impacts of temperature and relative humidity of moist air on the quality factor of micro-bridge resonators in atmospheric pressure and gas rarefaction for environmental monitoring are studied. The MMGL equation is solved using the effective viscosity ($\mu_{eff}$) for the SFD issue to consider the effects of temperature and relative humidity across a range of pressures, from atmospheric to gas rarefaction. Previous studies have only addressed the temperature and relative humidity concerning the resonant frequency and quality factor of micro-cantilevers [18, 19] in atmospheric pressure. However, the micro-bridge structure has not been explored and discussed to date. In this research, the quality factor of the micro-bridge resonator will be discussed and compared to enhance the quality factors of MEMS resonators in atmospheric pressure and gas rarefaction. The objective of this study is to examine the effects of temperature and relative humidity of moist air in order to optimise the quality factors of MEMS resonators based on the micro-bridge structure for environmental monitoring in both atmospheric pressure and gas rarefaction.

## 2. Materials and methods

### *2.1. The modified molecular gas lubrication equation for air damping of micro-beam resonators*

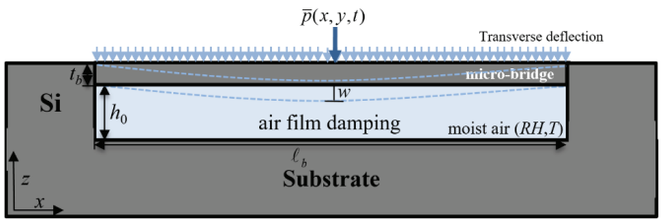


**Fig. 1. Transverse vibration of micro-beam or micro-bridge resonators under air film damping.**

In Fig. 1, the micro-bridge structure is used to discuss the effects of temperature and relative humidity on the quality factor of MEMS resonators in atmospheric pressure and gas rarefaction. In a moist air environment, the transverse motion of micro-beam resonators is resisted by the air film damping with a certain gas film pressure ($\bar{p}(x,y,t)$). The Poiseuille flow rate ($Q_P$) occurs in an ultra-thin gap spacing ($h_0$). In this instance, an isothermal air squeeze film is assumed for all the edges of the rectangular micro-bridge. The micro-beam temperature is assumed to be the same as the ambient temperature ($T=T_0$). A new MMGL equation [11] is utilised to model the SFD problem in order to obtain the pressure variations of the gas film as:

$$\frac{\partial}{\partial x}\left(\frac{\rho h^3}{12\mu_{eff}(RH,T)}\frac{\partial p}{\partial x}\right)+\frac{\partial}{\partial y}\left(\frac{\rho h^3}{12\mu_{eff}(RH,T)}\frac{\partial p}{\partial y}\right)=\frac{\partial}{\partial t}(\rho h) \quad (1)$$

where $RH$ is the water vapor relative humidity (%); $p$ is the air pressure, $\rho$ is the density of moist air; $h$ is the air gap spacing; $T$ is the ambient temperature (°C).

The water vapor molar fraction of moist air [14] is expressed as:

$$x_v=\frac{n_v}{n_v+n_a}=\frac{p_v}{p} \quad (2)$$

where $p_v$ is the water vapor partial pressure; $p$ is the total pressure partial pressure; $x_v$ is the water vapor mole fraction; $n_v$ and $n_a$ are the water vapor and dry air mole numbers, respectively.

The relative humidity ($RH$) of moist air [14] is given by:

$$RH=\frac{x_v}{x_{sv}}=\frac{p_v}{p_{sv}} \quad (3)$$

with

$$x_v=x_{sv}\times RH \quad (4)$$

where $p_v$ is the water vapor partial pressure; $p_{sv}$ is the water vapor saturated pressure at a given temperature; $x_{sv}$ is the saturated water vapor molar fraction.

The water vapor molar fraction ($x_v$) can be calculated as:

$$x_v = f(p,T) \times \frac{p_v}{p} = f(p,T) \times RH \times \frac{p_{sv}}{p} \quad (5)$$

with the total pressure ($p$) of moist air is given by:

$$p = p_v + p_a \quad (6)$$

where $p_a$ is the partial pressure of dry air.

The enhancement factors ($f(p, T)$) [20] are calculated by:

$$f(p,T) = \exp\left[\alpha \times \left(1 - \frac{p_{sv}}{p}\right) + \beta \times \left(\frac{p}{p_{sv}} - 1\right)\right] \quad (7)$$

with

$$\alpha = \sum_{i=1}^{4} A_i \times T^{(i-1)} \quad (8)$$

and

$$\beta = exp\left(\sum_{i=1}^{4} B_i \times T^{(i-1)}\right) \quad (9)$$

where the numerical values of the coefficients in Eqs. (8) and (9) are: $A_1$=3.53624×10$^{-4}$, $A_2$=2.93228×10$^{-5}$, $A_3$=2.61474×10$^{-7}$, $A_4$=8.57538×10$^{-9}$, $B_1$=-10.7588, $B_2$=6.32529×10$^{-2}$, $B_3$=-2.53591×10$^{-4}$, and $B_4$=6.33784×10$^{-7}$, in the temperature range between 0 and 100°C.

The saturated vapor pressure ($p_{sv}$) [21] is expressed by

$$p_{sv} = 10^3 \times 0.1 \times 10^e \quad (10)$$

where

$$e = E_0 + E_1\left(1 - \frac{273}{T+273}\right) - E_2\, log_{10}\left(\frac{T+273}{273}\right) + E_3\left(1 - 10^{-8.2969\times\left(\frac{T+273}{273}-1\right)}\right) + E_4\left(10^{4.76955\times\left(1-\frac{273}{T+273}\right)}\right)$$

and

$E_0$=0.78614, $E_1$=10.79574, $E_2$=5.028, $E_3$=1.50475×10$^{-4}$, $E_4$=0.42873×10$^{-3}$.

At atmospheric pressure, the dynamic viscosity of humid air ($\mu$) [14] is calculated by:

$$\mu = \frac{\mu_a \times (1-x_v)}{[(1-x_v)+x_v\Phi_{av}]} + \frac{x_v \times \mu_v}{[x_v+(1-x_v)\times\Phi_{va}]} \quad (11)$$

where $\mu_a$ and $\mu_v$ are the dynamic viscosity of dry air and water vapor, respectively, as:

$$\mu_a = M_{A_0} + \sum_{i=1}^{4} M_{A_i}(T+273)^i \quad (12)$$

$$\mu_v = M_{V_0} + M_{V_1} T \quad (13)$$

and

$M_{A0}$=-9.8601×10$^{-7}$, $M_{A1}$=9.08012×10$^{-8}$, $M_{A2}$=-1.1764×10$^{-10}$, $M_{A3}$=1.2350×10$^{-13}$, $M_{A4}$=-5.797×10$^{-17}$, $M_{V0}$ =8.058×10$^{-6}$, and $M_{V1}$=4.0005×10$^{-8}$

Also, $\Phi_{av}$ and $\Phi_{va}$ are calculated by

$$\Phi_{av} = \frac{\sqrt{2}}{4}\left(1 + \frac{M_a}{M_v}\right)^{-0.5} \times \left[1 + \left(\frac{\mu_a}{\mu_v}\right)^{0.5} \times \left(\frac{M_v}{M_a}\right)^{0.25}\right]^2 \quad (14)$$

$$\Phi_{va} = \frac{\sqrt{2}}{4}\left(1 + \frac{M_v}{M_a}\right)^{-0.5} \times \left[1 + \left(\frac{\mu_v}{\mu_a}\right)^{0.5} \times \left(\frac{M_a}{M_v}\right)^{0.25}\right]^2 \quad (15)$$

where $\Phi_{av}$ and $\Phi_{va}$ are interaction factors for calculating $\mu_a$ and $\mu_v$, respectively; $M_{Ai}$ and $M_{Vi}$ are interpolation constants for the dynamic viscosity of dry air and water vapor, respectively; $M_a$ and $M_v$ are the dry air and water vapor molar mass, respectively.

For the effect of gas rarefaction, the Poiseuille flow rate $Q_P(D)$ [13] is derived for arbitrary inverse Knudsen number ($D$) with the accommodation coefficients of two surfaces ($\alpha_1$=$\alpha_2$=1.0) by:

$$Q_P(D) = 1 + 3\sqrt{\pi} \times a \times D^{-1} + 6b \times D^c \quad (16)$$

where $a$=0.01807, $b$=1.35355, $c$=-1.17468.

The inverse Knudsen number ($D$) is expressed by:

$$D = \frac{\sqrt{\pi}}{2K_n} = \frac{\sqrt{\pi}h}{2\lambda} \quad (17)$$

where $h$ is the gap spacing.

The mean free path of gas is estimated from the kinetic theory of gases [22] is expressed as:

$$\lambda = \frac{RT}{\sqrt{2}\pi \times N_a d^2 p} \quad (18)$$

where $d$ is the gas molecular diameter; $R$=8.314 (J/mol) is the gas constant; $N_a$=6.0221×10$^{23}$ is Avogadro's number.

From Eqs. (3), (7), and (18), the mean free path of moist air (λ) can be expressed by:

$$\lambda = \frac{\lambda_0 p_0' T}{p T_0'} = \frac{\lambda_0 p_0' T}{(p_a + RH \cdot p_{sw}) T_0'}, \quad (19)$$

where $\lambda_o$=66.5 nm, $p_0'$=101325 Pa, $T_0'$=300 K are the reference gas mean free path, reference pressure, and reference temperature, respectively.

The effective viscosity ($\mu_{eff}$) of moist air [11] is expressed by:

$$\mu_{eff} = \frac{\mu}{Q_P} \quad (20)$$

where $\mu_{eff}$ ($RH$, $T$) can be used to consider the effects of temperature and relative humidity in atmospheric pressure and gas rarefaction.

### 2.2. The linear transverse vibration equation for micro-beam resonators

Under small displacement ($w$), the linear transverse vibration equation of a micro-beam in Fig. 1 governs the transverse displacement [23], which is expressed as:

$$D_p\left(\frac{\partial^4 w}{\partial x^4}+2\frac{\partial^4 w}{\partial x^2\partial y^2}+\frac{\partial^4 w}{\partial y^4}\right)+\rho_m t_b\frac{\partial^2 w}{\partial t^2}=-\bar{p}(x,y,t) \quad (21)$$

where $D_P$ ($=Et_b^3/12(1-v^2)$) is the rigidity of the material; $E$ is Young's modulus; ν is the Poisson's ratio; $t_b$ is the structural thickness; $\bar{p}(x,y,t)$ is the gas pressure variation; $w(x, y, t)$ is the transverse displacement at positions along the structure $(x, y)$ over time $(t)$; $p_m$ is the density of the material.

For a micro-cantilever beam [18, 19], single-clamped boundary conditions are used at one edge of the cantilever ($x$=0):

$$w(0,y,t)=0 \quad (22)$$

$$\frac{\partial w(0,y,t)}{\partial x}=0 \quad (23)$$

and three free boundaries are used at the other edges of the cantilever ($x=l_b$, $y=0$, and $y=w_b$):

$$\frac{\partial^2 w(\ell_b,y,t)}{\partial x^2}=\frac{\partial^3 w(\ell_b,y,t)}{\partial x^3}=0 \quad (24)$$

$$\frac{\partial^2 w(x,0,t)}{\partial y^2}=\frac{\partial^3 w(x,0,t)}{\partial y^3}=0 \quad (25)$$

$$\frac{\partial^2 w(x,w_b,t)}{\partial y^2}=\frac{\partial^3 w(x,w_b,t)}{\partial y^3}=0 \quad (26)$$

For a micro-bridge, the two double-clamped boundary conditions are set at two edges of the micro-bridge ($x=0$) and ($x=l_b$):

$$(0,y,t)=w(\ell_b,y,t)=0 \quad (27)$$

$$\frac{\partial w(0,y,t)}{\partial x}=\frac{\partial w(\ell_b,y,t)}{\partial x}=0 \quad (28)$$

and two free-edge conditions at other edges of the micro-bridge ($y=0$, $y=w_b$):

$$\frac{\partial^2 w(x,0,t)}{\partial y^2}=\frac{\partial^3 w(x,0,t)}{\partial y^3}=0 \quad (29)$$

$$\frac{\partial^2 w(x,w_b,t)}{\partial y^2}=\frac{\partial^3 w(x,w_b,t)}{\partial y^3}=0 \quad (30)$$

### 2.3. Quality factors of micro-beam resonators

In the eigen-value problem, the quality factor of the MEMS resonators in the SFD problem is numerically estimated by obtaining the eigenvalue ($\bar{\lambda}=\delta+i\omega$). Then, the quality factor for the SFD problem ($Q_{SFD}$) [14] can be calculated as the ratio between the natural frequency ($\omega_0$) ($Im|\bar{\lambda}|$) and the damping factor (δ) ($\delta$) ($Re|\bar{\lambda}|$) by:

$$Q_{SFD}=\left|\frac{Im(\bar{\lambda})}{2\,Re(\bar{\lambda})}\right|=\frac{\omega_0}{2\delta} \quad (31)$$

where $\bar{\lambda}(=\delta+i\omega)$ is the complex eigenvalue.

In micro-beam resonators, the total quality factor ($Q_T$) can be evaluated by the quality factor of the main damping sources of the SFD ($Q_{SFD}$), TED ($Q_{TED}$), and the support loss ($Q_{sup}$). Therefore, the total quality factor ($Q_T$)) of the micro-cantilever and bridge beam resonators are calculated as:

$$\frac{1}{Q_T}=\frac{1}{Q_{SFD}}+\frac{1}{Q_{TED}}+\frac{1}{Q_{sup}} \quad (32)$$

where the basic operating conditions are listed in Table 1. $Q_{TED}$ is calculated by C. Zener's models [6, 7] (Eq. (14) in [7]) in Table 2. $Q_{sup}$ is also calculated by Z. Hao, et al. (2003) [10] (Eq. (18) in Table 3).

**Table 1. Basic geometric and operating conditions of MEMS resonators.**

| Symbol | Description | Values |
|---|---|---|
| $l_b$ | Length of beam | 250 µm |
| $w_b$ | Width of beam | 10 µm |
| $t_b$ | Thickness of beam | 1 µm |
| $E$ | Young's modulus of silicon | $130\times10^9$ Pa |
| $\rho_m$ | Density of silicon | 2330 kg/m$^3$ |
| $v$ | Poisson's ratio of silicon | 0.28 |
| $\alpha_m$ | Thermal expansion coefficient of silicon | $2.6\times10^{-6}$ 1/K |
| $\kappa$ | Thermal conductivity of silicon | 90 W/(m.K) |
| $C_P$ | Specific heat capacity of silicon cantilever | 700 J/(kg.K) |
| $h_0$ | Basic gas film thickness | 4 µm |
| $T_0$ | Basic temperature | 50°C |
| $p$ | Ambient pressure of moist air | 101325 Pa |
| $T$ | Ambient temperature | 0-100°C |
| $RH$ | Relative humidity of moist air | 0-100% |

**Table 2. The quality factor of thermoelastic damping (TED) ($Q_{TED}$) for micro-beam resonators in the 1st mode of vibration.**

| Resonators | Mode shape | (Hz) | $Q_{TED}$ *in* FEM [24] | $Q_{Zener}$ in Zener [6, 7] | % Error $\left\|\frac{Q_{TED}-Q_{Zener}}{Q_{TED}}\right\|\times 100\%$ |
|---|---|---|---|---|---|
| Cantilever |  | 19,344 | 21,738,340 | 22,589,923 | 3.77 |
| Bridge |  | 123,539 | 3,283,491 | 3,491,068 | 5.94 |

**Table 3. The quality factor of support loss ($Q_{sup}$) for micro-beam resonators in the 1st mode of vibration.**

| Resonators | Mode shape | $f_n$ (Hz) | $C_{(F(n))}$ | $\lambda_T$ | $\lambda_T/w_b$ | $Q_{sup}$ [10] |
|---|---|---|---|---|---|---|
| Cantilever |  | 19,344 | 2.081 | 0.241 | 24,133 | 32,515,625 |
| Bridge |  | 123,539 | 0.638 | 0.038 | 3,778 | 9,968,750 |

## 3. Results and discussion

### *3.1. Effective viscosity, $\mu_{eff}(RH, T)$*

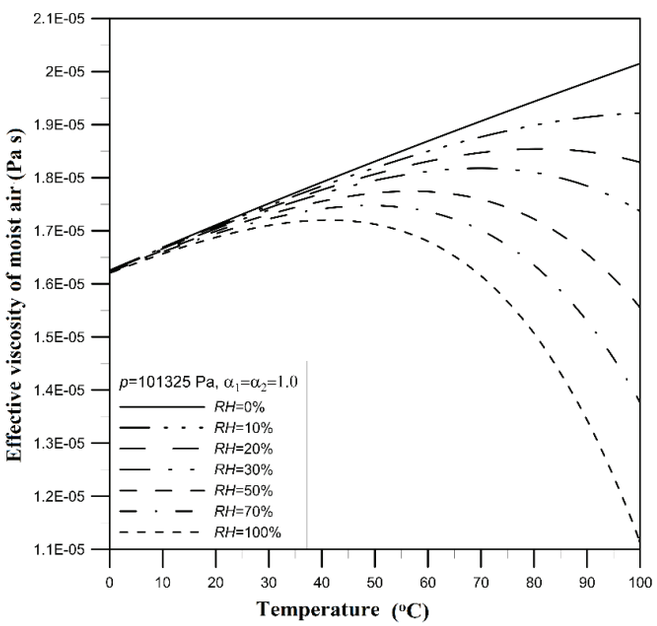


**Fig. 2. Effective viscosity of moist air ($\mu_{eff}$) versus temperature ($T$) for different relative humidity values ($RH$) at atmospheric pressure.**

In Fig. 2, the effective viscosity of moist air ($\mu_{eff}$), Eq. (20), in dry air linearly increases with $T$ in the dry air ($RH$=0%). Meanwhile, $\mu_{eff}$ of moist air decreases gradually as temperature and relative humidity increase. Therefore, we note that the effective viscosity ($\mu_{eff}$) decreases more significantly as temperature and relative humidity increase.

### *3.2. Effects of temperature (T) and relative humidity (RH) on quality factors ($Q_{SFD}$, $Q_T$)*

In Table 2, the results show that $Q_{TED}$ and $Q_{Zener}$ are very high because the TED is very small in the 1st mode of cantilever and bridge resonators. Moreover, $Q_{TED}$ from the FEM (COMSOL Multiphysics) [24] and $Q_{Zener}$ from the C. Zener's models [6, 7] are nearly identical with an error of less than 5.94%. Therefore, $Q_{TED}$ in the FEM [24] can be accurately used to calculate the total quality factor ($Q_T$) of MEMS resonators.

In Table 3, the result showed that $Q_{sup}$ is very high because the support loss is very small in the 1st mode of the resonators. Also, the results of $Q_{sup}$ can be used to calculate the total quality factor ($Q_T$) of micro-beam resonators.

In Fig. 3, the obtained results of $Q_{SFD}$ and $Q_T$ of the micro-beam resonators are nearly identical over a wide range of temperature and humidity values at atmospheric pressure ($p$=101325 Pa). Therefore, $Q_T$ can be calculated by the main contribution of $Q_{SFD}$ because the SFD is the dominant damping source and the other damping sources ($Q_{TED}$, $Q_{sup}$) are negligible in the 1st mode of the resonator. $Q_{SFD}$ and $Q_T$ of dry air decreases as $T$ increases. $Q_{SFD}$ and $Q_T$ of moist air increases as $T$ increases while $Q_{SFD}$ and $Q_T$ of moist air increases as relative humidity ($RH$) increases from 0 to 100 % at atmospheric pressure. Then, $Q_{SFD}$ and

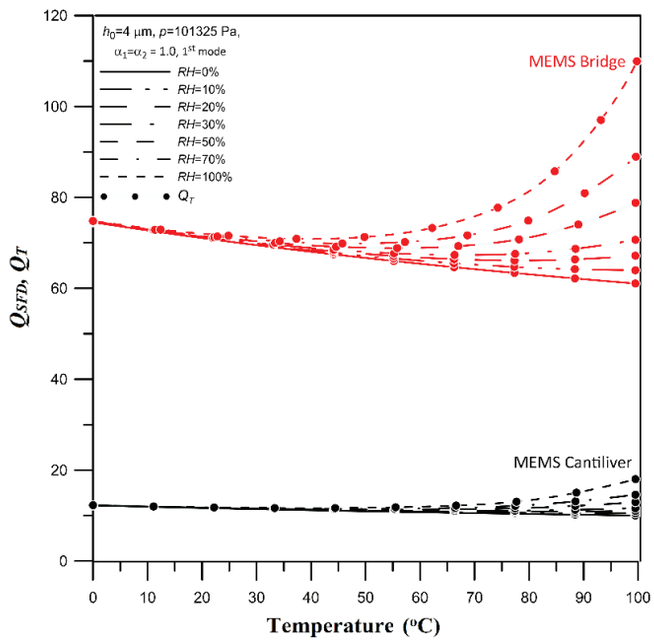


**Fig. 3. The quality factor by SFD ($Q_{SFD}$) and total quality factor ($Q_T$) versus ambient temperature ($T$) for different relative humidity ($RH$) values in the 1st modes of MEMS cantilever and bridge beam resonators at atmospheric pressure ($p$=101325 Pa).**

$Q_T$ of moist air increases with temperature and relative humidity at $p$=101325 Pa. Also, $Q_{SFD}$ and $Q_T$ of the micro-cantilever with temperature and relative humidity is lower than that of the micro-bridge because of SFD influences on the cantilever being much stronger than that on the micro-bridge.

## 4. Conclusions

In these results, the quality factors of micro-beam resonators are numerically calculated by solving the MMGL equation, the equation of transverse vibration of the micro-beam, and their appropriate boundary conditions simultaneously using the FEM. The effective viscosity ($\mu_{eff}(RH, T)$) is utilised to modify the MMGL equation to consider the effects of temperature and relative humidity in atmospheric pressure and gas rarefaction. Some of the obtained results are shown as follows: (a) The quality factor of micro-beam resonators increases as the temperature and relative humidity increase in atmospheric pressure and gas rarefaction; (b) The quality factor of the micro-bridge resonator with temperature and relative humidity is much higher than that of the micro-cantilever resonator.

These highlighted results can be utilised to design for a high-quality factor and a fast resonant response of MEMS resonators. In future work, the design and fabrication process of temperature and humidity sensors based on micro-bridge resonators can be addressed and fabricated using MEMS technologies for environmental monitoring.

## CRediT author statement

Nguyen Chi Cuong: Supervision, Conceptualisation, Writing - Reviewing; Trinh Xuan Thang, Lam Minh Thinh, Vuong Dinh Duy Phuc, Phan Minh Truong, Truong Huu Ly, Ngo Vo Ke Thanh, Le Quoc Cuong: Reviewing and Editing.

## ACKNOWLEDGEMENTS

This research was supported by the Ho Chi Minh City Department of Science and Technology of Vietnam, Contract number 12/2021/HD-QKHCN on 24th March 2021. Also, this research was supported by the annual projects of the Research Laboratories of Saigon High-Tech Park, Board of Management of Saigon High-Tech Park, Decision number 17/QD-KCNC on 1st February 2023 (Project number 1).

## COMPETING INTERESTS

The authors declare that there is no conflict of interest regarding the publication of this article.

## REFERENCES

[1] L. Wei, X. Kuai, Y. Bao, et al. (2021), "The recent progress of MEMS/NEMS resonators", *Micromachines*, **12(6)**, DOI: 10.3390/mi12060724.

[2] P. Wei, Z. Ning, S. Ye, et al. (2018), "Impact analysis of temperature and humidity conditions on electrochemical sensor response in ambient air quality monitoring", *Sensors*, **18(2)**, DOI: 10.3390/s18020059.

[3] Y. Zou, J.D. Clark, A.A. May (2021), "A systematic investigation on the effects of temperature and relative humidity on the performance of eight low-cost particle sensors and devices", *J. Aerosol. Sci.*, **152**, DOI: 10.1016/j.jaerosci.2020.105715.

[4] D. Zhao, Y. Wang, J. Shao, et al. (2021), "Temperature and humidity sensor based on MEMS technology", *AIP Advances*, **11(8)**, DOI: 10.1063/5.0053342.

[5] H. Hosaka, K. Itao, S. Kuroda (1995), "Damping characteristics of beam-shaped micro-oscillators", *Sensors and Actuators A: Physical*, **49(1-2)**, pp.87-95, DOI: 10.1016/0924-4247(95)01003-J.

[6] C. Zener (1937), "Internal friction in solids I theory of internal friction in reeds", *Phys. Rev.*, **52(3)**, pp.230-235.

[7] C. Zener (1938), "Internal friction in solids II general theory of thermoelastic internal friction", *Phys. Rev.*, **53(1)**, pp.90-99.

[8] Y. Fu, L. Li, Y. Hu (2019), "Enlarging quality factor in microbeam resonators by topology optimization", *Journal of Thermal Stresses*, **42(3)**, pp.341-360, DOI: 10.1080/01495739.2018.1489744.

[9] Y. Fu, L. Li, H. Chen, et al. (2022), "Rational design of thermoelastic damping in microresonators with phase-lagging heat conduction law", *Applied Mathematics and Mechanics*, **43**, pp.1675-1690, DOI: 10.1007/s10483-022-2914-5.

[10] Z. Hao, A. Erbil, F. Ayazi (2003), "An analytical model for support loss in micromachined beam resonators with in-plane flexural vibrations", *Sensor. Actuat. A-Phy.*, **109(1-2)**, pp.156-164, DOI: 10.1016/j.sna.2003.09.037.

[11] C.C. Nguyen, W.L. Li (2017), "Effect of gas rarefaction on the quality factors of micro-beam resonators", *Microsyst. Technol.*, **23(8)**, pp.3185-3199, DOI: 10.1007/s00542-016-3068-z.

[12] A.K. Pandey, R. Pratap (2007), "Effect of flexural modes on squeeze film damping in MEMS cantilever resonators", *J. Micromech. Microeng.*, **17(12)**, pp.2475-2484, DOI: 10.1088/0960-1317/17/12/013.

[13] C.C. Hwang, R.F. Fung, R.F. Yang, et al. (1996), "A new modified Reynolds equation for ultrathin film gas lubrication", *IEEE Trans. Magn.*, **32(2)**, pp.344-347, DOI: 10.1109/20.486518.

[14] P.T. Tsilingiris (2008), "Thermophysical and transport properties of humid air at temperature range between 0 and 100°C", *Energ. Convers. Manage.*, **49(5)**, pp.1098-1110, DOI: 10.1016/j.enconman.2007.09.015.

[15] E. Hosseinian, P.O. Theillet, O.N. Pierron (2013), "Temperature and humidity effects on the quality factor of a silicon lateral rotary micro-resonator in atmospheric air", *Sensors and Actuators A: Physical*, **189**, pp.380-389, DOI: 10.1016/j.sna.2012.09.020.

[16] H. Hosseinzadegan, O.N. Pierron, E. Hosseinian (2014), "Accurate modeling of air shear damping of a silicon lateral rotary micro-resonator for MEMS environmental monitoring applications", *Sensors and Actuators A: Physical*, **216**, pp.342-348, DOI: 10.1016/j.sna.2014.06.008.

[17] M.T. Jan, F. Ahmad, N.H.B. Hamid, et al. (2016), "Experimental investigation of temperature and relative humidity effects on resonance frequency and quality factor of CMOS-MEMS paddle resonator", *Microelectron. Reliab.*, **63**, pp.82-89, DOI: 10.1016/j.microrel.2016.05.007.

[18] Q.C. Le, M.T. Phan, X.T. Trinh, et al. (2021), "Temperature and relative humidity dependence of quality factors of mems cantilever resonators in atmospheric pressure", *Sensing and Imaging*, **22(36)**, pp.1-30, DOI: 10.1007/s11220-021-00359-x.

[19] C.C. Nguyen, M.T. Phan, X.T. Trinh, et al. (2022), "Effects of temperature and relative humidity on resonant frequency of MEMS cantilever resonators under atmospheric pressure", *Vietnam Journal of Science and Technology*, **60(4)**, pp.724-736, DOI: 10.15625/2525-2518/16347.

[20] L. Greenspan (1976), "Functional equations for the enhancement factors for $CO_2$-free moist air", *J. Res. National. Bureau. Standards - A Phys. Chem.*, **80A(1)**, pp.41-44, DOI: 10.6028/jres.080A.007.

[21] M.H. Hasan (2018), *Influence of Environmental Conditions on The Response of MEMS Resonators*, Master of Science Thesis, University of Nebraska-Lincoln, 114pp.

[22] Z. Tan (2014), "Air pollution and greenhouse gases from basic concepts to engineering applications for air emission control", *Green Energy and Technology*, Springer, DOI: 10.1007/978-981-287-212-8.

[23] A.W. Leissa (1969), *Vibration of Plates*, NASA Technical Reports Server, 362pp.

[24] COMSOL Multiphysics (2022), *Thermoelastic Damping in a MEMS Resonator*, https://www.comsol.com/model/thermoelastic-damping-in-a-mems-resonator-1439, accessed 24 November 2022.

DOI: 10.31276/VJSTE.66(1).10-15

# Effect of annealing temperature and doping concentrations on structure and optical properties of $Eu^{3+}$-doped $TiO_2$ nanomaterials

**Nguyen Tri Tuan[1*], Tong Thi Hao Tam[2*], Nguyen Tu[3], Do Quang Trung[3], Nguyen Van Du[3], Tran Minh Tien[3], Vu Thi Hang[1], Nguyen Trong Tuan[1], Nguyen Van Quang[4], Manh Trung Tran[5]**

*[1]College of Natural Sciences, Can Tho University,*
*Campus II, 3/2 Street, Xuan Khanh Ward, Ninh Kieu District, Can Tho City, Vietnam*
*[2]School of Information Technology and Digital Economics, National Economics University,*
*207 Giai Phong Street, Dong Tam Ward, Hai Ba Trung District, Hanoi, Vietnam*
*[3]Faculty of Fundamental Sciences, Phenikaa University,*
*Yen Nghia Ward, Ha Dong District, Hanoi, Vietnam*
*[4]Department of Chemistry, Hanoi Pedagogical University 2,*
*Nguyen Van Linh Street, Xuan Hoa Ward, Phuc Yen City, Vinh Phuc Province, Vietnam*
*[5]Faculty of Materials Science and Engineering, Phenikaa University,*
*Yen Nghia Ward, Ha Dong District, Hanoi, Vietnam*

Received 9 March 2023; revised 13 April 2023; accepted 1 August 2023

***Abstract:***

**In this study, we successfully synthesized europium-doped $TiO_2$ ($TiO_2$:$Eu^{3+}$) nanomaterials (NMs) with crystalline sizes ranging from 6.5 to 71.7 nm through a sol-gel method. Analysis of X-ray diffraction (XRD) patterns and ultraviolet-visible (UV-Vis) spectra indicates that the substitution of smaller-sized $Ti^{4+}$ ions (0.745 Å) by larger-sized $Eu^{3+}$ ions (0.947 Å) was more efficient at higher doping concentrations and annealing temperatures. Photoluminescence (PL) and photoluminescence excitation (PLE) spectra of the synthesized $TiO_2$:7%$Eu^{3+}$ NMs exhibit a strong red emission band peaking at 613 nm and remarkable absorption in the blue light region centered at 463 nm, making them suitable for use in white light-emitting diode (WLED) applications. Our findings reveal that both annealing temperature and doping concentration significantly influence the structure and properties of these materials. Besides, the research team has seen, under the experimental conditions, the $TiO_2$:7%$Eu^{3+}$ sample annealed at 800°C exhibits the highest PL intensity. These results underscore the potential of the synthesized $TiO_2$:$Eu^{3+}$ NMs as red-emitting materials for WLED applications.**

***Keywords:*** **$Eu^{3+}$ doped $TiO_2$, nanomaterials (NMs), photoluminescence, sol-gel method, $TiO_2$.**

***Classification numbers:*** **2.1, 2.3**

## 1. Introduction

In the present era, the realization of WLEDs can be achieved through three distinct techniques, namely: i) the combination of red, green, and blue LED chips; ii) the utilization of near-ultraviolet (NUV) LED chips in conjunction with tricolor phosphors (blue, green, and red phosphors); iii) the employment of a yellow-emitting $Y_3Al_5O_{12}$:$Ce^{3+}$ phosphor with a blue LED chip [1]. Nonetheless, current commercial WLEDs frequently suffer from a deficiency in the red light spectrum, resulting in a low color rendering index (CRI<80) [2]. Consequently, the incorporation of a red light emission component into WLEDs becomes imperative for achieving high CRI values. To address this challenge, the development of red-emitting phosphors that can be efficiently excited by blue or near-NUV light has become a pressing need [1-3]. Unfortunately, existing red-emitting nitride or sulfide-based materials, which are excitable by blue or NUV light, are marred by chemical instability and environmental hazards [4, 5]. Recent research efforts have thus focused on red-emitting $Eu^{3+}$-doped oxide phosphors that can be excited by NUV light, such as $Y_2O_3$, $CaMoO_4$ [6, 7]. Amongst semiconductor oxides, anatase-phase titanium dioxide ($TiO_2$) emerges

*Corresponding author: Email: trituan@ctu.edu.vn

as a promising host lattice due to its attributes of a high band gap (3.2 eV), chemical stability, facile synthesis, affordability, non-toxicity, and non-hygroscopic behavior [2]. Recent studies have demonstrated that $Eu^{3+}$-doped $TiO_2$ can be effectively excited by blue light and exhibit a red emission band spanning from 540 to 740 nm, attributed to the $^5D_0$-$^7F_j$ (j=1-4) transitions of $Eu^{3+}$ ions [1, 8]. However, optimizing the procedure for synthesizing $Eu^{3+}$-doped $TiO_2$ phosphors remains challenging owing to the significant differences in ionic radius and charge imbalance [2].

This study presents successful doping of $Eu^{3+}$ ions into the $TiO_2$ host lattice using a sol-gel method. It comprehensively investigates and discusses the impact of annealing temperature and doping concentration on the structure and optical properties of $Eu^{3+}$-doped $TiO_2$ NMs.

## 2. Materials and methods

### *2.1. Synthesis of $Eu^{3+}$ doped $TiO_2$ NMs*

$Eu^{3+}$-doped $TiO_2$ ($TiO_2$:x%$Eu^{3+}$, x=1-10) NMs were synthesized via a sol-gel method. Initially, a mixture of $Eu(NO_3)_3$ and 20 ml of ethanol was stirred for 30 minutes. Subsequently, 5 ml of titanium butoxide ($Ti(OBu)_4$) and 0.85 ml of acetic acid ($CH_3COOH$) were added and stirred continuously for 10 minutes. Nitric acid ($HNO_3$) was gradually introduced to maintain a pH of 2 in the solution. It is worth noting that the calculated mole ratio of $Eu^{3+}$ ions in $TiO_2$ ranged from 1 to 10 mol%. In the subsequent step, the solution was further stirred for 2 hours and then air-dried at room temperature for 24 hours to yield a dry gel product. Finally, this dry gel was subjected to annealing at 100°C for 12 hours, followed by a second annealing process in air, ranging from 200 to 1000°C for 2 hours, to obtain the $TiO_2$:$Eu^{3+}$ NMs.

### *2.2. Characterisation*

The surface morphology and crystallite structure of $TiO_2$:$Eu^{3+}$ NMs were analyzed using a field emission scanning electron microscope (FESEM-JEOL JSM-7600F) and XRD, D8 Advanced). The band gap energy was determined through UV-Vis absorption spectra, employing the JASCO V-750 Spectrophotometer. PL and PLE spectra were recorded using a Nanolog spectrophotometer, excited by a 450 W Xenon lamp, at room temperature.

## 3. Results and discussion

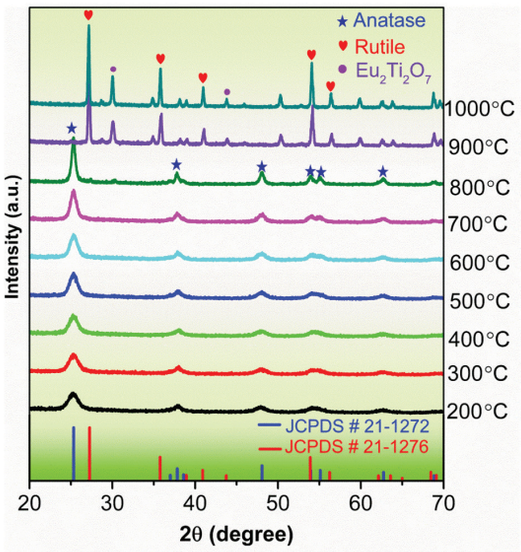


**Fig. 1. XRD patterns of as-synthesized $TiO_2$:7%$Eu^{3+}$ NMs annealed in air at different temperatures of 200-1000°C for 2 hours.**

The XRD patterns of the as-synthesized $TiO_2$:7%$Eu^{3+}$ NMs, annealed in air in the range of 200-1000°C for 2 hours, are presented in Fig. 1. At the lower temperature of 700°C, distinct diffraction peaks are observed at 2θ=25.28, 37.88, 48.09°, 53.98, 55.20, and 62.69°, corresponding to the (101), (004), (200), (105), (211), and (204) planes of the $TiO_2$ anatase phase (JCPDS # 21-1272), without any evidence of impurity phases [1]. When the temperature [8] is raised to 800°C, in addition to the anatase phase, new diffraction peaks attributed to rutile (JCPDS # 21-1276) [9] and $Eu_2TiO_7$ (JCPDS 01-087-1852) phases emerge in the XRD pattern. These peaks become prominent in samples annealed at higher temperatures (900 and 1000°C), indicating a phase transition from anatase to $TiO_2$ rutile and $Eu_2TiO_7$ at 800°C.

Figure 2 presents the focused XRD patterns within the 2θ range of 20 to 45°, revealing an increase in peak intensity and a reduction in the full width at half maximum (FWHM) with increasing temperature. This observation confirms the formation of a more well-defined crystalline structure with higher annealing temperatures. Furthermore, a slight shift in the peak position towards a larger angle at higher temperatures is noted. This shift can be attributed to the enhanced substitution of smaller-sized $Ti^{4+}$ ions (0.745 Å) by larger-sized $Eu^{3+}$ ions (0.947 Å) within the $TiO_2$ host lattice [10, 11].

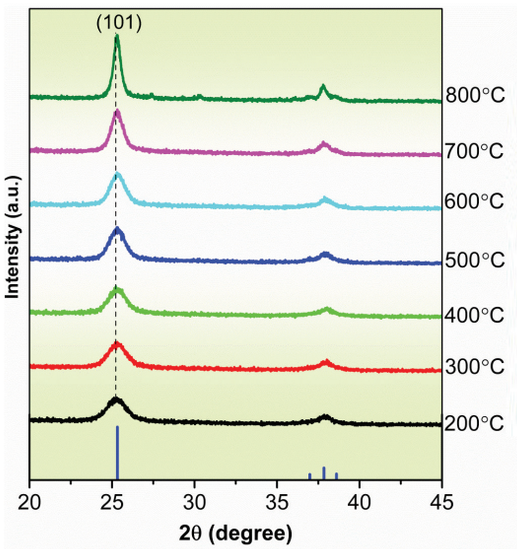


**Fig. 2. XRD patterns focused in 2θ range from 20 to 45° of as-synthesized $TiO_2$:7%$Eu^{3+}$ NMs annealed in air in the range of 200-800°C for 2 hours.**

Moreover, the average crystallite size of all samples was determined using Debye-Scherrer's Eq. (1) based on the FWHM of the (101) peak [12]:

$$D = \frac{K\lambda}{\beta\cos\theta} \text{ (nm)} \quad (1)$$

where λ=1.54 Å, β, θ and K=0.9 are the X-ray wavelength, full width at half maximum of a diffraction peak, diffraction angle, and Scherrer constant, respectively. The calculated results are listed in Table 1, indicating a gradual increase in average crystallite size ranging from 6.5 Å to 71.7 Å with an increase in annealing temperature from 200 to 1000°C. A similar trend has also been reported in a previous study [12].

**Table 1. An average crystalite size of $TiO_2$:7%$Eu^{3+}$ NMs calculated at the (101) plane.**

| Temperature (°C) | β (degree) | 2θ (degree) | ~D (nm) |
|---|---|---|---|
| As-synthesize $TiO_2$:7%$Eu^{3+}$ | 1.22 | 25.3 | 6.5 |
| 200 | 1.22 | 25.3 | 6.5 |
| 300 | 1.19 | 25.3 | 6.7 |
| 400 | 1.17 | 25.3 | 6.8 |
| 500 | 1.03 | 25.3 | 7.7 |
| 600 | 0.93 | 25.3 | 8.6 |
| 700 | 0.80 | 25.4 | 10.0 |
| 800 | 0.43 | 25.4 | 18.5 |
| 900 | 0.30 | 27.2 | 51.3 |
| 1000 | 0.21 | 27.2 | 71.7 |

Figure 3 illustrates XRD patterns of $TiO_2$:x%$Eu^{3+}$ (x=0-10) NMs annealed in air at 800°C for 2 hours. Notably, only diffraction peaks corresponding to the $TiO_2$ anatase phase (JCPDS # 21-1272) were detected [1]. Additionally, the XRD patterns reveal a decrease in peak intensity with an increase in the concentration of doped $Eu^{3+}$ ions, suggesting that higher doping concentrations result in reduced crystallinity of $TiO_2$. This phenomenon can be attributed to the presence of $Eu^{3+}$ ions, which may impede the phase transition process in $TiO_2$ materials. Furthermore, the peak position exhibits a slight shift towards larger angles with higher doping concentrations, which can be attributed to the enhanced substitution of smaller-sized $Ti^{4+}$ ions (0.745 Å) by larger-sized $Eu^{3+}$ ions (0.947 Å) within the $TiO_2$ lattice [2].

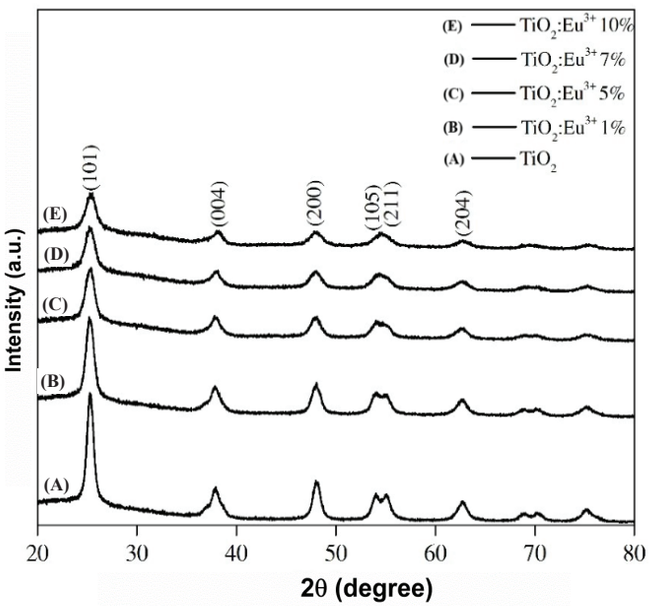


**Fig. 3. XRD patterns of $TiO_2$:*x*%$Eu^{3+}$ (x=0-10) NMs annealed in air at 800°C for 2 hours.**

Figure 4 presents field emission scanning electron microscope (FESEM) images of $TiO_2$:7%$Eu^{3+}$ NMs annealed in air at different temperatures ranging from 200 to 1000°C for 2 hours. The observations indicate a gradual increase in particle size with rising annealing temperature. This phenomenon is likely caused by the agglomeration of small clusters, resulting in the formation of larger particles at elevated temperatures [13]. The largest particle size from 200 nm at 200°C to 1 μm was obtained at 1000°C.

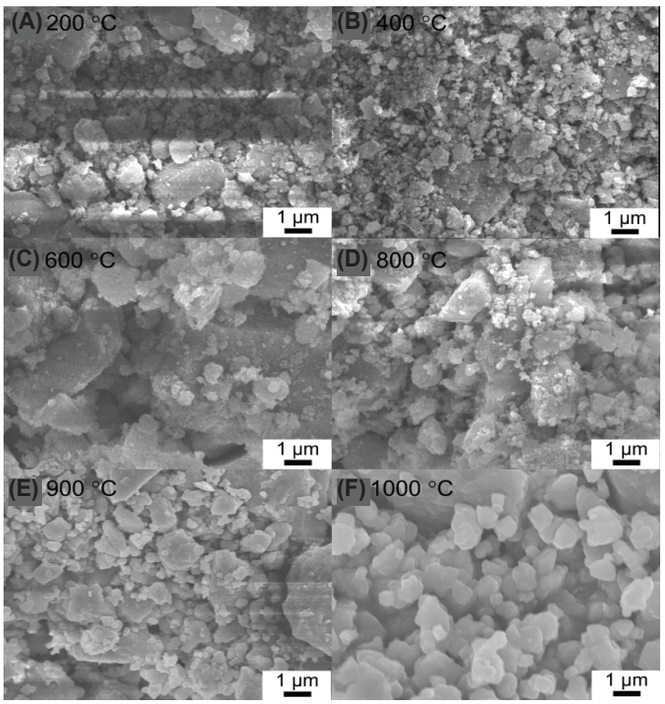


**Fig. 4. FESEM images of $TiO_2$:7%$Eu^{3+}$ NMs annealed in air at different temperatures ranging from 200-1000°C for 2 hours (A-F).**

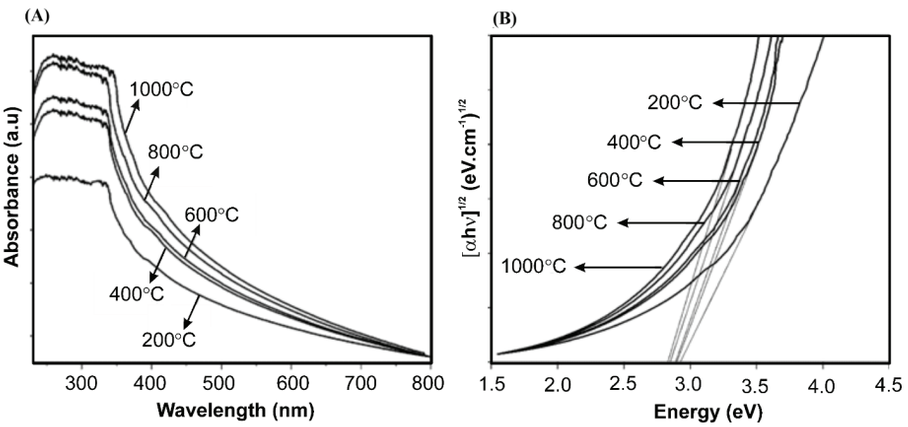


**Fig. 5. UV-Vis absorption spectra of $TiO_2$:7%$Eu^{3+}$ NMs annealed at 200, 400, 600, 800, and 1000°C (A), relationship between hv and $(\alpha hv)^2$ (B).**

Figure 5A displays the UV-Vis spectra of $TiO_2$:7%$Eu^{3+}$ NMs annealed in air at various temperatures within the range of 200 to 1000°C for 2 hours. It is evident that $TiO_2$:7%$Eu^{3+}$ NMs exhibit strong absorption in the ultraviolet region (200-350 nm) and a weaker absorbance band in the NUV to visible range (350-500 nm). The former is attributed to the near band-edge absorption of $TiO_2$, while the latter is likely associated with the presence of $Eu^{3+}$ ions doped into the $TiO_2$ lattice [3]. Furthermore, an increase in absorption intensity with rising annealing temperature can be attributed to the substitution of larger-sized $Eu^{3+}$ ions for smaller $Ti^{4+}$ ions. This phenomenon is also supported by the XRD pattern analysis presented in Fig. 2. The bandgap energy ($E_g$) of $TiO_2$:$Eu^{3+}$ NMs can be estimated from the absorption spectra in Fig. 5A using the Tauc Eq. (2) [1-3]:

$$(\alpha hv)^{1/n} = K(hv - E_g) \quad (2)$$

where α, hν, K are the absorption coefficient, photon energy and characteristic constant of the specific material, respectively. For an indirect semiconductor like $TiO_2$, n=2. Utilising the Tauc Eq. (2), the $E_g$ values for $TiO_2$:7%$Eu^{3+}$ NMs annealed at 200, 400, 600, 800, and 1000°C were calculated to be 2.94, 2.90, 2.89, 2.85, and 2.82 eV, respectively. These values indicate that the bandgap of $TiO_2$:7%$Eu^{3+}$ NMs is smaller than that of pure $TiO_2$ ($E_g$=3.2 eV) and gradually decreases with higher annealing temperatures [4, 5, 14]. This phenomenon can be attributed to the increased substitution of smaller-sized $Ti^{4+}$ ions with larger-sized $Eu^{3+}$ ions within the $TiO_2$ lattice, consistent with findings reported in recent studies [1-3].

It has been reported that the incorporation of $Eu^{3+}$ ions into the $TiO_2$ lattice introduces intermediate energy levels located below the conduction band, resulting in the narrowing of the energy band gap of $TiO_2$ [Ceramics International 43 (2017) 9838-9845]. Conversely, when $Eu^{3+}$ is introduced into the host lattice of $TiO_2$, it can increase the density of absorption centers, subsequently leading to higher absorbance in the UV-Vis spectrum. Therefore, a higher substitution of larger-sized $Eu^{3+}$ ions can increase the density of absorption centers, resulting in enhanced absorption.

Figure 6 presents the PLE spectrum measured at 613 nm (A) and the PL spectrum excited at 463 nm (B) of the $TiO_2$:7%$Eu^{3+}$ NMs annealed in air at 800°C for 2 hours. The PL spectrum exhibits a red emission band spanning from 540 to 740 nm, with peak wavelengths at 577, 594, 613, 655, and 703 nm. These peaks correspond to the $^5D_0$-$^7F_0$, $^5D_0$-$^7F_1$, $^5D_0$-$^7F_2$, $^5D_0$-$^7F_3$, and $^5D_0$-$^7F_4$ transitions of $Eu^{3+}$ ions, respectively [2, 4, 15-17]. As depicted in Fig. 6B, the PLE spectrum displays notable absorption in the blue light region centred at 463 nm, which is well explained by a $^7F_0$-$^5D_2$ transition of $Eu^{3+}$ ions [2, 5].

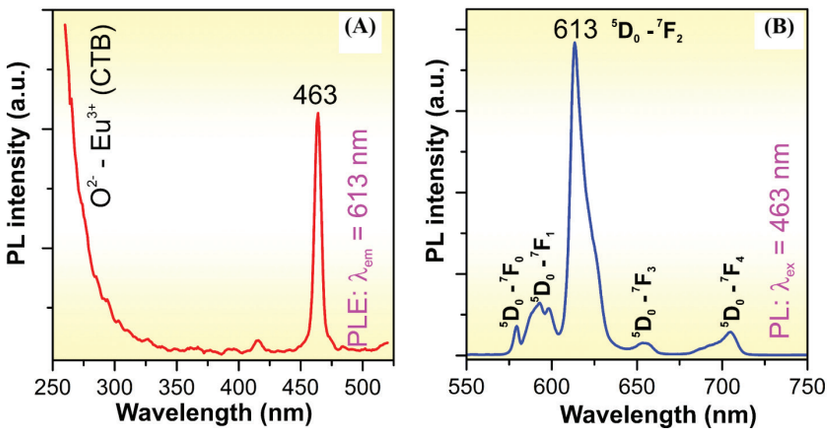


**Fig. 6. PLE spectrum measured at 613 nm (A) and PL spectrum excited at 463 nm (B) of the $TiO_2$:7%$Eu^{3+}$ NMs annealed in air at 800°C for 2 hours.**

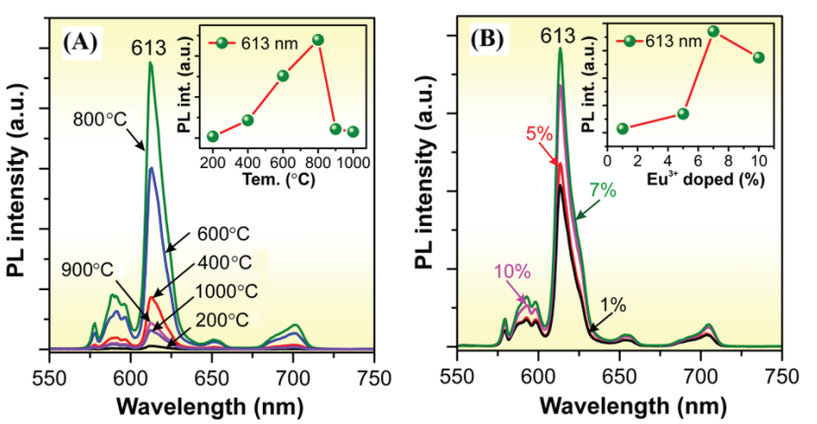


**Fig. 7. PL spectra of $TiO_2$:7%$Eu^{3+}$ NMs annealed in air at different temperatures ranging from 200-1000°C for 2 hours (A) and $TiO_2$:x%$Eu^{3+}$ (x=0-10) NMs annealed in air at 800°C for 2 hours (B).**

Figure 7A presents the PL spectra excited at 463 nm of $TiO_2$:7%$Eu^{3+}$ NMs annealed in air at different temperatures within the range of 200 to 1000°C for 2 hours. All PL spectra exhibit a similar shape, but their intensities are significantly dependent on the annealing temperature. As the annealing temperature increases from 200 to 800°C, there is a gradual enhancement in PL intensity. This improvement can be attributed to the formation of a more well-defined crystalline structure or the substitution of larger-sized $Eu^{3+}$ ions for smaller-sized $Ti^{4+}$ ions within the $TiO_2$ host lattice [13, 18, 19]. However, after reaching 800°C, there is a marked reduction in PL intensity, which can be attributed to the phase transition from anatase to rutile or the formation of the $Eu_2TiO_7$ compound.

Figure 7B illustrates the PL spectra of $TiO_2$:x%$Eu^{3+}$ (x=0-10) NMs annealed in air at 800°C for 2 hours. While the shape of the spectra remains consistent, there is a significant variation in PL intensity with increasing $Eu^{3+}$ ion concentration. The PL intensity gradually increases within the range of $Eu^{3+}$ ion concentrations from 1 to 7%, and then decreases at a higher concentration of 10%. This phenomenon can be explained by PL quenching due to concentration effects [5, 15, 20]. At low doping concentrations, the $Eu^{3+}$ ions are widely spaced apart, resulting in a low density of luminescent centres and, consequently, a low luminescent intensity. Conversely, at high concentrations, the proximity of $Eu^{3+}$ ions reaches a threshold where energy transfer among the $Eu^{3+}$ ions is facilitated, leading to a decrease in PL intensity (as seen in Fig. 7B). This is known as the PL quenching phenomenon. In this study, the PL quenching effect is observed at a higher $Eu^{3+}$ doping concentration of 7%. Thus, the optimal concentration of $Eu^{3+}$ ions to achieve the highest PL intensity is determined to be 7%.

## 4. Conclusions

In summary, we have successfully synthesised red-emitting $Eu^{3+}$-doped $TiO_2$ NMs (NMs) through a sol-gel method. Our study highlights the significant influence of annealing temperature and doping concentration on the crystalline structure and optical properties of $TiO_2$:$Eu^{3+}$ NMs. Notably, annealing at 800°C facilitated a phase transition from the anatase phase to a combination of $TiO_2$ rutile and $Eu_2TiO_7$ phases. Furthermore, a gradual increase in annealing temperature within the range of 200 to 1000°C led to a more pronounced substitution of smaller-sized $Ti^{4+}$ ions (0.745 Å) by larger-sized $Eu^{3+}$ ions (0.947 Å) within the $TiO_2$ lattice. The PL spectra, excited at 463 nm, exhibited a substantial red emission band with peak wavelengths at 577, 594, 613, 655, and 703 nm, corresponding to the $^5D_0$-$^7F_0$, $^5D_0$-$^7F_1$, $^5D_0$-$^7F_2$, $^5D_0$-$^7F_3$, and $^5D_0$-$^7F_4$ transitions of $Eu^{3+}$ ions, respectively. Remarkably, the $TiO_2$:7%$Eu^{3+}$ sample annealed at 800°C demonstrated the highest PL intensity, indicating the optimal conditions for emission enhancement. In conclusion, our study underscores the promising potential of $TiO_2$:$Eu^{3+}$ NMs for applications in WLEDs, owing to their unique optical properties and tunability.

## CRediT author statement

Nguyen Tri Tuan: Reviewing, Methodology, Formal analysis, Writing, Editing; Tong Thi Hao Tam, Nguyen Tu, Do Quang Trung, Nguyen Van Du, Tran Minh Tien, Vu Thi Hang: Data analysis; Nguyen Trong Tuan, Nguyen Van Quang: Editing; Manh Trung Tran: Reviewing, Editing.

## ACKNOWLEDGEMENTS

This research is funded by the Vietnam National Foundation for Science and Technology Development (NAFOSTED) under grant number 103.03-2017.375.

## COMPETING INTERESTS

The authors declare that there is no conflict of interest regarding the publication of this article.

## REFERENCES

[1] W. Chen, A. Zhou, X. Yang, et al. (2013), "Structure and luminescence properties of $TiO_2$:$Eu^{3+}$ for WLED", *J. Alloys Compd.*, **581**, pp.330-334, DOI: 10.1016/j.jallcom.2013.07.072.

[2] A.K. Kunti, S.K. Sharma (2017), "Structural and spectral properties of red light emitting $Eu^{3+}$ activated $TiO_2$ nanophosphor for white LED application", *Ceram. Int.*, **43(13)**, pp.9838-9845, DOI: 10.1016/j.ceramint.2017.04.166.

[3] M. Pal, U. Pal, J.M.G.Y. Jimenez, et al. (2012), "Effects of crystallisation and dopant concentration on the emission behavior of $TiO_2$:Eu nanophosphors", *Nanoscale Res. Lett.*, **7(1)**, pp.1-12, DOI: 10.1186/1556-276X-7-1.

[4] S. Stojadinovic, N. Radic, B. Grbic, et al. (2016), "Structural, photoluminescent and photocatalytic properties of $TiO_2$:$Eu^{3+}$ coatings formed by plasma electrolytic oxidation", *Appl. Surf. Sci.*, **370**, pp.218-228, DOI: 10.1016/j.apsusc.2016.02.131.

[5] D. Komaraiah, E. Radha, J. James, et al. (2019), "Effect of particle size and dopant concentration on the Raman and the photoluminescence spectra of $TiO_2$:$Eu^{3+}$ nanophosphor thin films", *J. Lumin.,* **211**, pp.320-333, DOI: 10.1016/j.jlumin.2019.03.050.

[6] N.D.Q. Anh, H.Y. Lee, T.T. Phuong, et al. (2017), "$Y_2O_3$:$Eu^{3+}$ phosphor: A novel solution for an increase in color rendering index of multi-chip white LED packages", *J. Chinese Inst. Eng. Trans. Chinese Inst. Eng. A.*, **40(3)**, pp.228-234, DOI: 10.1080/02533839.2017.1299592.

[7] E. Red, C. Bi, S. Yan, et al. (2007), "Enhanced red emission in $CaMoO_4$:$Bi^{3+}$, $Eu^{3+}$", *J. Phys. Chem. C*, **111(35)**, pp.13256-13260, DOI: 10.1021/jp073991c.

[8] X. Xu, S. Wen, Q. Mao, et al. (2018), "N-Anchoring in rare earth-doped amorphous $TiO_2$ as a route to broadband down-conversion phosphor", *ACS Appl. Mater. Interfaces*, **10(45)**, pp.39238-39244, DOI: 10.1021/acsami.8b11998.

[9] D. Padayachee, A.S. Mahomed, S. Singh, et al. (2020), "Effect of the $TiO_2$ anatase/rutile ratio and Interface for the oxidative activation of n-Octane", *ACS Catal.*, **10(3)**, pp.2211-2220, DOI: 10.1021/acscatal.9b04004.

[10] O. Örnek, Z.A. Kösemen, S. Öztürk, et al. (2017), "Performance enhancement of inverted type organic solar cells by using Eu doped $TiO_2$ thin film performance enhancement of inverted type organic solar cells by using Eu doped $TiO_2$ thin film", *Surfaces and Interfaces*, **9**, pp.64-69, DOI: 10.1016/j.surfin.2017.08.003.

[11] Z. Rao, X. Xie, X. Wang, et al. (2019), "Defect chemistry of $Er^{3+}$-doped $TiO_2$ and its photocatalytic activity for the degradation of flowing gas-phase VOCs", *J. Phys. Chem. C.*, **123(19)**, pp.12321-12334, DOI: 10.1021/acs.jpcc.9b02093.

[12] X. Xue, R.L. Penn, E.R. Leite, et al. (2014), "Crystal growth by oriented attachment: Kinetic models and control factors", *Cryst. Eng. Comm.*, **16(8)**, DOI: 10.1039/c3ce42129e.

[13] N.V. Quang, N.T. Huyen, N. Tu, et al. (2021), "A high quantum efficiency plant growth LED by using a deep-red-emitting α-$Al_2O_3$:$Cr^{3+}$ phosphor", *Dalt. Trans.*, **50(36)**, pp.12570-12582, DOI: 10.1039/d1dt00115a.

[14] M. Fhoula, T. Kallel, M. Messaoud, et al. (2019), "Morphological, spectroscopic and photocatalytic properties of $Eu^{3+}$:$TiO_2$ synthesised by solid-state and hydrothermal-assisted sol-gel processes", *Ceram. Int.*, **45(3)**, pp.3675-3679, DOI: 10.1016/j.ceramint.2018.11.029.

[15] B. Kee, I. Kwon, H. Kyoung, et al. (2008), "Spectroscopy of nanocrystalline $TiO_2$:$Eu^{3+}$ phosphors", *Colloids and Surfaces A: Physicochemical and Engineering Aspects*, **313-314**, pp.82-86, DOI: 10.1016/j.colsurfa.2007.04.075.

[16] B. Mili, K. Vukovi, G. Dra (2017), "Effects of $Li^+$co-doping on properties of $Eu^{3+}$ activated $TiO_2$ anatase nanoparticles", *Optical. Materials*, **72**, pp.316-322, DOI: 10.1016/j.optmat.2017.06.029.

[17] S. Culubrk, J.M. Nedeljkovi (2014), "Sensors and actuators B : Chemical temperature sensing with $Eu^{3+}$ doped $TiO_2$ nanoparticles", *Sensors and Actuators B: Chemical*, **201**, pp.46-50, DOI: 10.1016/j.snb.2014.04.108.

[18] N.T. Huyen, N. Tu, N.V Quang, et al. (2022), "Excellent quantum efficiency and superior color purity red-emitting $CaAl_{12}O_{19}$-$CaAl_4O_7$-$MgAl_2O_4$:$Mn^{4+}$ phosphors for plant growth and high color rendering index white light-emitting diode applications", *ACS Appl. Electron. Mater.*, **4(9)**, pp.4322-4331, DOI: 10.1021/acsaelm.2c00603.

[19] M.T. Tran, N. Tu, N.V. Quang, et al. (2021), "Excellent thermal stability and high quantum efficiency orange-red-emitting $AlPO_4$:$Eu^{3+}$ phosphors for WLED application", *J. Alloys Compd.*, **853**, DOI: 10.1016/j.jallcom.2020.156941.

[20] H. Li, Y. Sheng, H. Zhang, et al. (2011), "Synthesis and luminescent properties of $TiO_2$:$Eu^{3+}$ nanotubes", *Powder Tech.*, **212(2)**, pp.372-377, DOI: 10.1016/j.powtec.2011.06.019.

 DOI: 10.31276/VJSTE.66(1).16-23

# Analysis of hydraulic drive circuit selection for a carrot collecting system

**Ngoc Danh Dang*, Xuan Thiet Nguyen**

*Faculty of Engineering, Vietnam National University of Agriculture, Trau Quy Town, Gia Lam District, Hanoi, Vietnam*

Received 23 February 2023; revised 9 May 2023; accepted 10 July 2023

***Abstract:***

**Compared to conventional mechanical transmissions, hydraulic transmission has the disadvantage of lower energy efficiency. However, it is widely employed in various working machines such as construction machines, off-road vehicles, forest logging machines, and especially agricultural machinery, owing to its flexibility in design, geometric arrangement, and simplicity in operation. In the development project for carrot harvesting machinery conjugate, hydraulic transmission is the optimal solution for the design and implementation of the carrot collecting roller system. This project is oriented towards achieving a practical result where the system structure is simple and effective, utilising hydraulic components available on the market in Vietnam. Given the myriad of hydraulic transmission circuits available, this paper undertakes an analysis based on numerical simulations of the functionality and energy efficiency of potential system design options and proposes a new practical speed control circuit. This suggested circuit uses a pressure-compensated flow control valve arranged parallel to the hydraulic motor. The study is carried out in the Matlab/Simulink simulation environment, where the circuit models are constructed using hydraulic components with practical parameter settings sourced from component suppliers. The analysis results indicate that the proposed circuit strikes a balance between functionality and economic efficiency.**

***Keywords:*** **carrot collecting machine, hydraulic transmission, speed regulating circuit, 3-way flow control valve.**

***Classification numbers:*** **2.1, 2.3, 3.1**

## 1. Introduction

The soil separating and collecting machine is the concluding unit of the carrot harvesting machine conjugate, which is part of the research products of the "Research on the procedure and synchronisation of mechanised equipment in producing carrot in Vietnam" project.

The basic structure of the soil separating and collecting machine is a roller-type separating system that removes soil, grass, and trash from carrot roots and then collects the carrot roots into containers. The entire arrangement of the machine conjugate is illustrated in Fig. 1.

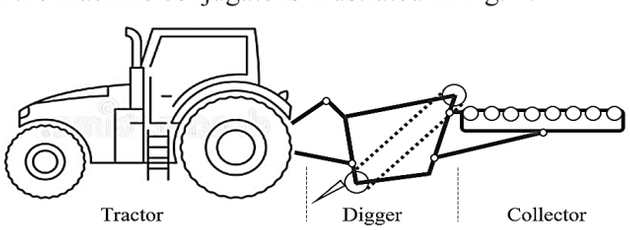


**Fig. 1. Arrangement of the carrot harvesting machine conjugate.**

Given the chosen configuration of the machine conjugate, the design of the transmission for the collecting machine over a long distance needs to be considered. Moreover, the collecting machine needs to be capable of lifting during the operational process; thus, flexibility in the transmission line is essential.

**Fig. 2. Roller system of the carrot collecting machine.**

*Corresponding author: Email: dangngocdanh@gmail.com

The structure of the roller system of the carrot collecting machine is depicted in Fig. 2. To maintain the functionality of the system, the revolution speed of the rollers must be adjustable based on the harvesting conditions such as soil moisture, soil hardness, and supply volume from the digger. This ensures efficient carrot separation from soil, grass, and trash. Additionally, the revolution speed must remain stable at a chosen value, essentially constant, regardless of the random variation in the actual load impacting the roller system due to the working conditions.

Given the mentioned structural and operational aspects, it's evident that using a mechanical transmission line for the collecting machine is not advantageous. The hydraulic transmission line, on the other hand, appears more suitable, utilising the hydraulic power supply from the tractor. Nonetheless, the operational cost of the machine conjugate during the cultivation process remains a significant concern. Given that the machine conjugate is designed based on a commercial tractor, which already possesses a fixed configuration with a constant hydraulic flow source, optimising hydraulic power supply for the collecting machine isn't feasible. The primary objective of a hydraulic transmission line design in this instance is to minimise power loss as much as possible. The remainder of this article delves into an analysis of potential hydraulic circuit options to determine the most effective design solution for efficient hydraulic transmission deployment.

## 2. Materials and methods

### *2.1. Analysis on hydraulic circuit options*

From the foregoing discussion, the hydraulic transmission design needs to cater to the roller collecting machine's flexible operational needs while utilising a constant hydraulic flow source from the tractor. Furthermore, for realistic deployment and to curtail manufacturing costs, the design should be straightforward and utilise affordable components readily available in the market. Detailed operational requirements include: the revolution velocity of the roller system should be continuously adjustable; roller velocity should remain consistent at a specific level; power loss should be minimised; the design should be simple design and cost-effective for deployment.

### *2.2. Speed control using variable displacement motor*

There are two fundamental methods to construct a speed control circuit: (1) Utilising variable displacement pumps; (2) Combining fixed displacement pumps with flow control valves [1]. In the first method, the hydraulic motors' speed can be modulated by adjusting the pumps' volumetric displacement, thereby regulating fluid flow from the pumps to the motors. When pumps' displacement remains fixed, analogous circuits can be achieved with variable displacement motors. Circuits based on this principle, exemplified in Fig. 3, ensure high hydraulic efficiency, minimising power loss and providing prompt response to control actions [2].

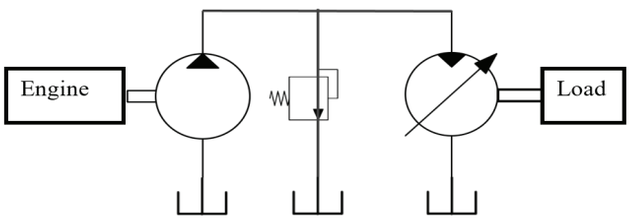


**Fig. 3. Speed control circuit using a variable displacement motor.**

However, speed regulation in the circuit depicted in Fig. 3 necessitates a closed-loop control system (illustrated in Fig. 4) to maintain the motor's constant angular velocity [3, 4]. This feedback mechanism involves feeding the output value (either load or motor angular velocity) back to the controller. This system's inherent complexity, especially considering the cost of variable displacement motors, sensors, and control equipment, makes it an expensive proposition.

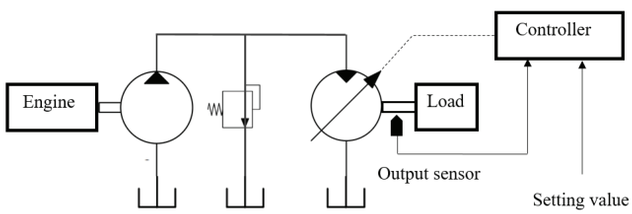


**Fig. 4. Principle of the closed loop control system.**

### *2.3. Speed control using hydraulic orifice*

Orifices are commonplace in hydraulic component markets. By pairing fixed displacement pumps/motors with orifices, one can devise a speed control circuit. This method typically offers a more economical alternative for a speed control hydraulic circuit compared to methods relying on variable volumetric displacement pumps/motors [5]. The generally lower costs of fixed displacement pumps/motors, owing to their uncomplicated structure, account for this affordability.

Figure 5 showcases a speed control circuit iteration with an orifice in the main line. The design calls for a pressure relief valve, which caps the system's maximum pressure, effectively establishing an almost uniform pressure source while concurrently controlling the hydraulic fluid flow into the motors.

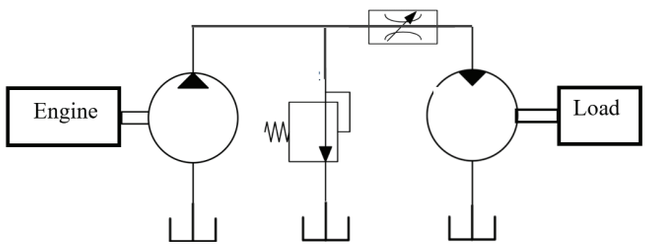


**Fig. 5. Speed control circuit with orifice in main line.**

While this configuration boasts simplicity and cost-effectiveness, it is marred by considerable power loss. This inefficiency stems from the continuous need for high system pressure irrespective of load demand. Two factors contribute to this power loss: (1) Speed control necessitates reaching the pressure relief valve's set value due to orifice adjustments; (2) The orifice induces pressure loss as given by:

$$P=\Delta P_{tl}+\Delta P_{t} \quad (1)$$

where $P$ is the system pressure; $\Delta P_{tl}$ represents the drop pressure at the orifice; $\Delta P_{t}$ stands for the drop pressure at the load motor.

Under uncertain load conditions, the system pressure - dictated by the pressure relief valve - must be sufficiently high to ensure the system operates optimally. Large magnitude load fluctuations lead to further power loss. Another inherent flaw is the orifices' inability to stabilise motor speed. Theoretically, when the load alters, the pressure at the orifice's inlet shifts correspondingly, causing fluctuating fluid volumes returning to the tanks. Consequently, the fluid volume supplied to load motors becomes inconsistent, changing motor speed.

Practically, if the pressure relief valve exhibits a broad regulation spectrum, as demonstrated in Fig. 6, and load changes remain relatively minor, motor speed can be considered nearly constant with negligible error [6]. However, pinpointing the real load proves challenging, especially when trying to confine its variation to align with the pressure relief valve's specifications.

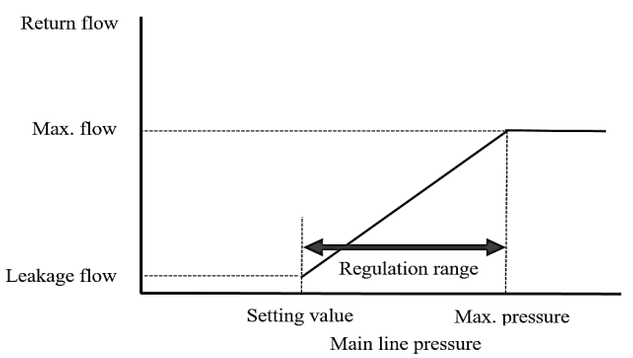


**Fig. 6. Characteristics of the pressure relief valve.**

To attenuate power loss, one could position the orifice in the return line [5, 7]. Circuits adopting this strategy are depicted in Fig. 7. These designs can adjust system pressure in line with the load, hence reducing power loss. However, this circuit cannot regulate speed since the return flow through the orifice depends on the main line pressure, leading to varied flow into the load motors. In this context, the pressure relief valve merely acts as a safety mechanism [7].

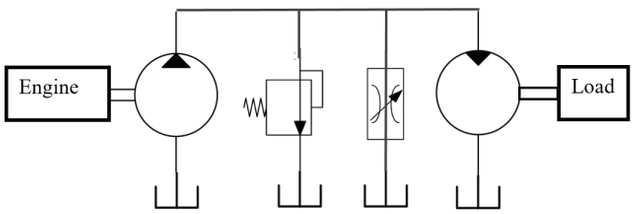


**Fig. 7. Circuits using an orifice in the return line.**

### *2.4. Proposed approaches using pressure compensated flow control valves*

Pressure compensated flow control valves are a type of flow valve. They are designed to produce a set constant flow rate, largely independent of the load. The principal structure of a pressure compensated flow control valve with a variable flow rate is presented in Fig. 8.

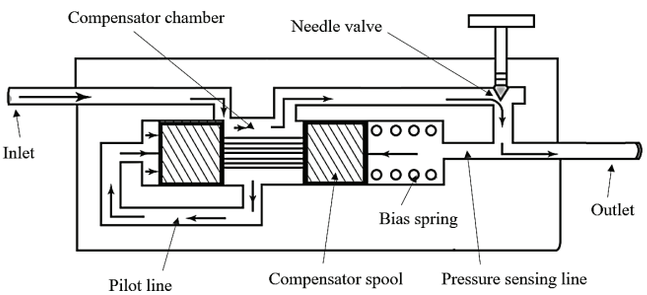


**Fig. 8. Principle of pressure compensated flow control valves.**

Using pressure compensated flow control valves in place of orifices in a speed control circuit offers an effective solution, especially in cases of fluctuating loads [5, 8]. Theoretically, these valves can sustain a constant flow rate, regardless of load. The flow rate value is derived from the differential pressure between the outlet and inlet of the valve, as follows:

$$Q=C.A.\sqrt{\frac{2.\Delta P_{tl}}{\rho}} \quad (2)$$

where C stands for the discharge coefficient; A represents the open area of needle valve; $\Delta P_{tl}=P_k-P_r$ defines the drop pressure through the valve with inlet pressure $P_k$ and outlet pressure $P_r$; $\rho$ denotes the hydraulic oil density.

Once other parameters are established, the flow rate relies solely on the differential pressure $\Delta P_{tl}$. At

equilibrium, the differential pressure across the needle valve satisfies the following equation:

$$P_k \times A_p - F_l - P_r \times A_p = 0 \quad (3)$$

or equivalently

$$P_k - P_r = \frac{F_l}{A_p} \quad (4)$$

where $F_l$ is the force generated by the bias spring; $A_p$ denotes the compensator spool area. As inferred, this differential pressure is always set by the bias spring force, ensuring the flow rate remains independent of the load pressure ($P_r$). In real scenarios, the flow rate is still alter when the load fluctuates significantly and rapidly [9-11].

Considering the effect of wide-ranging load variations on the flow rate through a pressure compensated flow control valve, the bias spring force component, $F_l$, in Eq. (4) is given by:

$$F_l = k\left(x_0 + \Delta x\right) \quad (5)$$

where $k$ denotes the spring hardness; $x_o$ is the initial compression of the spring; $\Delta x$ represents the change of spring compression when load varies.

For minor load alterations (corresponding to a low $\Delta x$ value), the variation in bias spring force is negligible. According to Eq. (4), the differential pressure remains fairly constant, resulting in a constant flow rate. However, with extensive load shifts, $\Delta x$ must be taken into account. The discrepancy between the actual and ideal differential pressures can be calculated as follows:

$$\tilde{\Delta}P = \frac{k.\Delta x}{A_p} \quad (6)$$

This introduces errors in the flow rate through the valve. Moreover, research results in [11] reveal that while flow rate errors are minimal at low fluid flow velocities, they become significant at higher velocities.

Load change rates also considerably influence the performance of the flow control valve due to the valve mechanism's dynamics. Mechanical dynamics invariably introduces a transitional phase at the outset of the regulation process. The length of this phase varies depending on individual valve structural parameters. This dynamic mechanism is explained by a second-order dynamical equation; see [11, 12] for specifics. Research of D.T. Hieu, et al. (2009) [11] also indicates that the transitional phase's duration is affected by the rate of load change; a faster change rate elongates the transition, increasing flow rate discrepancies.

Pressure compensated flow control valves can be implemented in two configurations, akin to orifice-based setups. It's important to note that to achieve continuous motor speed control, the flow control valve must be of the variable flow rate variety, integrated with a needle valve (as illustrated in Fig. 8). In the primary configuration, with the flow control valve situated in the main line (refer to Fig. 9), the circuit results in substantial power loss. Nonetheless, the motor speed remains more stable, especially when compared to orifice-based circuits.

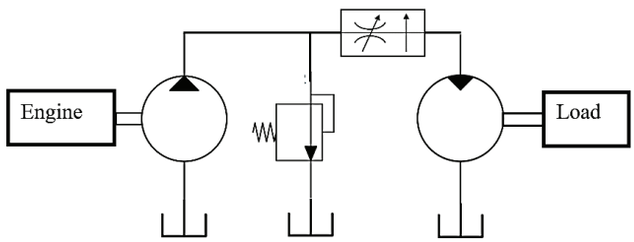


**Fig. 9. Speed control circuit using a pressure compensated flow control valve in the main line.**

In the second configuration, where flow control valves are positioned in the return line [5, 13], the circuit proves more efficient compared to the previously mentioned options (see Fig. 10). However, its capability to maintain a constant speed is compromised because the flow control valve, responsible only for the return flow [14], cannot detect changes in the main line's flow.

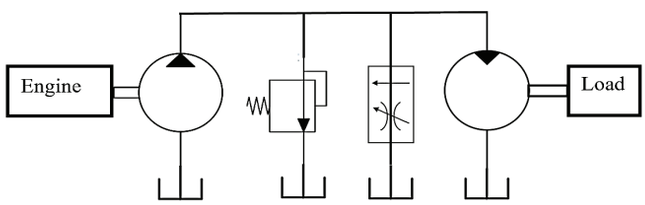


**Fig. 10. Circuit using a pressure compensated flow control valve in the return line.**

By substituting the two-way pressure compensated flow control valve with a three-way version in the main line (as depicted in Fig. 11), the resulting circuit's efficiency matches that of Fig. 10. Moreover, speed regulation improves as the valve directly controls the flow into the load motor.

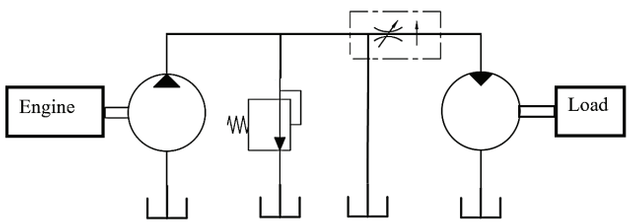


**Fig. 11. Circuit using three-way pressure compensated flow control valves.**

A circuit that utilises a flow control valve in the main line paired with an orifice in the return line (illustrated in Fig. 12) to modulate the motor speed has been implemented in agricultural and forestry machines [15]. This setup can sustain a steady motor speed. Nevertheless, the system's pressure must be at its peak, resulting in significant power loss similar to the circuit in Fig. 5.

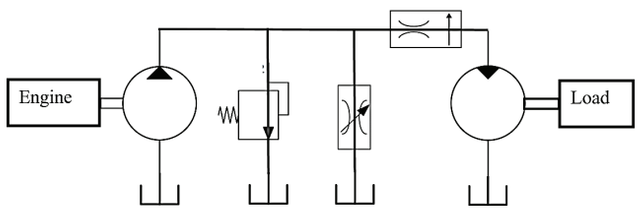


**Fig. 12. Circuit using flow control valves and variable orifices.**

For scenarios where the maximum load value is known, circuits with pressure compensated flow control valves in the main lines serve as optimal solutions for speed regulation. To mitigate power loss, a variable pressure relief valve can be integrated into the return line, maintaining the lowest pressure in line with the load demand. This configuration is illustrated in Fig. 13.

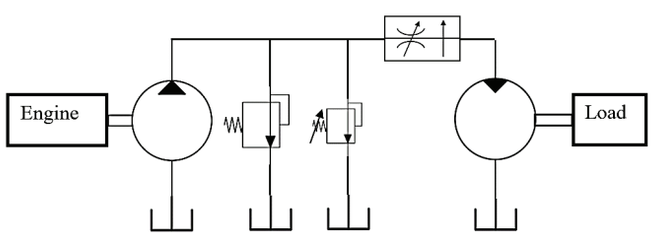


**Fig. 13. Circuits using an auxiliary variable pressure relief valve.**

From the speed control circuits analysed, those that employ: 1. A variable flow control valve in main line (Fig. 9); 2. A variable flow control valve in return line (Fig. 10); 3. A variable three-way flow control valve (Fig. 11); 4. A combination of a variable flow control valve and an auxiliary pressure relief valve (Fig. 13) appear to satisfy the system's operational requirements.

In the Fig. 9 circuit, the pressure relief valve acts solely as a safety feature. Notably, this valve is already integrated into the hydraulic system of the tractor. Thus, implementing this circuit demands only a fixed displacement motor and a common pressure compensated flow control valve, both readily available at affordable prices. Similarly, the Fig. 10 circuit comprises the same hydraulic components. Setting up the Fig. 11 circuit necessitates a three-way flow control valve to replace the two-way version. Recent designs for this type of hydraulic valve employ electro-mechanical actuator mechanisms, making them more costly than standard flow control valves. The final circuit in Fig. 13, besides requiring a flow control valve, also needs an auxiliary pressure relief valve - a component commonly available in the market.

### *2.5. Research approach*

This article is not intended to systematically prove the characteristics of speed control circuits, which have been analysed in previous content. Instead, its focus is on application results, where the circuits are constructed using selected low-cost hydraulic components available on the market. The working capabilities of the proposed circuits are analysed using the professional hydraulic simulation toolbox, Simscape/Hydraulic, provided by Matlab/Simulink software. The simulation results help in deciding the most suitable circuit to deploy on real systems.

## 3. Results and discussion

The carrot harvesting machine system is powered by a Kubota L4508VN tractor. This tractor is equipped with an auxiliary hydraulic power system of 9 kW. The maximum flow rate of the hydraulic pump is 31.7 litres per minute, and the maximum hydraulic pressure is 17.7 MPa [16]. The collecting roller system requires an adjustable speed range from 300 to 500 rpm, depending on actual working conditions. Due to structural space limitations, the rollers are directly driven by the hydraulic motor without a reduction gearbox. Consequently, low-speed hydraulic motors are chosen for their high torque and efficiency.

According to the datasheet of available hydraulic motors on the market [17], motor BMR50, with a volumetric displacement of 51.7 ml/r, is suitable. Its speed ranges from 10 to 775 rpm, corresponding to the flow rate from 0.527 to 40.06 litres per minute. This motor, therefore, requires a flow rate from 15.5 to 25.85 litres per minute for the desired speed range. This flow rate matches the supply value from the source pump, ensuring continuous speed control. The motor's pressure, with an intermittent maximum of 17.5 MPa and a continuous maximum of 14 MPa, nearly meets the system's pressure requirements.

Based on preliminary calculations, the pressure-compensated flow control valve needs to accommodate a maximum flow rate of 16.2 litres per minute when placed in the return line (Fig. 10) and 28.85 litres per minute when located in the main line (Fig. 9). Based on the datasheet for two-way flow control valves [18], valve

FG-02-30-30 - adjustable for flow rates from 0.05 to 30 litres per minute with a maximum pressure of 21 MPa - is suitable. Similarly, a three-way pressure-compensated flow control valve, EFG-02-30, is chosen for the circuit in Fig. 11. This valve's flow rate ranges from 0.3 to 30 litres per minute with a maximum pressure of 20.6 MPa. For the pressure relief valve in the Fig. 13 circuit, valve DT-02-C-22 can be used. Its regulation pressure ranges from 3.5 to 14 MPa with a maximum flow rate of 16 litres per minute. The specifications of the selected valves are summarised in Table 1.

**Table 1. Specification of the selected hydraulic valves.**

| Selected valve | Min. flow rate | Max. flow rate | Regulation pressure | Max. pressure |
|---|---|---|---|---|
| FG-02-30-30 | 0.05 l/min | 30 l/min | - | 21 MPa |
| EFG-02-30 | 0.3 l/min | 30 l/min | - | 20.6 MPa |
| DT-02-C-22 | - | 16 l/min | 3.5 to 14 MPa | 21 MPa |

Using the machine system's design parameters and the selected circuit components, circuit analysis is performed with the Simscape/Hydraulic toolbox. This toolbox offers a realistic simulation environment with a library of common hydraulic components. These components factor in the effects of hydraulic losses in the circuits, making model implementation straightforward. Two admission criteria are specified: motor speed regulation capability; circuit energy efficiency.;

The energy losses in circuits is defined as follows:

$$\Delta E = \frac{E_v - E_r}{E_v} 100 \quad (7)$$

where $E_v = \int_0^t n_p . M_p dt$ (8)

which denotes the input energy supplied from the tractor engine to the hydraulic pump during simulation time $t$. Here, the pump speed $n_p$ is assumed to be constant and $M_P$ stands for the torque at pump shaft. Similarly,

$$E_r = \int_0^t n_m . M_m dt \quad (9)$$

defines the output energy of the hydraulic motors. The two variables $n_m$, $M_m$ are the speed and torque of hydraulic motor, respectively. Defining energy loss this way includes all system losses such as leakage in pumps/motors, valves, and losses in pipelines.

Technical specifications [18] for the chosen valves corresponding to each circuit are input into the parameter settings of relevant Simulink/Simscape models. The circuits are initially set with a fixed load torque of 40 Nm on the motor shaft, with the motor speed set at 400 rpm. To analyse the circuits under varying loads, a Gaussian random signal is added, with a frequency of 3 Hz, zero mean, and a standard deviation of 0.3. The resulting random load signal is displayed in Fig. 14.

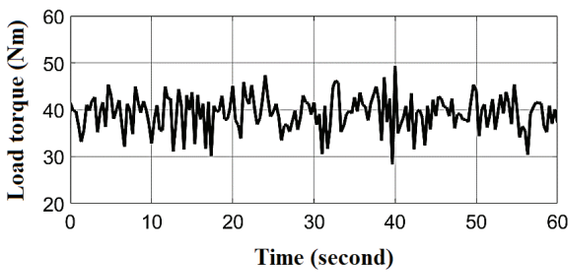


**Fig. 14. Random load torque applied at the motor shaft.**

As can be seen from Fig. 14, the load varies over a broad range from 30 to 50 Nm with rapid and random fluctuations. The test results for the four selected circuits are presented in Figs. 15-18.

The plots in Fig. 15 depict changes in motor speed under the impact of random variation in load for the four analysed circuits: the first circuit (Circ. 1) uses the FG-02-30-30 two-way pressure compensated flow control valve in return line (Fig. 10); the second one (Circ. 2) uses the EFG-02-30 three-way pressure compensated valve (Fig. 11); the third one (Circ. 3) exploits FG-02-30-30 valve in main line with an auxiliary pressure relief valve DT-02-C-22 in return line (Fig. 13); and the fourth one (Circ. 4) is the conventional speed control circuit using FG-02-30-30 valve in main line (Fig. 9). The errors in motor speed compared to the set value of 400 rpm are summarized in Table 1.

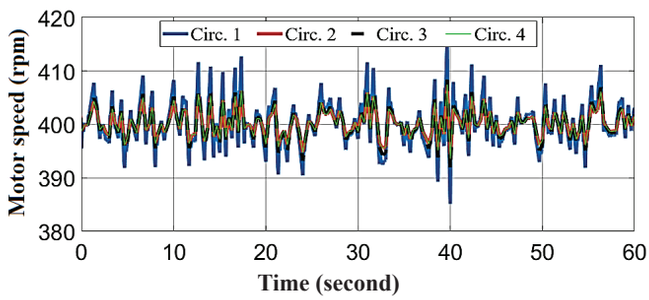


**Fig. 15. Motor speed of the four analysed circuits.**

**Table 2. Summary of motor speed error.**

| Speed regulation error | Circ. 1 | Circ. 2 | Circ. 3 | Circ. 4 |
|---|---|---|---|---|
| Maximum absolute error (rpm) | 15.20 | 7.45 | 8.55 | 7.48 |
| Relative error (%) | 3.8 | 1.9 | 2.1 | 1.9 |

From the results in Table 2, it's evident that the second and fourth circuits are the optimal solutions for motor speed regulation with a minor relative error of 1.9%. Meanwhile, the third circuit maintains the error within 2.1%, and the first circuit has a maximum error of 3.8%.

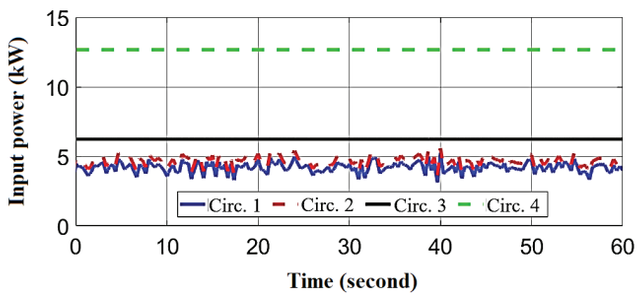


**Fig. 16. Mechanical power consumption of the circuits.**

Figure 16 illustrates the power sourced from the tractor engine to the circuits. The third and fourth circuits employ flow control valves in the main line. In the fourth circuit, system pressure consistently reaches its peak, leading to a maximum power consumption of 13 kW. The third circuit features an auxiliary pressure relief valve, thereby allowing for significant power conservation when compared to the fourth one. The first circuit, with its flow control valve in the return line, demands the least input power, followed by the second circuit, which employs a three-way flow control valve.

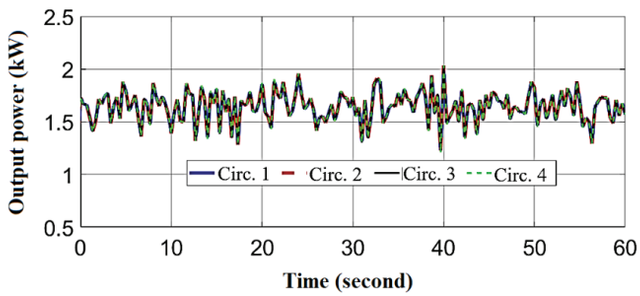


**Fig. 17. Mechanical output power of the circuits.**

Figure 17 showcases the mechanical power measured at the motor shaft. Given the minor differences in motor speed amongst the circuits, their output powers are relatively similar, hovering around 1.7 kW.

The energy efficiency of each circuit is determined by the ratio of input to output powers. As these figures fluctuate with the load, energy efficiency metrics adjust accordingly. Using Eqs. (7-9), the average values of efficiency are determined based on input and output energy computations. Fig. 18 provides insights into the percentage of energy losses for each circuit.

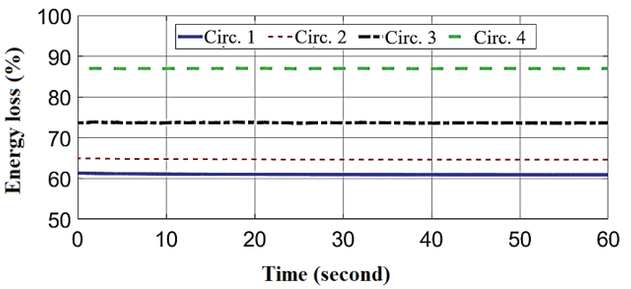


**Fig. 18. Energy losses in the analysed circuits.**

From Fig. 18, it's clear that the fourth circuit, with the FG-02-30-30 valve in the main line, incurs the highest energy loss at 88%. The third circuit, equipped with an auxiliary pressure relief valve, reduces energy loss to 73% for the given load. The second circuit, utilising the EFG-02-30 three-way flow control valve, sees a loss of 64%. Impressively, the first circuit, with the FG-02-30-30 in the return line, records the lowest energy loss at around 61%. Comparison criteria are presented in Table 3.

**Table 3. Summary of comparison criteria.**

| Comparison criteria | Circ. 1 | Circ. 2 | Circ. 3 | Circ. 4 |
|---|---|---|---|---|
| Relative speed error (%) | 3.8 | 1.9 | 2.1 | 1.9 |
| Energy loss (%) | 61 | 64 | 73 | 88 |
| Component cost (estimated level) | 1 | 3 | 2 | 1 |

Upon evaluating the comparison criteria, decisions regarding the most viable speed control circuit for practical application can be made. Clearly, the second and fourth circuits excel in speed regulation. However, the fourth circuit's high energy loss and the second circuit's elevated component cost render them less appealing. The third circuit, marked by significant energy loss, high cost, and large error, is also less than ideal. The first circuit emerges as the preferred option due to its cost-effectiveness, minimal energy loss, and a manageable error of 3.8% - well within an acceptable range.

## 4. Conclusions

This paper has delved into the functionality and efficiency of four distinct options for the speed regulation hydraulic circuit in a carrot collecting machine, specifically examining energy loss and implementation costs. Of the four circuits, Circs. 2-4 are conventional and frequently employed in hydraulic drive systems. Conversely, Circ. 1 represents a novel arrangement in which the pressure-compensated flow control valve is positioned in the return line, parallel to the hydraulic motor. With an aim

towards genuine working conditions, these circuits were tested under fluctuating loads imposed on the hydraulic motor. Subsequently, their speed regulation functionality and energy efficiency were critically examined.

The simulation tests, conducted using real component parameters, offer a dependable analysis, underlining the proficiency and adequacy of each circuit in meeting system operational demands. It's clear from the findings that there isn't a singular, 'one-size-fits-all' solution for the speed control circuit; different contexts demand different compromises among the selection criteria.

From this standpoint, the first circuit - deploying the FG-02-30-30 pressure-compensated flow control valve in the return line (Fig. 10) - emerges as a favoured choice. Its strengths lie in its cost-effective implementation and diminished energy loss. These benefits translate into better fuel economy and a reduced burden on the cooling system, rendering it particularly advantageous for use in a carrot collecting machine.

## CRediT author statement

Ngoc Danh Dang: Conceptualisation, Methodology, Software, Validation, Formal analysis, Investigation, Writing - Original draft preparation; Xuan Thiet Nguyen: Writing - Reviewing and Editing, Resources, Project administration.

## ACKNOWLEDGEMENTS

This work is a part of the research project "Research on the procedure and the synchronization of mechanized equipment in producing carrot in Vietnam", which is supported by the Vietnam Ministry of Science and Technology.

## COMPETING INTERESTS

The authors declare that there is no conflict of interest regarding the publication of this article.

## REFERENCES

[1] Power and Motion (2016), "Speed control of hydraulic motors", https://www.powermotiontech.com/hydraulics/hydraulic-pumps-motors/article/21885011/speed-control-of-hydraulic-motors, accessed 21 October 2022.

[2] C.S. Kim, C.O. Lee (1996), "Speed control of an over-centered variable-displacement hydraulic motor with a load-torque observer", *Control Engineering Practice*, **4(11)**, pp.1563-1570, DOI: 10.1016/0967-0661(96)00170-0.

[3] A. Kong, X. Zhang, G. Hao (2011), "Simulation study on constant speed output control of fixed displacement pump-variable displacement motor hydraulic system", *Proceedings of 2011 International Conference on Fluid Power and Mechatronics*, pp.276-281, DOI: 10.1109/FPM.2011.6045772.

[4] L. Wei, P. Zhan, Z. Liu, et al. (2019), "Modeling and analysis of maximum power tracking of a 600 kW hydraulic energy storage wind turbine test rig", *Processes*, **7(10)**, DOI: 10.3390/pr7100706.

[5] B.H. Trieu, N.N. Que, D.H. Quyet, et al. (2006), *Hydraulic And Pneumatic Transmission Curriculum*, Agricultural Academy Publishing House, 403pp (in Vietnamese).

[6] J.S. Cundiff (2001), *Fluid Power Circuits and Controls: Fundamentals and Applications*, CRC Press, 560pp.

[7] Y. Ji, H. Wang, H. Chen, et al. (2019), "Analysis and simulation of throttle speed regulation in hydraulic system", *IOP Conference Series: Earth and Environmental Science*, **330(3)**, DOI: 10.1088/1755-1315/330/3/032095.

[8] S. Skinner (2016), "A guide to selecting the right hydraulic flow control valve to optimise system performance and efficiency", *Webtec*, 10pp.

[9] A. Hitchcox (2016), "Gain control of the flow", *Power and Motion*, pp.34-39.

[10] Editorial Staff (2016), "Bleed-off circuit: Advantages, disadvantages and applications", *Engineering Arena*, https://www.enggarena.net/bleed-off-circuit-working/, accessed 21 October 2022.

[11] D.T. Hieu, B.H. Trieu (2009), "Designed multi-point hydraulic transmission controlling circuit on self-propelled forestry - Agricultural machines", *Vietnam Journal of Agricultural Sciences*, **7(5)**, pp.678-686 (in Vietnamese).

[12] M. Cheng (2005), "Modeling and analysis of a pressure compensated flow control valve", *Proceedings Fluids Engineering Division Summer Meeting and Exhibition*, DOI: 10.1115/FEDSM2005-77057.

[13] R. Jasiński (2021), "Volumetric and torque efficiency of pumps during start-up in low ambient temperatures", *Advances in Hydraulic and Pneumatic Drives and Control*, DOI: 10.1007/978-3-030-59509-8_3.

[14] M. Xu, X. Wang (2011), "An in-depth modeling and analysis of pressure-compensated flow control valve", *International Conference on Electric Information and Control*, pp.1164-1168, DOI: 10.1109/ICEICE.2011.5778164.

[15] H.M. Handroos, M.J. Vilenius (1987), "Flexible semi-empirical models for hydraulic flow control valves", *Journal of Mechanical Design*, **113(3)**, pp.232-238, DOI: 10.1115/1.2912774.

[16] Kubota Vietnam (2008), *Kubota Tractor L4508VN Manual*.

[17] Kinde (2022), *BMR Series Hydraulic Motor*, https://www.pyphidraulica.com.ar/catalogo/Motor-BMR.pdf, accessed 5 October 2022.

[18] Yuken (2022), *YUKEN Hydraulic Equipment Specification*, https://www.yuken.co.jp/upload/tenant_1/catalog_pdf/EC-10004-5.pdf, accessed 5 October 2022.

DOI: 10.31276/VJSTE.66(1).24-33

# Study on the equilibrium and kinetics of nickel (II) adsorption on cellulose from peanut shell modified with chitosan

**Thi Lan Phung*, Thi Kim Giang Nguyen, Phuong Hien Ho, Thanh Nga Pham**

*Faculty of Chemistry, Hanoi National University of Education, 136 Xuan Thuy Street, Dich Vong Hau Ward, Cau Giay District, Hanoi, Vietnam*

Received 12 December 2022; revised 8 March 2023; accepted 20 March 2023

***Abstract:***

**In this study, cellulose was produced by activating peanut shells with 5% NaOH as an alkaline agent and bleaching with 5 wt.% $H_2O_2$. Before being modified with chitosan, the cellulose was slightly oxidized with ammonium persulfate to introduce carboxyl groups. The equilibrium and kinetics of nickel adsorption on the as-prepared material were investigated. Langmuir, Freundlich, and Temkin isotherm models were used to describe the equilibrium isotherms. The Langmuir and Temkin adsorption isotherms were better fits to the equilibrium data than the Freundlich equation. The Langmuir monolayer adsorption capacity of nickel ions on cellulose from peanut shells modified with chitosan was found to be 25.70 mg/g. The Temkin adsorption constant was calculated as 0.45 kJ/mol. Therefore, the interaction between nickel ions and the surface of the as-prepared material are assumed to be weak. Kinetic data were evaluated by pseudo-first-order and pseudo-second-order models, and rate constants were determined. Simulations demonstrated that the pseudo-second-order equation could adequately describe the adsorption of nickel ions.**

***Keywords:*** **adsorption, cellulose, chitosan, isotherms, kinetics, peanut shell.**

***Classification numbers:*** **2.2, 2.3**

## 1. Introduction

The presence of heavy metal ions such as lead, nickel, cadmium, chromium, arsenic, etc. in industrial effluents poses a significant threat to human health and the environment [1]. These ions easily accumulate in living organisms through the food chain and cause various diseases and metabolic disorders because of their high toxicity and non-degradability in the ecosystem [2, 3]. However, their use cannot be avoided because of their necessity in industries such as tanneries, batteries, electronics, dyeing, textile mills, etc. [4].

Various methods are used to remove heavy metal ions from industrial effluents, such as precipitation, membrane filtration, ion-exchange processes, reverse osmosis methods, and adsorption. Among these methods, adsorption is considered a simple and effective treatment method. Many adsorbents have been successfully studied for heavy metal ion adsorption, such as activated carbon [5], activated agricultural waste materials [6], and biopolymer materials such as cellulose [7] and chitosan [8], whether natural or modified, due to their high mechanical strength, chemical stability, large adsorption capacity, abundance of synthetic materials, low cost, and high reversibility.

In recent years, there has been a trend of using low-cost, highly biodegradable agricultural waste materials [6] such as rice husks, peanut shells, fruit shells, sawdust, bagasse, etc. to limit the emission of agricultural waste after harvest. Peanut shells are one of the most abundant agricultural by-products in Vietnam. The main chemical components of peanut shells include cellulose (40-45%), hemicellulose (<14%), lignin (26-28%), and other components. Therefore, extracting cellulose from peanut shells is also quite attractive [9, 10].

Cellulose is a biodegradable natural polymer composed of thousands of D-glucose units linked β-(1→4) with hydrogen bonding between parallel chains. Cellulose contains many mobile hydroxyl functional groups that easily combine with heavy metal ions and organic pigments [8, 9]. Similarly, chitosan, a linear polysaccharide containing many β -(1-4) D-glucosamine units, possesses both amine and hydroxyl functional

*Corresponding author: Email: lanpt@hnue.edu.vn

groups. These functional groups act as the main complexing agents with metal cations and other agents, making chitosan have a high adsorption capacity for heavy metal ions [11, 12]. Additionally, chitosan is a biodegradable polymer and is also considered as a good candidate to modify cellulose [13, 14].

Prior to modification, cellulose can be partly oxidized from the hydroxyl functional group, such as the $CH_2$-OH group in the cellulose structure, to the carboxyl functional group to improve its ability to bind with modifying agents. TEMPO and ammonium persulfate are two oxidizing agents frequently used for the mild oxidation of cellulose to introduce carboxyl functional groups on the surface of cellulose. Ammonium persulfate is a cost-effective and environmentally friendly oxidizing agent because of its nontoxicity and mild oxidation conditions. The bond of –O–O– in ammonium persulfate is unstable and readily decomposed into hydrogen peroxide ($H_2O_2$) and a radical ($SO_4^{-*}$), which has a strong oxidizing capacity to produce cellulose containing carboxyl groups directly from the raw materials of cellulose [15-17]. The mild oxidation of the $CH_2OH$ group to the COOH group in the cellulose structure increases the association with denaturing agents to increase the adsorption properties and durability of cellulose.

For cellulose/chitosan material, cellulose combines with chitosan through hydrogen bonding between hydroxyl groups of cellulose and chitosan, as well as the electrostatic interaction between the negatively charged carboxylic group of the cellulose matrix and the positively protonated amine of the chitosan solution in acetic acid [16, 18].

This study presents the nickel adsorption capacity of chitosan-modified cellulose material. Cellulose is prepared from peanut shells by alkaline hydrolysis to completely remove lignin, bleached with $H_2O_2$, and then mild oxidized by ammonium persulfate agent to introduce carboxylic groups, and finally modified with chitosan under suitable experimental conditions. Peanut shells are lignocellulosic materials composed of cellulose (44.8%), hemicellulose (5.6%), and lignin (36.1%) with a complex fibrous structure. The nickel adsorption capacity of chitosan-modified cellulose material was evaluated by changing the contact time and pH of the solution. Additionally, isothermal adsorption models and kinetic models were investigated.

## 2. Materials and methods

### *2.1. Chemicals*

Nickel sulphate salt ($NiSO_4.6H_2O$), dimethylglyoxime ($C_4H_8N_2O_2$), chitosan, ammonium persulfate ($(NH_4)_2S_2O_8$), sodium hydroxide (NaOH solid and NaOH 0.02 N), acid acetic ($CH_3COOH$), sodium hydrogen carbonate ($NaHCO_3$ 0.02 N), and hydrochloric acid (HCl) possessed greater than 98% purity and were imported from China. Peanut shells were provided from the region of North Vietnam.

### *2.2. Preparation of adsorbent*

Peanut shells were crushed to sizes in the range of 0.1-0.2 mm. Peanut shell powders were hydrolysed in an alkaline solution with 5% sodium hydroxide solution and bleached with 5% hydrogen peroxide solution to completely remove lignin. Next, the solid was mildly oxidized by ammonium persulfate with a ratio of 1 g/50 ml (peanut shell (g)/ammonium persulfate solution 0.1 M (ml)), by mechanically stirring for 5 h at a temperature of 70°C (denoted as APS-VL) [16, 17]. Finally, the APS-VL sample (2 g) was modified with chitosan solution by impregnation. The chitosan solution was prepared by dissolving 0.35 g of chitosan in 60 ml of 1% acetic acid and mechanically stirred for 3 h. The modifying ratio was equal to 15 wt.% chitosan. The obtained sample was denoted as CTS-APS-VL. The impregnation method was carried out three times. After each impregnation, the CTS-APS-VL sample was dried at 60°C for 4 h. Then, the temperature was raised to 100°C for 3 h to increase the interaction between the surface functional groups of chitosan and the APS-VL sample.

### *2.3. Characterisation of adsorbent*

*Amounts of functional groups:* The amounts of hydroxyl and carboxyl functional groups on the surface of the APS-VL and CTS-APS-VL samples were determined by Boehm titration. The Boehm agents used were 0.02 N NaOH solution to determine amount of hydroxyl functional group and 0.02 N $NaHCO_3$ solution to determine amount of carboxyl functional group.

Briefly, 0.5 g of adsorbent was added to 50 ml of Boehm agents and then mechanically stirred (150 rpm) for 24 h at room temperature. After the neutral reaction, the solutions were titrated with standardized aqueous HCl (0.02 M) until the end point of phenolphthalein. For 10

ml of solution titrated with 0.02 M HCl, the concentration of hydroxyl and carboxyl functional groups can be calculated as follows, respectively:

$$m_{hydroxyl}(mmol.g^{-1}) = \frac{C_{HCl} \times V^{01}_{HCl} - 5C_{HCl} \times V^{1}_{HCl}}{m} \quad (1)$$

$$m_{carboxyl}(mmol.g^{-1}) = \frac{C_{HCl} \times V^{02}_{HCl} - 5C_{HCl} \times V^{2}_{HCl}}{m} \quad (2)$$

where $V^{01}_{HCl}$, $V^{1}_{HCl}$ are the volumes of 0.02 HCl used to titrate 50 ml of the initial NaOH solution before the neutralization reaction and 10 ml of the NaOH solution after the neutralization reaction, respectively; $C_{HCl}$ is the concentration of HCl solution. Also; $V^{02}_{HCl}$ and $V^{2}_{HCl}$ are the volumes of 0.02 HCl used to titrate 50 ml of the initial $NaHCO_3$ solution before the neutralization reaction and 10 ml of the $NaHCO_3$ solution after the neutralization reaction, respectively.

*Point of zero charge (PZC*): Eight solutions of 0.1 M NaCl with different initial $pH_i$ values in the range of 3 and 11 were prepared by adjusting the pH of the solutions using 0.1 M HCl and NaOH. A 0.1-g dosage of the CTS-VL-APS sample was added to 50.0 ml of the 0.1 M NaCl solutions with different initial $pH_i$ values and mechanically stirred (150 rpm) for 24 h at room temperature. Then, the equilibrium $pH_j$ values were measured using a pH meter to calculate the $pH_{PZC}$ value.

*EDX analysis:* The CTS-APS-VL sample loaded with nickel ions was analysed on an SEM-EDX spectrometer (UV 2600 Shimadzu Instruments) and X-flash 6100 detector to detect the presence of nickel on the surface of the as-prepared sample.

### *2.4. Methods*

The nickel adsorption process was carried out through batch adsorption studies at room temperature. Briefly, 0.4 g of adsorbent was added to 200 ml of nickel solution at a suitable concentration and pH value. After adsorption, the nickel solution was removed to determine the remaining concentration by UV-Vis absorption spectroscopy. The contact time (*t*) was varied from 10 to 140 min. The effect of pH value of the nickel solution was measured from 3.2 to 8.0. The pH value of the nickel solution must be lower than pH 8.0 to avoid the formation of hydrolysed species and precipitation. Additionally, the initial concentration of nickel solutions was changed from 20 to 120 ppm. All other conditions unrelated to the present survey remained constant.

The UV-vis absorption spectra and the standard curve of the complex between nickel solution and dimethylglyoxime at 470 nm are displayed in Figs. 1 and 2, respectively.

Metal ions adsorption capacity of the adsorbents at equilibration time ($q_e$) and at arbitrary time t ($q_t$) was calculated according to the following equations:

Adsorption capacity at equilibrium $q_e$ (mg/g):

$$q_e = \frac{(C_o - C_e)xV}{m} \quad (3)$$

Adsorption capacity at arbitrary time t, $q_t$ (mg/g):

$$q_t = \frac{(C_o - C_t)xV}{m} \quad (4)$$

where $C_o$, $C_e$, and $C_t$ (ppm) are the concentrations of heavy metal solution at initial time, equilibrium time,

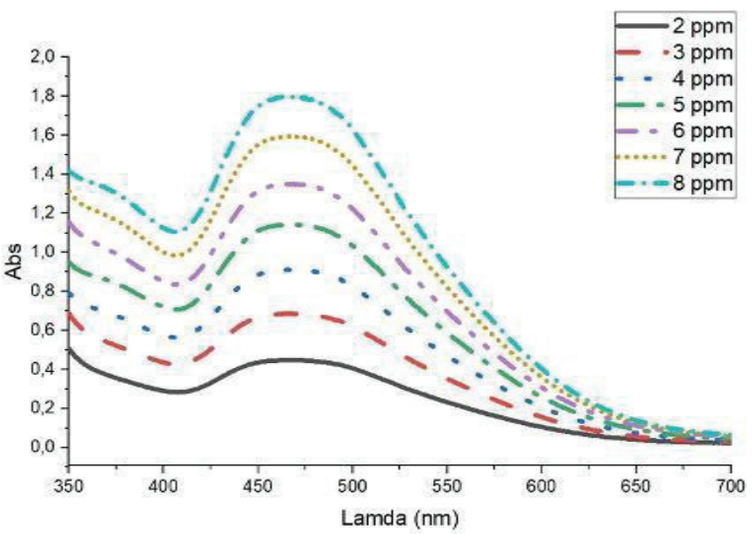


**Fig. 1. UV-vis absorption spectrum of the complex between nickel and dimethylglyoxime at 470 nm.**

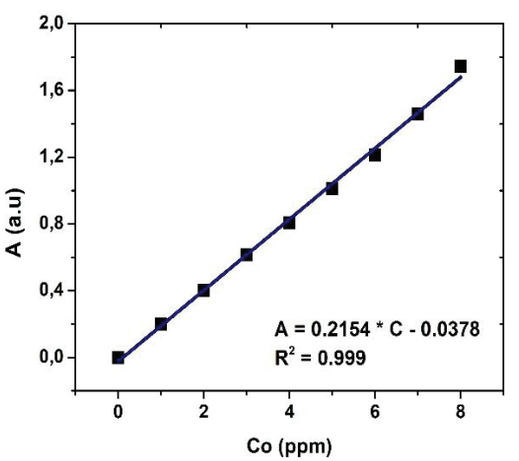


**Fig. 2. Standard curve equation of the complex between nickel and dimethylglyoxime at 470 nm.**

and contact time, respectively. V is the volume (L) of the heavy metal solution and m is the mass (g) of the adsorbents.

*Adsorption Kinetics:* Pseudo-first-order and pseudo-second-order models in linearized form were applied to the adsorption kinetic data as follows [19-20]: Pseudo-first-order model in linearised form:

$$\ln(q_{e1} - q_t) = \ln q_{e1} - k_1.t \quad (5)$$

Pseudo-second-order model in linearised form:

$$\frac{t}{q} = \frac{t}{q_{e2}} + \frac{1}{k_2 q_{e2}^2} \quad (6)$$

where the adsorption capacities for the pseudo-first-order model and pseudo-second-order model at equilibria and time $t$ are denoted by $q_{e1}$, $q_{e2}$, and $q_t$, respectively, while $k_1$ and $k_2$ are the pseudo-first-order and pseudo-second-order rate constants, respectively.

*Equilibrium isotherm modelling:* The most common types of models describing equilibrium isotherms are the Langmuir, Freundlich, and Temkin isotherms [19, 20].

The Langmuir isotherm model in linearized form is expressed as:

$$\frac{C_e}{q_e} = \frac{1}{q_m} C_e + \frac{1}{q_{m*K_L}} \quad (7)$$

where $q_m$ (mg/g) and $K_L$ (l/mg) are the maximum monolayer adsorption capacity and a constant related to the heat of adsorption, respectively.

The Freundlich isotherm model in linear form is expressed as:

$$\log q_e = \log K_F + \frac{1}{n} \log C_e \quad (8)$$

where $K_F$ ((mg/g) (L/mg)$^{(1/n)}$) and n are the Freundlich constants related to bonding energy and deviation in adsorption from linearity, respectively. A linear adsorption process is indicated by n=1, a chemical adsorption process is indicated by n<1, and a physical adsorption process is indicated by n>1.

The Temkin isotherm model in non-linear and expressed as:

$$q_e = B \text{ x } \ln (K_T \text{ x } C_e) \quad (9)$$

where $K_T$ is the Temkin's isotherm equilibrium constant (L/g) and $B = RT/b_T$ in which $b_T$ is the Temkin constant; B is constant (J/mol); R is the ideal gas constant (8.314 mol/K); T is absolute temperature (K).

*Error analysis:* In this study, both $R^2$ and were used to evaluate the best fit of the isotherm model to the experimental data. The correlation factor was determined from the graphical plots of the isotherms while the chi-squared test was calculated according to Eq. (10):

$$\chi^2 = \sum_1^n \frac{(q_{e\,exp} - q_{e\,(cal.)})^2}{q_{e\,cal.}} \quad (10)$$

where $q_{e\ exp}$ is the experimental metal concentration at equilibrium; $q_{e\ cal}$ is the calculated metal concentration at equilibrium. The best fit is interpreted as the one with the highest correlation coefficient and lowest chi-squared value.

## 3. Results and discussion

### 3.1. Characterisation of adsorbent

*Amount of functional groups:* Table 1 shows the results of the functional group dosage experiments according to the Boehm titration method.

**Table 1. The functional group dosage according to the Boehm titration method.**

| Sample | Hydroxyl group dosage (mmol/g) | Carboxyl group dosage (mmol/g) |
|---|---|---|
| APS-VL | 1.41 | 0.55 |
| CTS-APS-VL | 2.15 | 0.26 |

From Table 1, the APS-VL sample possessed 1.41 mmol/g of hydroxyl groups, which were determined by neutralising with 0.02 N NaOH solution. The carboxyl group dosage was found to be 0.55 mmol/g, which was determined by neutralizing with 0.02 N $NaHCO_3$ solution. The presence of the carboxyl functional group in the cellulose structure after mild oxidation by ammonium persulfate (APS-VL sample) can be explained by the fact that the bond of –O–O– in ammonium persulfate is unstable and readily decomposes into hydrogen peroxide ($H_2O_2$) and radicals (e.g., $HO^*$ and $SO_4^{-*}$). After that, these radicals oxidize the hydroxyl groups at the C-6 position in the cellulose structure into carboxyl groups [15-17].

When cellulose was modified by chitosan at a weight ratio of 15% (CTS-APS-VL), the hydroxyl groups in the CTS-APS-VL sample increased to 2.15 mmol/g. This increase could be due to the presence hydroxyl functional groups in the structure of chitosan. However, the carboxyl groups in the CTS-APS-VL sample slightly decreased to 0.26 mmol/g due to the combination of a portion of the carboxyl groups on the surface of cellulose with the amine functional groups on chitosan via the electrostatic interaction between the negatively charged

surfaces of carboxylic groups in the cellulose matrix and the positively protonated amines in the chitosan solution in acetic acid [16, 18]. It is known that the hydroxyl and carboxyl functional groups in the adsorbent may donate protons and become deprotonated groups (C-$O^-$ and $COO^-$), which are involved in coordination with nickel ions, resulting in an increase in the adsorption of the nickel ions [21].

*Point of zero charge (PZC):* The point of zero charge (PZC) parameter is used to assess the surface properties of an adsorbent. The pH of the solution required to yield a net zero surface charge is denoted by $pH_{PZC}$. Therefore, the surface of an adsorbent has a net positive surface charge at $pH<pH_{PZC}$, while it has a net negative surface charge at $pH>pH_{PZC}$. Fig. 3 displays the plot of $H = pH_i - pH_j$ vs $pH_i$ to calculate the $pH_{PZC}$ value.

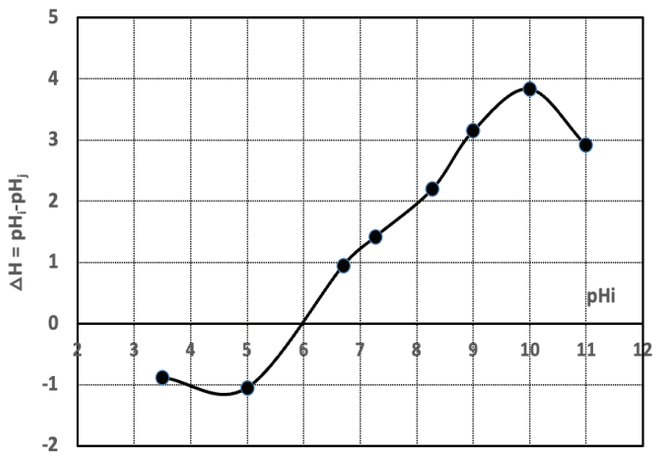


**Fig. 3. The plot of $H = pH_i - pH_j$ vs $pH_i$ of the CTS-APS-VL sample.**

From Fig. 3, the $pH_{PZC}$ value of the CTS-APS-VL sample was determined to be 6.0. At pH<6 the surface of the material is positively charged due to protonation of the hydroxyl and carboxyl functional groups, while it is negatively charged at pH>6 as a result of deprotonation. At pH>6, the material favours metal cation adsorption. Therefore, the $pH_{PZC}$ value for the CTS-APS-VL sample indicates that the adsorption of nickel ions will occur at pH≥6.0

*EDX spectroscopy:* The EDX spectroscopy clearly shows that nickel ions are adsorbed onto the chitosan-modified peanut shell (as shown Fig. 4). From EDX analysis, the nickel content was found to be about 5.7 wt.%, indicating the successful adsorption of nickel on cellulose from chitosan-modified peanut shells.

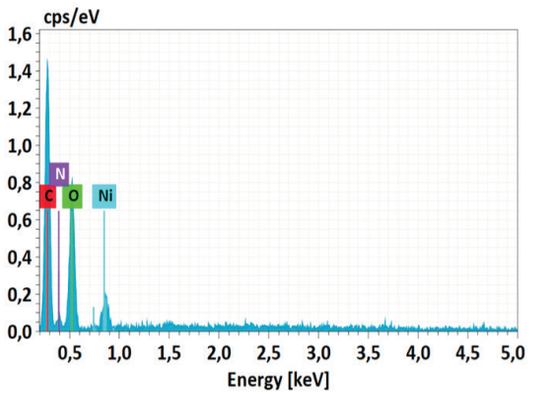


**Fig. 4. EDX spectroscopy of CTS-APS-VL loaded with nickel.**

### *3.2. Nickel adsorption capacity of chitosan-modified peanut shell*

Figure 5 shows the nickel adsorption capacity of cellulose from chitosan-modified peanut shells at different times.

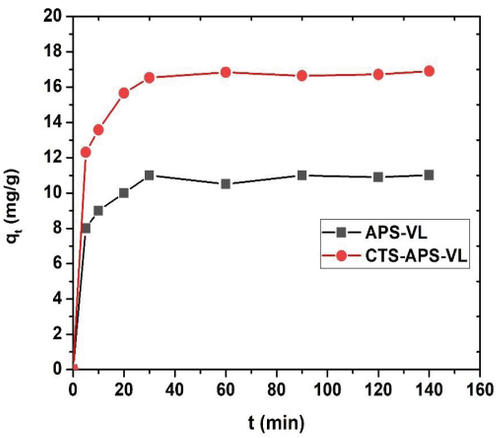


**Fig. 5. Nickel adsorption capacity of the APS-VL and CTS-APS-VL samples using 200 ml of nickel solution with an initial concentration of 80 ppm at pH 7.0, and 0.4 g of adsorbent over an adsorption period of 10-140 min.**

The experimental data showed that the nickel adsorption capacity increased as the adsorption time increased from 10 to 60 min, and it reached equilibrium after 90 min. In the as-prepared samples, the hydroxyl and carboxyl functional groups played a major role in nickel adsorption. The adsorption of nickel ions on the surface of the as-prepared samples was accomplished through physical processes including both weak electrostatic interaction and Van der Waals forces, or through the formation of complexation between the nickel ion and carboxyl and hydroxyl anion on the surface of as-prepared materials.

The adsorption capacities at equilibrium time ($q_e$ in mg/g) of the APS-VL and CTS-APS-VL samples were found to be 11.10 and 16.90 mg/g, respectively. Therefore, the nickel adsorption capacity of the CTS-APS-VL sample was higher than that of the APS-VL sample. Furthermore, the amount of hydroxyl groups in the CTS-APS-VL sample was higher than that of APS-VL and the amount of carboxyl groups in CTS-APS-VL was lower than that of APS-VL. This result suggests that the presence of hydroxyl groups is the main agent for adsorbing nickel ions onto the CTS-APS-VL sample.

Similar to adsorption time, the pH of the working solution has a strong influence on the adsorption capacity of metal ions by affecting surface charge density of the adsorbent (dissociation of oxygen containing functional groups) and the degree of ionization and state of heavy metal ion species in the solution. In this study, nickel adsorption was investigated in the pH range of 3.2-8.0. The obtained results are depicted in Fig. 6.

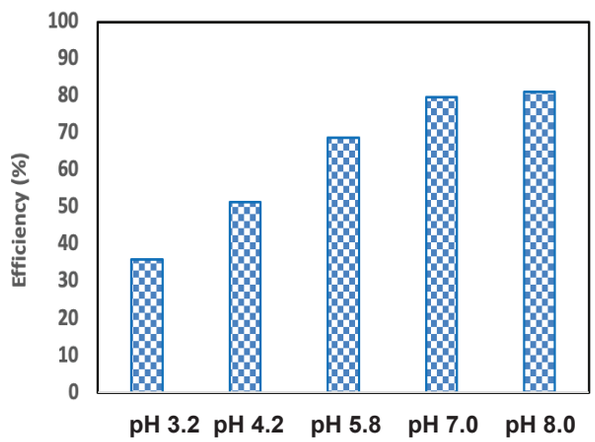


**Fig. 6. Effect of pH on the adsorption of nickel (II) onto the CTS-APS-VL sample with 200 ml of nickel solution with an initial concentration of 80 ppm, 0.4 g of adsorbent, and an adsorption time 90 min in pH range of 3.2-8.0.**

As depicted in Fig. 6, the nickel adsorption capacity (in terms of percent efficiency) increased with increasing solution pH. A maximum adsorption efficiency of about 81.05% occurred at pH 7.0 and 8.0, and the adsorption capacity at equilibrium time ($q_e$ in mg/g) of the APS-VL sample was 16.90 mg/g. The minimum nickel adsorption efficiency of 35.98% at pH 3.2 may be due to the high concentration and high mobility of $H^+$ ions. Thus, the hydrogen ions are preferentially adsorbed rather than the metal ions (e.g., nickel ions). At higher pH values, the nickel adsorption efficiency was enhanced because the hydrogen ions were less preferentially adsorbed than the metal ions due to the lower number of $H^+$. On the other hand, the $pH_{PZC}$ of the CTS-APS-VL sample and different species of nickel ions in the solution could be used to describe how the pH of the solution affects the adsorption capacity of CTA-APS-VL. The point of zero charge ($pH_{pzc}$) of the CTS-APS-VL sample was determined to be 6.0 (as shown in Fig. 3), and the nickel solution comprises nickel species with different coordination numbers such as $Ni^{2+}$, $Ni(OH)^+$, and $Ni(OH)_2$ in a pH range of 3.2 to 8.0. These species are adsorbed onto the surface of CTS-APS-VL by an ion exchange mechanism with the functional groups present in CTS-APS-VL or by hydrogen bonding, as shown below:

Ion exchange:

$$2(–ROH) + Ni^{2+} \rightarrow 2(RO)Ni + 2H^+ \; –ROH + Ni(OH)^+ \rightarrow (–RO)\,Ni(OH) + H^+$$

Hydrogen bonding:

$$2(–ROH) + Ni(OH)_2 \rightarrow (–ROH)_2 + Ni(OH)_2$$

where R represents the matrix of CTS-APS-VL.

At a low pH of 3.2, the surface of CTS-APS-VL is positively charged due to protonation of the hydroxyl and carboxyl functional groups and unfavourable conditions for the adsorption of the $Ni^{2+}$ and $Ni(OH)^+$ species. As the pH solution increased, the surface of CTS-APS-VL became less positive and therefore electrostatic attraction between the $Ni^{2+}$ and $Ni(OH)^+$ species and the surface groups likely increased.

In this study, the pH value of each metal ion solution had to be lower than 8 to prevent the formation of hydrolysed species and precipitation. If the pH value exceeds 8, the adsorption mechanism changes, affecting the efficiency of the adsorption.

### *3.3. Adsorption kinetics*

In order to understand the kinetics of nickel adsorption using cellulose from chitosan-modified peanut shells as an adsorbent, pseudo-first-order and pseudo-second-order kinetic models were tested with the experimental data.

*Pseudo-first-order model:* The pseudo-first-order model in linearized form is expressed in Eq. (3). The rate constant, $k_1$, was calculated from the slope and intercept of the plot of $\log(q_e\text{-}q_t)$ vs time (as shown in Fig. 7). The equilibrium adsorption capacity ($q_e$) calculated from Eq. (3) is referred to as the calculated value of equilibrium adsorption capacity ($q_{e(TT)}$).

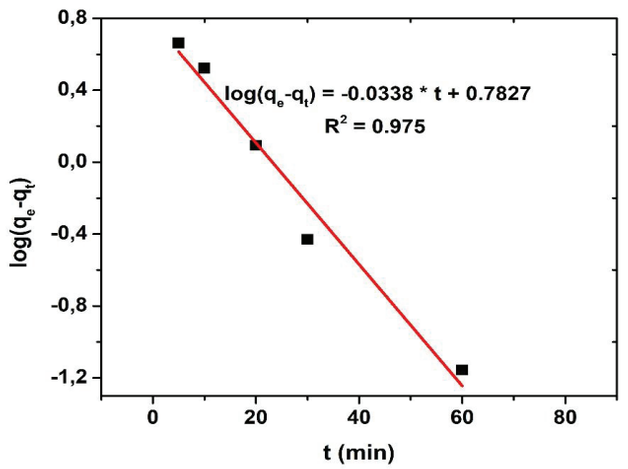


**Fig. 7. Linear plot of $\log(q_e-q_t)$ vs t of nickel adsorption onto the CTS-APS -VL sample with 200 ml of nickel solution with an initial concentration of 80 ppm, pH 7.0, 0.4 g of adsorbent, and a range of adsorption time of 10-60 min.**

As shown in Fig. 7, the rate constant $k_1$ was determined to be 0.077 $min^{-1}$. It is also possible to calculate the equilibrium adsorption capacity, which was found to be 6.06 mg/g (denoted $q_{e\ cal}$). In fact, the calculated equilibrium adsorption capacity, $q_{ecal}$, should be in accordance with the experimental adsorption capacity $q_{e\ exp}$ [19, 20]. Although the correlation coefficient values ($R^2$) are very high, the calculated ones, obtained from the linear plots (Table 2), did not agree with experiment ($q_{e\ exp}$ =16.90 mg/g). This suggests that nickel adsorption does not follow pseudo-first-order kinetics.

**Table 2. Kinetic parameters for nickel adsorption on cellulose from chitosan-modified peanut shells.**

| Kinetic models | Parameters | |
|---|---|---|
| Pseudo-first-order model | $k_1$ ($min^{-1}$) | 0.077 |
| | $q_{e\ cal}$ (mg/g) | 6.06 |
| | $R^2$ | 0.975 |
| Pseudo-second-order model | $k_2$ (g/(mg x min) | 0.024 |
| | $q_{e\ cal}$ (mg/g) | 17.54 |
| | $R^2$ | 0.999 |

*Pseudo-second-order model:* The nickel adsorption kinetic data can also be described by pseudo-second-order model, which is expressed in Eq. (4).

The pseudo-second-order rate constant, $k_2$, and $q_{e\ cal}$ values were calculated from the slope and intercept of the plots t/q vs. t (as shown in Fig. 8). The rate constant, $k_2$, was 0.024 g/(mg.min). The calculated equilibrium adsorption capacity ($q_{e\ cal}$) was 17.54 mg/g. Therefore, the calculated $q_e$ values agreed well with experimental $q_e$ values (Table 2), thus the pseudo-second-order kinetic model well described the nickel adsorption kinetic data.

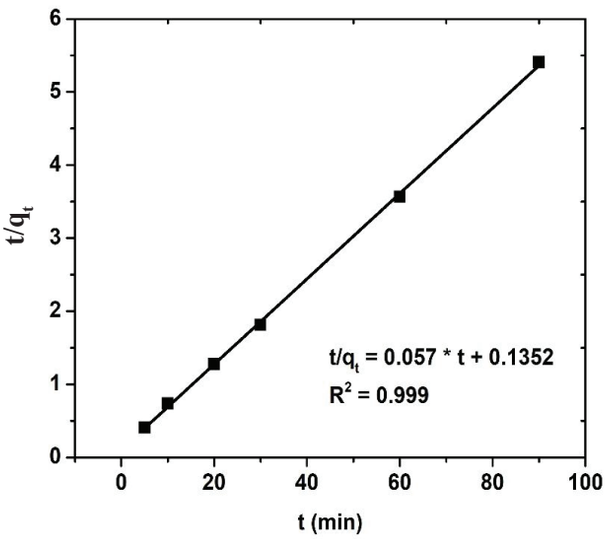


**Fig. 8. Linear plot of $t/q_t$ vs t of nickel adsorption onto the CTS-APS-VL sample with 200 ml of nickel solution with an initial concentration of 80 ppm, a pH of 7.0, 0.4 g of adsorbent, and an adsorption period of 10-90 min.**

### *3.4. Adsorption isotherms*

Adsorption isotherms indicate how adsorbates interact with adsorbents and how equilibrium is established between adsorbed metal ions on the adsorbent. The maximum adsorption capacity is determined by equilibrium isotherms. The most common types of models are the Langmuir, Freundlich, and Temkin isotherms.

*Langmuir isotherm model:* The Langmuir isotherm assumes a monolayer of adsorbates covering a homogeneous adsorbent surface. This suggests that once an adsorbate occupies an available adsorption site, no further adsorption can take place at that site. Additionally, the adsorption activation energy is assumed to be equal for each molecule that adsorbs onto the surface.

Figure 9 presents a linear plot of $C_e/q_e$ vs $C_e$ for the experimental adsorption isotherm of nickel ions on chitosan-modified peanut shells at room temperature. The Langmuir isotherm constant and correlation coefficients are given in Table 3, with a maximum monolayer adsorption capacity ($q_m$) for nickel removal of 25.70 mg/g.

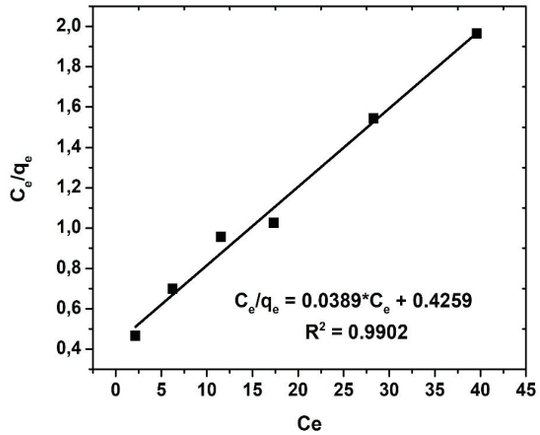


**Fig. 9. Linear plot of $C_e/q_e$ vs $C_e$ for nickel adsorption onto the CTS-APS -VL sample with 200 ml of nickel solution over a range of initial concentrations (20-120 ppm), pH of 7.0, equilibrium adsorption time of 90 min, and 0.4 g of adsorbent.**

**Table 3. Adsorption isotherm parameters.**

| Isotherm model | Parameters | Non-linear equation |
|---|---|---|
| Langmuir model | $q_m$=25.70 mg/g<br>$K_L$=0.09 l/mg<br>$R^2$=0.990<br>$\chi^2$=0.234 | $q_e = \frac{2.34 * C_e}{(1 + 0.09 * C_e}$ |
| Freundlich model | $K_F$=3.35<br>n=1.94<br>$R^2$=0.974<br>$\chi^2$=0.632 | $q_e = 3.35 * C_e^{0.51}$ |
| Temkin model | $b_T$=4.52 kJ/mol<br>$K_T$=0.94<br>$R^2$=0.974<br>$\chi^2$=0.433 | $q_e = 5.70 \times \ln(0.45 \times C_e)$ |

*Freundlich isotherm model:* Unlike the Langmuir isotherm model, the Freundlich isotherm model assumes that the adsorption process occurs in multilayers, where each adsorption centre can adsorb more than one adsorbed molecule.

Figure 10 shows the linear plot of $\log(q_e)$ vs. $\log(C_e)$ for the experimental adsorption isotherm of nickel ions on the CTS-APS-VL sample at room temperature.

The Freundlich adsorption constants, evaluated from the isotherms, with correlation coefficients and are listed in Table 3.

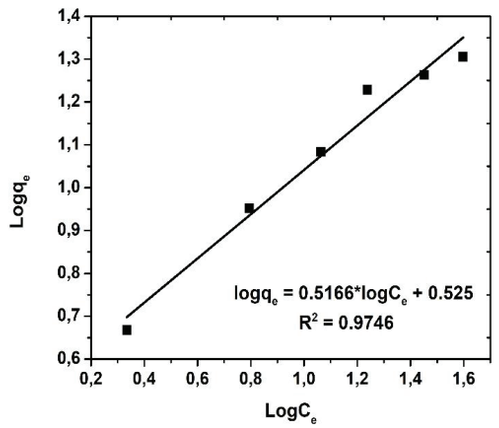


**Fig. 10. Linear plot of $\log(q_e)$ vs. $\log(C_e)$ of nickel adsorption onto the CTS-APS-VL sample with 200 ml of nickel solution over a range of initial concentrations of 20-120 ppm, pH 7.0, equilibrium adsorption time of 90 min, and 0.4 g of adsorbent.**

*Temkin isotherm model:* The Temkin isotherm model is concerned with the influence of adsorbent-adsorbent interaction on the adsorption equilibrium. The model assumes that the adsorption heat (as a function of temperature) of all adsorbents in a layer will decrease linearly, rather than logarithmically, with increasing surface coverage.

Figure 11 shows a linear plot of $q_e$ vs $\ln(C_e)$ of the experimental adsorption isotherm of nickel ions on modified peanut shells at room temperature.

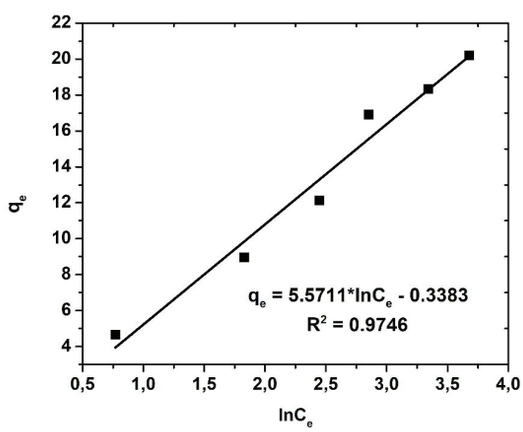


**Fig. 11. The linear plot of $q_e$ vs $\ln(C_e)$ onto the CTS-APS-VL sample with 200 ml of nickel solution over a range of initial concentrations of 20-120 ppm, pH 7.0, an equilibrium adsorption time of 90 min, and 0.4 g of adsorbent.**

The Temkin adsorption constant was calculated to be 0.45 kJ/mol, which is lower than 8 kJ/mol. Therefore, it can be assumed that the interaction between nickel ions and the surface of the as-prepared adsorbent was weak.

As shown in Table 3, the values of $R^2$ and indicate that the Langmuir and Temkin isotherm models exhibited a better fit than the Freundlich model for nickel adsorption. The lower the value, the better the fit of the line to the data, and the higher the $R^2$ value, the better the fit.

Table 4 displays a comparison of the maximum adsorption capacity of nickel onto various modified agro-wastes. CTS-AP-VL was found to have a relatively large adsorption capacity, and this indicates that it is a promising material for the removal of metal ions from aqueous solutions.

**Table 4. Comparison of maximum adsorption capacity of nickel onto other agro-wastes.**

| Materials | Maximum sorption capacity (mg/g) | References |
|---|---|---|
| Chemically Treated Mahogany Sawdust | 13.42 | [21] |
| Chemically modified orange peel | 162.6 | [20] |
| Phthalate-functionalized sugarcane bagasse | 53.94 | [22] |
| $Na_2CO_3$-modified Miller leaf powder | 28.98 | [23] |
| HCl modified meranti sawdust | 35.97 | [24] |
| CTS-APS-VL | 25.70 | This study |

## 4. Conclusions

The cellulose isolated from chitosan-modified peanut shells (CTS-APS-VL) showed better adsorption capacity compared to cellulose isolated from peanut shells (APS-VL) under the same experimental conditions. The adsorption capacity at equilibrium time ($q_e$ in mg/g) of the APS-VL and CTS-APS-VL samples were found to be 11.10 and 16.90 mg/g, respectively, at an adsorption time of 90 min, initial nickel concentration of 80 ppm, volume of 200 ml, and adsorbent mass of 0.4 g. The pseudo-second-order kinetics model was better suited to the data than the pseudo-first-order model. The rate constant, $k_2$, was determined to be 0.024 (g/(mg.min)). The calculated equilibrium adsorption capacity ($q_{e\ cal}$) was 17.54 mg/g. The Langmuir and Temkin isotherm models showed slightly better results than the Freundlich model for the as-prepared material, indicating monolayer coverage. According to the Langmuir model, the maximum monolayer adsorption capacity ($q_m$) for nickel removal was 25.70 mg/g. The Temkin adsorption constant was calculated as 0.45 kJ/mol and it can be assumed that the interaction between the nickel ions and the surface of the as-prepared adsorbent was weak.

## CRediT author statement

Thi Lan Phung: Conceptualisation, Methodology, Formal analysis, Writing, Reviewing, Editing; Thi Kim Giang Nguyen: Data analysis; Phuong Hien Ho: Reviewing, Data analysis; Thanh Nga Pham: Reviewing, Editing.

## ACKNOWLEDGEMENTS

The research funding from the Vietnam Ministry of Education and Training under grant code B2021-SPH 14 was acknowledged.

## COMPETING INTERESTS

The authors declare that there is no conflict of interest regarding the publication of this article.

## REFERENCES

[1] J. Li, X. Wang, G. Zhao, et al. (2018), "Metal-organic framework-based materials: superior adsorbents for the capture of toxic and radioactive metal ions", *Chem. Soc. Rev*., **47(7)**, pp 2322-2356, DOI: 10.1039/C7CS00543A.

[2] W. Ouyang, Y. Wang, C. Lin, et al. (2018), "Heavy metal loss from agricultural watershed to aquatic system: A scientometrics review", *Sci. Total Environ*., **637**, pp.208-220, DOI: 10.1016/j.scitotenv.2018.04.434.

[3] C. Zhu, F. Liu, Y. Zhang, et al. (2016), "Nitrogen-doped chitosan-Fe(III) composite as a dual-functional material for synergistically enhanced co-removal of Cu(II) and Cr(VI) based on adsorption and redox", *Chem. Eng. J*., **306**, pp.579-587, DOI: 10.1016/j.cej.2016.07.096.

[4] K.H. Vardhan, P.S. Kumar, R.C. Panda (2019), "A review on heavy metal pollution, toxicity and remedial measures: Current trends and future perspectives", *J. Mol. Liq*., **290**, DOI: 10.1016/j.molliq.2019.111197.

[5] M.D. Vedenyapina, A.Y. Kurmysheva, S.A. Kulaishin, et al. (2021), "Adsorption of heavy metals on activated carbons: A review", *Solid Fuel Chem*., **55**, pp.83-104, DOI: 10.3103/S0361521921020099.

[6] M. Bilal, I. Ihsanullah, M. Younas, et al. (2022), "Recent advances in applications of low-cost adsorbents for the removal of heavy metals from water: A critical review", *Separation and Purification Technology*, **278**, DOI: 10.1016/j.seppur.2021.119510.

[7] A. Jamshaid, A. Hamid, N. Muhammad, et al. (2017), "Cellulose-based materials for the removal of heavy metals from wastewater - An overview", *Chem. Bio. Eng. Rev.*, **4(4)**, pp.1-18.

[8] E. Khademian, E. Salehi, H. Sanaeepur, et al. (2020), "A systematic review on carbohydrate biopolymers for adsorptive remediation of copper ions from aqueous environments-part A: Classification and modification strategies", *Science of The Total Environment*, **738**, DOI: 10.1002/cben.201700002.

[9] O. Bobet, S. Nassio, M. Seynou, et al. (2020), "Characterization of peanut shells for their valorization in earth brick", *Journal of Minerals and Materials Characterization and Engineering*, **8(4)**, pp.301-315, DOI: 10.4236/jmmce.2020.84018.

[10] P. Ganguly, S. Sengupta, P. Das, et al. (2020), "Synthesis of cellulose from peanut shell waste and its use in bioethanol production", *Bioresource Utilization and Bioprocess Book*, pp.81-91, DOI: 10.1007/978-981-15-1607-8_10.

[11] I. Sargın, G. Arslan (2015), "Chitosan/sporopollenin microcapsules: Preparation, characterisation and application in heavy metal removal", *Int. J. Biol. Macromol*., **75**, pp.230-238, DOI: 10.1016/j.ijbiomac.2015.01.039.

[12] L. Zhang, Y. Zeng, Z. Cheng (2016), "Removal of heavy metal ions using chitosan and modified chitosan: A review", *Journal of Molecular Liquids*, **214**, pp.175-191, DOI: 10.1016/j.molliq.2015.12.013.

[13] M.D.H. Rahaman, A. Islam, M. Islam, et al. (2021), "Biodegradable composite adsorbent of modified cellulose and chitosan to remove heavy metal ions from aqueous solution", *Current Research in Green and Sustainable Chemistry*, **4**, pp.100-119, DOI: 10.1016/j.crgsc.2021.100119.

[14] D. Zhang, L. Wang, H. Zeng, et al. (2019), "A three-dimensional macroporous network structured chitosan/cellulose biocomposite sponge for rapid and selective removal of mercury (II) ions from aqueous solution", *Chemical Engineering Journal*, **363**, pp.192-202, DOI: 10.1016/j.cej.2019.01.127.

[15] K. Zhanga, P. Suna, H. Liua, et al. (2016), "Extraction and comparison of carboxylated cellulose nanocrystals from bleached sugarcane bagasse pulp using two different oxidation methods", *Carbohydrate Polymers*, **138**, pp.237-243, DOI: 10.1016/j.carbpol.2015.11.038.

[16] A.M. Adel, A.M.E. Shafei, M.T.A. Shemy, et al. (2017), "Influence of cellulose polymorphism on tuneable mechanical and barrier properties of chitosan/oxidized nanocellulose bio-composites", *Egypt. J. Chem*., **60(4)**, pp.639-652, DOI: 10.21608/ejchem.2017.1194.1062.

[17] Y. Liu, K. Wang, H. Zhang, et al. (2020), "Modified ammonium persulfate oxidations for efficient preparation of carboxylated cellulose nanocrystals", *Carbohydrate Polymers*, **229**, DOI: 10.1016/j.carbpol.2019.115572.

[18] B. Soni, E.B. Hassan, M.W. Schilling, et al. (2016), "Transparent bionanocomposite films based on chitosan and TEMPO-oxidized cellulose nanofibers with enhanced mechanical and barrier properties", *Carbohydrate Polymers*, **151**, pp.779-789, DOI: 10.1016/j.carbpol.2016.06.022.

[19] J. Febrianto, A.N. Kosasih, J. Sunarso, et al. (2009), "Equilibrium and kinetic studies in adsorption of heavy metals using biosorbent: A summary of recent studies", *J. Hazard. Mater*., **162**, pp.616-645.

[20] N. Feng, X. Guo, S. Liang, et al. (2011), "Biosorption of heavy metals from aqueous solutions by chemically modified orange peel", *Journal of Hazardous Materials*, **185(1)**, pp.49-54, DOI: 10.1016/j.jhazmat.2010.08.114.

[21] R. Chanda, A.H. Mithun, A. Hasan, et al. (2021), "Nickel removal from aqueous solution using chemically treated mahogany sawdust as biosorbent", *Hindawi Journal of Chemistry*, **2021**, DOI: 10.1155/2021/4558271.

[22] S.N.D.C. Ramos, A.L.P. Xavier, F.S. Teodoro, et al. (2016), "Removal of cobalt(II), copper(II), and nickel(II) ions from aqueous solutions using phthalate-functionalized sugarcane bagasse: Monoand multicomponent adsorption in batch mode", *Industrial Crops and Products*, **79**, pp.116-130, DOI: 10.1016/j.indcrop.2015.10.035.

[23] S. Gupta, S.K. Sharma, A. Kumar (2019), "Biosorption of Ni(II) ions from aqueous solution using modified Aloe barbadensis Miller leaf powder", *Water Science and Engineering*, **12(1)**, pp.27-36, DOI: 10.1016/j.wse.2019.04.003.

[24] M. Rafatullaha, O. Sulaiman, R. Hashim, et al. (2009), "Adsorption of copper (II), chromium (III), nickel (II) and lead (II) ions from aqueous solutions by meranti sawdust", *Journal of Hazardous Materials*, **170(2-3)**, pp.969-977, DOI: 10.1016/j.jhazmat.2009.05.066.

 DOI: 10.31276/VJSTE.66(1).34-45

# Preparation of pyridinium-based ionic liquid and application as a green catalyst for the synthetic route of 4*H*-1-benzopyran-5(6*H*)-ones

**Huong Ngoc Thi Dao[1, 2], The Thai Nguyen[1, 2], Tran Huyen Thi Nguyen[1, 2], Thuy Hong Ngoc Phan[1, 2], Phuong Hoang Tran[1, 2*]**

[1]*Department of Organic Chemistry, Faculty of Chemistry, University of Science, Vietnam National University - Ho Chi Minh City, Linh Trung Ward, Thu Duc City, Ho Chi Minh City, Vietnam*

[2]*Vietnam National University - Ho Chi Minh City, Linh Trung Ward, Thu Duc City, Ho Chi Minh City, Vietnam*

Received 19 July 2023; revised 1 August 2023; accepted 11 September 2023

***Abstract:***

**1-(4-sulfobutyl)pyridinium chlorozincate ionic liquid was synthesised in high yield (89%) through a simple route and characterised using FT-IR, NMR, and HRMS spectroscopy. The one-pot reaction was employed for the condensation reaction of benzaldehydes, 5,5-dimethyl-1,3-cyclohexanedione, and dicyanomethane, utilising the prepared ionic liquid catalyst. The optimal conditions for the reaction were achieved with a catalyst loading of 10 mol%, a solvent mixture of water and ethanol (1:1, v/v), maintained at 100°C for 180 minutes. A broad spectrum of benzopyran-5(6*H*)-one derivatives was prepared, yielding moderate to good results. The notable features of this procedure include readily available substrates, short reaction times, the use of environmentally friendly solvents, and the elimination of the need for chromatography in the isolation of products. A new acidic pyridinium-based ionic liquid was successfully synthesised and used as a catalyst in the synthetic process of 2-amino-3-cyano-4-phenyl-7,7-dimethyl-7,8-dihydro-4*H*-1-benzopyran-5(6*H*)-ones. These reactions involved a condensation reaction of aromatic benzaldehydes, 5,5-dimethyl-1,3-cyclohexanedione, and dicyanomethane in a solvent mixture of ethanol and water, resulting in the desired products in moderate to good yields. The procedure is efficient and eco-friendly, and the products can be easily obtained by recrystallisation. Thus, this protocol offers an alternative to existing methods.**

***Keywords:*** **Brønsted-Lewis acidic ionic liquid, green catalyst, multicomponent reaction, 1-(4-sulfobutyl) pyridinium chlorozincate, 4*H*-1-benzopyran-5(6*H*)-one.**

***Classification numbers:*** **2.2, 2.3**

## 1. Introduction

After being discovered and initially published by Paul Walden in 1914, numerous reports have explored the properties and applications of ionic liquids in various fields. Nowadays, ionic liquids are recognised as environmentally friendly solvents and catalysts in organic synthesis [1]. In comparison to traditional volatile organic solvents, ionic liquids offer increased safety during synthetic procedures due to their low vapour pressure and recyclability [2]. The solubility of ionic liquids can be tailored by designing specific ions. In many instances, ionic liquids have proven to be efficient catalysts in various reactions [3, 4]. A notable feature of ionic liquids is their ease of preparation, with the availability of various active sites, such as basic properties (-OH, -$NH_2$...), Brønsted or Lewis acidic properties (-$SO_3H$, -COOH, or $Al_xCl_y$, $Zn_xCl_y$...). Particularly, a novel type of acidic ionic liquid containing both Lewis and Brønsted acidic groups in its structure has garnered significant attention. These task-specific ionic liquids are considered environmentally friendly and hold potential in many catalytic processes that require the presence of both Brønsted and Lewis acidic sites [5].

Currently, the one-pot multicomponent reaction carried out under green conditions has become a popular and sustainable trend in organic synthesis. One-pot three-component reactions, referred to as convergent chemical approaches, are rapid and efficient methods in organic synthesis due to their high levels of atom efficiency [6, 7]. The advantages of multicomponent reactions include cost-effectiveness, high selectivity, good yields, and time savings [8, 9]. Moreover, multicomponent

*Corresponding author: Email: thphuong@hcmus.edu.vn

reactions have garnered attention from chemists for their ability to minimize steps and reduce waste in experiments. The three-component transformation is the preferred choice and is applied across a wide range of organic reactions, such as the synthesis of polyhydroquinoline [10], dihydropyrimidinones [11], 1-(α-aminoalkyl)-2-naphthols [12], and 1,3-thiazole derivatives [13], as well as pyranopyrazole and pyranopyrimidine derivatives [14]. Additionally, pseudo-six-components have been employed in the synthesis of tetrahydrodipyrazolopyridines [15].

Pyran is a six-membered heterocyclic compound containing oxygen, and it serves as a valuable building block in many organic compounds. Chromene, also known as benzopyran, is a crucial subgroup in these heterocyclic derivatives and is categorised into chroman, 2*H*-chromene, and 4*H*-chromene, which are commonly observed frameworks in numerous complex natural products [16]. Benzopyrans are described as fundamental structural units found in polyphenols and are explored in alkaloids, tocopherols, flavonoids, and anthocyanins [17]. Due to their significant biological and pharmacological activities, including antibacterial, antitumor, antiallergic, antibiotic, anticancer, antitubercular, antimicrobial, anti-coagulant, antibiotic, and hypolipidemic properties [18-23], benzopyrans have found extensive use in the pharmaceutical industry. Given the attractive bioactivity of benzopyrans, various synthetic protocols for pyrans have been published [24]. The most widely adopted method for preparing benzopyrans involves a three-component reaction of 5,5-dimethyl-1,3-cyclohexanedione, an aldehyde, and dicyanomethane, which undergoes Knoevenagel condensation and Michael addition reactions [24]. A wide range of homogeneous catalysts have been investigated for this reaction, including boric acid [25], ammonium acetate [26], potassium phosphate [27], MgO [28], $K_2CO_3$ [29], $CeCl_3.H_2O$ [30], $Mg(ClO_4)_2$ [31], DBU [32], triethylamine [33], iodine [34], and methane sulfonic acid [35]. However, a drawback of these methods is the difficulty of separating the catalysts from the reaction mixture. To address these issues, heterogeneous or solid catalysts, such as amino-functionalized silica gel [36], $SiO_2$-Pr-$SO_3H$ [37], NMPs-$PhSO_3H$ [38], $CeO_2$ [39], CuO-$CeO_2$ nanocomposite [40], $CeO_2$-$Al_2O_3$ nanocomposite [41], $Ni_{0.5}Zn_{0.5}Fe_2O_4$@HA-PRS [42], and $CeMg_xZr_{1-x}O_2$ [43], have been prepared and applied in this reaction. Nevertheless, other limitations include the use of volatile organic solvents and the high cost of these catalysts.

Recently, ionic liquids have emerged as potential catalysts for this transformation due to their high efficiency and recyclability. 1-Butyl-3-methyl imidazolium hydroxide was employed as an efficient homogeneous catalyst in the synthesis of substituted 2-amino-2-chromenes by K. Gong, et al. (2008) [44]. This condensation reaction involving malononitrile, aldehydes, and naphthols was conducted in aqueous media. M.N. Elinson, et al. (2015) [24] reported a three-component reaction of benzaldehydes, 5,5-dimethyl-1,3-cyclohexanedione, and dicyanomethane using 1-butyl-4-methylimidazolium tetrafluoroborate as the catalyst. Subsequently, A.R.M. Zare, et al. (2014) [45] synthesised tetrahydrobenzo[*b*]-pyrans through Knoevenagel-Michael cyclocondensation, employing (1-carboxymethyl-3-methylimidazolium bromide ionic liquid as an efficient catalyst under solvent-free conditions. Another acidic ionic liquid catalyst utilised in the preparation of 2-amino-4*H*-chromene derivatives was $Li(OHCH_2CH_2NH_2)(CF_3OAC)$. E.A. Gilandeh, et al. (2014) [46] demonstrated that this ionic liquid efficiently catalysed the cyclisation of aldehydes, malononitrile, and various enol compounds. A green synthetic route for 2-amino-4H-chromene using a basic ionic liquid in water was reported by V.P. Pagore, et al. (2015) [47]. The condensation reactions occurred in the presence of 1-ethyl-3-methyl imidazolium hydroxide under microwave irradiation, resulting in high yields [47]. 2-(2-Hydroxyethoxy)ethaneammonium formate ionic liquid was described as an ammonium-type basic catalyst for synthesising various derivatives of chromenes with excellent yields [48]. To enhance the recycling capability of the catalyst, *N*-propyl-imidazolium hydrogen sulfate was grafted onto the surface of silica by K. Niknam, et al. (2013) [49]. The synthesis of 3,4-dihydropyrano[*c*]-chromenes was effectively carried out under solvent-free conditions. Similarly, a newly supported ionic liquid (HAP-Pd-[BMIM][OH]) was found to be an efficient heterogeneous catalyst in the multicomponent cyclocondensation of 2-amino-4*H*-chromenes by P. Sharma, et al. (2016) [50]. In this study, a new environmentally friendly synthetic method for benzopyran compounds was developed through the condensation of three substrates, namely benzaldehydes, 5,5-dimethyl-1,3-cyclohexanedione, and dicyanomethane, in the presence of an ionic liquid containing Brønsted-Lewis acidic sites as a catalyst.

## 2. Materials and methods

### 2.1. Chemicals

All reactants were purchased from Merck. Organic solvents were purchased from Xilong. Deuterated solvents for NMR experiments, including $CDCl_3$, $CD_3OD$, $(CD_3)_2SO$ and $(CD_3)_2CO$, were purchased from Cambridge Isotope Laboratories (Andover, MA).

### 2.2. Methods

The melting point was determined using a Buchi B-545 melting point apparatus. Fourier-transform infrared (FT-IR) spectra were recorded with a Bruker E400 FT-IR spectrometer. Nuclear magnetic resonance ($^1H$ and $^{13}C$ NMR) experiments were conducted on a Bruker Advance 500 MHz NMR spectrometer. Mass spectrometry (MS) was performed in negative ionization mode using an Agilent 1200 series HPLC coupled to a Bruker micrOTOF-QII EIS mass spectrometer detector.

*Synthesis of 1-(4-sulfobutyl)pyridinium chlorozincate (IL3):* A mixture of pyridine (10.0 mmol, 790 mg) and 1,4-butane sultone (10.0 mmol, 1360 mg) was initially combined and heated to 40°C. After 6 h, the resulting white solid was washed with $Et_2O$ and dried at 80°C for 30 min to yield an intermediate zwitterion. Next, the intermediate 4-(pyridinium-1-yl)butane-1-sulfonate (10.0 mmol, 2150 mg) was reacted with hydrochloric acid (10.0 mmol, 365 mg) at 80°C for 15 min to produce 1-(4-sulfobutyl) pyridinium chloride (IL0). Finally, 1-(4-sulfobutyl) pyridinium chloride (10.0 mmol, 2514 mg) and zinc chloride (10.0 mmol, 1363 mg) were added to a round-bottom flask containing 20 ml of toluene and refluxed for 10 h. The resulting acidic ionic liquid was decontaminated with $Et_2O$ and dried under reduced pressure for 60 min. The 1-(4-sulfobutyl)pyridinium chlorozincate ionic liquid (IL3) was characterised by FT-IR, $^1H$ and $^{13}C$ NMR, and HRMS. Similarly, 1-(4-sulfobutyl)pyridinium chlorotinate (IL1) and 1-(4-sulfobutyl)pyridinium chlorocopperate (IL2) were also prepared by mixing 1-(4-sulfobutyl)pyridinium chloride with tin chloride and copper chloride, respectively.

*Synthetic procedure of 2-amino-3-cyano-4-phenyl-7,7-dimethyl-7,8-dihydro-4H-1-benzopyran-5(6H)-one:* 5,5-Dimethyl-1,3-cyclohexanedione (1.0 mmol, 140 mg), benzaldehyde (1.0 mmol, 106 mg) and dicyanomethane (1.0 mmol, 66 mg) were added into round-bottom flask containing a solvent mixture (4 ml) of ethanol and water (1:1, v/v). Next, the ionic liquid catalyst (10 mol%, 35.4 mg) was added dropwise to the mixture. The reaction was carried out by heating at 100ºC for 180 min, and its progress was monitored using thin-layer chromatography. After the completion of the reaction, the crude product was collected by filtration and recrystallized in ethanol. The melting point was measured, and the $R_f$ value was calculated based on thin-layer chromatography. The product was characterized using $^1H$ and $^{13}C$ NMR spectroscopy.

*General procedure for catalyst recycle test:* A mixture of 5,5-dimethyl-1,3-cyclohexanedione (1.0 mmol, 140 mg), benzaldehyde (1.0 mmol, 106 mg), and dicyanomethane (1.0 mmol, 66 mg) was blended in a solvent mixture of ethanol and water (1:1, v/v). The IL3 catalyst (10 mol%, 35.4 mg) was added to the reactor, and the reaction mixture was refluxed at 100ºC for 180 min. After cooling to room temperature, 10 ml of water was introduced into the reactor. Following 5 min of stirring, vacuum filtration was used to remove the solvents. The solid was purified to obtain the product, while the liquid solution containing the ionic liquid was dried at 110°C for 6 h to remove water and organic solvent. Finally, the ionic liquid was washed with 10 ml of diethyl ether and dried at 110°C for 1 h. The purified ionic liquid was reused for the next cycles.

## 3. Results and discussion

### 3.1. Synthesis and characterization of acidic ionic liquid

1-(4-sulfobutyl)pyridinium chlorozincate (IL3) was prepared through a three-step procedure (Scheme 1). Initially, the nucleophilic substitution reaction between pyridine and 1,4-butane sultone was conducted at 40°C for 6 h. The resulting solid, 4-(pyridinium-1-yl)butane-1-sulfonate zwitterion, was then protonated using hydrochloric acid. In the final step, 1-(4-sulfobutyl) pyridinium chloride was reacted with zinc chloride salt to yield the desired ionic liquid, with a yield of 89%.

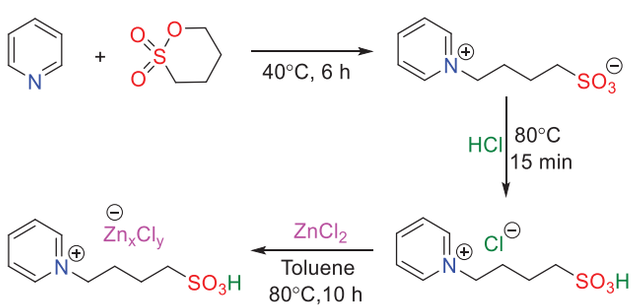


**Scheme 1. Synthetic procedure of 1-(4-sulfobutyl) pyridinium chlorozincate.**

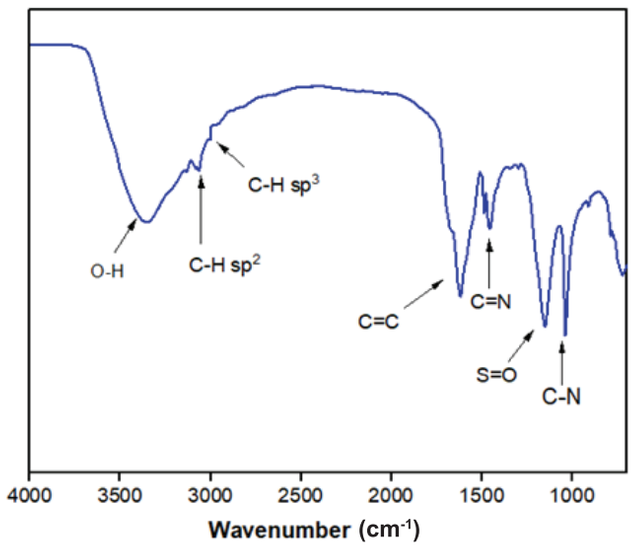


**Fig. 1. FT-IR of 1-(4-sulfobutyl)pyridinium chlorozincate.**

The structure of the acidic ionic liquid was analysed using Fourier-transform infrared spectroscopy (FT-IR), nuclear magnetic resonance spectroscopy (NMR), and high-resolution mass spectrometry (HRMS). In the FT-IR spectrum (Fig. 1), the ionic liquid exhibited a broad stretching absorption band for the O-H bond at 3340 $cm^{-1}$ and a characteristic stretching absorption of the S=O bond in the $SO_3H$ group at 1145 $cm^{-1}$. Pyridine displayed characteristic absorptions at 3056 and 1610 $cm^{-1}$ corresponding to the H-$Csp^2$ and C=C bonds. Furthermore, the presence of methylene was confirmed by the peak at 2982 $cm^{-1}$, representing H-$Csp^3$ stretching absorption. Absorption bands at 1456 and 1037 $cm^{-1}$ were attributed to the C=N and C-N bonds.

The $^1$H NMR spectrum (Fig. 2) revealed characteristic absorptions of pyridine, including peaks at 9.04 (d, *J*=5.0

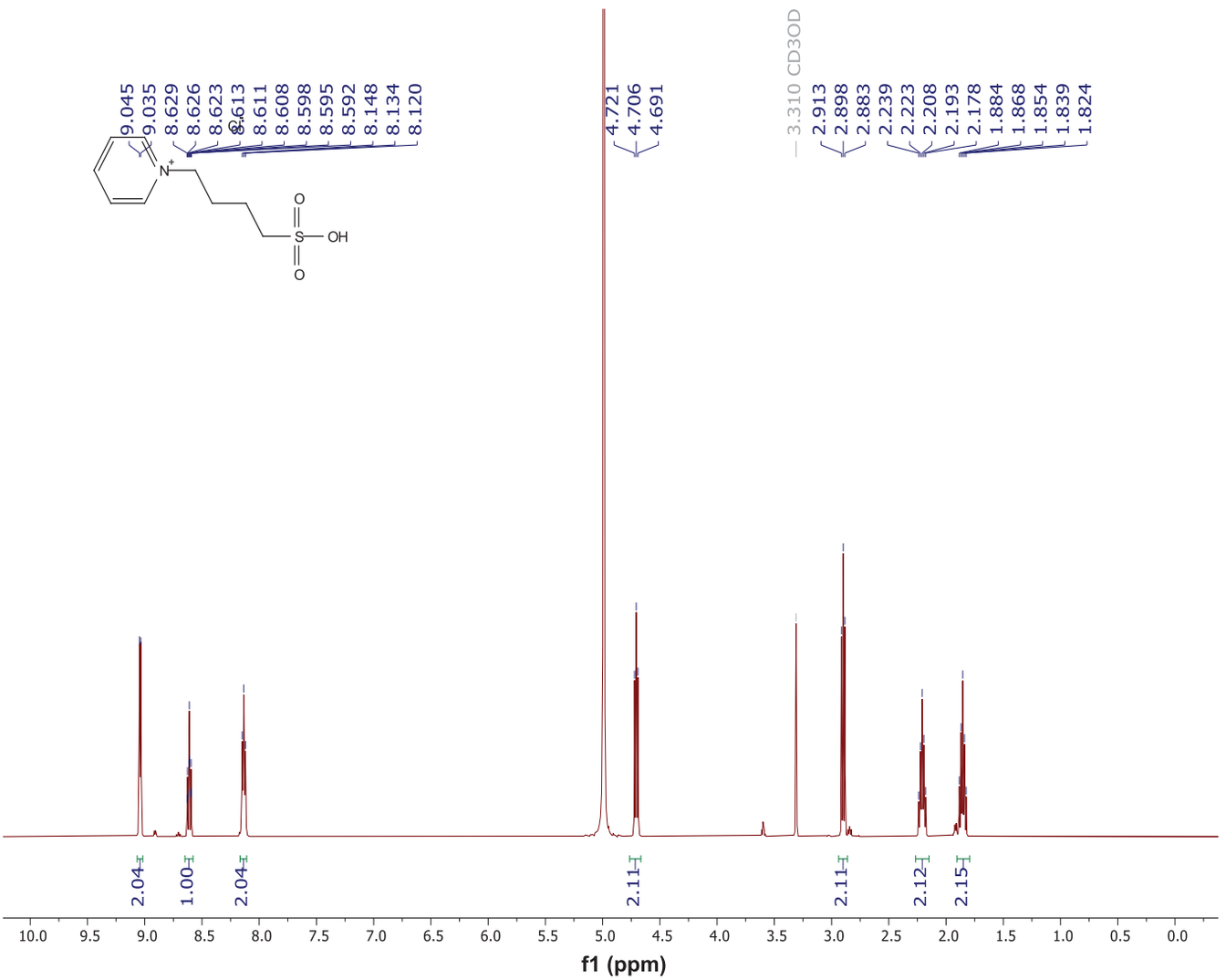


**Fig. 2. $^1$H NMR of 1-(4-sulfobutyl)pyridinium chlorozincate.**

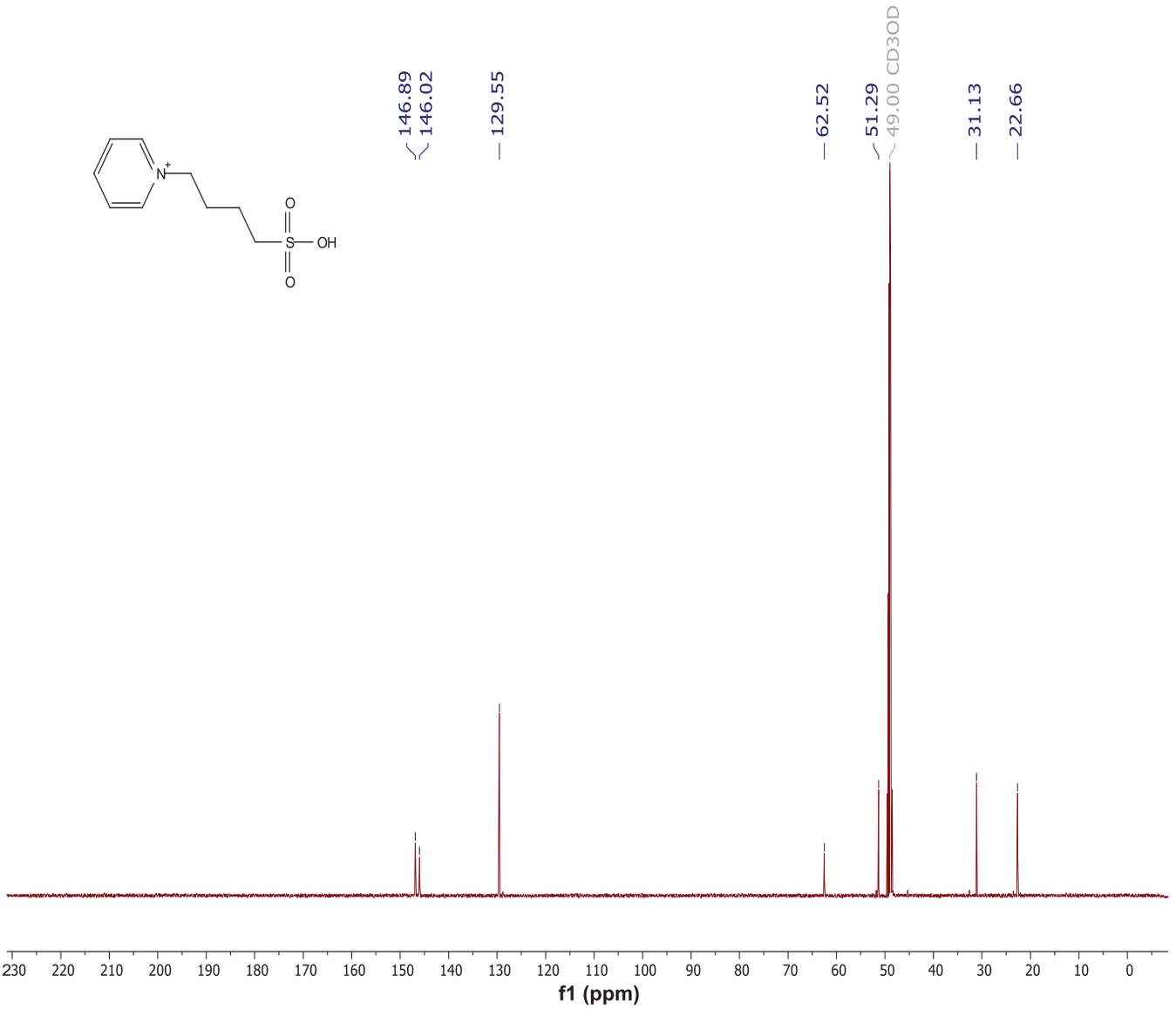


**Fig. 3. $^{13}$C NMR of 1-(4-sulfobutyl)pyridinium chlorozincate.**

Hz, 2H), 8.61 (tt, *J*=8.0, 1.5 Hz, 1H), and 8.13 (t, *J*=7.0 Hz, 2H). A triplet signal corresponding to protons in the -$CH_2$-N- group was observed at 4.71 (t, *J*=7.5 Hz, 2H). The chemical shift of the protons in the -$CH_2$-$SO_2$- group was observed at 2.89 (t, *J*=7.5 Hz, 2H). Additionally, two quintets corresponding to other methylene groups were detected at 2.21 (qui, *J*=8.0 Hz, 2H) and 1.85 (qui, *J*=8.0 Hz, 2H).

The data from the $^{13}$C NMR spectrum supported the above findings (Fig. 3). Indeed, the signals of carbon atoms within the pyridine ring were observed at 146.89, 146.02 and 129.55 ppm. Carbon atoms linked to heteroatoms, including nitrogen and sulphur, were characterized by signals at 62.5 and 51.29 ppm. The singlets at 31.13 and 22.66 ppm corresponded to the carbon atoms in the methylene groups.

In addition, the mass spectrum of the ionic liquid corresponded to the molecular cation at m/z 216.0398 ($C_9H_{14}NO_3S^+$) and the peak at m/z 169.0444 in the HRMS was attributed to the $ZnCl_3^-$ anion (Fig. 4). Consequently, the above data confirms the successful synthesis of 1-(4-sulfobutyl)pyridinium chlorozincate.

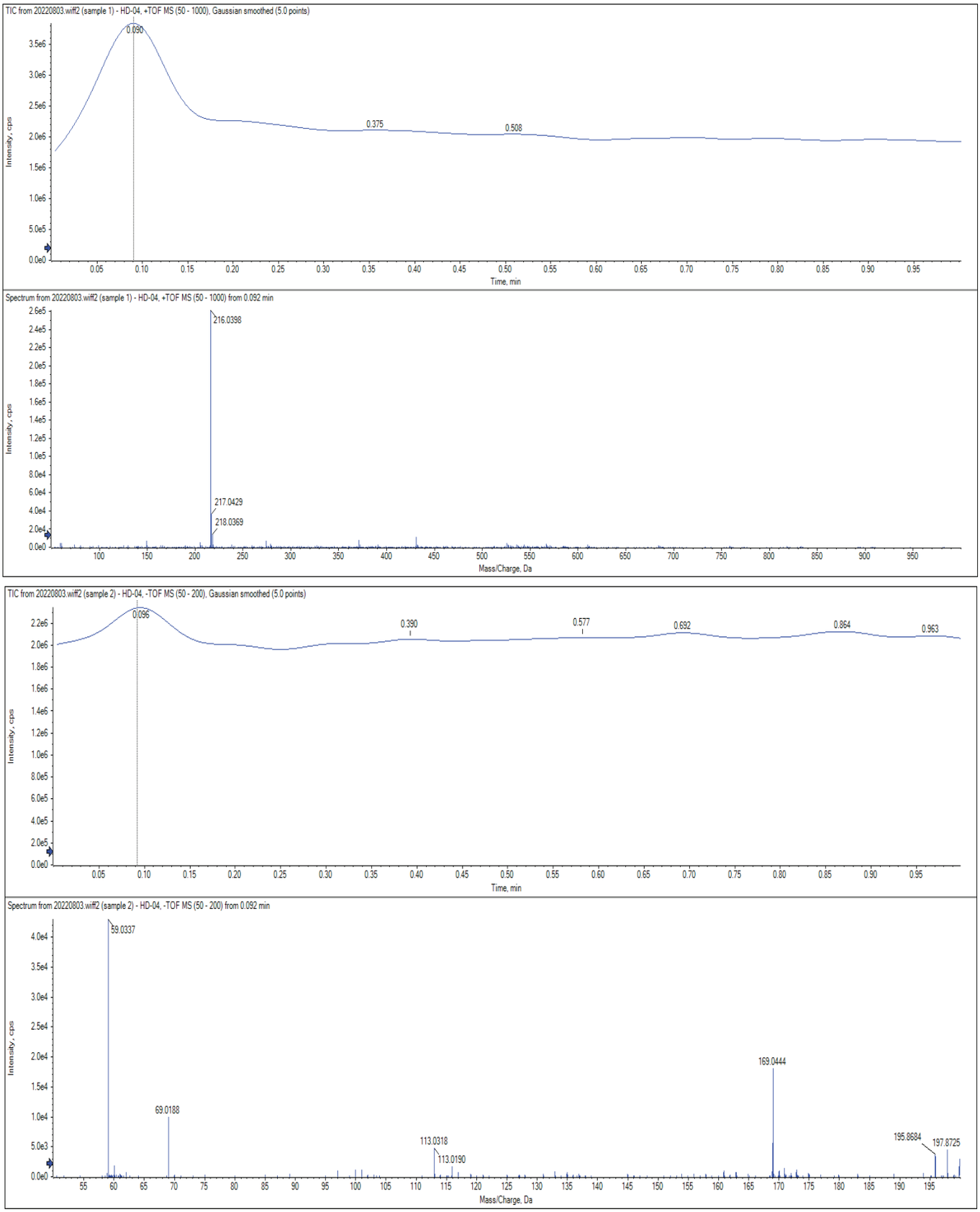


**Fig. 4. HR-MS of 1-(4-sulfobutyl)pyridinium chlorozincate.**

### *3.2. Reaction condition optimisation for the synthesis of 4H-1-benzopyran-5(6H)-one*

The optimal conditions for the catalytic condensation of benzaldehydes, 5,5-dimethyl-1,3-cyclohexanedione, and dicyanomethane were investigated. When 1-(4-sulfobutyl)pyridinium chloride (IL0) was initially employed as the catalyst in this reaction, it provided the target product (**4a**) with a yield of 35% (Table 1, entry 2). To compare the catalytic activity of various ionic liquids (IL1, IL2, and IL3) with different anions, cyclization reactions were conducted in the presence of these three ionic liquid catalysts. The results demonstrated that the ionic liquid containing the chlorozincate anion was more effective than those containing the chlorotinate and chlorocopperate anions (Table 1, entries 3, 4, and 5). Furthermore, the catalytic activity of IL3 was higher than that of zinc chloride salt (Table 1, entries 1 and 5). This can be attributed to the involvement of both the sulfonic acid group and the chlorozincate anion in the structure of IL3 in this catalytic cyclocondensation.

Subsequently, various types of solvents were applied in this reaction (Table 1, entries 4-9). Polar solvents, including ethanol and methanol, yielded low yields of the target product in this three-component reaction. Notably, water provided a good yield for this reaction (Table 1, entry 6). To further enhance the reaction yield, we performed this reaction by mixing water and an organic solvent. The mixture of water and ethanol (1:1, v/v) as the reaction solvent offered a satisfactory yield of 69% for the target product **(4a)** (Table 1, entry 4). Moreover, this solvent mixture was selected for subsequent experiments due to its non-toxic properties.

The effect of temperature was investigated in this reaction, and the results are presented in Fig. 5. The reaction yield increased rapidly from 24 to 69% as the temperature was raised from 30 to 100°C. However, a 60% yield of the desired product was achieved at 120°C. Subsequently, we also examined the effect of reaction time at the same temperature. From Fig. 6, it can be observed that the reaction yield slightly increased from 53 to 69% when the reaction time was extended to 180 minutes. Further prolonging the reaction time led to slight decreases in the reaction yield. Consequently, the optimal reaction time of 180 minutes was chosen for this cyclisation.

**Table 1. Effect of catalyst and solvent[a].**

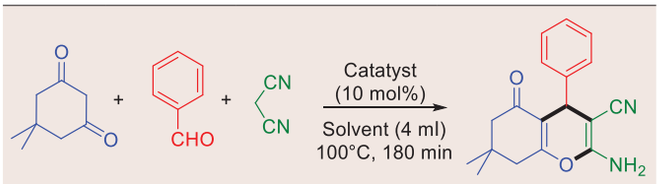


| Entry | Catalyst | Solvent | Isolated yield (%) |
|---|---|---|---|
| 1 | $ZnCl_2$ | $H_2O$:EtOH (1:1) | 42 |
| 2 | IL0 | $H_2O$:EtOH (1:1) | 35 |
| 3 | IL1 | $H_2O$:EtOH (1:1) | 10 |
| 4 | IL2 | $H_2O$:EtOH (1:1) | 11 |
| 5 | IL3 | $H_2O$:EtOH (1:1) | 69 |
| 6 | IL3 | $H_2O$:EtOH (1:2) | 51 |
| 7 | IL3 | $H_2O$ | 47 |
| 8 | IL3 | EtOH | 6 |
| 9 | IL3 | MeOH | 4 |
| 10 | IL3 | Solvent-free | 15 |

[a]: 5,5-dimethyl-1,3-cyclohexanedione (0.5 mmol), benzaldehyde (0.5 mmol), dicyanomethane (0.5 mmol), catalyst (10 mol%), solvent (4 ml), 100°C, 180 min.

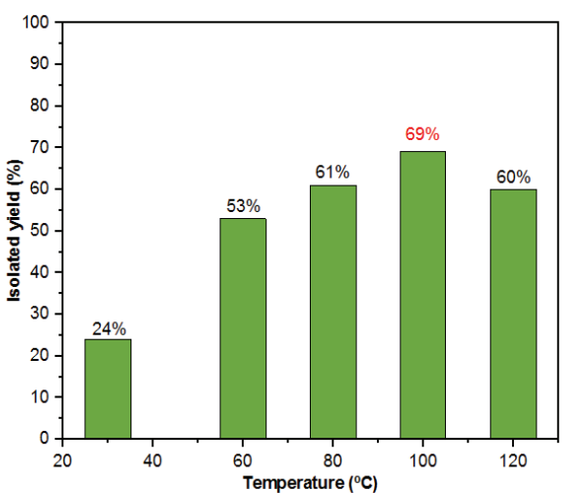


**Fig. 5. Temperature screening.**

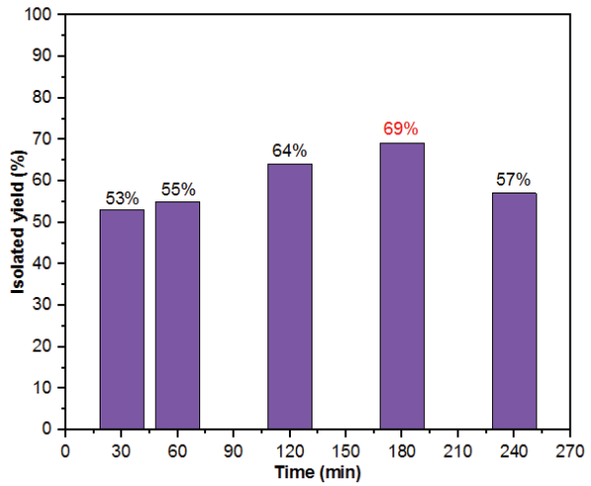


**Fig. 6. Reaction time investigation.**

The use of 5 mol% of 1-(4-sulfobutyl)pyridin-1-ium chlorozincate resulted in the production of 2-amino-3-cyano-4-phenyl-7,7-dimethyl-7,8-dihydro-4*H*-1-benzopyran-5(6*H*)-one with a relatively low yield (48%). However, increasing the catalyst amount to 10 mol% led to a significant improvement in the reaction yield, reaching up to 69%. It should be noted that the results indicated a pronounced negative effect when 20 mol% and 30 mol% of the catalyst were employed under the same conditions (Fig. 7). Consequently, 10 mol% was determined to be the optimal amount of catalyst for this method. Notably, one-pot three-component reactions in organic synthesis often result in by-product formation, but fortunately, only the major product was obtained under the optimal conditions.

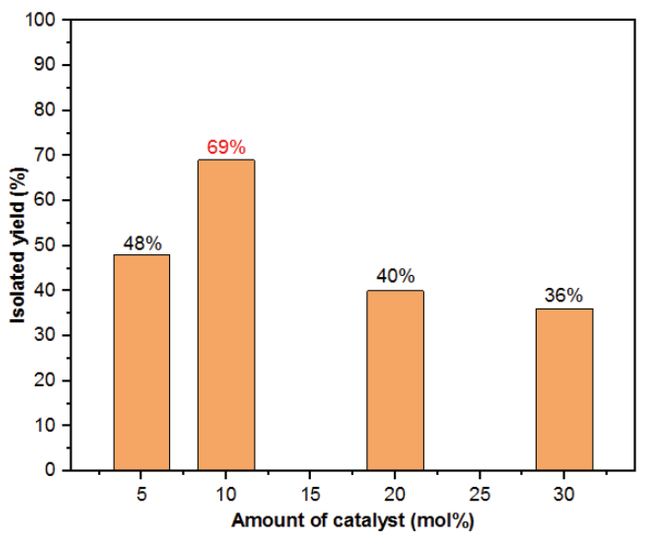


**Fig. 7. Amount of catalyst screening.**

Based on the aforementioned optimal conditions, we investigated the reactions involving five aromatic aldehydes with dimedone and dicyanomethane (Scheme 2). In general, aldehydes containing electron-donating groups such as *p*-Me and *p*-MeO proved to be viable substrates under the current reaction conditions, yielding the corresponding products (**4b** and **4c**) in moderate to good yields. Aromatic aldehydes containing chlorine on their aromatic ring were also successfully employed in the reaction, for instance, *p*-Cl derivatives (**4d**) were obtained in moderate yields. Aldehydes containing *p*-$NO_2$ groups provided the target products (**4e**) with a yield of 33%. The structures of all derivatives were confirmed through NMR methods, and the data from the $^{1}H$ and $^{13}C$ NMR spectra are presented in Table 2.

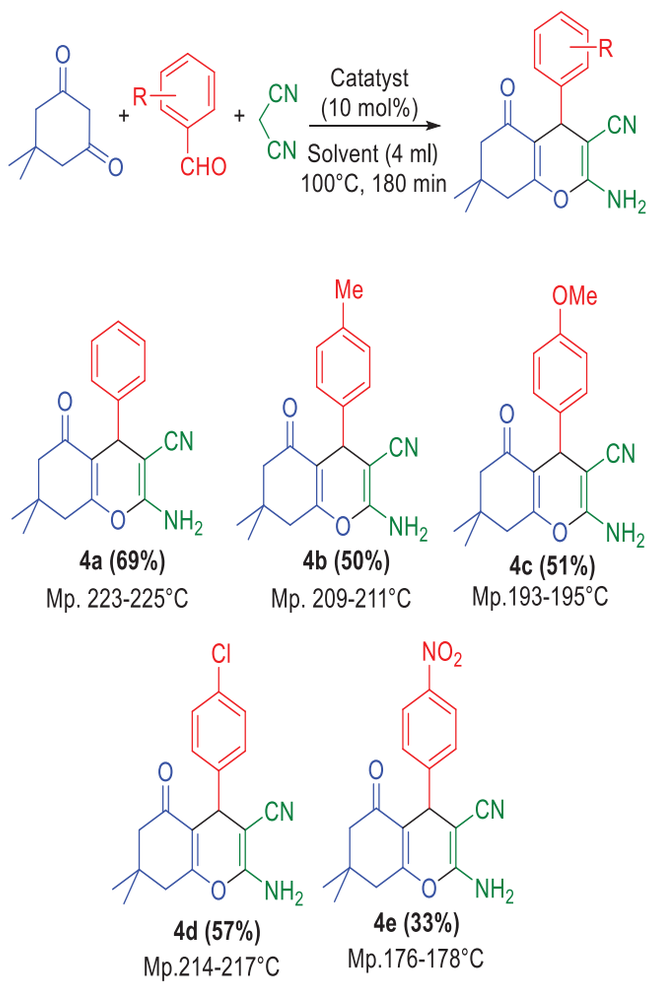


**Scheme 2. Scope of reaction.**

**Table 2. Nuclear magnetic resonance data of benzopyran-5(6*H*)-ones.**

| Compounds | $^1$H NMR (500 MHz, $(CD_3)_2SO$) $\delta_H$ (ppm) | $^{13}$C NMR (125 MHz, $(CD_3)_2SO$) $\delta_C$ (ppm) |
|---|---|---|
| **4a** | 7.29 (t, *J*=7.5 Hz, 2H), 7.20 (d, *J*=7.5 Hz, 1H), 7.17-7.13 (m, 2H), 6.98 (s, 2H), 4.18 (s, 1H), 2.54-2.51 (m, 2H), 2.26 (d, *J*=16.0 Hz, 1H), 2.11 (d, *J*=16.0 Hz, 1H), 1.05 (s, 3H), 0.96 (s, 3H). | 196.1, 163.0, 159.0, 145.2, 128.8, 127.6, 127.0, 120.2, 113.2, 58.9, 50.5, 36.1, 32.3, 28.9, 27.3 |
| **4b** | 7.09 (d, *J*=7.5 Hz, 2H), 7.02 (d, *J*=8.0 Hz, 2H), 6.96 (s, 2H), 4.13 (s, 1H), 2.51 (dd, *J*=4.0, 2.0 Hz, 2H), 2.24 (d, *J*=9.5 Hz, 4H), 2.10 (d, *J*=15.5 Hz, 1H), 1.04 (s, 3H), 0.96 (s, 3H). | 196.1, 162.8, 159.0, 142.3, 136.1, 129.3, 127.6, 120.2, 113.4, 59.0, 50.5, 35.7, 32.3, 28.9, 27.3, 21.1. |
| **4c** | 7.06 (d, *J*=9.0 Hz, 2H), 6.95 (s, 2H), 6.84 (d, *J*=9.0 Hz, 2H), 4.12 (s, 1H), 3.72 (s, 3H), 2.51-2.50 (m, 2H), 2.25 (dd, *J*=16.0, 5.5 Hz, 1H), 2.12-2.07 (m, 1H), 1.04 (s, 3H), 0.95 (s, 3H). | 196.1, 162.6, 158.9, 158.4, 137.3, 128.7, 120.3, 114.2, 113.5, 59.1, 55.5, 50.5, 35.2, 32.3, 28.9, 27.3. |
| **4d** | 7.34 (d, *J*=8.5 Hz, 2H), 7.17 (d, *J*=8.5 Hz, 2H), 7.05 (s, 2H), 4.19 (d, *J*=1.0 Hz, 1H), 2.51-2.50 (m, 2H), 2.25 (d, *J*=16.0 Hz, 1H), 2.10 (d, *J*=16.0 Hz, 1H), 1.03 (s, 3H), 0.95 (s, 3H). | 195.7, 162.6, 158.5, 143.7, 131.1, 129.1, 128.3, 119.5, 112.3, 57.8, 49.9, 35.1, 31.8, 28.3, 26.9. |
| **4e** | 8.18 (d, *J*=8.5 Hz, 2H), 7.45 (d, *J*=9.0 Hz, 2H), 7.17 (s, 2H), 4.37 (s, 1H), 2.56-2.53 (m, 2H), 2.27 (d, *J*=16.0 Hz, 1H), 2.12 (d, *J*=16.0 Hz, 1H), 1.06-1.04 (m, 3H), 0.97 (s, 3H). | 195.7, 163.1, 158.6, 152.3, 146.3, 128.6, 123.7, 119.3, 111.7, 57.0, 49.9, 35.7, 31.8, 28.2, 26.9. |

### *3.3. The possible mechanism*

Based on our work and previous literature [26, 51, 52], the mechanistic steps of this condensation are illustrated in Scheme 3. Both the -$SO_3H$ group and the $Zn_xCl_y^-$ anion in the structure of the IL3 catalyst, known as Brønsted and Lewis acidic sites, respectively, play similar roles in each step of the reaction mechanism.

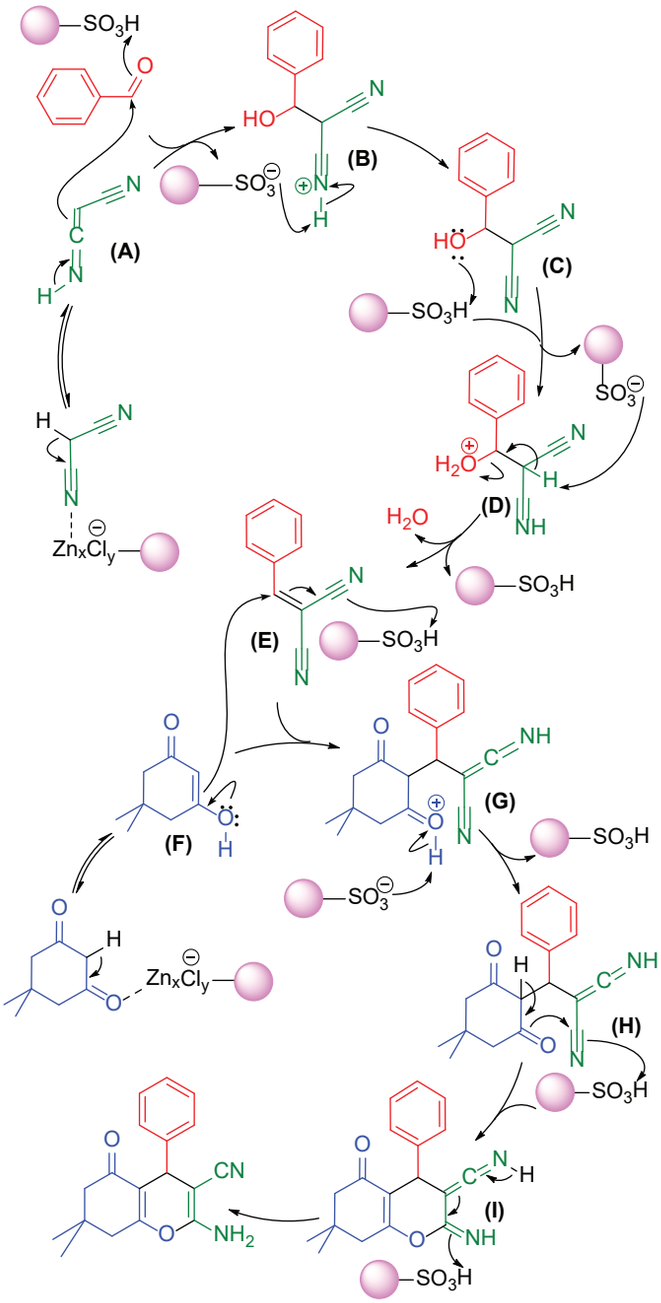


**Scheme 3. The possible mechanism.**

The first step involves a nucleophilic addition reaction between benzaldehyde and dicyanomethane, known as Knoevenagel condensation. Under the acidic catalyst conditions, dicyanomethane undergoes tautomerization to form 3-iminoacrylonitrile (A). The π electron in C=C of (A) nucleophilically attacks the electrophilic carbon of benzaldehyde, facilitated by the acidic ionic liquid,

resulting in intermediate (B). After the removal of a proton from the nitrogen atom, 2-(hydroxy(phenyl)methyl) dicyanomethane (C) is formed, followed by protonation to provide intermediate (D). Subsequently, the elimination of water from (D) yields 2-benzylidenedicyanomethane (E). Finally, 5,5-dimethylcyclohexane-1,3-dione tautomerizes to 3-hydroxy-5,5-dimethylcyclohex-2-en-1-one (F).

The second step involves a Michael addition reaction between an electron-poor alkene and 1,3-diketone *via* 1,4-addition. In this step, intermediate (E) is attacked by the π electron from the nucleophilic double bond of (F) with the assistance of an acidic catalyst, leading to intermediate (G). After the formation of 2-((4,4-dimethyl-2,6-dioxocyclohexyl)(phenyl)methyl)-3-iminoacrylonitrile (H) through proton removal, intramolecular cyclization of intermediate (H) occurs through nucleophilic incursion between the C=O group and the nitrile group, resulting in 2-imino-3-(iminomethylene)-7,7-dimethyl-4-phenyl-2,3,4,6,7,8-hexahydro-5*H*-chromen-5-one (I). Finally, the target products are obtained through the isomerization of intermediate (I) with the support of an acidic catalyst.

### *3.4. Recycling of 1-(4-sulfobutyl)pyridinium chlorosincate*

At the conclusion of this study, we investigated the recyclability of 1-(4-sulfobutyl)pyridinium chlorozincate. Under the optimized conditions, recycling experiments were conducted using a three-component reaction of benzaldehyde, dimedone, and dicyanomethane. After filtering and recrystallizing the crude product, the catalyst was easily separated through filtration and dried at 80°C. As seen in Fig. 8, there was a slight decrease in yield after each cycle (approximately 1-4% for each cycle). This decrease can be attributed to the loss of catalyst after each recycling. However, the ionic liquid catalyst retained its catalytic activity even after four cycles. Notably, the reaction yield reached 61% after the fourth-time reuse of IL3 catalyst, which is less than 8% lower than the reaction yield using fresh IL3 catalyst. This result demonstrates that IL3 is a green catalyst suitable for industrial applications.

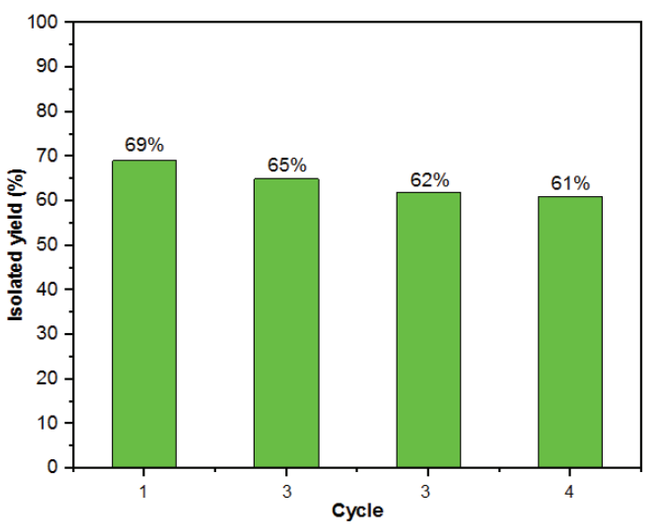


**Fig. 8. Recycling of 1-(4-sulfobutyl)pyridinium chlorozincate.**

## 4. Conclusions

In conclusion, a new acidic pyridinium-based ionic liquid was successfully synthesized and used as a catalyst in the synthetic process of 2-amino-3-cyano-4-phenyl-7,7-dimethyl-7,8-dihydro-4*H*-1-benzopyran-5(6*H*)-ones. These reactions involved a condensation reaction of aromatic benzaldehydes, 5,5-dimethyl-1,3-cyclohexanedione, and dicyanomethane in a solvent mixture of ethanol and water, resulting in the desired products in moderate to good yields. The procedure is efficient and eco-friendly, and the products can be easily obtained by recrystallization. Thus, this protocol offers an alternative to existing methods.

## CRediT author statement

Huong Ngoc Thi Dao, The Thai Nguyen, Tran Huyen Thi Nguyen, Thuy Hong Ngoc Phan: Conceptualisation, Methodology, Formal analysis, Software, Data curation, Validation, Visualisation, Investigation; Phuong Hoang Tran: Conceptualisation, Methodology, Formal analysis, Supervision, Original draft preparation, Writing - Reviewing and Editing, Project administration.

## ACKNOWLEDGEMENTS

The research is funded by the University of Science, Vietnam National University - Ho Chi Minh City under grant number U2022-14.

## COMPETING INTERESTS

The authors declare that there is no conflict of interest regarding the publication of this article.

## REFERENCES


[1] B.C.Z. Lei, Y.O. Koo, D.R. MacFarlane (2017), "Introduction: Ionic liquids", *Chem. Rev.*, **117(10)**, pp.6633-6635, DOI: 10.1021/acs.chemrev.7b00246.

[2] K. Ghandi (2014), "A review of ionic liquids, their limits and applications", *Green Sustain. Chem.*, **4**, pp.44-53, DOI: 10.4236/gsc.2014.41008.

[3] T. Welton (2004), "Ionic liquids in catalysis", *Coord. Chem. Rev.*, **248(21)**, pp.2459-2477, DOI: 10.1016/j.ccr.2004.04.015.

[4] R.L. Vekariya (2017), "A review of ionic liquids: Applications towards catalytic organic transformations", *J. Mol. Liq.*, **227**, pp.44-60, DOI: 10.1016/j.molliq.2016.11.123.

[5] A.S. Amarasekara (2016), "Acidic ionic liquids", *Chem. Rev.*, **116(10)**, pp.6133-6183, DOI: 10.1021/acs.chemrev.5b00763.

[6] M. Syamala (2005), "A decade of advances in three-component reactions", *Org. Prep. Proced. Int.*, **37(2)**, pp.103-171.

[7] M. Syamala (2009), "Recent progress in three-component reactions: An update", *Org. Prep. Proced. Int.*, **41(1)**, pp.1-68, DOI: 10.1080/00304940802711218.

[8] B. Jiang, T. Rajale, W. Wever, et al. (2010), "Multicomponent reactions for the synthesis of heterocycles", *Chem. Asian J.*, **5(11)**, pp.2318-2335, DOI: 10.1002/asia.201000310.

[9] D.M. D'Souza, T.J. Mueller (2007), "Multi-component syntheses of heterocycles by transition-metal catalysis", *Chem. Soc. Rev.*, **36(7)**, pp.1095-1108, DOI: 10.1039/B608235C.

[10] M. Kassaee, H. Masrouri, F. Movahedi (2010), "ZnO-nanoparticle-promoted synthesis of polyhydroquinoline derivatives via multicomponent Hantzsch reaction", *Monatsh. fur. Chem.*, **141(3)**, pp.317-322, DOI: 10.1007/s00706-010-0252-1.

[11] J.P. Wan, Y. Liu (2010), "Synthesis of dihydropyrimidinones and thiones by multicomponent reactions: Strategies beyond the classical Biginelli reaction", *Synth.*, **2010(23)**, pp.3943-3953, DOI: 10.1055/s-0030-1258290.

[12] M.A. Zolfigol, S. Baghery, A.R.M. Zare, et al. (2015), "Synthesis and characterisation of new 1-(α-aminoalkyl)-2-naphthols using pyrazine-1,4-diium trinitromethanide {[1,4-DHPyrazine][$C(NO_2)_3$]$_2$} as a novel nano-structured molten salt and catalyst in compared with Ag-$TiO_2$ nano composite", *J. Mol. Catal. A. Chem.*, **409**, pp.216-226, DOI: 10.1016/j.molcata.2015.09.001.

[13] E. Abedini, H.R. Shaterian (2023), "L-leucine supported on silica gel encapsulating γ-$Fe_2O_3$ nanoparticles: A new recoverable magnetic catalyst for preparation of 1,3-thiazole derivatives", *Eurasian Chem. Commun.*, **5(3)**, pp.228-245.

[14] A.R. Salih, Z.A.K.A. Messri (2021), "Synthesis of pyranopyrazole and pyranopyrimidine derivatives using magnesium oxide nanoparticles and evaluation as corrosion inhibitors for lubricants", *Eurasian Chem. Commun.*, **3(8)**, pp.533-541.

[15] A.R.M. Zare, H. Goudarziafshar, Z. Jalilian, et al. (2022), "Efficient pseudo-six-component synthesis of tetrahydro-pyrazolopyridines using [Zn-BSMP]$Cl_2$", *Chem. Methodol.*, **6(8)**, pp.571-581.

[16] N. Thomas, S. Zachariah (2013), "Pharmacological activities of chromene derivatives: An overview", *Asian J. Pharm. Clin. Res.*, **6**, pp.11-15.

[17] M. Costa, T.A. Dias, A. Brito, et al. (2016), "Biological importance of structurally diversified chromenes", *Eur. J. Med. Chem.*, **123**, pp.487-507, DOI: 10.1016/j.ejmech.2016.07.057.

[18] F.M. Abdelrazek, P. Metz, E.K. Farrag (2004), "Synthesis and molluscicidal activity of 5-oxo-5,6,7,8-tetrahydro-4*H*-chromene derivatives", *Arch. Pharm.*, **337(9)**, pp.482-485, DOI: 10.1002/ardp.200400881.

[19] S. Khaksar, A. Rouhollahpour, S.M. Talesh (2012), "A facile and efficient synthesis of 2-amino-3-cyano-4*H*-chromenes and tetrahydrobenzo[b]pyrans using 2,2,2-trifluoroethanol as a metal-free and reusable medium", *J. Fluor. Chem.*, **141**, pp.11-15, DOI: 10.1016/j.jfluchem.2012.05.014.

[20] W. Kemnitzer, S. Kasibhatla, S. Jiang, et al. (2005), "Discovery of 4-aryl-4*H*-chromenes as a new series of apoptosis inducers using a cell-and caspase-based high-throughput screening assay", *Bioorganic Med. Chem. Lett.*, **15(21)**, pp.4745-4751, DOI: 10.1016/j.bmcl.2005.07.066.

[21] N.R. Kamdar, D.D. Haveliwala, P.T. Mistry, et al. (2010), "Design, synthesis and *in vitro* evaluation of antitubercular and antimicrobial activity of some novel pyranopyrimidines", *Eur. J. Med. Chem.*, **45(11)**, pp.5056-5063, DOI: 10.1016/j.ejmech.2010.08.014.

[22] J. Skommer, D. Wlodkowic, M. Mättö, et al. (2006), "HA14-1, a small molecule Bcl-2 antagonist, induces apoptosis and modulates action of selected anticancer drugs in follicular lymphoma B cells", *Leuk. Res.*, **30(3)**, pp.322-331, DOI: 10.1016/j.leukres.2005.08.022.

[23] N. Yu, J.M. Aramini, M.W. Germann, et al. (2000), "Reactions of salicylaldehydes with alkyl cyanoacetates on the surface of solid catalysts: Syntheses of *4H*-chromene derivatives", *Tetrahedron Lett.*, **41(36)**, pp.6993-6996, DOI: 10.1016/S0040-4039(00)01195-3.

[24] M.N. Elinson, F.V. Ryzhkov, T.A. Zaimovskaya, et al. (2015), "Non-catalytic solvent-free synthesis of 5,6,7,8-tetrahydro-4*H*-chromenes from aldehydes, dimedone and malononitrlie at ambient temperature", *Mendeleev Commun.*, **25(3)**, pp.185-187, DOI: 10.1016/j.mencom.2015.05.008.

[25] H. Adibi, R. Khodarahmi, K. Mansouri, et al. (2013), "Synthesis of 4-aryl-4*H*-chromene derivatives with boric acid: Evaluation of their *in vitro* anti-angiogenesis effects and possible mechanism of action", *Pharm. Sci.*, **19(1)**, pp.23-30.

[26] A.M. Zonouz, S. Okhravi, D. Moghani (2016), "Ammonium acetate as a catalyst and/or reactant in the reaction of dimedone, aromatic aldehyde, and malononitrile: synthesis of tetrahydrobenzo[*b*]pyrans and hexahydroquinolines", *Monatsh. fur Chem.*, **147(10)**, pp.1819-1824, DOI: 10.1007/s00706-016-1683-0.

[27] D. Pore, K. Undale, B. Dongare, et al. (2009), "Potassium phosphate catalyzed a rapid three-component synthesis of tetrahydrobenzo[*b*]pyran at ambient temperature", *Catal. Letters*, **132(1)**, pp.104-108, DOI: 10.1007/s10562-009-0074-0.

[28] M. Seifi, H. Sheibani (2008), "High surface area MgO as a highly effective heterogeneous base catalyst for three-component synthesis of tetrahydrobenzopyran and 3,4-dihydropyrano[*c*] chromene derivatives in aqueous media", *Catal. Letters*, **126(3)**, pp.275-279, DOI: 10.1007/s10562-008-9603-5.

[29] Y. He, R. Hu, R. Tong, et al. (2014), "$K_2CO_3$-mediated synthesis of functionalised 4-substituted-2-amino-3-cyano-4*H*-chromenes via Michael-cyclization reactions", *Molecules*, **19(12)**, pp.19253-19268, DOI: 10.3390/molecules191219253.

[30] G. Sabitha, K. Arundhathi, K. Sudhakar, et al. (2009), "Cerium(III) chloride-catalyzed one-pot synthesis of tetrahydrobenzo[*b*]pyrans", *Synth. Commun.*, **39(3)**, pp.433-442, DOI: 10.1080/00397910802378399.

[31] M.M. Zeydi, S. Ahmadi (2016), "$Mg(ClO_4)_2$ as a recyclable catalyst for synthesis of 4*H*-chromenes", *Orient. J. Chem.*, **32(4)**, pp.2215-2219, DOI: 10.13005/ojc/320453.

[32] A. Zonouzi, R. Mirzazadeh, M. Safavi, et al. (2013), "2-Amino-4-(nitroalkyl)-4*H*-chromene-3-carbonitriles as new cytotoxic agents", *Iran. J. Pharm. Res.*, **12(4)**, pp.679-685, DOI: 10.22037/ijpr.2013.1396.

[33] A.M. Shestopalov, Y.M. Emelianova, V.N. Nesterov (2003), "One-step synthesis of substituted 2-amino-5,6,7,8-tetrahydro-4*H*-benzo[*b*]pyrans. Molecular and crystal structure of 2-amino-3-(2-methoxyethoxycarbonyl)-4-(2-nitrophenyl)-5-oxo-5,6,7,8-tetrahydro-4*H*-benzo[*b*]pyran", *Russ. Chem. Bull.*, **52**, pp.1164-1171, DOI: 10.1023/A:1024721710597.

[34] R.S. Bhosale, C.V. Magar, K.S. Solanke, et al. (2007), "Molecular iodine: An efficient catalyst for the synthesis of tetrahydrobenzo[*b*]pyrans", *Synth. Commun.*, **37(24)**, pp.4353-4357, DOI: 10.1080/00397910701578578.

[35] P. Kulkarni (2015), "Methane sulphonic acid is green catalyst in organic synthesis", *Orient. J. Chem.*, **31(1)**, pp.447-451.

[36] V.M. Joshi, R.L. Magar, P.B. Throat, et al. (2014), "Novel one-pot synthesis of 4*H*-chromene derivatives using amino functionalized silica gel catalyst", *Chin. Chem. Lett.*, **25(3)**, pp.455-458, DOI: 10.1016/j.cclet.2013.12.016.

[37] G.M. Ziarani, A. Badiei, Z. Dashtianeh, et al. (2013), "Green one-pot synthesis of 1*H*- and 4*H*-chromenes derivatives using $SiO_2$-Pr-$SO_3H$ as catalyst", *Rev. Roum. Chim.*, **58(9-10)**, pp.765-772.

[38] H.F. Niya, N. Hazeri, M.R. Kahkhaie, et al. (2020), "Preparation and characterization of MNPs-$PhSO_3H$ as a heterogeneous catalyst for the synthesis of benzo[*b*]pyran and pyrano[3,2-*c*]chromenes", *Res. Chem. Intermed.*, **46(3)**, pp.1685-1704, DOI: 10.1007/s11164-019-04056-z.

[39] B. Baghernejad, S.M.H. Taromsari (2022), "Aqueous media preparation of 2-amino-4*H*-benzopyran derivatives using cerium oxide nanoparticles as a recyclable catalyst", *Asian J. Green Chem.*, **6(3)**, pp.194-202.

[40] J. Albadi, A. Razeghi, A. Mansournezhad, et al. (2013), "CuO-$CeO_2$ nanocomposite catalyzed efficient synthesis of aminochromenes", *J. Nanostructure Chem.*, **3(1)**, pp.1-5, DOI: 10.1186/2193-8865-3-85.

[41] B. Baghernejad, M.R. Harzevili (2021), "Nano-cerium oxide/aluminum oxide: An efficient and useful catalyst for the synthesis of tetrahydro[*a*]xanthenes-11-one derivatives", *Chem. Methodol.*, **5(2)**, pp.90-95.

[42] A. Javid, F. Moeinpour (2018), "$Ni_{0.5}Zn_{0.5}Fe_2O_4$@HA-PRS nanoparticle: A recoverable green catalyst for the synthesis of tetrahydrobenzo[*b*]pyrans in water", *Bull. Chem. Soc. Ethiop.*, **32(3)**, pp.501-511, DOI: 10.4314/bcse.v32i3.9.

[43] S. Rathod, B. Arbad, M. Lande (2010), "Preparation, characterization, and catalytic application of a nanosized $Ce_1Mg_xZr_{1-x}O_2$ solid heterogeneous catalyst for the synthesis of tetrahydrobenzo[*b*]pyran derivatives", *Chinese J. Catal.*, **31(6)**, pp.631-636, DOI: 10.1016/S1872-2067(09)60078-4.

[44] K. Gong, H.L. Wang, D. Fang, et al. (2008), "Basic ionic liquid as catalyst for the rapid and green synthesis of substituted 2-amino-2-chromenes in aqueous media", *Catal. Commun.*, **9(5)**, pp.650-653, DOI: 10.1016/j.catcom.2007.07.010.

[45] A.R.M. Zare, M.A. Zolfigol, O. Khaledian, et al. (2014), "Tandem knoevenagel-michael-cyclocondensation reactions of malononitrile, various aldehydes and dimedone using acetic acid functionalized ionic liquid", *New. J. Chem.*, **38(6)**, pp.2342-2347, DOI: 10.1039/C3NJ01509B.

[46] E.A. Gilandeh, S.C. Azimi (2014), "$Li(OHCH_2CH_2NH_2)(CF_3OAC)$: A novel and homogeneous acidic ionic liquid catalyst for efficient synthesis of 2-amino-4*H*-chromene derivatives", *Iran. J. Catal.*, **4(4)**, pp.281-288.

[47] V.P. Pagore, S.U. Tekale, B.D. Rupnar, et al. (2015), "Efficient and green synthesis of 2-amino-4*H*-chromenes", *J. Chem. Pharm. Res.*, **7**, pp.1057-1061.

[48] K. Amani, M. Yarie, F. Shahbazi (2018), "Ammonium-type basic ionic liquid, 2-(2-hydroxyethoxy)ethaneammonium formate: Promote green and efficient multicomponent tandem synthesis of 4*H*-pyrans and 4*H*-chromenes", *Org. Chem. Res.*, **4(1)**, pp.58-66, DOI: 10.22036/ORG.CHEM.2017.97958.1112.

[49] K. Niknam, A. Piran (2013), "Silica-grafted ionic liquids as recyclable catalysts for the synthesis of 3,4-dihydropyrano[*c*] chromenes and pyrano[2,3-*c*]pyrazoles", *Green Sustain. Chem.*, **3(2)**, pp.8-12, DOI: 10.4236/gsc.2013.32A001.

[50] P. Sharma, M. Gupta, R. Kant, et al. (2016), "One-pot synthesis of various 2-amino-4*H*-chromene derivatives using a highly active supported ionic liquid catalyst", *RSC Adv.*, **6(38)**, pp.32052-32059, DOI: 10.1039/C6RA06523F.

[51] N.M.A.E. Rahman, A.A.E. Kateb, M.F. Mady (2007), "Simplified approach to the uncatalyzed Knoevenagel condensation and Michael addition reactions in water using microwave irradiation", *Synth. Commun.*, **37(22)**, pp.3961-3970, DOI: 10.1080/00397910701572696.

[52] N.G. Shabalala, N.P. Hadebe, N. Kerru, et al. (2022), "An efficient and sustainable protocol for the synthesis of poly-functionalized-pyran derivatives under ultrasound irradiation", *Polycycl. Aromat. Compd.*, **42(2)**, pp.505-516, DOI: 10.1080/10406638.2020.1743331.

DOI: 10.31276/VJSTE.66(1).46-52

# Antifungal activity of a methanolic extract of *Glycyrrhiza uralensis* Fisch. root against *Fusarium oxysporum* and *Phytophthora capsici*

**Dang-Minh-Chanh Nguyen[1, 2*], Thi-Hoan Luong[3], Van-Viet Nguyen[2], Woo-Jin Jung[1]**

[1]*Department of Agricultural Chemistry, Institute of Environmentally Friendly Agriculture (IEFA), College of Agriculture and Life Sciences, Chonnam National University, 77 Yongbong-ro, Buk-gu District, Gwangju City, Republic of Korea*

[2]*Research and Development Institute for Agriculture Nafoods, 162A Nguyen Tuan Street, Thanh Xuan Trung Ward, Thanh Xuan District, Hanoi, Vietnam*

[3]*National Institute of Medicinal Materials (NIMM), 3B Quang Trung Street, Trang Tien Ward, Hoan Kiem District, Hanoi, Vietnam*

Received 4 August 2023; revised 29 August 2023; accepted 20 November 2023

***Abstract:***

**In the present study, we investigated the antifungal activity of a methanolic extract of *Glycyrrhiza uralensis* Fisch. root, which inhibited the growth of the plant pathogens *Fusarium oxysporum* and *Phytophthora capsici*. The $EC_{50}$ values of the *G. uralensis* Fisch. extract three, six, and nine days after treatment were 113.4, 150.6, and 191.4 µg/ml for *F. oxysporum* and 84.7, 148.6, and 190.1 µg/ml for *P. capsici*, respectively, and the antifungal activity exhibited a dose-dependent response. The MIC value of *G. uralensis* Fisch. extract was found to be 100, 200, and 400 µg/ml at three, six, and nine days after treatment for *F. oxysporum*. In contrast, for *P. capsici*, the MIC value was 50, 100, and 100 µg/ml at three, six, and nine days after treatment. After three days of incubation with 400 µg/ml *G. uralensis* Fisch. extract, the hyphae of *F. oxysporum* exhibited abnormalities and atrophy, leading to mycelial collapse. In contrast, the hyphae of *P. capsici* displayed swelling with increased branching. These results furnish valuable insights into the antifungal metabolites present in *G. uralensis* Fisch. extract, contributing to the development of environmentally friendly products aimed at controlling the growth of pathogenic fungi.**

***Keywords:*** **antifungal activity, medicinal plant, mycelial morphology, pathogenic fungus.**

***Classification numbers:*** **2.2, 3.1**

## 1. Introduction

*Fusarium* species are ubiquitous soil-borne pathogens in a wide range of horticultural and food crops, causing destructive vascular wilt, rot, and damping-off diseases [1], which curtail plant production and yield. *F. oxysporum*, in particular, results in the demise of both young and mature plants, leading to significant economic losses [2]. Various strategies have been implemented to mitigate the impact of this pathogen, encompassing the elimination of afflicted plants, sanitation measures, the utilisation of disease-free tissue-cultured plants, and tolerant cultivars [3]. *P. capsici* is a soilborne oomycete pathogen afflicting several cash crops including solanaceous, leguminous, and most cucurbitaceous species [4, 5]. This pathogen carries substantial economic and scientific significance, responsible for annual losses exceeding one billion dollars in global vegetable production [5, 6]. Moreover, due to its resistance to currently available compounds, there is an urgent need to identify novel promising agents for its management.

Chemical fungicides are widely employed worldwide for the control of pathogenic fungi in various crops. Nevertheless, these fungicides possess a broad spectrum of activity, affecting beneficial soil microorganisms and leading to a swift resurgence of soil-borne pathogens. Additionally, their usage is constrained due to the presence of toxic residues, causing substantial environmental harm [7, 8]. Although several effective fungicides are recommended for root rot disease, they are not regarded as long-term solutions [9]. Consequently, there is an imminent requirement for alternative methods of fungal control in agriculture that are both less detrimental to human health and the environment [10, 11].

Plant preparations offer potential alternatives to nematode control products since they often serve as

*Corresponding author: Email: ndmchanh75@gmail.com

alternative sources of treatment chemicals, degrade into non-toxic by-products, and exert minimal detrimental effects on non-target organisms and the environment. Numerous plants possessing antifungal properties have been identified and can be harnessed for disease management [12]. Furthermore, natural products exhibit low mammalian toxicity, high target specificity, biodegradability, and contain numerous active ingredients, thus displaying biocidal activity against multiple pests and pathogens [13]. Extracts from specific plants have traditionally been employed as natural fungicides in small-scale farming systems where the economic feasibility of synthetic chemicals was limited [14, 15]. Many medicinal plants represent a rich source of antifungal agents, and these plants are employed medicinally in various countries as sources of potent and efficacious drugs [12]. Researchers have conducted studies aimed at identifying novel antifungal substances produced by plants in recent years. These investigations have focused on the discovery of compounds with broad-spectrum activity that could be valuable for the treatment of plant diseases, resulting in the isolation of numerous antifungal compounds [16, 17].

*G. uralensis* Fisch. is a perennial medicinal plant indigenous to China, Mongolia, Russia, and Korea [18]. It predominantly thrives in arid and semi-arid desert grasslands, desert margins, and loess hilly regions [19]. The plant thrives in dark, humid, and dry climates with prolonged sunshine and low temperatures [19]. Its root, measuring 1-3 cm in diameter, possesses brown skin and a light yellow interior, exhibiting a sweet taste. The plant boasts robust roots, an upright stem, multiple branches, a height ranging from 30-120 cm, spiny glands, and white or brown hairs [18]. Biologically, liquorice extract has demonstrated antioxidant, anti-inflammatory, antiviral, cytotoxic, and anti-diabetic activities, and is extensively employed in the treatment of hepatitis, bronchitis, and malaria [20-22]. The primary pharmacological components found in the root of *G. uralensis* Fisch. are glycyrrhizic acid and liquiritin [21, 22]. Despite numerous studies exploring the applications of *G. uralensis* Fisch. extracts for medicinal purposes [23], their antagonistic effects against plant pathogenic fungi have yet to be investigated. Thus, the objective of this study is to evaluate the antifungal activity of *G. uralensis* Fisch. extract.

## 2. Materials and methods

### *2.1. Plant materials and chemicals*

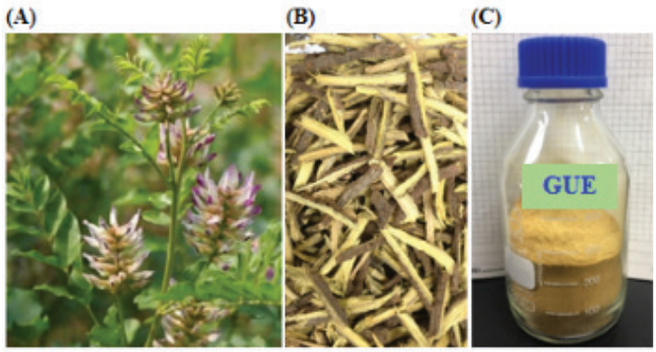


**Fig. 1. Morphological characteristics of (A) the plant and (B) the stem, and (C) the crude powder obtained from methanolic extraction of the roots of *G. uralensis* Fisch. (GUE) (Sapa, Lao Cai province, Vietnam).**

Samples of *G. uralensis* Fisch. were gathered from Sapa (Lao Cai province, Vietnam) in November 2022. The plant exhibits an upright growth with a stem measuring 0.5-1.5 m in height. Its leaves are feather-like, featuring 9-17 ovate leaflets, and its flowers are butterfly-shaped and pale purple (Fig. 1A). The stem displays a light yellow colour (Fig. 1B). The extraction process was adapted from the procedure outlined in [9]. In summary, dried *G. uralensis* Fisch. roots (1.0 kg) were cut into 3-5 cm segments and subjected to extraction using 80% methanol (5 l×3) with agitation at 150 rpm, maintained at 27±1°C for a duration of 72 hours. Subsequently, the methanolic extract was filtered, evaporated to dryness under vacuum conditions at 40±2°C (Eyela N-1000, Tokyo, Japan), and freeze-dried to obtain *G. uralensis* Fisch. extract (GUE) in the form of a yellow powder (Fig. 1C). The collected GUE was stored at 4°C until further use.

Fungal pathogens *F. oxysporum* f. sp *lycopesici* KACC 40032 and *P. capsici* KACC 40473 were obtained from the Korean Agricultural Culture Collection (Suwon, Republic of Korea). All chemicals and solvents utilised were of analytical grade.

### *2.2. Determination of the effect of GUE on mycelial growth*

The toxicity of GUE against the tested fungi was assessed using a method that included the poison medium technique employing the PDA (potato dextrose agar) medium and the broth micro-dilution method [24]. In brief, mycelial culture blocks (6 mm in diameter) of the same age were placed in Petri dishes (90×15 mm)

containing 10 ml of PDA medium, resulting in final GUE concentrations of 0, 25, 50, 100, 200, or 400 µg/ml. An equal volume of methanol was used as a control. The samples were incubated in darkness at 25±1°C, and mycelial growth was assessed at 3, 6, and 9 days after treatment (day 3, day 6, and day 9, respectively). The effective concentration that inhibited mycelial growth was computed using the following formula [25]:

$$Inhibition\ (\%) = \left[\frac{C-T}{C} - 6\right] \times 100$$

where $C$ and $T$ are the hyphal extension in the control and plates treated with GUE, respectively. The experiments were performed twice, with three replicates for each treatment. The $EC_{50}$ (half-maximal effective concentration) values of the GUE were calculated on day 3, day 6, and day 9.

### *2.3. Determination of minimum inhibitory concentration (MIC)*

The MIC of GUE against the pathogens was determined using the microtiter broth dilution method with 2-fold serial dilutions, covering various GUE concentrations (0, 25, 50, 100, 200, and 400 µg/ml) [26]. The lowest GUE concentration that completely inhibited fungal growth, as observed visually, was defined as the MIC value.

### *2.4. Determination of the effect of GUE on mycelial morphology*

The impact of GUE on the hyphal morphology of *F. oxysporum* and *P. capsici* was assessed following the procedures detailed in [27] and [8]. On day 3, fungal blocks were sectioned into 3 mm fragments and subsequently stained with lactophenol blue. To eliminate excess lactophenol blue solution, the samples underwent three washes with sterile water. The mycelial morphology of both the control and GUE-treated *F. oxysporum* and *P. capsici* was examined under a light microscope (40X magnification). PDA fungal culture devoid of GUE served as the control. The experiments were replicated three times for each treatment.

### *2.5. Statistical analysis*

All data were presented as the mean ± standard deviation, based on the number of observations. A one-way analysis of variance (ANOVA) followed by Tukey's test was conducted to evaluate the significance of differences among the treatment means, with a significance level set at $p \leq 0.05$. The Statistical Analysis System 9.4 (SAS Institute Inc., Cary, NC, USA) was employed for statistical analysis.

## 3. Results and discussion

### *3.1. The inhibitory effect of GUE on the mycelial growth of F. oxysporum and P. capsici*

Several extracts of *G. uralensis* Fisch. have been documented for their antibacterial, antifungal, and antiviral properties, encompassing crude alcoholic root extracts or its predominant purified compounds against human pathogens (*Arthrinium sacchari*, *Chaetonmium funicola*, and *Candida albicans*) [28-30]. However, to the best of our knowledge, there have been limited reports on the antifungal activity of a *G. uralensis* Fisch. extract against plant pathogenic fungi. In our investigation, we observed that GUE exhibited antifungal activity against both *F. oxysporum* and *P. capsici*, as depicted in Figs. 2 and 3, respectively. It is evident that GUE

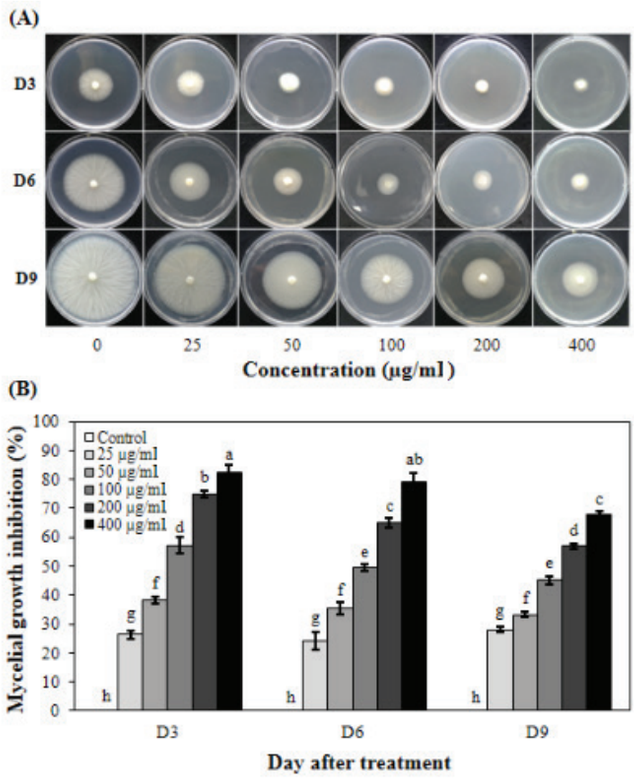


**Fig. 2. Mycelial growth inhibition of *F. oxysporum* by GUE at various concentrations and treatment times. (A)** Petri dishes of *F. oxysporum* incubated on PDA medium at 25°C in the dark with a final concentration of *G. uralensis* Fisch. extract (GUE) of 0, 25, 50, 100, 200, or 400 µg/ml (0 µg/ml is the methanol control); **(B)** Graphical representation of mycelial growth inhibition by GUE. The mean values followed by different letters in each column represent statistically significant differences based on Tukey's HSD test ($p \leq 0.05$). The error bars indicate the standard deviation of the mean (n=3). D3, D6, and D9 correspond to 3, 6, and 7 days after treatment, respectively.

significantly impeded the mycelial growth of both species, with inhibition ranges of 26.3-82.6, 24.1-79.2, and 28.1-67.8% for *F. oxysporum* and 27.4-83.7, 33.1-78.5, and 20.0-70.1% for *P. capsici*, observed three, six, and nine days after treatment with 25-400 µg/ml of GUE. Consequently, the $EC_{50}$ values for GUE mycelial inhibition were calculated as 113.4, 150.6, and 191.4 µg/ml for *F. oxysporum* and 84.7, 148.6, and 190.1 µg/ml for *P. capsici*, respectively (Table 1). As portrayed in Figs. 2 and 3, the antifungal activities of GUE were highly pronounced in inhibiting the mycelial growth of *F. oxysporum* and *P. capsici* utilising the paper disc method. Specifically for *F. oxysporum,* the MIC value of GUE was found to be 100, 200, and 400 µg/ml at 3, 6, and 9 days post-treatment. In contrast, for *P. capsici*, the MIC value was 50, 100, and 100 µg/ml at 3, 6, and 9 days post-treatment.

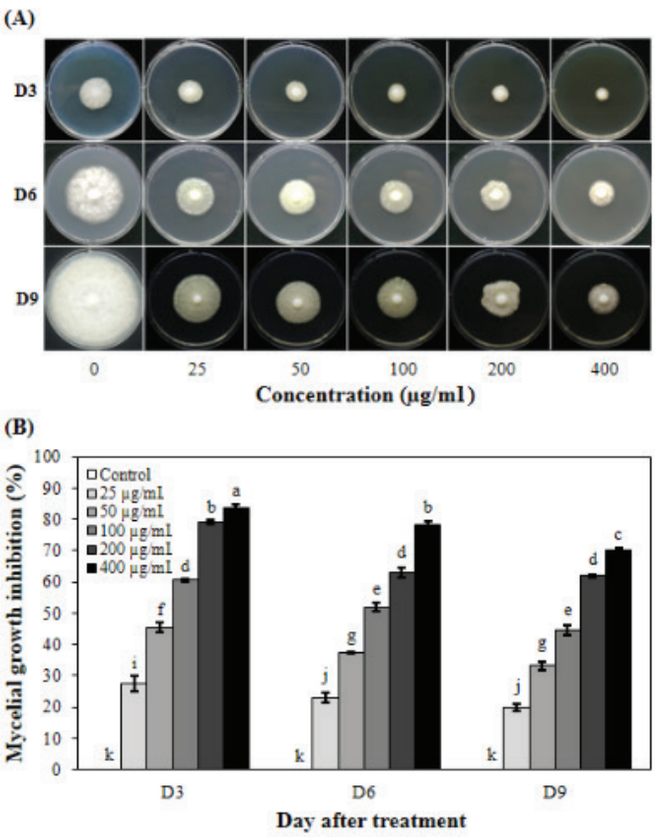


**Fig. 3. Mycelial growth inhibition of *P. capsici* by GUE at various concentrations and treatment times. (A)** Petri dishes of *P. capsici* incubated on PDA medium at 25°C in the dark with a final concentration of *G. uralensis* Fisch. extract (GUE) of 0, 25, 50, 100, 200, or 400 µg/ml (0 µg/ml is the methanol control); **(B)** Graphical representation of mycelial growth inhibition by GUE. The mean values followed by different letters in each column represent statistically significant differences based on Tukey's HSD test (p≤0.05). The error bars indicate the SD of the mean (n=3). D3, D6, and D9 correspond to 3, 6, and 9 days after treatment, respectively.

**Table 1. The $EC_{50}$ values for inhibiting the mycelial growth of *F. oxysporum* and *P. capsici* by the methanolic extract of the roots of *G. uralensis* Fisch. after various treatment times.**

| Pathogenic fungus | $EC_{50}$ (µg/ml) | | |
|---|---|---|---|
| | *Day 3* | *Day 6* | *Day 9* |
| *F. oxysporum* | 113.4±1.8$^{c}$ | 150.6±2.2$^{b}$ | 191.4±1.1$^{a}$ |
| *P. capsici* | 84.7±1.6$^{d}$ | 148.6±2.3$^{b}$ | 190.1±2.5$^{a}$ |

Each value is the mean ± standard deviation from 2 experiments with three replicates. The mean values followed by different letters in each column represent statistically significant differences based on Tukey's HSD test (p≤0.05).

In separate studies, numerous compounds present in Chinese liquorice roots and rhizomes have exhibited anti-H1N1 virus activity, with inhibitory rates ranging from 47 to 82% at concentrations of 100 µM, corresponding to $IC_{50}$ values within the range of 39.6-49.1 µM. These compounds include glycyrrhizin, β-acetoxyglycyrrhizin, and liquorice saponins A3, E2, and G2 [20]. Aqueous and ethanolic extracts from Chinese liquorice have also demonstrated a broad inhibitory spectrum against Gram-positive and -negative bacteria, yeast, and fungi. Moreover, *G. glabra* extract at concentrations of 10 to 100 mg/ml has displayed significant anti-yeast activity against *C. parapsilosis* [31]. The majority of antimicrobial effects attributed to Chinese liquorice extract can be attributed to isoflavonoid components, particularly hispaglabridin, β,4'-O-methylglabridin, glabridin, glabriol, and 3-hydroxyglabrol [31-33]. Dodecamethyl cyclohexasiloxane extracted from *Argemone ochroleuca* latex has demonstrated antifungal activity against *Candida* species and *Drechslera halodes* [34]. S. Hermann, et al. (2022) [23] reported that *G. glabra* leaf extract effectively controls a variety of bacterial plant pathogens and the oomycete *P. infestans*, not only *in vitro* or on the model plant *Arabidopsis*, but also on a crop plant (tomatoes). Furthermore, *Pseudomonas syringae* was eradicated by a 0.2% *G. glabra* leaf extract *in vitro*.

### *3.2. The effect of GUE on the mycelial morphology of F. oxysporum and P. capsici*

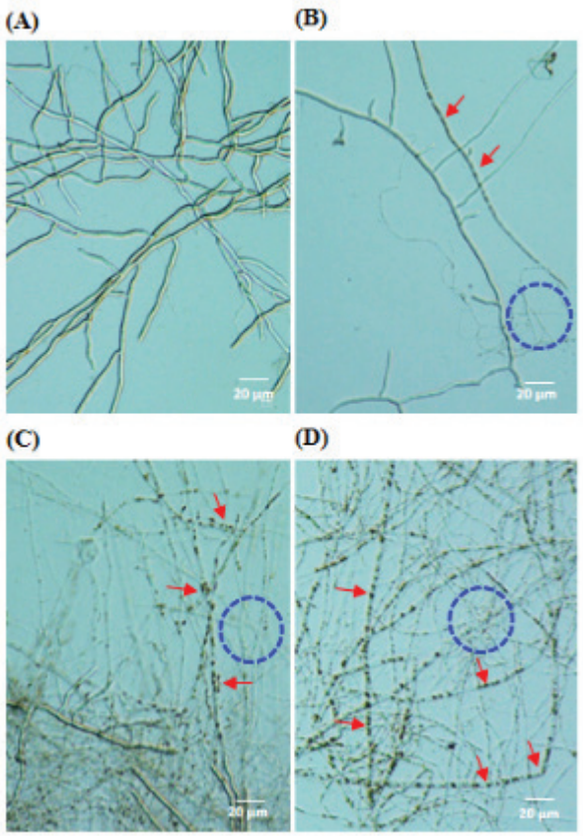


**Fig. 4. Light microscope images (40X magnification) of the mycelial morphology of *F. oxysporum* after 3 days with and without treatment with *G. uralensis* Fisch. extract.**

The mycelial morphology of *F. oxysporum* on day 3, with and without treatment with GUE, is presented in Fig. 4. In the case of *F. oxysporum*, Fig. 4A illustrates the growth of healthy mycelia on the control plates, while Fig. 4B reveals their slight impairment, featuring transparent cytoplasm, when exposed to 100 µg/ml GUE. Further treatment with 200 µg/ml GUE resulted in atrophied and fragmented mycelia, as indicated by the arrow in Fig. 4C. Subsequently, treatment with 400 µg/ml GUE resulted in abnormal, atrophied, and collapsed mycelia, as shown by the arrow and circle in Fig. 4D.

Figure 5 displays the mycelial morphology of *P. capsici* on day 3, with and without treatment with GUE. In the case of *P. capsici*, Fig. 5A demonstrates the growth of healthy mycelia on the control plates, while Fig. 5B reveals their mild perturbation, featuring transparent cytoplasm, when exposed to 100 µg/ml of GUE. Furthermore, Fig. 5C exhibits several swollen and

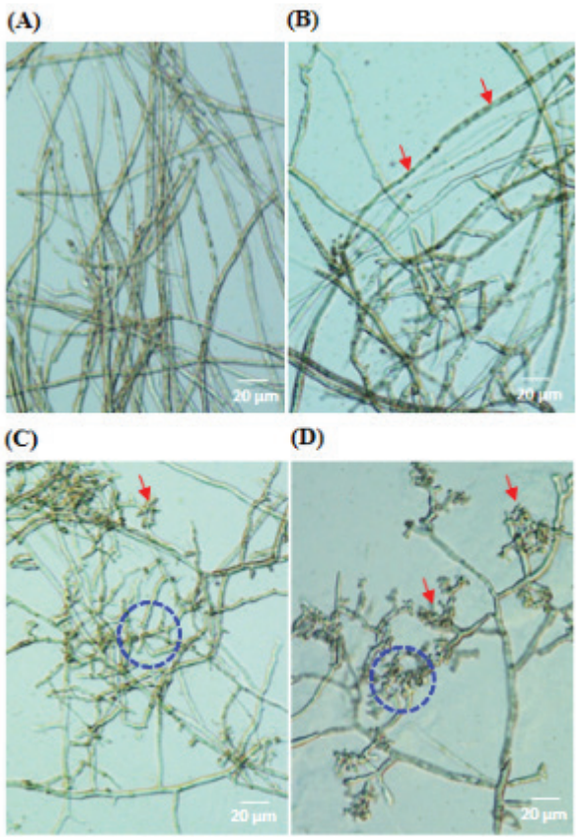


**Fig. 5. Light microscope images (40X magnification) of the mycelial morphology of *P. capsici* after 3 days with and without treatment with *G. uralensis* Fisch. extract.**

aberrant mycelium tips following treatment with 200 µg/ml of GUE, as indicated by the arrow and circle. Finally, when treated with 400 µg/ml of GUE, Fig. 5D shows a majority of swollen mycelium tips with increased branching, again illustrated by the arrow and circle. These results are in line with existing literature, suggesting that essential oils can exert versatile effects on cell walls, cell membranes, and cytoplasmic contents [35-38].

Mechanisms of action for crude extracts or compounds from *G. uralensis* Fisch. on fungi and oomycetes have been scarcely investigated. One plausible mechanism underlying their antifungal activity involves the degradation of fungal cell walls by inhibiting chitin synthesis [39]. Additionally, Q. OuYang, et al. (2019) [40] reported the dissolution of the cell wall of *Geotrichum citri-aurantii*, along with a reduction in chitin content, concluding that active compounds can hinder mycelial growth by compromising the integrity of fungal cell walls. In a similar vein, D.M.C. Nguyen, et al. (2013) [9] observed the collapse and shrinkage of *F. solani* hyphae

following incubation with gallic acid (500 µg/ml) purified from *Terminalia nigrovenulosa* for 24 hours. Likewise, Y. Wang, et al. (2021) [8] demonstrated the distortion and shrivelling of *P. capsici* mycelium 3 days after treatment with 140 mg/l cinnamaldehyde.

## 4. Conclusions

In this study, we explored the antifungal potential of the methanolic extract of *G. uralensis* Fisch.. It exhibited significant promise as an alternative to synthetic fungicides for combating plant pathogens. Future investigations should aim to identify the chemical structure of the active compounds present in *G. uralensis* Fisch. extract. Once these structures are elucidated, efforts should be directed towards developing their fungicidal potency and stability, with the goal of reducing costs and rendering them practical for field applications.

## CRediT author statement

Dang-Minh-Chanh Nguyen: Methodology, Data analysis, Writing, Editing; Thi-Hoan Luong: Methodology, Data analysis, Writing; Van-Viet Nguyen: Methodology, Data analysis, Writing; Woo-Jin Jung: Methodology, Data analysis, Writing.

## ACKNOWLEDGEMENTS

This work was supported by the Korean Institute of Planning and Evaluation for Technology in Food, Agriculture, and Forestry (IPET) through the "Agricultural machinery/equipment localisation technology development program (No. 321055-05) and the Agricultural machinery/equipment localisation technology development program (No. 122020-3)", both funded by the Korea Ministry of Agriculture, Food, and Rural Affairs (MAFRA).

## COMPETING INTERESTS

The authors declare that there is no conflict of interest regarding the publication of this article.

## REFERENCES

[1] C. Srinivas, D.N. Devi, K.N. Murthy, et al. (2017), "*Fusarium oxysporum* F. sp. *lycopersici* causal agent of vascular wilt disease of tomato: Biology to diversity - A review", *Saudi J. Biol. Sci.*, **26(7)**, pp.1315-1324, DOI: 10.1016/j.sjbs.2019.06.002.

[2] F.G. Rojo, M.M. Reynoso, N.C. Sofia, et al. (2007), "Biological control by *Trichoderma* species of *F. solani* causing peanut brown root rot under field condition", *Crop Protection*, **26(4)**, pp.549-555, DOI: 10.1016/j.cropro.2006.05.006.

[3] W.R. Carlile (1995), *Control of Crop Diseases*, Second Edition, Cambridge University Press, DOI: 10.1017/S0889189300006937.

[4] P.V. West, A.A. Appiah, N.A. Gow (2003), "Advances in research on oomycete root pathogens", *Physiol. Mol. Plant Pathol.*, **62(2)**, pp.99-113, DOI: 10.1016/S0885-5765(03)00044-4.

[5] K.H. Lamour, R. Stam, J. Jupe, et al. (2012), "The oomycete broad-host-range pathogen *Phytophthora capsici*", *Mol. Plant Pathol.*, **13(4)**, pp.329-337, DOI: 10.1111/j.1364-3703.2011.00754.x.

[6] X.R. Chen, Y.P. Xin, Y.P. Li, et al. (2013), "RNA-Seq reveals infection-related gene expression changes in *Phytophthora capsici*", *PLOS ONE*, **8(9)**, DOI: 10.1371/annotation/3be2cab2-9116-49c1-acce-7d51f4ccd887.

[7] S.C. Knight, V.M. Anthony, A.M. Brady, et al. (1997), "Rationale and perspectives on the development of fungicides", *Annual Review of Phytopathology*, **35**, pp.349-372, DOI: 10.1146/annurev.phyto.35.1.349.

[8] Y. Wang, M. Wang, M. Li, et al. (2021), "Cinnamaldehyde inhibits the growth of *Phytophthora capsici* through disturbing metabolic homoeostasis", *PeerJ*, **9**, DOI: 10.7717/peerj.11339.

[9] D.M.C. Nguyen, D.J. Seo, H.B. Lee, et al. (2013), "Antifungal activity of gallic acid purified from *Terminalia nigrovenulosa* bark against *F. solani*", *Microb. Pathog.*, **56**, pp.8-15, DOI: 10.1016/j.micpath.2013.01.001.

[10] T.R. Costa, F.L.F. Fernandes, S.C. Santos, et al. (2000), "Antifungal activity of volatile constituents of *Eugenia dysenterica* leaf oil", *J. Ethnopharm.*, **72(1-2)**, pp.111-117, DOI: 10.1016/s0378-8741(00)00214-2.

[11] S. Kordali, A. Cakir, H. Zengin, et al. (2003), "Antifungal activities of the leaves of three *Pistacia* species grown in Turkey", *Fitoterapia*, **74(1-2)**, pp.164-167, DOI: 10.1016/s0367-326x(02)00320-9.

[12] A.O. Mwamula, M.D.F. Kabir, D.W. Lee (2022), "A review of the potency of plant extracts and compounds from key families as an alternative to synthetic nematicides: History, efficacy, and current developments", *Plant Pathol. J.*, **38(2)**, pp.53-77, DOI: 10.5423/PPJ.RW.12.2021.0179.

[13] S. Harish, D. Saravanakumar, R. Radjacommare, et al. (2008), "Use of plant extracts and biocontrol agents for the management of brown spot disease in rice", *BioControl*, **53**, pp.555-567, DOI: 10.1007/s10526-007-9098-9.

[14] J.C. Kim, G.J. Choi, S.W. Lee, et al. (2004), "Screening extracts of *Achyranthes japonica* and *Rumex crispus* for activity against various plant pathogenic fungi and control of powdery mildew", *Pest. Manag. Sci.*, **60(8)**, pp.803-808, DOI: 10.1002/ps.811.

[15] G. Tegegne, J.C. Pretorius (2007), "*In vitro* and *in vivo* antifungal activity of crude extracts and powdered dry material from Ethiopian wild plants against economically important plant pathogens", *BioControl*, **52**, pp.877-888, DOI: 10.1007/s10526-007-9088-y.

[16] A.C.G. Fiori, K.R.F.S. Estrada, J.R. Stangarlin, et al. (2000), "Antifungal activity of leaf extracts and essential oils of some medicinal plants against *Didymella bryoniae*", *J. Phytopathol.*, **148(7-8)**, pp.483-487, DOI: 10.1046/j.1439-0434.2000.00524.x.

[17] Y.L. Chu, W.C. Ho, W.H. Ko (2006), "Effects of Chinese herb extracts on spore germination of *Oidium murrayae* and nature of inhibition substances from Chinese Rhubarb", *Plant Dis.*, **90(7)**, pp.848-861, DOI: 10.1094/PD-90-0858.

[18] S. Ma, G. Zhu, F. Yu, et al. (2018), "Effects of manganese on accumulation of glycyrrhizic acid based on material ingredients distribution of *Glycyrrhiza uralensis*", *Industrial Crops and Products*, **112**, pp.151-159, DOI: 10.1016/j.indcrop.2017.09.035.

[19] C. Chen, C. Zhong, X. Gao, et al. (2022), "*Glycyrrhiza uralensis* Fisch. root-associated microbiota: The multifaceted hubs associated with environmental factors, growth status and accumulation of secondary metabolites", *Environmental Microbiome*, **17(1)**, DOI: 10.1186/s40793-022-00418-0.

[20] S. Ji, Z. Li, W. Song, et al. (2016), "Bioactive constituents of *Glycyrrhiza uralensis* (Licorice): Discovery of the effective components of a traditional herbal medicine", *Journal of Natural Products*, **79(2)**, pp.281-292, DOI: 10.1021/acs.jnatprod.5b00877.

[21] H.C. Zhang, J.M. Liu, H.Y. Lu, et al. (2009), "Enhanced flavonoid production in hairy root cultures of *Glycyrrhiza uralensis* Fisch. by combining the over-expression of chalcone isomerase gene with the elicitation treatment", *Plant Cell Reports*, **28(8)**, pp.1205-1213, DOI: 10.1007/s00299-009-0721-3.

[22] E.A. Mohammed, Y. Peng, Z. Wang, et al. (2022), "Synthesis, antiviral, and antibacterial activity of the glycyrrhizic acid and glycyrrhetinic acid derivatives", *Russian Journal of Bioorganic Chemistry*, **48(5)**, pp.906-918, DOI: 10.1134/S1068162022050132.

[23] S. Hermann, M. Orlik, P. Boevink, et al. (2022), "Biocontrol of plant diseases using *Glycyrrhiza glabra* leaf extract", *Plant Dis.*, **106(12)**, pp.3133-3144, DOI: 10.1094/PDIS-12-21-2813-RE.

[24] A. Mishra, N. Dubey (1994), "Evaluation of some essential oils for their toxicity against fungi causing deterioration of stored food commodities", *Appl. Environ. Microbiol.*, **60(4)**, pp.1101-1105, DOI: 10.1128/aem.60.4.1101-1105.1994.

[25] E.M. Soylu, S. Soylu, S. Kurt (2006), "Antimicrobial activities of the essential oils of various plants against tomato late blight disease agent *P. infestans*", *Mycopathologia*, **161(2)**, pp.119-128, DOI: 10.1007/s11046-005-0206-z.

[26] M.E. Milici, C.M. Maida, E. Spreghini, et al. (2007), "Comparison between disk diffusion and microdilution methods for determining susceptibility of clinical fungal isolates to caspofungin", *J. Clin. Microbiol.*, **45(11)**, pp.3529-3533, DOI: 10.1128/JCM.00826-07.

[27] V.N. Nguyen, D.M.C. Nguyen, D.J. Seo, et al. (2009), "Antimycotic activities of Cinnamon-derived compounds against *Rhizoctonia solani in vitro*", *BioControl*, **54(5)**, pp.697-707, DOI: 10.1007/s10526-009-9220-2.

[28] J. He, L. Chen, D. Heber, et al. (2006), "Antibacterial compounds from *Glycyrrhiza uralensis*", *J. Nat. Prod.*, **69(1)**, pp.121-124, DOI: 10.1021/np058069d.

[29] T.K. Lim (2016), *Edible Medicinal and Non-Medicinal Plants*, Springer, DOI: 10.1007/978-94-017-7276-1.

[30] R. Yang, B.C. Yuan, Y.S. Ma, et al. (2017), "The anti-inflammatory activity of liquorice, a widely used Chinese herb", *Pharm. Biol.*, **55(1)**, pp.5-18, DOI: 10.1080/13880209.2016.1225775.

[31] F. Karahan, C. Avsar, I.I. Ozyigit, et al. (2016), "Antimicrobial and antioxidant activities of medicinal plant *Glycyrrhiza glabra* var. *glandulifera* from different habitats", *Biotech. & Biothech. Equipment.*, **30(4)**, pp.797-804, DOI: 10.1080/13102818.2016.1179590.

[32] V.K. Gupta, A. Fatima, U. Faridi, et al. (2018), "Antimicrobial potential of *Glycyrrhiza glabra* root", *J. Ethnopharmacol.*, **16(2)**, pp.377-380, DOI: 10.1016/j.jep.2007.11.037.

[33] G.M. Hamad, A.I.A. Elaziz, S.A. Hassan, et al. (2020), "Chemical composition, antioxidant, antimicrobial and anticancer activities of licorice (*Glycyrrhiza glabra* L.) root and its application in functional yoghurt", *J. Food Nut. Res.*, **8(12)**, pp.707-715, DOI: 10.12691/jfnr-8-12-3.

[34] M.F.M. Moustafa, S.A. Alamri, T.H. Taha, et al. (2013), "*In vitro* antifungal activity of *Argemone ochroleuca* sweet latex against some pathogenic fungi", *Afr. J. Biotech.*, **12(10)**, pp.1132-1137, DOI: 10.5897/AJB12.2649.

[35] F.G. Xing, H.J. Hua, J.N. Selvaraj, et al. (2014), "Growth inhibition and morphological alterations of *Fusarium verticillioides* by cinnamon oil and cinnamaldehyde", *Food Control*, **46**, pp.343-350, DOI: 10.1016/j.foodcont.2014.04.037.

[36] X. Shao, B. Cao, F. Xu, et al. (2015), "Effect of postharvest application of chitosan combined with clove oil against citrus green mold", *Postharvest Biol. Technol.*, **99**, pp.37-43, DOI: 10.1016/j.postharvbio.2014.07.014.

[37] Y. Wei, Y. Wei, F. Xu, et al. (2018), "The combined effects of tea tree oil and hot air treatment on the quality and sensory characteristics and decay of strawberry", *Postharvest Biol. Technol.*, **136**, pp.139-144, DOI: 10.1016/j.postharvbio.2017.11.008.

[38] D.M.C. Nguyen, T.H. Luong, T.C. Nghiem, et al. (2023), "Chemical composition, antioxidant and antifungal activities of rhizome essential oil of *Kaempferia parviflora* Wall. ex Baker grown in Vietnam", *J. Appl. Biol. Chem.*, **66(3)**, pp.15-22, DOI: 10.3839/jabc.2023.003.

[39] Y.J. Liu, K.Q. Zhang (2004), "Antimicrobial activity of selected *Cyathus* species", *Mycopathologia*, **157(2)**, pp.185-189, DOI: 10.1023/b:myco.0000020598.91469.d1.

[40] Q. OuYang, X. Duan, L. Li, et al. (2019), "Cinnamaldehyde exerts its antifungal activity by disrupting the cell wall integrity of *Geotrichum citri-aurantii*", *Front. Microb.*, **10**, DOI: 10.3389/fmicb.2019.00055.

# Development of direct C-3 difluoromethylation reaction for application in synthesis of quinoline-related drugs

**Thanh Tung Truong[1, 2*], John Nielsen[3]**

[1]*Faculty of Pharmacy, Phenikaa University, Yen Nghia Ward, Ha Dong District, Hanoi, Vietnam*
[2]*Phenikaa Institute for Advanced Study (PIAS), Phenikaa University, Yen Nghia Ward, Ha Dong District, Hanoi, Vietnam*
[3]*University of Copenhagen, Norregade 10, 1172 Kobenhavn, Denmark*

Received 16 November 2022; revised 2 January 2023; accepted 5 January 2023

***Abstract:***

**Fluorine holds a prominent position within the realm of drug discovery and development, substantiated by its presence in approximately 25% of drugs approved by the US Food and Drug Administration (FDA). Consequently, the advancement of new fluorination reactions stands as a pivotal area in medicinal chemistry. In particular, the monofluoro-, difluoromethyl-, and trifluoromethyl- are three groups that appear most frequently in drug structure. Quinoline, owing to its privileged structural status, plays a crucial role in drug design and synthesis. Various approaches have been documented for the direct difluoromethylation of the C-2 and C-4 positions of the quinoline ring. However, achieving direct C-3 difluoromethylation has remained an elusive objective. In this study, we introduce a novel method for effecting the direct difluoromethylation at the C-3 position of the quinoline ring. Comprehensive characterizations, including $^{1}$H-NMR, $^{13}$C-NMR, and $^{19}$F-NMR for all compounds are performed. We believe that this novel method will open a new way to access the hitherto untapped C-3-difluoromethylation active compounds.**

***Keywords:*** **C-H activation, difluoromethylation, drug synthesis, quinoline.**

***Classification numbers:*** **2.2, 3.3**

## 1. Introduction

The fluorine atom assumes a pivotal role in medicinal chemistry, particularly in drug design and development [1, 2]. Approximately 25% of FDA-approved drugs presently incorporate fluorine (F) or related functional groups such as monofluoromethyl ($-CFH_2$), difluoromethyl ($-CF_2H$), trifluoromethyl ($-CF_3$), among others [1-4]. Notable examples of such fluorinated drugs encompass voriconazole for fungal infection treatment, Sitagliptin for type II diabetes management, and Fulvestrant for cancer therapy (Fig. 1A). Among these fluorinated moieties, it is well-established that the difluoromethyl $CF_2H$ group serves as a bioisostere substitute for numerous functional groups, including OH, SH, and NH [5]. This bioisosteric replacement significantly enhances the biological activity of compounds [5, 6]. Consequently, a substantial body of research is dedicated to developing

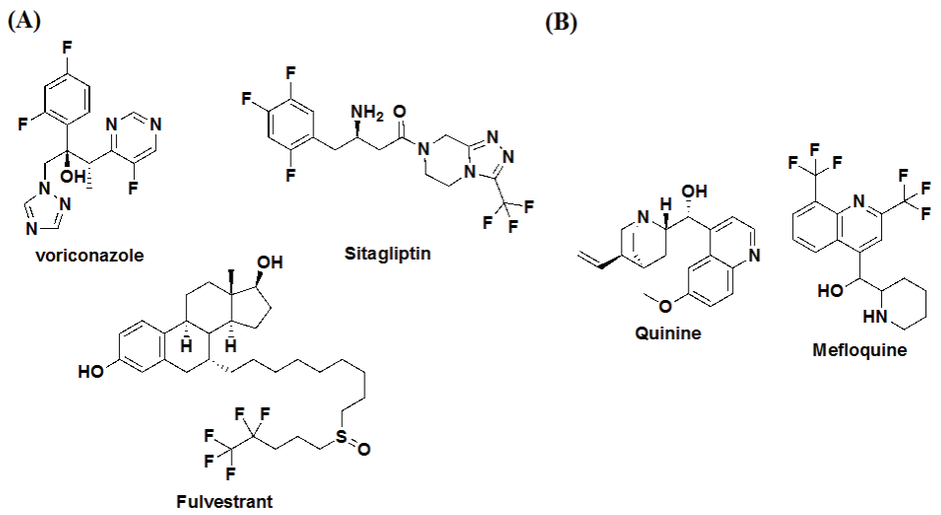


**Fig. 1. Most notable drugs containing (A) fluorine atoms and (B) quinoline.**

*Corresponding author: Email: tung.truongthanh@phenikaa-uni.edu.vn

novel difluoromethylation reactions to introduce the $CF_2H$ group into bioactive compounds [7].

Quinoline represents a privileged structural motif in drug design, with numerous bioactive compounds and drugs featuring this moiety (Fig. 1B) [8]. Therefore, our research group is keenly interested in discovering new methodologies for constructing currently inaccessible quinoline derivatives. To date, only a limited number of methods have been reported for the direct difluoromethylation of quinoline (Scheme 1) [9-11]. However, all of these reported methods exclusively yield the C-2-$CF_2H$ and C-4-$CF_2H$ derivatives. In this report, we present the inaugural controlled-direct C-3 difluoromethylation of quinoline.

## 2. Materials and methods

### *2.1. Chemicals*

Reagents and solvents were procured from commercially available suppliers, including Deajung (South Korea), Sigma Aldrich, and Alfa Aesar. All reagents and solvents exhibited a minimum purity of 98% and were utilized without further purification. Reaction progress was monitored via thin-layer chromatography (Merck Kieselgel 60F254) and visualized under UV light at wavelengths of 254 or 365 nm. NMR analyses were conducted using a Bruker Avance 400 MHz instrument with TMS serving as the internal standard.

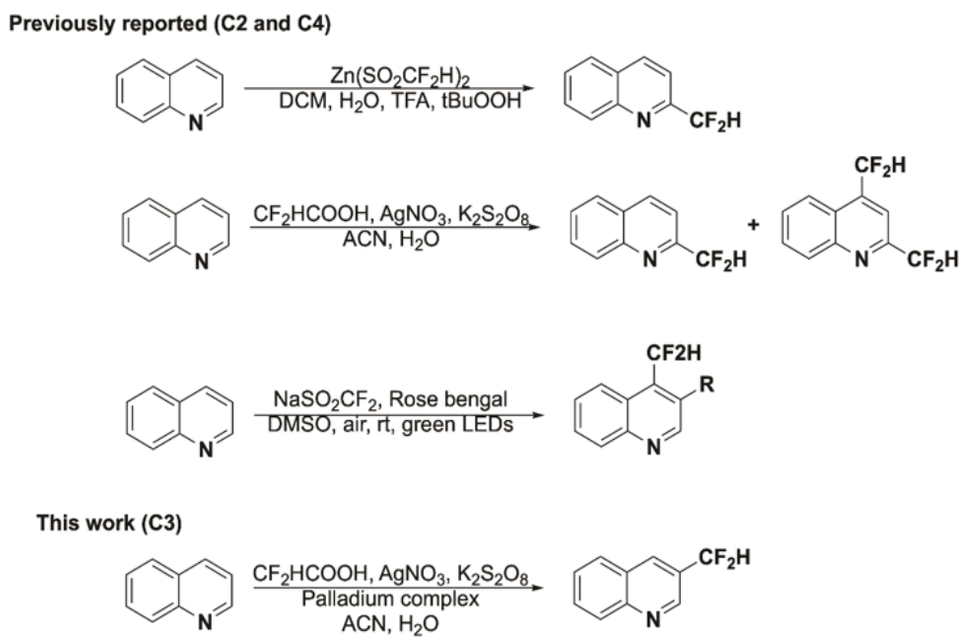


**Scheme 1. Current methods of direct difluoromethylation.**

### *2.2. Methods*

General procedure: Quinoline (1 equiv.), palladium complex (0.5 mol%), $AgNO_3$ (0.5 equiv.), and $K_2S_2O_8$ (5 equiv.) were combined in a 10 ml round-bottom flask. Acetonitrile (1 ml) was subsequently added, followed by $H_2O$ (0.5 ml). The difluoromethylating reagent $CF_2HCOOH$ (2 equiv.) was introduced. The mixture was stirred at 50°C for 6 hours. Reaction progress was monitored by thin-layer chromatography until completion. The reaction mixture was then diluted with $H_2O$ (20 ml), followed by the addition of saturated $NaHCO_3$ (20 ml). Extraction was performed using ethyl acetate. The product was purified via silica-gel flash column chromatography.

## 3. Results and discussion

### *3.1. Investigation of direct C-3 difluoromethylation*

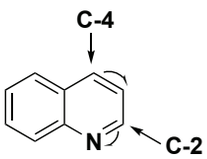


**Fig. 2. Electron flow of quinoline.**

Previously, difluoroacetic acid and its derivatives have been reported as a new means for direct difluoromethylation of quinoline [9-11]. However, the authors exclusively yielded the C-2-$CF_2H$/C-4-$CF_2H$ and bis-difluoromethylated products (C-2 + C-4) (Scheme 1). The common mechanism underlying this reaction involves the nucleophilic CF2H radical species generated through the redox process of $AgNO_3/K_2S_2O_8$, which preferentially attaches to the electron-deficient carbons within the quinoline system (C-2 and C-4) (Fig. 2) [9-11]. Building upon these findings, we hypothesized that the inclusion of a metal catalyst could stabilise the electrophilic $CF_2H$ radical species, thereby enabling attachment to C-3 of quinoline. Among metal catalysts, palladium

is renowned for its involvement in various mechanisms of both nucleophilic and electrophilic radical reactions [12]. Consequently, we conducted a screening of several palladium catalysts using the previously optimised reaction conditions (Table 1, Scheme 2).

**Table 1. Representative results of the screening of palladium complexes.**

| Entry | Pd Catalyst | Catalyst (mol%) | Yields (%)* | | |
|---|---|---|---|---|---|
| | | | *1* | *2* | *3* |
| 1 | None | - | 50 | <1 | - |
| 2 | $Pd(OAc)_2$ | 0.5 | 44 | <1 | 0 |
| 3 | $Pd(PPh_3)_4$ | 0.5 | 31 | <5 | 0 |
| 4 | $Pd(PPh_3)_4Cl_2$ | 0.5 | <5 | <1 | 72 |
| 5 | $Pd(PPh_3)_4Cl_2$ | 1 | <5 | <1 | 70 |

Reactions were carried out at 50°C. *NMR yields. Other palladium complexes did not exhibit any significant effects on the reaction (data not shown).

As illustrated in Table 1, the standard reaction conditions without palladium yielded a 50% yield of C-2 product 1 and less than 1% of product 2, consistent with the literature [10] (Entry 1, Table 1). No C-3 product was obtained when employing $Pd(OAc)_2$ and $Pd(PPh_3)_4$, though the overall reaction yield was diminished (Entries 2 and 3, Table 1). Among the tested palladium complexes, $Pd(PPh_3)_4Cl_2$ emerged as a regioselective catalyst for the formation of the C-3 product, with a minor amount of C-2 (1) and bis C-2/C-4 (2) (Entry 4, Table 1). The TLC pattern also indicated that the more polar spot corresponds to C-3 (3) (Fig. 3). This observation can be elucidated by the presence of the electron-withdrawing group $-CF_2H$ at C-2 in 1 and 2, rendering these compounds less polar in comparison to 3. Employing 0.5 mol% of $Pd(PPh_3)_4Cl_2$ was deemed optimal, as increasing the amount did not enhance the reaction yield (Entry 5, Table 1).

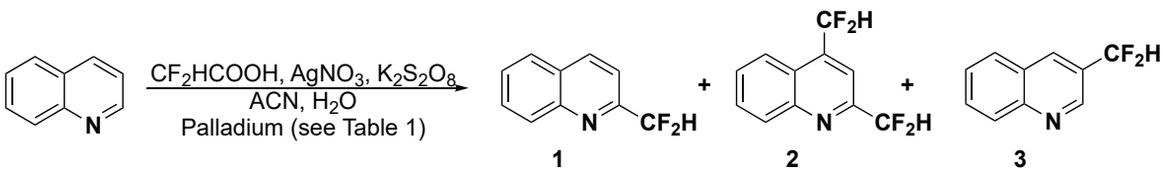


**Scheme 2. Synthetic scheme corresponding to the experiments detailed in Table 1.**

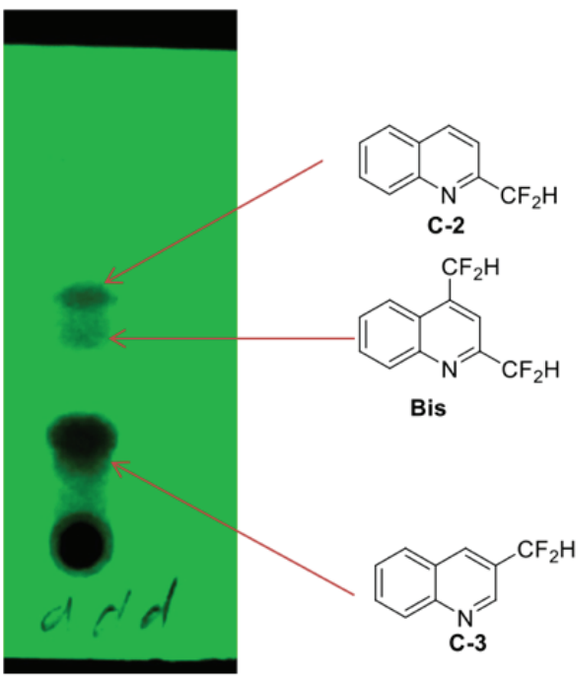


**Fig. 3. TLC of reaction mixture when adding $Pd(PPh_3)_4Cl_2$.**

### *3.2. Confirmation of compound's structures*

Comparison of the $^{19}$F-NMR spectra of 1, 2, and 3 (Fig. 4) revealed distinct features: a single peak at -114.2 ppm for compound 1, corresponding to C-2-$CF_2H$; a single peak at -115.1 ppm for compound 2, indicative of C-3-$CF_2H$; and two peaks at -114.5 and -115.2 corresponding to C-2-$CF_2H$ & C-3-$CF_2H$ in compound 3. Overall, the $^{19}$F-NMR analysis unequivocally differentiated the $CF_2H$ group in compounds 1-3.

In terms of $^1$H-NMR, the presence of triplet peaks within the range of 6.60-7.30 ppm (JH-F~55 Hz) for the hydrogen atoms of the $CF_2H$ group confirmed the existence of C-2-$CF_2H$ and C-3-$CF_2H$ in the synthesised compounds 1-3 (Fig. 5). Furthermore, the proton peak at 8.96 ppm for compound 3 affirmed that the hydrogen at C-2 of quinoline remained unaltered, a feature not

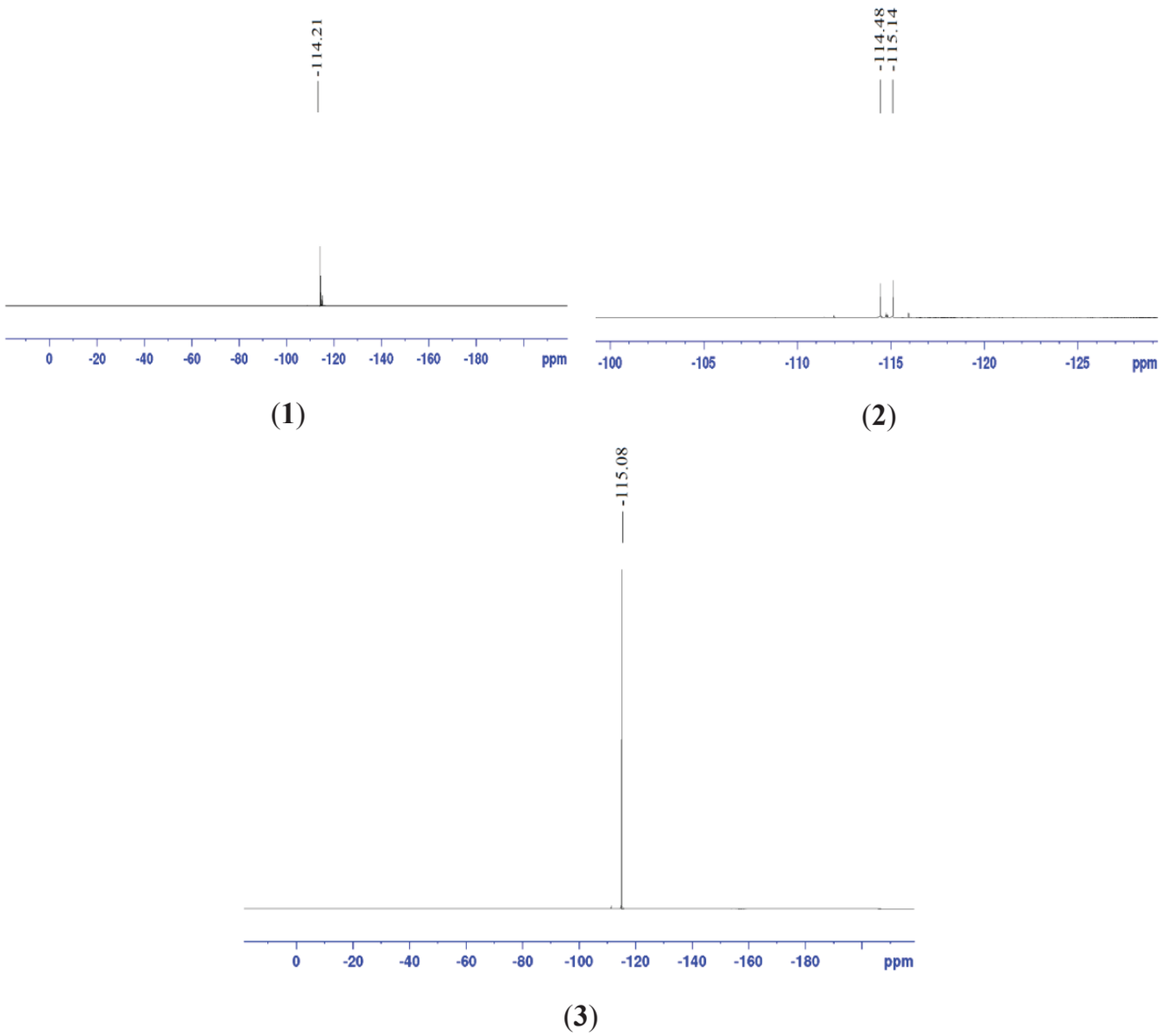


**Fig. 4. $^{19}$F-NMR spectra of compounds 1, 2, and 3.**

observed in compounds 1 and 2. Collectively, the NMR data have substantiated the structures of the compounds.

In summary, we have developed novel reaction conditions to achieve direct C-3 difluoromethylation. Comprehensive characterisations, including $^{1}$H-NMR and $^{19}$F-NMR for known compounds 1,2, along with full characterisation for compound 3, are shown below:

Compound 1: $^{1}$H NMR (400 MHz, Chloroform-d) δ=8.26 (d, J=8.5, 1H), 8.07 (d, J=8.5, 1H), 7.86-7.78 (m, 1H), 7.71 (ddd, J=8.5, 6.8, 1.4, 1H), 7.66 (d, J=8.4, 1H), 7.56 (t, J=7.5, 1H), 6.71 (t, J=55.3, 1H). $^{19}$F NMR (376 MHz, $CDCl_3$) δ -114.22.

Compound 2: $^{1}$H NMR (400 MHz, Chloroform-d) δ 8.23 (d, J=8.6 Hz, 1H), 8.14 (dd, J=8.4 Hz, 1H), 7.92 (s, 1H), 7.82-7.89 (m, 1H), 7.74 (ddd, J=8.2, 6.7, 1.2 Hz, 1H), 7.18 (t, J=54.3 Hz, 1H), 6.81 (t, J=55.1 Hz, 1H). $^{19}$F NMR (376 MHz, $CDCl_3$) δ -114.5, -115.2.

Compound 3: yellow oil. $^{1}$H NMR (400 MHz, Chloroform-d) δ=9.03 (s, 2H), 8.22 (d, J=8.4, 2H), 8.10 (d, J=8.4, 2H), 7.80 (t, J=7.6, 2H), 7.66 (t, J=7.6, 2H),

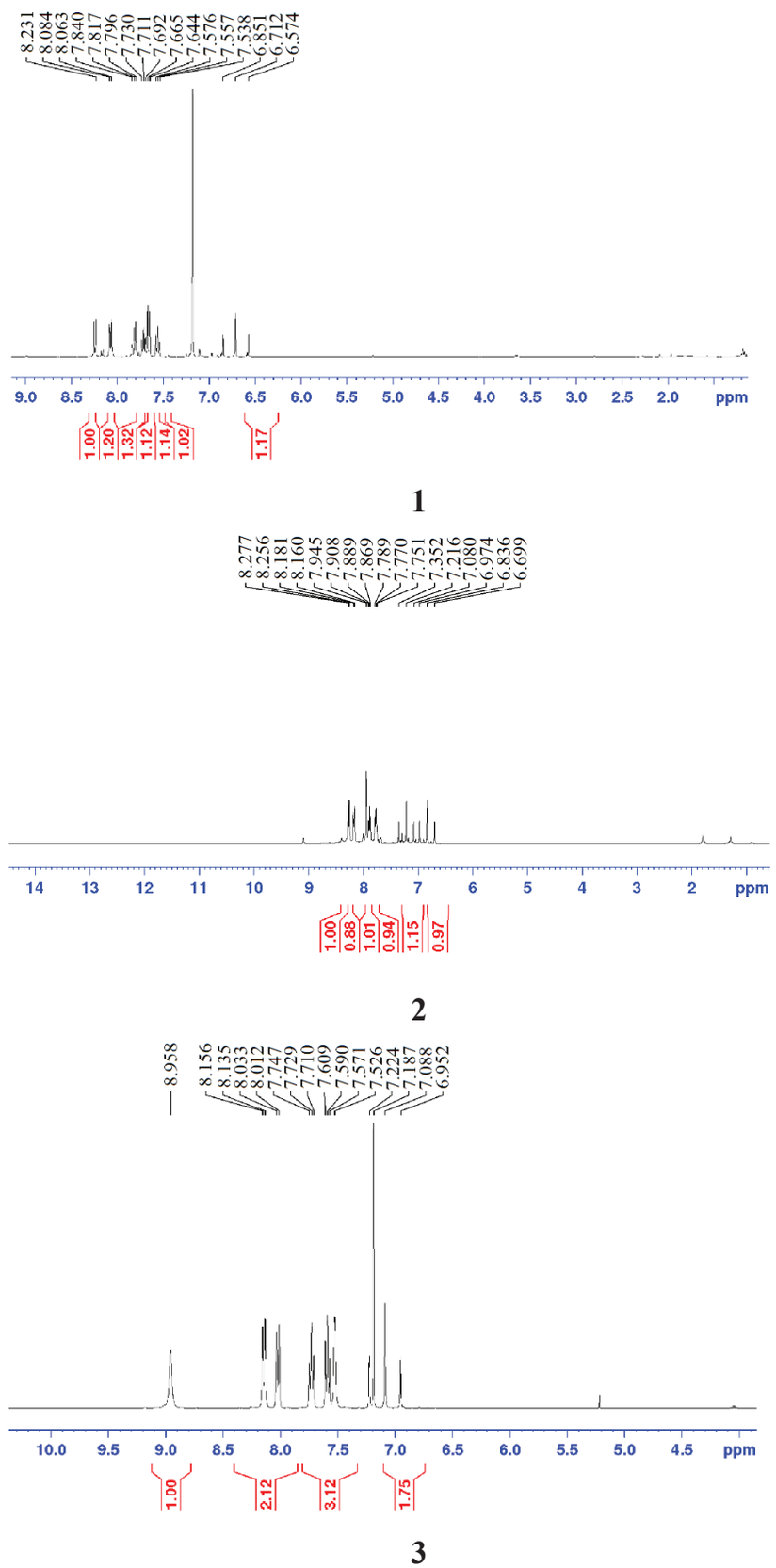


**Fig. 5. $^{1}$H-NMR spectra of compounds 1, 2, and 3.**

7.62-7.57 (m, 2H), 7.16 (t, t, J=55.3, 1H). $^{13}$C NMR (101 MHz, $CDCl_3$) δ 150.05, 148.55, 137.91(t), 130.41, 130.00, 127.87, 124.19, 123.31, 118.00(t), 113.31(t). $^{19}$F NMR (376 MHz, $CDCl_3$) δ -115.09.

## 4. Conclusions

We have successfully conducted the direct C-3 difluoromethylation of quinoline, employing difluoroacetic acid as the difluoromethylating reagent under the redox conditions of $AgNO_3/K_2S_2O_8$ and employing $Pd(PPh_3)_2Cl_2$ as the catalyst. The structure of the C-3 compound was meticulously confirmed through state-of-the-art NMR techniques, encompassing $^{1}$H-NMR, $^{13}$C-NMR, and $^{19}$F-NMR. As of now, this represents the sole direct method documented in the literature for synthesizing the C-3-$CF_2H$ derivative of quinoline. We anticipate that this work will serve as an accessible route for the direct synthesis of drugs containing the C-3-$CF_2H$ moiety.

## CRediT author statement

Thanh Tung Truong: Study conception, Design, Data collection, Analysis and Interpretation, Original draft preparation; John Nielsen: Analysis and Interpretation, Original draft preparation.

## ACKNOWLEDGEMENTS

This research is funded by the Phenikaa University Foundation for Science and Technology Development.

## COMPETING INTERESTS

The authors declare that there is no conflict of interest regarding the publication of this article.

## REFERENCES

[1] A. Vulpetti, C. Dalvit (2012), "Fluorine local environment: From screening to drug design", *Drug. Discov. Today.*, **17(15-16)**, pp.890-897, DOI: 10.1016/j.drudis.2012.03.014.

[2] J. Wang, M.S. Rosello, J.L. Aceña, et al. (2014), "Fluorine in pharmaceutical industry: Fluorine-containing drugs introduced to the market in the last decade (2001-2011)", *Chem. Rev.*, **114(4)**, pp.2432-2506, DOI: 10.1021/cr4002879.

[3] S. Purser, P.R. Peter, S. Swallow, et al. (2008), "Fluorine in medicinal chemistry", *Chem. Soc. Rev.*, **37(2)**, pp.320-330.

[4] N.A. Meanwell (2011), "Synopsis of some recent tactical application of bioisosteres in drug design", *J. Med. Chem*., **54(8)**, pp.2529-2591, DOI: 10.1021/jm1013693.

[5] Y. Zafrani, G.S. Moriah, D. Yeffet, et al. (2019), "$CF_2H$, a functional group - dependent hydrogen - bond donor: Is it a more or less lipophilic bioisostere of OH, SH, and $CH_3$?", *J. Med. Chem*., **62(11)**, pp.5628-5637, DOI: 10.1021/acs.jmedchem.9b00604.

[6] Y. Zafrani, D. Yeffet, G.S. Moriah, et al. (2017), "Difluoromethyl bioisostere: Examining the "lipophilic hydrogen bond donor", concept", *J. Med. Chem.*, **60(2)**, pp.797-804, DOI: 10.1021/acs.jmedchem.6b01691.

[7] P. Richardson (2016), "Fluorination methods for drug discovery and development", *Expert. Opin. Drug. Discov*., **11(10)**, pp.983-999, DOI: 10.1080/17460441.2016.1223037.

[8] A. Dorababu (2021), "Quinoline: A promising scaffold in recent antiprotozoal drug discovery", *Chemistry Select*, **6**, pp.2164-2177, DOI: 10.1002/slct.202100115.

[9] Y. Fujiwara, J.A. Dixon, R.A. Rodriguez, et al. (2012), "A new reagent for direct difluoromethylation", *J. Am. Chem. Soc*., **134(3)**, pp.1494-1497, DOI: 10.1021/ja211422g.

[10] T.T. Tung, S.B. Christensen, J. Nielsen (2017), "Difluoroacetic acid as a new reagent for direct C-H difluoromethylation of heteroaromatic compounds", *Chem. Eur. J.*, **23**, pp.18125-18128, DOI: 10.1002/chem.201704261.

[11] W. Zhang, X.X. Xiang, J. Chen, et al. (2020), "Direct C-H difluoromethylation of heterocycles via organic photoredox catalysis", *Nature Communications*, **11(1)**, DOI: 10.1038/s41467-020-14494-8.

[12] N. Lalloo, C.A. Malapit, S.M. Taimoory, et al. (2021), "Decarbonylative fluoroalkylation at palladium(II): From fundamental organometallic studies to catalysis", *J. Am. Chem. Soc.*, **143(44)**, pp.18617-18625, DOI: 10.1021/jacs.1c08551.

DOI: 10.31276/VJSTE.66(1).59-76



Review

# Vietnamese cassava varieties progression across 50 years

**Long Hoang[1*], Mai T.T. Nguyen[2], Doan. N.Q. Nguyen[3], Kim Hoang[1, 4], Clair Hershey[5], Reinhardt Howeler[5]**

*[1]Faculty of Agronomy, Nong Lam University - Ho Chi Minh City, Quarter 6, Linh Trung Ward, Thu Duc City, Ho Chi Minh City, Vietnam*
*[2]Department of Agriculture and Rural Development of Phu Yen Province, 64 Le Duan Street, Tuy Hoa City, Phu Yen Province, Vietnam*
*[3]Faculty of Economics, Phu Yen University, 18 Tran Phu Street, Ward 7, Tuy Hoa City, Phu Yen Province, Vietnam*
*[4]Vietnam National Cassava Program (VNCP), 121 Nguyen Binh Khiem Street, Dakao Ward, District 1, Ho Chi Minh City, Vietnam*
*[5]International Center for Tropical Agriculture (CIAT), Kilometro 17, Straight Cali - Palmira, Apartado Aéreo 6713, Cali, Colombia*

Received 22 October 2023; revised 20 November 2023; accepted 15 February 2024

***Abstract:***

**Vietnamese cassava varieties constitute the fundamental and pivotal element in the sustainable development programme for cassava. This article aims to encapsulate the advancements made over nearly five decades in breeding and enhancing Vietnamese cassava varieties. It delineates the suitable cassava variety structures for each period and ecological region. The selection of cassava varieties exhibiting high starch yield and disease resistance, coupled with the establishment of a suitable and efficient cassava cultivation model, exemplified by 10T for Vietnamese cassava varieties KM568, KM539, KM537, KM569, and KM94, stands as a cornerstone for sustaining cassava development over the years. Presently, we advocate for farmers to cultivate promising cassava varieties such as KM568 or KM539 (an enhanced version of the International Center for Tropical Agriculture (CIAT) cassava variety C39, refined through multiple breeding cycles from 2004 onwards), KM537, KM569, or HN1 (originally known as TMEB419), alongside popular cassava varieties: KM440, KM419, KM94, KM7, STB1, KM414, KM98-7, KM140, KM98-5, KM98-1. We have conducted Distinctness, Uniformity, and Stability (DUS) and Value for Cultivation and Use (VCU) tests, showcasing outstanding cassava varieties in large-scale farming, thereby providing compelling evidence for the prudent conservation and sustainable development of cassava. Vietnamese cassava progression (1975 to date) has traversed six stages, with five waves of restructuring cassava varieties, aligning with target orientations, farming conditions, and market demands, culminating in 16 popular cassava varieties and four promising cassava varieties KM568, KM539, KM537, and KM569.**

***Keywords:*** **Cassava varieties; Distinctness, Uniformity, and Stability (DUS) and Value for Cultivation and Use (VCU); progression; Vietnam.**

***Classification number:*** **3.1**

## 1. Introduction

Cassava (*Manihot esculenta* Crantz) emerges as a pivotal crop in the 21st century, serving purposes ranging from food and animal feed to starch processing and biofuel production worldwide. In Vietnam, cassava, alongside rice and corn, occupies a position of primacy in research and development according to the vision of the Government and the Ministry of Agriculture and Rural Development (MARD). This comprehensive article serves as a sequel to the work presented by K. Hoang, et al. (2018) [1] on "Conservation and sustainable development of Vietnamese cassava".

The aim of this review study is to amalgamate the findings of cassava breeding spanning the past five decades, elucidating the lineage of popular cassava varieties alongside promising ones in the ongoing development of Vietnamese cassava varieties from 1975 to the present. In response to requests from CIAT, the MARD, and Phu Yen province, this article encompasses six key sections: 1. Introduction; 2. The current status of cassava in Vietnam; 3. The process of breeding and developing Vietnamese cassava varieties (1975 to date); 4. Promising cassava varieties for the cassava program in Vietnam; 5. Conservation and sustainable development of Vietnamese cassava; and 6. Conclusions. Addressing

*Corresponding author: Email: long.hoang@hcmuaf.edu.vn*

these requests, the article integrates the aforementioned sections to provide further clarity: Identifying the significance of cassava, the current state of cassava cultivation in Vietnam, the history of breeding, breeding methodologies, main cassava varieties with their primary characteristics, recent advancements in cassava breeding, and the latest findings and references for each subgroup.

The sustained effort over nearly five decades has propelled significant advancements in cassava breeding, facilitated by the Vietnam National Cassava Program (VNCP) that connects various academic institutions such as the Nong Lam University - Ho Chi Minh City (NLU), University of Agriculture and Forestry, Hue University (HUAF), Thai Nguyen University of Agriculture and Forestry (TNAF), Hung Loc Agricultural Research Center (HARC), Root Crop Research and Development Centre (RCRDC), Tay Nguyen University (TNU), the One Commune One Product (OCOP) network of provinces, notably Phu Yen provinces, and the more recently established International Laboratory for Cassava Molecular Breeding (ILCMB), a collaborative effort between CIAT, RIKEN, and the Vietnamese Institute of Agricultural Genetics.

Vietnam's cassava production has witnessed remarkable progress in productivity owing to: i) increased breeding efforts and the adoption of new varieties and agricultural techniques; ii) progressively supportive governmental policies; and iii) sustained backing from international organisations, particularly the CIAT, and more recently, Australian Centre for International Agricultural Research (ACIAR).

## 2. The current status of cassava in Vietnam

Vietnamese cassava stands as a remarkable success story today [2]. The current cultivation of cassava in Vietnam spans an area exceeding half a million hectares annually, with exported cassava products valued between 0.8 and 1.2 billion USD [3]. Nationally, cassava has emerged as a significant export crop, offering avenues for increased income, livelihood enhancement, and improved living standards for millions of smallholder farmers.

The yield and total output of cassava in Vietnam have seen significant increases, soaring from 8.35 tons/ha and 1.98 million tons in 2000 to 17.90 tons/ha and 9.74 million tons in 2013, marking a doubling in yield and a fivefold increase in total production [4].

The cassava revolution in Vietnam serves as a distinguished model in Asia and globally, characterised by the selection of high-starch-yielding cassava varieties, widespread adoption of sustainable farming practices, and advancements in production, post-harvest processing, value chain enhancement, and market expansion [5].

The pivotal role of selecting Vietnamese cassava varieties cannot be overstated. Millions of Vietnamese farming households have reaped the benefits of improved cassava varieties, experiencing heightened productivity, increased profits, and enhanced livelihoods. The project on the "Conservation and sustainable development of cassava in Vietnam" has yielded notable success, substantiated by testing and demonstration results in Tay Ninh, Phu Yen, Dak Lak, and Dong Nai provinces, where farmers employing superior cassava varieties and appropriate intensive farming techniques have witnessed a surge in cassava yield from 8.5 tons/ha in 2000 to over 36.0 tons/ha on a large scale today, representing a substantial increase in yield and total output. The history of cassava breeding in Vietnam, methods of cassava multiplication, exchanges of cassava genetic resources between VNCP & CIAT, and the achievements and lessons from Vietnam's cassava revolution are encapsulated in the article "Conservation and sustainable development of cassava in Vietnam" by K. Hoang, et al. (2018) [1]. The collaborative efforts of VNCP, Phu Yen province, NLU, and the broader connected community bode well for the future of developing Vietnamese cassava varieties.

The surge in productivity, output, and economic efficiency of Vietnamese cassava has coincided with the emergence and spread of cassava witches' broom disease caused by *Phytoplasma* sp. (CWBD) on heavily infected cassava variety KM94 and Sri Lanka Cassava Mosaic virus disease on heavily infected cassava variety HLS11, inflicting serious damage in 17 provinces [6]. Improving and upgrading the most popular cassava varieties with high starch yield and resistance to pests and diseases stands as an effective solution to sustain and enhance cassava production [7].

In 2022, cassava production in Vietnam encompassed an area of 528.0 thousand hectares, yielding an average of 20.3 tons/ha of fresh roots, resulting in a total output of 10.7 million tons [8]. The five primary cassava-growing regions of Vietnam are: 1) The Central Highlands region, comprising 172.5 thousand hectares of cassava, accounting for 32.7% of the total cassava

area, with focal points in Gia Lai (81.0 thousand hectares), Dak Lak (45.0 thousand hectares), and Kon Tum (38.8 thousand hectares); 2) The South Central Coast region, encompassing 102.0 thousand hectares of cassava, accounting for 19.3% of the total cassava area, with major concentrations in Phu Yen (29.5 thousand hectares), Binh Thuan (28.0 thousand hectares), Quang Ngai (17.0 thousand hectares), and Quang Nam (10.0 thousand hectares); 3) The Southeast region, hosting 92.8 thousand hectares of cassava, accounting for 17.6% of the total cassava area, with significant presence in Tay Ninh (59.0 thousand hectares) and Dong Nai (17.0 thousand hectares); 4) The Northern midlands and mountains, with 99.3 thousand hectares of cassava, accounting for 18.9% of the total cassava area, scattered across mountainous provinces including Son La, Yen Bai, and Hoa Binh; and 5) The North Central region, with 53.0 thousand hectares of cassava, comprising 10% of the total cassava area, predominantly concentrated in Nghe An, Thanh Hoa, and Quang Tri (12-13 thousand hectares per province) [9].

Presently, selecting cassava varieties with high starch yield and disease resistance and implementing a suitable and effective cassava cultivation model like the 10T model for Vietnamese cassava varieties such as KM568, KM539, KM537, KM569, and KM94 remain crucial for maintenance and development. Farmers now prefer disease-resistant promising cassava varieties like KM568, KM539 (an excellent improved version of the imported CIAT cassava variety C39), KM537, KM569, and HN1 (originally known as TMEB419), alongside popular cassava varieties such as KM440, KM419, KM94, KM7, STB1, KM414, KM98-7, KM140, KM98-5, and KM98-1. The remarkable outcomes of VCU and DUS tests and large-scale demonstrations in farmers' fields serve as compelling evidence for the sustainable development of the cassava programme. Notably, the enhancement and improvement of cassava varieties KM419, KM440, and KM539 in Phu Yen province reflect significant achievements [10, 11]. The availability of superior cassava varieties and the '10T cassava farming techniques model' have paved the way for the application and expansion of the 'Sustainable agricultural and rural development strategy for the period 2021-2030' [12], alongside national target programmes and the VAEM & TNU VSTA initiative.

## 3. The process of breeding and developing Vietnamese cassava varieties (1975 to date)

The evolution of Vietnamese cassava varieties (1975 - present) has traversed six stages, marked by five waves of structural transformation in cassava varieties, aligning with target orientations amidst diverse farming conditions and market demands. This progression entails the cultivation of 16 popular cassava varieties and 4 elite promising varieties: KM568, KM569, KM539, and KM569 (refer to Fig. 1 and Table 1).

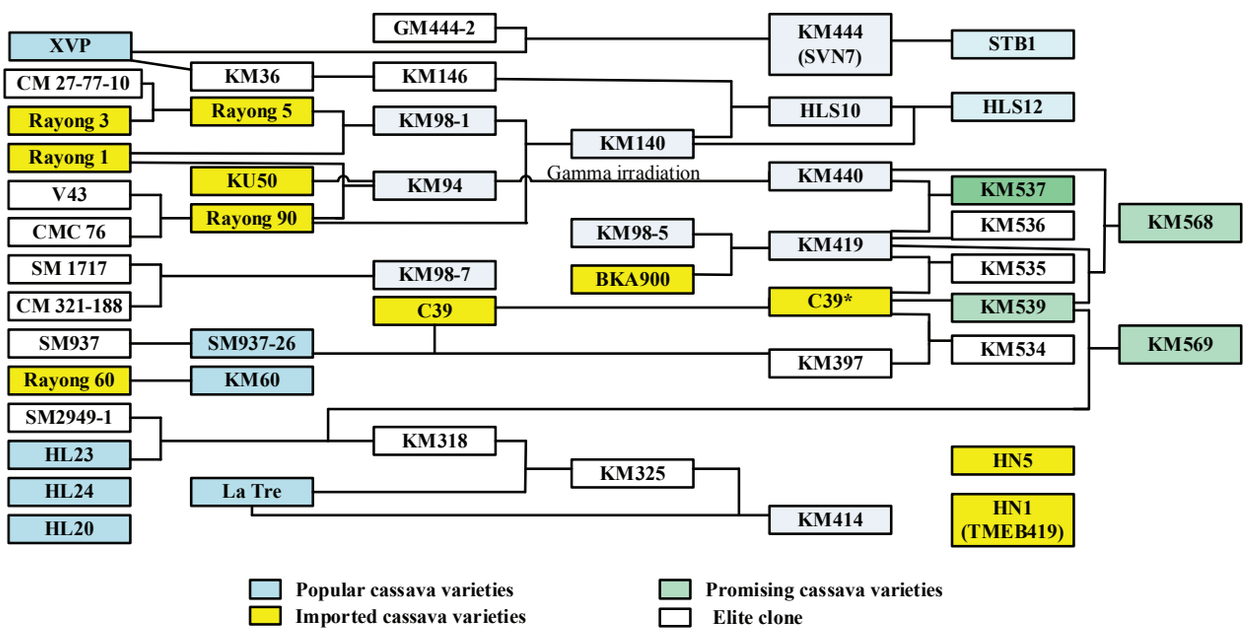


**Fig. 1. Flowchart illustrating the progression of Vietnamese cassava varieties from 1975 to the present.**

*Period 1975-1990:* The focus during this phase was on collecting and conserving genetic resources of root crops, selecting high-yield, quality cassava varieties suitable for both food and animal feed purposes. Notably, the HL23 cassava variety emerged as a pivotal production staple. Cassava cultivation extended across all ecological regions of the country except for the rice-growing lowlands in the Mekong delta and Red river delta. Productivity during this era ranged from 6 to 8 tons/ha [13]. Popular varieties included Gon, H34, and Xanh Vinh Phu before 1985, transitioning to HL23, HL20, and HL24 between 1986 and 1990. These selections, predominantly from the Hung Loc Agricultural Experimental Research Center, covered an area of 70,000-80,000 hectares, particularly in southern provinces, boasting yields exceeding 16.5 tons/ha [14].

The HL23 variety, renowned for its delectable taste, exhibited a yield of 29.8 tons/ha and starch content of 25.3% [15]. This period also marked the inception of the strategy for the "Conservation and sustainable development of cassava in Vietnam" [1, 16, 17], led by the VNCP connecting HARC (under Institute of Agricultural Science for Southern Vietnam), Department of Agronomy, NLU, RCRDC (under Vietnam Academy of Agricultural Sciences (VAAS) with international organizations such as CIAT, IDRC, Viet Nga, and Viet Tiep aimed at collecting, evaluating, using and preserving genetic resources of tubers and biodiversity [18, 19]. Similarly, VNCP collaborated with VEDAN and Ajinomoto to undertake a research and development program for cassava production, processing, and consumption markets.

*Period 1991-2000:* Characterised by an in-depth exploration of cassava production, processing, and market dynamics, this phase witnessed the selection of varieties with high starch yield and broad adaptability, tailored for starch and cassava chip export. Key varieties during this period included KM94, KM98-1, and SM937-26. The collaboration between VNCP and CIAT since 1988 brought about a notable transformation in the Vietnamese cassava program, leading to a robust national initiative for production, processing, and market expansion, as underscored in the Vietnam Cassava Strategy Workshop in Hanoi [20].

Some cassava varieties imported from CIAT Thailand, such as Rayong 60 and KU50, exhibited high starch yield through the cassava variety evaluation network. Further selection in Vietnam resulted in KM60 and KM94, respectively, which received certification from MARD in 1992 and 1995 [21-24]. Additionally, the selection and development of cassava variety SM937-26, derived from hybrid cassava seeds imported from CIAT Colombia and CIAT Thailand, occurred during this period [21, 22, 25-27].

*Cassava variety KM94 (KU50)* boasted a fresh tuber yield of 33.0 tons/ha with a starch content of 28.7%, exhibiting a wide adaptability spectrum suitable for Vietnam's cassava starch processing industry. KM94 was complemented by varieties KM98-1 and SM937-26.

*Cassava variety KM98-1,* with its high starch yield, was a versatile variety with a short growth duration, suitable for fresh consumption. It served as a valuable supplement and replacement for cassava varieties HL23, HL24, HL20, and Xanh Vinh Phu, which were renowned for their delicious taste and suitability for both fresh consumption and animal feed during this period.

*Cassava variety SM937-26,* characterised by high dry cassava chip yield, starch yield, drought tolerance, and disease resistance, underwent continuous improvement and upgrading from this period onwards. It eventually evolved into cassava variety KM7, an elite version of KM505, KM397, and KM937-26 x BKA900. The breeding and selection of this elite line from cassava crosses were conducted in Vietnam, following the method of selecting cassava lines from double haploid hybrid using CIAT technique [28-32]. Backcrossing, selective breeding, and sexual hybridisation were continuously implemented, resulting in cassava variety KM534 (KM397 x KM539). The results of multi-site testing, pilot model building, multiplication, and dissemination of cassava variety KM937-26 over many seasons were documented by numerous authors [33-37].

*Cassava variety KM98-1:* The method of pedigree selection was applied to develop KM98-1 from the hybrid of Rayong 1 x Rayong 5 in Vietnam [38-40]. The KM98-1 shares the same genetic pedigree as the widely popular Rayong 72 cassava variety in Thailand. In Cambodia, KM98-1, also known as cassava variety 81, thrived and showed promising results in Vietnam, Laos, and Myanmar. Another improved version of KM98-1, known as NA1 cassava variety in Vietnam, emerged

from the cooperation between Vietnam, Laos, Cambodia in transferring cassava seed technology advances and CIAT's Asian cassava program. At the 2000 Technical Innovation Contest, KM98-1, together with KM98-5, received the gold medal for Vietnamese brand, awarded by the People's Committee of Can Tho city and the Organising Committee of the Can Tho International Fair [1].

*Period 2001-2010:* Vietnam witnessed the emergence of a second wave of breakthrough cassava varieties, characterised by the crossing and selection to develop varieties with high starch yield, short growth duration, and suitability for diverse ecological regions. The primary aim was to meet the demands of starch and cassava chip production. Prominent varieties during this period included KM94, KM140, KM98-5, KM98-7, KM98-1, and KM397 (an improved version of SM937-26). Supported by the MARD from 2001 to 2005, the VNCP led a project on the development of cassava varieties. This initiative, chaired by the Institute of Agricultural Science for Southern Vietnam, closely collaborated with the CIAT Nippon project, VEDAN company, and cassava processing factories. The project's primary objective was to propagate key cassava varieties for starch and cassava chip production and distribute them to cassava-growing provinces nationwide.

A summary of cassava achievements and the three main lessons learned 6M, 10T, and 1F, focusing on the conservation and sustainable development of cassava in Vietnam, highlighted the preservation of rare genetic resources and the introduction and development of cassava lines from target-oriented hybrids. These efforts linked Vietnam's agricultural research, extension, and teaching system with a network of farmers, processors, consumers, and management businesses, facilitating comprehensive development [25, 26, 41]. The breakthrough achievements of this period included the selection and development of cassava varieties with an ideal plant shape, compact canopy, few branches, high harvest index, increased planting density, and superior fresh tuber yield and starch content. These varieties exhibited a shorter growth duration compared to the KM94 cassava variety, making them suitable for various ecological zones. Consequently, Vietnamese cassava varieties boasted super starchy tubers, compact canopies, short growth durations, and enhanced disease resistance [42].

In the northern region, 70-90% of farmers cultivated popular cassava varieties such as KM94, KM98-7, La Tre, KM95-3, and Xanh Vinh Phu during this period. These varieties were favoured for their high starch yield and versatility, making them suitable for local farming conditions. Farmers preferred readily available varieties for self-multiplication [43-45].

In the central region, 80-100% of farmers grew popular cassava varieties like KM94, KM140, KM98-5, KM98-1, and SM937-26 due to their high starch yield. Cassava variety KM98-1 was identified as multi-purpose, possessing high starch yield, low HCN content, and suitability for both industrial and human consumption [46-49].

In the southern and central highlands, 80-100% of farmers cultivated the main commercial cassava varieties, including KM94, KM140, KM98-5, KM98-1, and SM937-26. Among these, KM140 and KM98-5 were particularly popular during this period [50-53].

Cassava variety KM94 demonstrated widespread adaptability as a result of the "Developing cassava varieties" project supported by MARD. By 2010, it covered 75.5% of the nationwide cassava area. Following KM94 were KM140, KM98-5, KM98-1, SM937-26, KM98-7, HL23, and Xanh Vinh Phu, accounting for 5.40, 4.50, 3.24, 2.70, 1.44, 1.08, 2.70, and 3.40% of the total cassava area, respectively [54].

*KM140, KM98-7, KM98-5, KM98-1, SM937-26, and KM94,* the main cassava varieties, were widely adopted by numerous cassava producers, processors, and consumers. The KM140 cassava variety, renowned for its high starch yield, clinched the first prize at the Vifotec National Technical Innovation Contest, Government of Vietnam 2010, held at the Hanoi Opera House on January 19, 2010 [51, 55].

*Period 2011-2015:* Vietnamese cassava varieties entered a third-wave breakthrough, focusing on research and development for starch and biofuel production [56]. Efforts centred on selecting and transferring cassava varieties with high starch yield, ideal canopy shapes, resistance to major pests and diseases, and suitability for diverse farming conditions. However, this period also witnessed the emergence and spread of various diseases, such as cassava witches' broom disease (CWBD) caused by *Phytoplasma* in 2009 and caused serious damage to cassava variety KM94 in Quang Ngai [57]. In 2011,

Vietnamese cassava infected, cassava bacterial blight (CBB) in 2011, red spiders and pink mealy bugs in 2013, and cassava mosaic disease (CMD) in 2017. The structure of Vietnamese cassava varieties suitable for this period was KM419, KM94, KM440, KM140, KM397 (=KM505), KM98-5, KM98-1, KM98-7, KM444 (STB1), KM414 (KM325 x La Tre).

During this period, the primary cassava variety KM419 (BKA900 x KM98-5) and KM440 (mutant KM94) integrated a super starch gene and exhibited resistance to cassava bacterial blight disease (CBB), cassava witches' broom disease (CWBD), and were less susceptible to red spider mites, pink mealy bugs, and tuber rot disease. They boasted a compact canopy, few branches, and produced uniform and aesthetically pleasing tubers. Consequently, numerous proficient farmers within the VNCP network swiftly propagated these varieties, leading to a rapid transformation in the cassava variety structure in southern provinces [1, 58-61]. KM419, the primary cassava variety, and the popular KM440 accounted for nearly 85% of the cassava cultivation area in Phu Yen province. This resulted in the average cassava yield increasing from 17 tons/ha in 2016 to over 23.5 tons/ha in 2018, contributing more than 293.25 billion VND to the province's economy [62].

Cassava varieties KM101, HLS10, HLS11, HLS12, KM21-12, and Sa06 were imported, selected, and introduced into production concurrently during this phase [63-66]. According to K.C. Tran (2012) [50], three cassava varieties, namely KM140, KM98-5, and KM94, had become the primary cassava varieties in the Southeast and Central Highlands ecological regions. Subsequently, the VNCP initiated a state-level project to evaluate the most promising national cassava varieties across ecological regions throughout the country [67, 68]). The findings identified the most prominent cassava varieties for various regions, including 1) Northern midland and mountainous regions: KM444 (also known as HL2004-28 or SVN7); KM414 (also known as HL2004-32 or SVN8); KM419 (also known as SVN5); 2) North Central region: KM444, KM419, KM414; 3) South Central region: KM444, OMR35-8 (also known as SVN9); GM155-7 (SVN10); 4) Southeast region includes KM419, KM444, KM414. KM419, in particular, was widely embraced by farmers due to its consistently high yield, excellent pest resistance, short growth duration, and ideal plant shape [1, 58].

*Period 2016-2020:* Marked a significant breakthrough in Vietnamese cassava varieties, characterised by the selection of varieties with high starch yield, resistance to major pests and diseases, and suitability for cultivation in diverse ecological regions. The cassava revolution in Vietnam gained international recognition at the Global Cassava Conference in Nanning, China. Five new Vietnamese cassava varieties were unveiled at this conference: KM419, KM440, KM444, KM414, and KM397 [5, 69]. However, the emergence of cassava leaf mosaic virus disease (CMD) in Tay Ninh in May 2017 led to a crisis affecting 17 provinces in the Southeast, South Central Coast, and North Central regions [6]. Following the CMD outbreak, popular cassava varieties for adaptive production included KM440, KM419, KM94, KM140, KM98-5, KM7 (also known as KM505 or KM397 or improved SM937-26), STB1 (KM444), KM414 (KM325 x La Tre), KM98-7, KM98-1, and HN1. According to K. Hoang, et al. (2018) [1], H.H. Le, et al. (2016) [5], and M.T.T. Nguyen (2017) [70], the five new cassava varieties KM419, KM440, KM444, KM397, and KM414 showed the most promise among Vietnamese cassava varieties during this period. Notably, KM419 emerged as the primary cassava variety widely cultivated in provinces such as Tay Ninh, Dong Nai, Dak Lak, and Phu Yen.

*Cassava variety KM414,* originating from testing cassava variety KM101, demonstrated high yield and resistance to some pests and diseases, particularly suited to the Southeast and Central Highlands regions [71]. However, it exhibited the drawback of yellow flesh and slight susceptibility to cassava brown leaf spot disease, bacterial blight of cassava, and red spider mites. KM101, initially named CMR 29-56-101 and imported from Thailand. According to K. Hoang, et al. (2006b) [26], KM101 cassava variety was imported from 3020 + 1982 cassava seeds from CIAT Thailand (import ticket number No. 28885), and underwent breeding by the NLU research team. It was crossed with La Tre to create KM325, later backcrossed to produce KM414 with white flesh, albeit with some susceptibility to diseases, alongside the widely adapted KM98-7 variety in the North (Fig. 1).

*Cassava variety STB1:* Evaluation results by T.D. Pham, et al. (2019) [72] highlighted STB1's high yield potential, ranging from 39.0 to 48.9 tons/ha, with increased productivity compared to the control variety KM94. Starch content in STB1 reached from 26.01% to

29.82%, making it highly regarded locally for raw material production in cassava factories. However, preferences varied regionally, with STB1 and KM7 favoured in the South-Central cassava region [73, 74], while STB1 and KM414 were preferred in the North Central Coast and Northern midland mountain areas [67, 68].

*Period 2021 - present:* The Vietnamese cassava variety programme has achieved a breakthrough in the fifth wave, focusing on selecting the main commercial cassava varieties in Vietnam to attain high starch yield, resistance to major pests and diseases, and an ideal cassava plant shape suitable for diverse ecological regions. T.T.K. Nguyen, et al. (2021) [75] highlight the significance of developing cassava varieties resistant to viruses as a key strategy in controlling CMD. The study suggests that resistant varieties can be developed using genetic technologies such as RNAi and gene editing, or by utilising naturally resistant gene sources, with the latter being deemed the most promising solution. Meanwhile, V.A. Nguyen, et al. (2021) [76] published descriptions and identified some popular cassava varieties in Vietnam. In another study, A.N. Le, et al. (2021) [77] determined the biological characteristics of the whitefly (*Bemisia tabaci*) on the four cassava cultivars KM419, H34, KM98-7 and KM94 under laboratory conditions at 30°C and 70% relative humidity.

*Cassava variety HN1 (TMEB419)* gained attention at the Conference on the current status and development orientation of cassava in Vietnam in October 2023. According to X. Zhang, et al. (2023) [78], organisations including AGI, CIAT, JICA, and FAO agreed to prioritise the rapid multiplication of six CMD-resistant cassava varieties, including HN1, HN3, HN5, HN36, HN80, and HN97. Originating from TMEB419, HN1 is regarded as the best-imported cassava variety in the CMD-resistant cassava variety source, boasting a standard CMD-resistant disease score level of 1, a fresh tuber yield of 42.5 tons/ha, and a starch content of 27.5%. However, it exhibits lower adaptability compared to common cassava varieties, along with a slightly lower starch content and taller stature [79].

*Cassava varieties Sa06, 13Sa05 and BK* have shown promise in Northern Vietnam and Nghe An province. According to H.T.T. Pham, et al. (2017, 2018, 2021) [80-82], Sa06 demonstrated high quality after selection and development efforts, while 13Sa05 and BK offer short growth durations and high yields, suitable for early harvesting to avoid floods.

*Cassava variety HL S12,* H.H. Nguyen, et al. (2021) [83] selected and tested cassava variety HL-S12 originating from the cross combination HL-S10 × KM140 and evaluated this variety at Hung Loc Center from 2014 to 2021. The results showed that HL-S12 was quite resistant to cassava witches' broom disease, red spider, and mosaic leaf disease. Productivity varied from 36.02-42.34 tons/ha; starch content reached 26.1-27.1%, starch yield ranged from 9.42-12.64 tons/ha, which is an increase of 7.5-13.5% compared to control (KM140) and by 4.5-13.4% compared to KM94 [83]. Large-scale testing of cassava variety HL-S12 from 2019 to 2020 in the Southeast and Central Highlands regions demonstrated a 2-year yield from 34.6-47.7 tons/ha and selling price ranges from 1,900-2,200 VND/kg depending on locality. Profits reached from 33.4-72.5 million VND/ha, an increase of 47-134% compared to the control variety.

*Cassava variety KM7 and KM140:* According to P.T. Nguyen (2021) [74], the development of technical measures for cultivating high-yield cassava varieties in Khanh Vinh and Khanh Hoa identified two cassava varieties SM937-26 and KM140 as two economically effective cassava varieties, suitable for Khanh Hoa area. Fresh tuber yield of the cassava variety SM937-26 (New name as KM7) was 43.1-45.7 tons/ha, 27.3-50.7% higher than the control KM94, with starch content of 26.2-27.5%. This variety produced a starch yield ranging from 11.3-12.6 tons/ha and demonstrated good lodging resistance and drought tolerance, with slight susceptibility to cassava witches' broom disease. Cassava variety KM140 had a yield of 43.0-47.2 tons/ha, 31.5-50.3% higher than the control KM94, a starch content 25.5-26.1%, and a starch yield ranges from 11.2-12.0 tons/ha.

*Cassava varieties KM568, KM537, KM539, KM569, KM94** are subject to regulations governing the DUS and VCU testing. These regulations align with the circular governing the testing and recognition of new agricultural plant varieties issued by the MARD, as stipulated in the Law on Cultivation No.31/2018/QH14, effective January 1, 2020. The purpose of these regulations is to prevent the premature propagation of cassava varieties that

have not undergone rigorous testing and lack sufficient self-declaration information. This measure aims to mitigate potential damage to the investments made by farmers, businesses, and stakeholders across the cassava production, processing, and business value chain [84].

M.T.T. Nguyen, et al. (2021, 2024) [10, 11] proposed solutions for sustainable cassava development in the period 2021-2025 in Phu Yen province recommend a selection of Vietnamese cassava varieties. These include KM568, KM539, KM537, KM569, KM94*, HN1, KM440, KM419, KM7, STB1, KM414, KM98-7, KM140, and KM98-1. Among these, cassava varieties KM568, KM539, and KM537 exhibit high starch yield and resistance to major pests and diseases, coupled with a short growth duration. Notably, the Phu Yen yellow cassava variety, KM569, is particularly esteemed for its taste. These four new cassava varieties hold potential to address the current production requirements of the Southeast region, the Central Highlands region, and the South-Central Coast cassava region. The existing structure of Vietnamese cassava varieties stems from a robust cassava genetic foundation, representing a primary solution for sustaining and advancing cassava cultivation.

## 4. Promising cassava varieties for the cassava program in Vietnam

H. Ceballos, et al. (2021) [92] reviewed the results of global cassava breeding over the past 50 years. Vietnam's cassava breeding program consulted CIAT's cassava breeding achievements and lessons from advanced countries to choose the appropriate method for the VNCP.

**Table 1. Progress of Vietnamese cassava varieties 1975-present with 16 popular cassava varieties and 4 promising cassava varieties KM568, KM537, KM539, KM569.**

| Varieties/ author/year of certification | Parents/genetic genealogy | Growth duration (month) | Fresh root yield (tons/ha) | Root starch content (%) | Root starch yield (tons/ha) | Harvest index HI (%) |
|---|---|---|---|---|---|---|
| KM568[10] | KM440 x (KM419 x KM539) | 8-10 | 54.0 | 28.4 | 15.3 | 65 |
| KM537[10] | (KM419 x KM539) x KM440 | 8-11 | 51.3 | 28.3 | 14.6 | 64 |
| KM539[10] | C39* select C39 from CIAT | 8-10 | 45.9 | 27.9 | 12.8 | 61 |
| KM569[10] | (SM2949-1 x HL23) x KM539 | 7-9 | 36.0 | 26.3 | 9.5 | 63 |
| HN1[7a, 7b] | TMEB419 | 8-10 | 42.5 | 27.5 | 11.7 | 61 |
| KM419[5, 6, 9, 10] | BKA900 x KM98-5 | 8-10 | 49.6 | 28.9 | 13.9 | 64 |
| KM440[5, 6, 9, 10] | KM94 mutation | 8-10 | 48.7 | 28.7 | 12.3 | 61 |
| KM397[5, 6, 9, 10] | SM937-26 x BKA900 | 8-10 | 45.6 | 28.4 | 11.8 | 63 |
| KM444[5, 6, 9, 10] | XVP x GM444-2 | 9-11 | 43.8 | 27.9 | 10.4 | 63 |
| KM414[5, 6, 9, 10] | KM325 x La Tre | 8-10 | 41.4 | 27.8 | 11.3 | 62 |
| KM7[8, 10] | SM937-26 x BKA900 | 8-10 | 40.0 | 27.9 | 10.3 | 65 |
| HLS12[4] | HL-S10 x KM140 | 8-10 | 38.4 | 26.6 | 9.6 | 62 |
| KM101[4] | CMR 29-56-101 | 8-10 | 45.0 | 27.7 | 12.5 | 64 |
| KM140[2] | (R5xR1) x KM36 | 8-10 | 39.6 | 28.1 | 10.3 | 67 |
| KM98-7[3] | SM1717 x CM321-188 | 9-11 | 31.9 | 27.3 | 9.3 | 65 |
| KM98-5[2] | R90 x KM98-1 | 8-10 | 34.5 | 28.5 | 9.8 | 63 |
| KM98-1[2] | R1xR5 seed from CIAT | 8-10 | 32.2 | 27.6 | 8.9 | 66 |
| SM937-26[2] | seeds SM937 from CIAT | 8-10 | 32.6 | 28.3 | 9.5 | 64 |
| KM94[2] | KM50 from Thailand | 9-11 | 33.0 | 28.7 | 9.5 | 54 |
| HL23[1] | Local variety | 8-10 | 29.8 | 25.3 | 7.5 | 53 |

Source: (1): [20]; (2): [85]; (3): [27]; (4): [71, 83]; (5): [1]; (6): [5]; (7): [78, 79]; (8): [73, 74]; (9): [86-89]; (10): [10, 11, 70, 90, 91].

**Table 2. Fresh root yield (tons/ha) of ten cassava varieties in eight cassava variety trials in Phu Yen province in 2022-2023.**

| Varieties | Trials of 27 cassava varieties | | DUS experiments with ten cassava varieties | | VCU experiments with ten cassava varieties | | | | Average fresh tuber yield (tons/ha) |
|---|---|---|---|---|---|---|---|---|---|
| | | | | | *Dong Xuan* | | *Song Hinh* | | |
| | *Spring* | *Summer* | *Spring* | *Summer* | *Spring* | *Summer* | *Spring* | *Summer* | |
| KM568 | 54.7 | 52.7 | 55.4$^{a}$ | 50.7$^{a}$ | 55.7$^{a}$ | 51.2$^{a}$ | 58.3$^{a}$ | 53.3$^{a}$ | 54.0 |
| KM569 | 38.5 | 35.8 | 37.5$^{d}$ | 33.6$^{cd}$ | 36.8$^{d}$ | 33.6$^{c}$ | 39.1$^{de}$ | 33.1$^{g}$ | 36.0 |
| KM539 | 48.6 | 43.5 | 47.2$^{abc}$ | 41.5$^{b}$ | 47.5$^{bc}$ | 42.6$^{b}$ | 49.6$^{c}$ | 46.7$^{cd}$ | 45.9 |
| KM440 | 53.7 | 51.9 | 52.6$^{a}$ | 45.9$^{ab}$ | 54.3$^{ab}$ | 47.5$^{ab}$ | 56.3$^{ab}$ | 51.4$^{ab}$ | 51.7 |
| KM419 | 52.9 | 47.7 | 49.5$^{ab}$ | 48.7$^{a}$ | 48.8$^{ab}$ | 46.4$^{ab}$ | 50.6$^{c}$ | 48.2$^{bc}$ | 49.1 |
| KM537 | 55.6 | 47.6 | 53.4$^{a}$ | 48.7$^{a}$ | 55.5$^{a}$ | 49.1$^{a}$ | 52.4$^{bc}$ | 48.1$^{bc}$ | 51.3 |
| KM536 | 52.4 | 45.5 | 51.6$^{a}$ | 47.6$^{a}$ | 51.5$^{ab}$ | 45.8$^{ab}$ | 51.8$^{bc}$ | 43.4$^{de}$ | 48.7 |
| KM535 | 38.9 | 38.7 | 39.8$^{cd}$ | 35.9$^{c}$ | 38.6$^{d}$ | 357$^{c}$ | 42.3$^{d}$ | 38.9$^{ef}$ | 38.6 |
| KM534 | 44.7 | 36.5 | 42.5$^{bcd}$ | 35.4$^{c}$ | 41.3$^{cd}$ | 36.9$^{c}$ | 40.4$^{d}$ | 39.1$^{ef}$ | 39.6 |
| KM94* | 35.8 | 31.2 | 37.6$^{d}$ | 30.5$^{d}$ | 37.5$^{d}$ | 32.5$^{c}$ | 35.4$^{e}$ | 34.7$^{fg}$ | 34.4 |
| CV (%) | | | 6.88 | 4.48 | 6.23 | 5.56 | 4.26 | 4.23 | |
| F test | | | 13.6** | 47.1** | 20.5** | 25.8** | 44.1** | 42.7** | |

In the same column, numbers with the same letters indicate statistically insignificant differences; ns: the difference is not meaningful; **: meaningful difference α=0.01; TB = Average. Source: [11].

Some promising cassava varieties have been identified and introduced in Tables 2 and 3 after DUS and VCU trials in Vietnam [11].

The goals of the cassava genetic improvement program in Vietnam for the period 2021-2025, with a vision to 2030, are as follows:

1. To increase yield potential, dry matter content, starch content, and resistance to a number of major diseases (mainly CMD and CWBD).

2. To choose a cassava variety with an ideal cassava plant shape: straight plant, 2.5-2.9 m height, few branches, many tubers, uniform, suitable for increased planting density, and capable of early harvesting.

3. To identify high-yielding, key pest-resistant varieties suitable for different agro-ecological zones and promote their integration into smallholder farming systems.

4. To select the best key commercial cassava varieties to serve starch production, processing, and exportation. Therefore, the selection, breeding, and testing of DUS and VCU [93] helped determine selection and breeding strategies to increase cassava productivity, agricultural digital transformation, and to build the Vietnamese cassava brand.

5. There are many new cassava varieties that have been bred and selected to be suitable for human food, dining, and ecotourism purposes, delicious, rich in carotene, yield >25 tons/ha, not bitter, low HCN content <5 mg/100 g fresh tubers.

Thanks to the financial support of the Phu Yen Province, research and breeding of cassava varieties with high starch yield, resistance to major pests and diseases, and suitability to the production conditions of Phu Yen province and other ecological regions met an urgent demand from farmers. The objectives were to select and create cassava varieties with high starch yield (at least 10% higher than controls KM419 and KM94), resistant to major pests and diseases, with a grade 1-2 disease score for CMD, and cassava witches' broom disease (CWBD), under production conditions in Phu Yen province. The research method was carried out according to VNCP & CIAT standards "Technological process of hybrid cassava selection and breeding". The results identified three promising cassava varieties KM568, KM539, and KM537 (Table 3).

**Table 3. Characteristics of cassava varieties KM568, KM539, KM537, and KM440, KM419, KM94 as checks.**

| QCVN and UPOV criteria for evaluating cassava varieties | KM568[6] | KM539[5] | KM537 | KM440[3] | KM419[2] | KM94*[1.4] |
|---|---|---|---|---|---|---|
| Growing duration (month) | 8-10 | 8-11 | 8-11 | 8-10 | 8-10 | 9-11 |
| Fresh tuber yield (tons/ha) | 54.0 | 45.9 | 51.3 | 51.7 | 49.1 | 34.4 |
| Yield potential (tons/ha) | 70.0 | 50.0 | 50.0 | 60.0 | 60.0 | 40.0 |
| Dry matter ratio (%) | 40.0 | 39.1 | 39.9 | 39.6 | 40.3 | 40.5 |
| Starch content (%) | 28.4 | 27.9 | 28.5 | 28.3 | 28.8 | 28.6 |
| Starch yield (tons/ha) | 15.1 | 12.4 | 14.6 | 14.0 | 14.1 | 9.8 |
| Productivity of dried chips (tons/ha) | 21.6 | 17.9 | 20.5 | 20.4 | 19.8 | 13.9 |
| Main pest resistance | | | | | | |
| + Leaf mosaic virus CMD | 1.5 | 1.0 | 1.5 | 2.0 | 3.0 | 3.0 |
| + Cassava witches' broom disease (CWBD) | 1.0 | 1.0 | 1.0 | 1.0 | 1.0 | 3.0 |
| + Leaf blight disease (CBB) | 2.0 | 2.0 | 2.0 | 2.0 | 2.5 | 2.5 |
| + Root rot disease | 2.0 | 2.5 | 2.0 | 2.5 | 2.5 | 2.5 |
| + Pink mealy bug | 3.0 | 3.0 | 3.0 | 3.0 | 3.0 | 3.0 |
| + Red spider | 3.0 | 3.5 | 3.5 | 3.0 | 3.0 | 3.0 |
| Characteristics DUS similar to cassava | | | | | | |
| + Plant evaluation score | 10 | 9 | 9 | 10 | 10 | 8 |
| + Root evaluation score | 10 | 9 | 9 | 10 | 10 | 9 |
| + Harvest index (%) | 63 | 61 | 64 | 64 | 61 | 57 |
| + Plant height (m) | 2.3-2.7 | 2.7-3.0 | 2.5-2.9 | 2.3-2.7 | 2.3-2.7 | 2.8-3.5 |
| + Straight and curved plant shape | Straight | Straight | Straight | Straight | Straight | Curved |
| + Degree of branching | Little | Little | Little | Little | Little | Little |
| + Stem colour | Green grey | Green brown | Green brown | Green grey | Green grey | Green brown |
| + Leaf colour | Green purple | Green purple | Green purple | Green purple | Green purple | Purple |
| + Leaf stem colour | Green red | Green red | Green red | Green | Green red | Green |
| + Number of tubers per stem (tubers/root) | 8-14 | 7-12 | 7-12 | 8-14 | 8-14 | 6-11 |
| + Outer skin colour | White grey | Brown grey | Brown grey | White grey | White grey | Brown grey |
| + Flesh colour | Cream | Cream | Cream | Cream | Cream | Cream |
| + Cassava root form | Cylinder | Cylinder | Cylinder | Cylinder | Cylinder | Cylinder |

*KM568,* a hybrid of KM440 x (KM419 x KM539), yielded fresh tubers at 54 tons/ha (56% higher than KM94 and 10% higher than KM419); starch content reached 28.4% at harvest after planting 10 months, resistant to CMD at a level of 1.5 and resistant to CWBD at a level of 1, with less tuber rot, red spider mite, and pink mealy bug; a harvest index of 0.63, uniform tuber size, 8-14 tubers/root, white flesh; with the ideal new plant type shape: straight and compact, erect stems, short internodes, less branching, plant height of 2.3-2.7 m, suitable for high planting density of 14,285 cuttings/ha.

KM539 cassava variety was selected from the original C39 cassava variety imported from CIAT in 2004, which was selected and improved through many cycles, using technologies of double haploid hybrid cassava lines from CIAT & VNCP standards. The fresh tubers yield of KM539 was 45.9 tons/ha (33% higher than KM94 but

7% lower than KM419); starch content reached 27.9% at harvest after planting 10 months, resistant to CMD at a level of 1.0; resistant to CWBD at a level of 1, with less tuber rot, red spider mite, but medium pink mealy bug; a harvest index of 0.61, uniform tuber size, 7-12 tubers/root, white rood flesh; with an ideal new plant type shape: straight, compact, and erect stems, short internodes, less branching, plant height of 2.7-3.0 m, suitable for high planting density of 14,285 cuttings/ha.

According to the DUS technical description of UPOV plant variety protection: variety name, variety author, year of publication: (1) Cassava variety KM94 [21, 85]; (2) Cassava variety KM419 [58]; (3) Cassava variety KM419 and cassava variety KM440 [70]; (4) The cassava variety K94* had been upgraded by sexually crossing KM94 x KM539 to add the CMD and CWBD resistance genes of KM539 into the widely adapted cassava variety KM94; (5) KM539 cassava variety was developed from the original C39 cassava variety imported from CIAT in 2004, and had been trained and upgraded through many cycles, using techniques and technology to create double haploid hybrid cassava lines (doubled haploid). CIAT & VNCP standards [56, 59]; (6) Cassava variety KM568, the cross of KM440 x (KM419x KM539) criteria evaluated and compared with V.A. Nguyen, et al. (2021) [76].

*KM537,* a hybrid of (KM419 x KM539) x KM440, yielded fresh tubers at 51.3 tons/ha (49% higher than KM94 and 4.5% higher than KM419); starch content reached 28.5% at harvest after planting 10 months, resistant to CMD at a level of 1.5; resistant to CWBD at a level of 1, with less tuber rot, red spider mite; a harvest index of 0.64, uniform tuber size, 7-12 tubers/root, white flesh; ideal new plant type shape: straight and compact, erect stems, short internodes, less branching, plant height of 2.5-2.9m, suitable for high planting density of 14,285 cuttings/ha.

*KM569,* the Phu Yen yellow cassava variety, is a cassava variety that is prioritised for preserving delicious fresh cassava gene sources. KM569 cassava variety was selected through 8 cycles with two trials groups of 27 cassava varieties, two DUS trials of 10 cassava varieties, and 4 basic trials of 10 cassava varieties in spring and summer crops on red and grey soils in Phu Yen province (Tables 2 and 3).

## 5. Conservation and sustainable development of Vietnamese cassava

The project titled "Conservation and sustainable development of cassava in Vietnam" yielded significant success, evidenced by trial and demonstration results in Tay Ninh, Dak Lak, Phu Yen, and Dong Nai provinces. Farmers adopting improved technologies and practices saw cassava yields surge from 8.5 tons/ha to 36 tons/ha, marking a more than fourfold increase. This outcome encapsulates the culmination of Vietnamese cassava breeding progress from 1975 to 2016, prioritising the preservation and development of suitable and sustainable cassava varieties [1]. Recent advancements in selecting Vietnamese cassava varieties and implementing ten techniques for intensive cassava farming were showcased through key demonstrations in Tay Ninh, Dak Lak, and Phu Yen provinces, predominantly employing cassava variety KM419. This variety boasted a fresh tuber yield of approximately 42-55 tons/ha (28% higher than KM94), starch content ranging from 28-31%, early maturity, and an ideal tuber and plant shape, suitable for increased planting density [5]. The combined usage of cassava varieties KM419 and KM440, alongside ten cassava intensification techniques, produced remarkable transformational outcomes in trials across the three provinces [86, 94, 95]. Notably, KM419 and KM440 comprised nearly 85% of the cassava area in Phu Yen province in 2019.

The high-yielding KM440 cassava variety, resistant to CMD disease at level 2, underwent traditional crossbreeding with the elite clone of (KM419 x KM539) - a high-yield, CMD-resistant variety at level 1. Subsequently, line selection was conducted using the pedigree method to identify cassava varieties with high starch yield, pest and disease resistance, short growth duration, and optimal plant shape. This approach presents a feasible and effective solution for sustainable cassava development [10]. KM440 and KM419 currently account for 54% of the cassava area in Tay Ninh and over 60% in Dak Lak province while awaiting the conversion of more disease-resistant cassava varieties.

The project "Research on developing cassava varieties with high starch yield, resistance to major pests and diseases, suitable for production conditions in Phu Yen province" has expanded its research scope to address

the needs of impoverished communities in challenging areas, characterised by indigenous minority groups and unique farming practices. The adoption of promising cassava varieties KM568, KM539, KM537, and KM569, coupled with the establishment of an efficient 10T cassava cultivation model, emerges as a key solution to preserve and develop sustainable cassava programs in Phu Yen province. In addition to the promising cassava varieties such as KM568, KM539, and KM537, which offer high starch yield and resistance to CMD leaf mosaic disease, Vietnam's cassava program today must focus on preserving and disseminating the Phu Yen yellow cassava variety KM569. The hybridisation of cassava varieties at CIAT, seed hybridisation, and selection in Vietnam are illustrated in Fig. 1, Tables 1-3 [11].

The Phu Yen yellow cassava variety KM569, a hybrid of SM2949-1 x HL23 x KM539, is the outcome of sexual hybridisation between the yellow cassava variety developed by H. Ceballos (2018) [28] (SM2949-1 x HL23) and cassava variety KM539 under the Phu Yen cassava project [11]. The hybrid cross SM2949-1 x HL23 involved backcrossing the SM2949-1 cassava variety, renowned for its delightful fresh taste, with the Vietnamese cassava variety HL23. The selected cassava variety HL23, with the CIAT conservation variety code of HMC1, yielded 29.8 tons/ha with a starch content of 25.3% [15]. KM569 cassava exhibits excellent boiling quality, with orange-yellow flesh, a fresh tuber yield of 36 tons/ha, and a starch content of 26.3%. It is resistant to CMD virus leaf mosaic disease at level 1.5, resistant to CWBD cassava witches broom disease at level 1, and shows resistance against major pests and diseases affecting cassava. This variety boasts an ideal cassava plant shape, with a harvest index of 61-63%, uniformly large tubers, 6-11 tubers per root, a smooth tuber shape, straight plant canopy, a plant height of 2.7-2.9 m, with 1.5-2.3 plants per bush, minimal branching, and suitability for high planting density of 14,500 cuttings/ha.

The provincial science and technology project "Research on developing cassava varieties with high starch yield, resistance to major pests and diseases, suitable for production conditions in Phu Yen province" has garnered attention from agricultural industries, households engaged in cassava cultivation, and has opened up numerous prospects for the Phu Yen cassava program [96, 97].

Based on the aforementioned results, five critical issues require special attention in current cassava production in Vietnam:

1. Cassava varieties with high starch yield, resistant to main pests CMD, CWBD, suitable for local production conditions.

2. Ten techniques for intensive cassava farming (10T).

3. Building gardens to develop lines from the most elite hybrid cassava combinations.

4. Applying technology to improve the agricultural value chain, especially cassava varieties and raw material areas, and communication to connect markets.

5. Developing appropriate and sustainable cassava production and consumption systems.

The ten techniques for intensive cassava farming (10T) encompass:

1. Utilising the best cassava cuttings of the most suitable cassava variety.

2. Identifying the optimal planting and harvest times to achieve maximum starch yield and economic efficiency.

3. Applying NPK fertiliser combined with microbial organic fertiliser and manure to enhance soil fertility and increase productivity.

4. Determining the optimal planting density for the best cassava varieties and suitable soil types.

5. Implementing IPM integrated control measures for pest-resistant cassava varieties.

6. Intercropping cassava with peanuts and legumes, planting cover crops with beans, and rotating crops suitable for the locality.

7. Implementing weed control measures, including timely weeding, herbicide application, mulching, and appropriate crop rotation.

8. Employing suitable land preparation techniques for cassava cultivation to protect soil fertility against erosion.

9. Developing a water management system for cassava cultivation.

10. Providing training on effective and appropriate cassava production, processing, and consumption value chains.

The cassava industry currently faces an imbalance between raw materials and processing products. Existing cassava raw material areas fail to meet factory requirements. Cassava and cassava product exports have exceeded 1 billion USD, with China being the primary consumer market [98]. While Vietnam's cassava selection and breeding technology connects OCOP with the new rural program, the production, processing, and consumption chain remains inadequate, resulting in a limited range of deeply processed products. Preserving and developing suitable and sustainable cassava varieties present both a new challenge and an opportunity.

## 6. Conclusions

Vietnamese cassava progression (1975 - present) has evolved through six stages, with five waves of restructuring cassava varieties to meet target orientation, farming conditions, and market requirements, resulting in the identification of 16 popular cassava varieties and 4 promising cassava varieties.

The current structure of Vietnam's cassava varieties necessitates the preservation and conservation of popular varieties suited to Vietnam's ecological regions, such as KM440, KM419, KM94, KM7, STB1, KM414, KM98-7, KM140, KM98-5, and KM98-1, while also promoting promising varieties like KM568, KM539, KM537, KM569, and HN1.

Selecting cassava varieties with high starch yield and disease resistance, and establishing a suitable and effective cassava cultivation model of 10T for Vietnamese cassava varieties such as KM568, KM539, KM537, KM569, and KM94 (also known as KU50 or KM94, preserved and developed sustainably through multiple breeding and selection cycles in Vietnam), represents a pivotal solution for conserving and sustaining the development of appropriate cassava programmes.

Despite significant achievements in breeding, selecting, developing, testing, demonstrating, and disseminating new cassava varieties, the cassava variety supply chain still faces numerous shortcomings and new challenges. The current mixture of good and bad cassava varieties leads to production and investment losses.

This literature review, titled "Progress in developing Vietnamese cassava varieties from 1975 to the present," aims to summarise nearly 50 years of progress in enhancing Vietnamese cassava varieties. This compilation of information on Vietnamese cassava genetic resources is vital for the conservation and sustainable development of cassava programmes in Vietnam.

## CRediT author statement

Long Hoang: Conceptualisation, Methodology, Software, Writing - Original draft preparation; Mai T.T. Nguyen: Data curation, Co-Writing - Original draft preparation; Doan N.Q. Nguyen: Visualisation, Investigation; Kim Hoang: Supervision, Reviewing and Editing; Clair Hershey: Software, Validation; Reinhardt Howeler: Methodology, Reviewing and Editing.

## ACKNOWLEDGEMENTS

The authors sincerely thank the People's Committee of Phu Yen province and the Phu Yen Department of Science and Technology for supporting the funding of the Project: "Research on creating cassava varieties with high starch yield, resistance to major pests and diseases, suitable for production conditions in Phu Yen province", together with many colleagues, farmers have wholeheartedly supported the conservation and development of good Vietnamese cassava varieties, participated and contributed to the VNCP and CIAT, as referenced below.

## COMPETING INTERESTS

The authors declare that there is no conflict of interest regarding the publication of this article.

## REFERENCES

[1] K. Hoang, N.T.T. Mai, N.B. Mai, et al. (2018), "Cassava conservation and sustainable development in Vietnam", *Conference on Proceedings 9th Regional Cassava Workshop: Sustainable Cassava Production in Asia for Multiple Uses and for Multiple Markets.* https://www.researchgate.net/publication/322160935_cassava_conservation_and_sustainable_development_in_vietnam, accessed 16 August 2023.

[2] B.B. Bui (2012), "45th anniversary of CIAT: Welcome from Vietnam", *Foodcrops*, http://foodcrops.blogspot.com/2012/09/45th-anniversary-of-founding-of-ciat.html, accessed 16 August 2023.

[3] Vietnam Ministry of Agriculture and Rural Development and People's Committee of Gia Lai province (2022a), "Report on the current status and orientation of the processing market for cassava and cassava products in Vietnam", *Proceedings of The Conference on Current Situation and Development Orientation of Cassava in Vietnam*, pp.53-69 (in Vietnamese).

[4] B.V. Nguyen, K. Hoang, D.Q. Le, et al. (2013), "Vietnam cassava achievement and learnt lessons", *Foodcrops*, http://foodcrops.blogspot.com/2013/09/vietnam-cassava-achievement-and-learnt.html, accessed 16 August 2023.

[5] H.H. Le, K. Hoang, M.T.T. Nguyen, et al. (2016), "The cassava revolution in Vietnam", *Proceedings of The GXAS- GSCRI-GCRI-CAS- CATAS- GCP 21-III Third Scientific Conference of The Global Cassava Partnership for The 21 Century - ISTRC*, https://youtu.be/81aJ5-cGp28, accessed 16 August 2023.

[6] Vietnam Ministry of Agriculture and Rural Development and People's Committee of Gia Lai province (2022b), "Report on the production situation and the direction of prevention of harmful organisms on cassava", *Proceedings of The Conference on The Current Situation and Development Orientation of Cassava in Vietnam*, pp.14-52 (in Vietnamese).

[7] R.H. Howeler, T.M. Aye (2014), *Sustainable Management of Cassava in Asia - From Research to Practice*, CIAT, Cali, Colombia, 168pp.

[8] Vietnam Ministry of Agriculture and Rural Development and People's Committee of Gia Lai province (2022c), "Report on production, processing, and consumption of cassava for the period 2015-2021, orientation and solutions to develop cassava in the coming time", *Proceedings of The Conference on The Current Situation and Development Orientation of Cassava in Vietnam*, pp.1-13 (in Vietnamese).

[9] General Statistics Office of Vietnam (2022), *Statistical Yearbook of Vietnam*, Statistical Publishing House, 1236pp (in Vietnamese).

[10] M.T.T. Nguyen, L. Hoang, D.N.Q. Nguyen, et al. (2021), "Phu Yen cassava solutions for sustainable development", *Conference on Summarising Scientific and Technological Activities in The Period 2016-2020*, https://hoangkimlong.wordpress.com/category/bao-ton-va-phat-trien-san/, accessed 16 August 2023.

[11] M.T.T. Nguyen, L. Hoang, D.N.Q. Nguyen, et al. (2024), "Selection and testing of promising cassava varieties KM568, KM539, KM537 in Phu Yen province", *The Journal of Agriculture and Development*, **23(1)**, pp.1-13, DOI: 10.52997/jad.1.01.2024 (in Vietnamese).

[12] Vietnam Government Portal (2022), *Decision No.150/QD-TTg of The Prime Minister: Approving The Sustainable Agriculture and Rural Development Strategy for The Period 2021 - 2030, Vision to 2050*, https://datafiles.chinhphu.vn/cpp/files/vbpq/2022/01/150-qd-ttg.signed.pdf, accessed 16 August 2023 (in Vietnamese).

[13] K. Hoang, B.V. Pham, R.H. Howeler (2003a), "Status of cassava in Vietnam: Implications for future research and development", *Validation Forum on The Global Cassava Development Strategy*, **3**, pp.103-184, http://www.globalcassavastrategy.net, accessed 16 August 2023.

[14] K. Hoang, Q.N. Tran, T.T. Nguyen (1990), "Select and create sweet potato and cassava varieties suitable for the agricultural ecological regions of southern Vietnam", *Journal of Science, Technology and Economic Management*, **9**, pp.538-544 (in Vietnamese).

[15] N.N. Tran, Q.N. Tran, K. Hoang (1992), "Cassava cultivars and breeding research in Vietnam", *A Benchmark Study on Cassava Production, Processing and Marketing in Vietnam*, pp.49-57 (in Vietnamese).

[16] B.V. Pham, K. Hoang (1992), "Cassava production and research in Vietnam historical review and future direction", *Cassava Breeding, Agronomy and Utilization Research in Asia*, pp.106-123.

[17] Q.V. Mai, K. Hoang (1995), "Contribution of germ bank of field crops for production in Vietnam", *Plant Resources in Vietnam*, pp.114-118 (in Vietnamese).

[18] M. Buresova, K. Hoang, Q.N. Tran (1987), "The economics of winged bean on manioc as natural support under the conditions of South Vietnam", *Agricultura Tropica et Subtropica, Universitas Agriculturae Praga*, **20**, pp.101-114.

[19] N.T. Nguyen, K. Hoang, H.V. Truong, et al. (1995), "Collection of root crops germplasm in Vietnam", *Root Crops Germplasm Research in Vietnam*, pp.1-11.

[20] R.H. Howeler (1992), *A Benchmark Study on Cassava Production, Processing and Marketing in Vietnam, Proceedings of a Workshop Held in Hanoi, Vietnam, Oct 29-31, 1992*, MAFI-CIAT, 290pp.

[21] Q.N. Tran, K. Hoang, T.V. Vo, et al. (1995), "Selection results of the new cassava varieties KM60, KM94, KM95 and SM937-26", *Scientific Council for Agriculture and Rural Development Ministr*y, pp.1-26 (in Vietnamese).

[22] K. Hoang, B.V. Pham (1995), *Cassava Book*, Agricultural Publishing House, Ho Chi Minh City, 70pp (in Vietnamese).

[23] L.T.P. Trinh, N.N. Tran, T.V. Hoang, et al. (1999), "Research results on cassava varietal selection in North Vietnam", *Results of Cassava Research and Extension*, *8th Vietnam Cassava Workshop* (in Vietnamese).

[24] H.H. Nguyen, K. Hoang, R.H. Howeler, et al. (2000), "Developing new varieties of high yield and high starch content, and methods of sustainable cassava cultivation in grey soil of An Vien commune, Thong Nhat district, Dong Nai province", *Proceedings of The 10th Conference on Information of Cassava in Vietnam*, pp.122-133 (in Vietnamese).

[25] K. Hoang, Q.N. Tran, T.T. Nguyen, et al. (2006a), "Final report, breeding of cassava and sweet potatoes suitable for agro-ecological regions of South Vietnam (1981-2006)", *Proceedings of The 90th Establishment Anniversary (1925-2015)*, Institute of Agricultural Sciences in Southern Vietnam (in Vietnamese).

[26] K. Hoang, B.V. Pham, R.H. Howeler, et al. (2006b), "Cassava development project summary (2001-2005)", *Proceedings of The 90th Establishment Anniversary (1925-2015)*, Institute of Agricultural Sciences in Southern Vietnam, pp.53-54.

[27] L.T.P. Trinh, N.N. Tran, T.V. Hoang, et al. (2001), "Results of research on selection and development of new cassava varieties in Northern Vietnam (1996-2000)", *Current Status of Vietnamese Cassava, Development Orientation and Solutions in The Early Years of The 21st Century*, **6**, pp.65-78 (in Vietnamese).

[28] H. Ceballos (2018), "Golden cassava award is awarded to CIAT researcher", *Alliance Bioversity & CIAT*, http://ow.ly/QKPL30jI9Bd, accessed 16 August 2023 (in Spanish).

[29] K. Hoang, T.X. Cao, P. Nguyen, et al. (2009), *Selection of Hybrid Monoclonal Hybrid Cassava Lines Imported from CIAT*, Ministry of Education and Training, 135pp (in Vietnamese).

[30] K. Hoang, N.V. Nguyen, R.H. Howeler, et al. (2008a), "Current situation of cassava in Vietnam and its potential as a biofuel", *Harnessing Water-Use Efficient Bio-Energy Crops for Enhancing Livelihood Opportunities of Smallholder Farmers in Asia, Africa, and Latin America*, 18pp.

[31] K. Hoang, B.V. Nguyen, R.H. Howeler, et al. (2008b), "The current situation of cassava in Vietnam and the selection of cassava doubled haploid (DH) lines derived from CIAT", *Cassava Meeting The Challenges of The New Millennium*, https://cgspace.cgiar.org/items/2bfdb2f3-f1bf-4e49-a4f9-f98c584f1db3, accessed 16 August 2023.

[32] K. Hoang, N.N. Tran, N.V. Nguyen, et al. (2008c), "New progress of cassava research and extension in Vietnam", *Centro Internacional de Agricultura Tropical (CIAT)*, https://cgspace.cgiar.org/items/6cf40093-9c41-4d76-9240-d619da495e6d, accessed 16 August 2023.

[33] K. Hoang, M.D Nguyen (2001a), "Vietnamese cassava, current status, orientation and development solutions in the early years of the 21st century", *The 10th Vietnam Cassava Workshop in Ho Chi Minh City, March 13-14, 2001*, pp.35-50 (in Vietnamese).

[34] K. Hoang, M.D Nguyen (1999a), "Results of research and extension of cassava in Vietnam", *The 8th Vietnam Cassava Workshop in Ho Chi Minh City, March 16-18, 1999*, pp.35-50 (in Vietnamese).

[35] K. Hoang, M.D Nguyen (1998), "Vietnamese cassava in the Asian cassava region, opportunities and challenges before the 21st century", *Information about The 7th Vietnam Cassava Workshop in Ho Chi Minh City, March 2-4, 1998*, 271pp (in Vietnamese).

[36] K. Hoang, M.D Nguyen (1997), "Vietnam cassava program towards the year 2000", *The 6th Vietnam Cassava Workshop in Ho Chi Minh City, March 4-6, 1997*, 272pp (in Vietnamese).

[37] K. Hoang, M.D Nguyen (1996), "New progress in research and extension of Vietnamese cassava", *The 5th Vietnam Cassava Workshop in Ho Chi Minh City, March 5-7, 1996*, 215pp (in Vietnamese).

[38] K. Hoang, K. Kawano, B.V. Pham, et al. (2001b), "Results of selection and development of cassava varieties for agricultural production in Southern Vietnam (1996-2000)", *Vietnamese Cassava, Current Status, Orientation, and Development Solutions in The Early Years of The 21st Century*, pp.35-50 (in Vietnamese).

[39] K. Hoang, K. Kawano, B.V. Pham, et al. (2001c), "Cassava breeding and varietal dissemination in Vietnam from 1975 to 2000", *Cassava's Potential in The 21st Century: Present Situation and Future Research and Development Needs*, pp.147-160, http://danforthcenter.org/iltab/cassavanet, accessed 16 August 2023.

[40] K. Hoang, K. Kawano, U.H. Tran, et al. (1999b), "Result of selection KM98-1 cassava variety", *KM98-1 Variety, Scientific Conference of Agriculture and Rural Development*, 29pp.

[41] B.V. Pham, K. Hoang, N.N. Tran, et al. (2007), "New developments in the cassava sector of Vietnam", *Cassava Research and Development in Asia. Exploring New Opportunities for an Ancient Crop*, pp.25-32, http://www.ciat.cgiar.org/asia-cassava, accessed 16 August 2023.

[42] K. Hoang, N.N. Tran, L.P. Trinh, et al. (2007), "Genetic improvement of cassava in Vietnam: Current status and future approaches", *Cassava Research and Development in Asia*, pp.118-124.

[43] H.V. Nguyen (2006), *Study on The Influence of Ecological Conditions on Yield and Quality of Cassava Varieties*, Doctoral Thesis in Agricultural Science, Thai Nguyen University, 157pp (in Vietnamese).

[44] N.N. Tran (2008), "Evolution of FPR methodologies used and results obtained in Vietnam", *Integrated Cassava-based Cropping Systems in Asia - Working with Farmers to Enhance Adoption of More Sustainable Production Practices*, pp.92-104.

[45] L.T.P. Trinh, H.T. Nguyen, C.H. Dao, et al. (2008), "The results of breeding and developing variety KM98-7", *Agricultural Research Workshop*, Vietnam Academy of Agricultural Science (VAAS), Hanoi.

[46] C.T. Nguyen (2008a), *Research on Some Technical Measures of Cassava Production in The Sustainable Farming System in Hilly Areas of Thua Thien Hue Province*, Doctoral Thesis in Agriculture, Hue University, 153pp (in Vietnamese).

[47] C.T. Nguyen (2008b), "The FPR cassava project in Thua Thien Hue province of Central Vietnam", *Integrated Cassava-based Cropping Systems in Asia - Working with Farmers to Enhance Adoption of More Sustainable Production Practices*, pp.124-129 (in Vietnamese).

[48] C.T. Nguyen, L.T.H. Nguyen, R.H. Howeler, et al. (2007), "Farmer participatory variety trials conducted in Vietnam", *Cassava Research and Development in Asia: Exploring New Opportunities for an Ancient Crop*, pp.363-376.

[49] L.V. Le (2008), *Evaluation of Limiting Factors and Research on Some Technical Measures to Improve Yield and Starch Content of Cassava Variety KM94 in Thua Thien Hue Province*, Doctoral Thesis of University of Agriculture and Forestry, Hue University, 135pp (in Vietnamese).

[50] K.C. Tran (2012), *Evaluation of The Adaptability of Some Cassava Varieties for The Southeast Region and the Central Highlands*, Doctoral Thesis of Agricultural Sciences, Vietnam Institute of Agricultural Sciences, 144pp (in Vietnamese).

[51] K.C. Tran, K. Hoang, V.T. Vo, et al. (2010), "Selective breeding and development of cassava variety KM140", *Proceedings of The 10th National Technical Innovation Contest (VIFOTEC) in Hanoi*, pp.146-149, https://iasvn.org/en/upload/files/000BZPHCF5bai5-cassava%20km140-c_0821104202.pdf, accessed 10 July 2023.

[52] K.C. Tran, K. Hoang, V.T. Vo, et al. (2009), *Results of Breeding and Developing Variety KM98-5*, Report for official recognition by the Scientific Council of the Ministry of Agriculture and Rural Development, Certificate No. 3468/QĐ-BNN-TT, 40pp (in Vietnamese).

[53] K.C. Tran, K. Hoang, V.T. Vo, et al. (2007), "Results of breeding and developing variety KM140", *Recognition Document of Variety KM140, Conference of Ministry of Agriculture and Rural Development*, 45pp (in Vietnamese).

[54] K. Hoang, B.V. Nguyen, L. Hoang, et al. (2010a), "Current situation of cassava in Vietnam", *A New Future for Cassava in Asia: Its Use as Food, Feed, and Fuel to Benefit the Poor*, *Proc. of The 8th Regional Workshop*, Lao PDR, http://ciat-library.ciat.cgiar.org/Articulos_Ciat/biblioteca/A_new_future_for_Cassava_in_Asia_Its_use_a_food_freed_and_fuel_to_benefit_the_poor-compressed.pdf, accessed 15 February 2022.

[55] H. Minh (2010), "VIFOTEC 2009 boasts for high applicability", *Government News*, http://news.gov.vn/Home/VIFOTEC-2009-boasts-forhigh-applicability/20101/6051.vgp, accessed 15 February 2022.

[56] K. Hoang, B.V. Nguyen, P. Nguyen, et al. (2010b), "Current situation of cassava in Vietnam and the breeding of improved cultivars", *Foodcrops.vn*, http://foodcrops.blogspot.com/2010/05/current-situation-of-cassava-in-vietnam.html, accessed 15 February 2022.

[57] K. Bang (2009), "Curing 'cassava witches' broom disease on cassava", *Nhan Dan Newspaper*, https://nhandan.vn/chua-benh-choi-rong-tren-cay-san-post546288.html, accessed 15 February 2022 (in Vietnamese).

[58] K. Hoang, N.N. Tran, M.T.T. Nguyen, et al. (2016), "New variety KM419", *Recognition Report of KM419 Variety*, Ministry of Agriculture and Rural Development, National Council of Plant Varieties, Hanoi, 89pp (in Vietnamese).

[59] K. Hoang (2014), *Cassava In Vietnam: Save And Grow. Recent Progress of Sustainable Cultivation Techniques for Cassava in Vietnam*, International Symposium on the Collaboration Between Japan and Vietnam for the Sustainable Future - Plant Science, Agriculture and Biorefinery.

[60] K. Hoang, H.H. Le, M. Ishitani, et al. (2013), *Vietnam Cassava Breeding Overview: The Broad Perspective*, Kick-off Meeting of a Cooperative Research Project under the East Asia Joint Research Program (e-ASIA JRP), https://cassavaviet.blogspot.com/2013/01/vietnam-cassava-breeding-overview-broad.html, accessed 15 February 2022.

[61] K. Hoang, B.V. Nguyen, R. Lefroy, et al. (2011), "Cassava for Biofuel in Vietnam", *Linking The Poor to Global Markets: Pro-poor Development of Biofuel Supply Chains*, Ho Chi Minh City.

[62] Vietnam Farmers' Union (2021), *Farmer's Scientist Links Take off Together*, Youth Publishing House, 166pp (in Vietnamese).

[63] H.H. Nguyen (2015), "Achievements of research and development of cassava and sweet potatoes in the period of 1975-2015", *Proceedings of The 90th Anniversary of Establishment (1925-2015)*, Institute of Agricultural Sciences for Southern Vietnam (in Vietnamese).

[64] H.T. Nguyen, L.T.P. Trinh, D.D. Ngo, et al. (2013), "Results of research, selection, and development of cassava varieties Sa21-12", *Proceedings of The National Conference on Crop Science* (in Vietnamese).

[65] H.T. Nguyen, M.V. Trinh, H.X. Nie, et al. (2012a), "Results of selection and development of cassava variety Sa21-12", *MARD Recognition for Trial Production in Decision No.168/QD-TT-CLT* (in Vietnamese).

[66] H.T. Nguyen, M.V. Trinh, H.X. Nie, et al. (2012b), "Results of selection and development of cassava variety Sa06", *MARD Recognition for Trial Production in Decision No.169/QD-TT-CLT* (in Vietnamese).

[67] N.N. Tran, V.H. Nguyen, K. Hoang, et al. (2015), *Final Report of The State-level Cassava Topics: Research and Development of Cassava as Raw Materials for The Manufacturing of Starch and Biofuels*, *Certificate No.2015-52-787/KQNC*, Ministry of Science and Technology, Department of Information Science and Technology (in Vietnamese).

[68] N.N. Tran, H.T. Nguyen, C.T. Nguyen, et al. (2014), "Results of regional cassava varietal yield trials at four locations in 2011-2013", *J. Agriculture and Rural Development*, **1(74)**, pp.8-14 (in Vietnamese).

[69] L. Hai (2015), "Four new varieties of cassava", *Vietnam Agriculture Newspaper*, https://nongnghiep.vn/4-giong-san-moi-d153736.html, accessed 15 February 2022.

[70] M.T.T. Nguyen (2017), *Study on The Selection of High-Yielding Cassava Varieties and Intensive Cultivation Techniques in Phu Yen Province*, Doctoral Thesis on Crop Science, University of Agriculture and Forestry, Hue University, 200pp (in Vietnamese).

[71] H.H. Nguyen, C.V. Dinh, N.T. Pham, et al. (2017), "Testing results of cassava variety KM101", *Journal of Vietnam Agricultural Science and Technology*, **1(74)**, pp.8-13 (in Vietnamese).

[72] T.D. Pham, L.V. Pham, H.Q. Nguyen, et al. (2019), "Testing of promising cassava varieties in Nghe An and Quang Tri provinces", *Journal of Vietnam Agricultural Science and Technology*, **8(105)**, pp.54-58 (in Vietnamese).

[73] C.S. Ho, C.H. Ho, H.H. Nguyen, et al. (2016), *The Cassava Variety KM505 (KM7)*, *Decision No.462/QD-TT-CLT*, Ministry of Agriculture and Rural Development (in Vietnamese).

[74] P.T. Nguyen (2021), "Results of developing technical measures for high-yielding cassava varieties SM937-26 and KM140 in Khanh Vinh, Khanh Hoa", *Some Plant and Animal Varieties Achieve Economic Efficiency and Suitable in The Area of Khanh Hoa Province*, pp.21-28 (in Vietnamese).

[75] T.T.K. Nguyen, N.N.M. Huynh, T.T.T. Nguyen, et al. (2021), "Identification of molecular markers linked to mosaic disease-resistant genes in cassava varieties in Southern Vietnam", *Journal of Vietnam Agricultural Science and Technology*, **2(123)**, pp.1-8 (in Vietnamese).

[76] V.A. Nguyen, T.N. Le, H. Nguyen, et al. (2021), "Characterization of some popular cassava varieties in Vietnam", *Journal of Vietnam Agricultural Science and Technology*, **3(124),** pp.1-17.

[77] A.N. Le, K.D. Nguyen, G.T.T. Ho (2021), "Biological characteristics of the whitefly *Bemisia tabaci* (Gennadius) (Homoptera: Aleyrodidae) on four cassava cultivars", *Vietnam J. Agri. Sci.*, **20(1)**, pp.18-23 (in Vietnamese).

[78] X. Zhang, T.T.L. Cu, P.D. Pham, et al. (2023), "Breeding in Southeast Asia: modernising breeding and develop new disease resistant varieties", *Establishing Sustainable Solutions to Cassava Diseases in Mainland Southeast Asia*, https://www.youtube.com/watch?v=Pz3dr3LJIj8, accessed 15 February 2023.

[79] N.T. Pham, T.B. Nguyen, T.V. Vo, et al. (2021), "Results of testing cassava varieties tolerant/resistant to leaf mosaic disease in Phu Yen in 2021", Working paper No.25 BC/TTHL, IAS - CIAT - Phu Yen Provincial Agricultural Extension Centre (in Vietnamese).

[80] H.T.T. Pham, H.T. Nguyen, H.V. Nguyen, et al. (2021), "Selection of cassava varieties suitable for Nghe An province", *Journal of Vietnam Agricultural Science and Technology*, **1(122)**, pp.16-21 (in Vietnamese).

[81] H.T.T. Pham, H.X. Nie, H.T. Nguyen, et al. (2018), *Report on Results of Cassava Variety Selection 13Sa05* (in Vietnamese).

[82] H.T.T. Pham, L.T. Nguyen, H.T. Nguyen, et al. (2017), "Selection and development of high yield and quality cassava variety Sa06 in the Northern region of Vietnam", *Journal of Vietnam Agricultural Science and Technology*, **2(75)**, pp.26-31 (in Vietnamese).

[83] H.H. Nguyen, N.T. Pham, T.V. Vo, et al. (2021), "Selection and testing of cassava variety HL-S12", *Journal of Vietnam Agricultural Science and Technology*, **6(127)**, pp.10-16 (in Vietnamese).

[84] Vietnam National Assembly (2018), *Law on Cultivation 31/2018/QH14*, https://thuvienphapluat.vn/van-ban/Linh-vuc-khac/Luat-Trong-trot-2018-336355.aspx, accessed 15 February 2022 (in Vietnamese).

[85] K. Hoang (2003b), "Technology of cassava breeding", *Varietal Technology of Plant, Animal and Forestry*, Agricultural Publishing House, **2**, pp.95-108 (in Vietnamese).

[86] M.B. Nguyen (2018), *Research Cultural Techniques to Scatter Harvest Season for Cassava in Dak Lak Province*, Doctoral Thesis on Crop Science, Tay Nguyen University, 244pp (in Vietnamese).

[87] M.B. Nguyen, K. Hoang, T.C. Trinh, et al. (2018), "Effect of time of planting and harvesting on tuber yield and starch content of cassava varieties KM 419 and HL S11 in Dak Lak", *Journal of Agricultural Science and Rural Development*, pp.22-30 (in Vietnamese).

[88] M.B. Nguyen, K. Hoang, H.H. Nguyen (2017), "Selection of cassava varieties suitable for spreading of crops in Dak Lak province", *Journal of Agricultural Science and Rural Development*, pp.52-60 (in Vietnamese).

[89] M.B. Nguyen, A.M. Nguyen, K. Hoang (2015), "Results of testing and selection of high yielding cassava varieties in Dak Lak", *Journal of Agricultural Science and Rural Development*, pp.108-112 (in Vietnamese).

[90] M.T.T. Nguyen, H.M. Nguyen, K. Hoang, et al. (2017), "Results of research on technical measures of intensive spreading of cassava crop in Phu Yen province", *Journal of Agricultural Science and Rural Development*, pp.50-56 (in Vietnamese).

[91] M.T.T. Nguyen, H.M. Nguyen, K. Hoang, et al. (2016), "Results of testing and selection of cassava variety KM419 with high starch yield for Phu Yen province", *Journal of Agricultural Science and Rural Development*, **124(10)**, pp.131-142 (in Vietnamese).

[92] H. Ceballos, C. Hershey, C. Iglesias, et al. (2021), "Fifty years of a public cassava breeding program: Evolution of breeding objectives, methods, and decision-making processes", *Theoretical and Applied Genetics*, **134(8)**, pp.2335-2353, DOI: 10.1007/s00122-021-03852-9.

[93] Vietnam Ministry of Agriculture and Rural Development (2011), *National Technical Regulation on Testing for Value of Cultivation and Use of Cassava varieties, QCVN 01-61:2011/BNNPTNT*, https://luatvietnam.vn/nong-nghiep/quy-chuan-qcvn-01-61-2011-bnnptnt-gia-tri-canh-tac-su-dung-cua-giong-san-161412-d3.html, accessed 15 February 2022 (in Vietnamese).

[94] C.M. Nguyen (2014), *Selection of Varieties and Determination of The Amount of Potassium, and Its Appropriate Application for KM419 cultivation in Tay Ninh*, Master Thesis on Science, Nong Lam University - Ho Chi Minh City, 147pp (in Vietnamese).

[95] M.T.T. Nguyen, H.M. Nguyen, K. Hoang, et al. (2019), "Cassava conservation and sustainable development in Vietnam: A key study in Phu Yen province", *VNCP CIAT GCP21 IAS NLU DARD HUAF,* Working Papers of a Workshop held in Ho Chi Minh City, Vietnam, July 21, 29pp.

[96] V. Tai (2023), "Initial results in breeding disease-resistant cassava varieties", *Phu Yen Newspaper*, https://baophuyen.vn/79/310545/ket-qua-buoc-dau-trong-chon-tao-giong-san-moi-khang-benh.html, accessed 10 October 2023 (in Vietnamese).

[97] Phu Yen Television Station Science and Life (2023), "Research on creating cassava varieties with high starch yield, resistant to major pests and diseases, suitable for production conditions in Phu Yen province", https://www.youtube.com/watch?v=gZZk9OL4fg, accessed 10 October 2023 (in Vietnamese).

[98] C. Khoi (2023), "Export of cassava and cassava products reaches over 1 billion USD, China is still the main consumption market", *VnEconomy*, https://vneconomy.vn/xuat-khau-san-va-san-pham-tu-san-dat-tren-1-ty-usd-trung-quoc-van-la-thi-truong-tieu-thu-chinh.htm, accessed 10 October 2023 (in Vietnamese).

# Nursery rearing freshwater prawn, *Macrobrachium rosenbergii*, in biofloc system integrated with red seaweed, *Gracilaria tenuistipitata*, at different stocking densities under zero water exchange

**Tien Hai Ly[1], Le Hoang Vu[1], Ly Van Khanh[2], Nguyen Thi Ngoc Anh[2*]**

*[1]College of Agriculture, Bac Lieu University, 178 Vo Thi Sau Street, Ward 8, Bac Lieu City, Bac Lieu Province, Vietnam*
*[2]College of Aquaculture and Fisheries, Can Tho University, Campus II, 3/2 Street, Xuan Khanh Ward, Ninh Kieu District, Can Tho City, Vietnam*

Received 7 January 2024; revised 18 February 2024; accepted 27 February 2024

***Abstract:***

**This study was conducted to assess the effects of stocking densities on the water quality, survival and growth of the freshwater prawn *Macrobrachium rosenbergii* postlarvae (PL) cultured in a biofloc system integrated with red seaweed (*Gracilaria tenuistipitata*). Postlarvae prawns weighing 0.012±0.001 g were stocked at densities of 1,000, 1,500, 2,000, and 2,500 PL/m$^3$, noted as D1, D1.5, D2, and D2.5, respectively. Each density treatment was replicated three times and randomly assigned to 12 plastic tanks of 150 l at a salinity of 10 ppt. Red seaweed was added at a rate of 1.5 kg/m$^3$, and molasses was used as a carbon source to maintain a C:N ratio of 15:1. No water exchange occurred during the 30-day rearing period. Results indicated that water quality parameters, including TAN and $NO_2^-$, biofloc volume, total heterotrophic bacteria, and *Vibrio* spp. counts, increased at higher prawn densities but remained within the appropriate range for prawn performance. Growth rate in weight and survival of prawns decreased as stocking density increased, with D1 and D1.5 showing comparable and significantly higher results compared to D2 and D2.5. Prawn production increased with rising stocking density, with a significant difference among treatments ($p<0.05$). Furthermore, prawns in D1 and D1.5 exhibited significantly higher feed efficiency than those in D2 and D2.5. These findings suggest that nursery rearing of prawn PL at a density of 1,500 ind/m$^3$ in a biofloc system integrated with red seaweed offers optimal growth and feed efficiency, while maintaining good water quality and conserving water resources.**

***Keywords:*** **biofloc, feed efficiency, freshwater prawn, *Gracilaria tenuistipitata*, growth rate, water quality.**

***Classification numbers:*** **3.1, 5.3**

## 1. Introduction

The freshwater prawn, *Macrobrachium rosenbergii*, is a tropical species commonly cultured in Asia, including Vietnam, due to its ability to thrive in diverse environments, ranging from freshwater to brackish water [1]. This species demonstrates optimal development within a salinity range of 0-15 ppt [2]. As noted by T.N. Hai, et al. (2020) [3], freshwater prawn emerges as a significant candidate for culture in the brackish waters of the Mekong Delta in Vietnam, particularly in response to salinity intrusion induced by climate change.

Biofloc technology has emerged as a sustainable aquaculture approach, contributing to reduced feed input, water consumption, and enhanced water quality [4, 5]. It has found widespread application in nursery phases of shrimp and prawns in recent years [6-9]. According to M.E. Hosain, et al. (2021) [8], rearing *M. rosenbergii* PL at a salinity of 10-15 ppt using biofloc technology resulted in improved survival and prawn production. Additionally, integrated aquaculture systems that co-culture organic extractive aquaculture species (such as seaweed) with fed aquaculture species (like fish/shrimp/prawn) offer both environmental sustainability and economic stability [10, 11]. N.T.N. Anh (2019) [12] revealed that co-culturing freshwater prawns with red seaweed *Gracilaria tenuistipitata* enhanced growth rates and survival, reduced feed costs, and maintained good water quality. Similar research on red seaweed integration with postlarvae of whiteleg shrimp [13] and black tiger shrimp [14] during the nursery phase significantly improved water quality and shrimp survival at high

*Corresponding author: Email: ntnanh@ctu.edu.vn

stocking densities compared to monoculture. Another study found that using red seaweed *G. tenuistipitata* in rearing crablets, *Scylla paramamosain*, greatly enhanced survival and provided an ideal culture medium for crab performance [15].

Several investigations highlight the benefits of the nursery phase for postlarvae of shrimps and prawns, including increased size uniformity, reduced predation, shorter pond grow-out cycles, more harvests per year, improved feed efficiency, and enhanced biosecurity [6, 9, 16]. Stocking density is a critical factor influencing the growth, survival, productivity, and production efficiency of cultured species during the nursery phase [7, 13, 14, 16, 17]. This study aims to determine the optimal stocking density of prawns concerning water quality and prawn performance in a biofloc system integrated with red seaweed under zero water exchange conditions.

## 2. Materials and methods

### *2.1. Biological materials*

High-quality all-male prawn *M. rosenbergii* postlarvae (PL12) were procured from a commercial hatchery in Bac Lieu province, Vietnam, and acclimatised in a 2 $m^3$ tank for three days to adjust to experimental conditions. Red seaweed, *G. tenuistipitata*, was sourced from an improved extensive pond in Bac Lieu province. The specimens underwent thorough cleaning to remove sediments and fouling before acclimatisation to an experimental salinity of 10 ppt over three days.

### *2.2. Experimental design, management and monitoring*

Prawn PL15 were reared in a biofloc system integrated with *G. tenuistipitata* under a transparent roof at the College of Aquaculture and Fisheries, Can Tho University, Vietnam. Four treatments were randomly assigned in triplicate with different stocking densities: 1,000 (D1), 1,500 (D1.5), 2,000 (D2), and 2,500 PL/$m^3$ (D2.5). Initial prawn sizes were 0.012±0.001 g body weight and 1.13±0.05 cm total length. They were reared in 150 l tanks at a salinity of 10 ppt with continuous aeration to maintain dissolved oxygen levels of 5-6 mg/l. Red seaweed was added to the rearing tanks at a biomass of 1.5 kg/$m^3$. During nursery rearing, water temperature, pH, and alkalinity in the rearing tanks fluctuated within the ranges of 25.1-28.3°C, 7.9-8.13, and 90-126 mg $CaCO_3$/l, respectively.

To promote biofloc formation, carbohydrates (molasses containing 46.7% carbohydrate and 0.95% protein) were added to the rearing tanks after prawn stocking to maintain a C:N ratio of the biofloc system at 15:1, following Avnimelech's protocol [4]. Prawn postlarvae were fed four times daily (at 7:00, 11:00, 16:00, and 21:00 h) with commercial feed containing 40% protein (Grobest, Vietnam). Feeding ration was set at 8-10% of the estimated prawn biomass, monitored, and adjusted based on feed presence or absence after one hour of feeding. Throughout the rearing period, no water exchange occurred, and freshwater was only added to the rearing tank to compensate for evaporation and maintain initial salinity and culture volume. The experiment lasted for 30 days.

### *2.3. Data collection*

Water temperature and pH were monitored every three days at 07:00 and 14:00 hours using a multi-channel meter (Mettler Toledo, USA). Alkalinity level was measured using a test kit (Sera, Germany), while the concentrations of total ammonia nitrogen (TAN) and $NO_2$- were determined at 10-day intervals using the standard method of APHA [18]. Biofloc volume was measured every ten days by collecting a 1l water sample in an Imhoff cone and allowing it to settle undisturbed for 30 minutes; settled floc was recorded as ml/l [4].

At the experiment's conclusion, total heterotrophic bacterial and *Vibrio* spp. densities in water were analysed using Zobell marine agar medium and TCBS (thiosulphate-citrate-bile salts-sucrose agar), respectively, following standard procedures [19, 20]. The red seaweed biomass in each tank was harvested, excess water was removed, and it was weighed to calculate the percentage biomass increment (BI).

BI (%) = (Final biomass - Initial biomass)/Initial biomass x 100

The initial weight and total length of prawns were determined by randomly selecting 40 animals from the conditioning tank and measuring them with a 0.01 g precision balance and callipers, respectively. At the experiment's conclusion, the total prawn biomass in each rearing tank was weighed to record the final weight and growth rate, and survival rate was determined by counting all harvested prawns. Forty

shrimp were randomly selected from each rearing tank to measure the final length of the prawn. Growth performance of prawns, such as specific growth rate in length ($SGR_L$) and weight ($SGR_W$), survival, feed conversion ratio (FCR), and feed efficiency (FE), were calculated as follows:

$SGR_L$ (%/day) = [ln(Final length) - ln(Initial length)]/ Day of culture x 100

$SGR_W$ (%/day) = [ln(Final weight) - ln(Initial weight)]/ Day of culture x 100

Survival (%) = Final number of prawn/Initial number of prawn x 100

FCR = Consumed feed (g)/(Final weight - Initial weight) (g)

FE (%) = [Consumed feed/(Final weight - Initial weight)] x 100

### *2.4. Statistical analysis*

All percentage values were arcsine transformed, and variance homogeneity was tested using Levene's test. A one-way ANOVA was employed to determine the overall effect of the treatment. The Duncan test was used to identify significant differences between the mean values at a significance level of $p<0.05$ (SPSS, version 20.0).

## 3. Results and discussion

### *3.1. Water quality parameters*

Water quality parameters during the experiment are shown in Table 1. Results indicated that water temperature, pH, and alkalinity in the rearing tanks fluctuated within the ranges of 25.1-28.3°C, 7.9-8.13, and 90-126 mg$CaCO_3$/l, respectively. These values remained consistent across density treatments, falling within the appropriate range for prawn culture, as suggested by M.B. New (2012) [1].

Figure 1 shows that the concentrations of TAN and $NO_2^-$ increased with rearing duration, with higher levels observed at higher prawn density. The D1 and D2.5 treatments had the lowest and highest values, respectively, and were significantly different ($p<0.05$) from the other density treatments (Table 1). Although the highest prawn density (2,500 PL/$m^3$) resulted in the highest levels of TAN (0.39 mg/l) and $NO_2^-$ (1.68 mg/l) at the experiment's conclusion, these values are considered safe for prawn rearing [21, 22].

Notably, the water quality in the culture medium remains within an acceptable range for prawn performance under a no-water-exchange system in the present study. This could be attributed to (1) The presence of red seaweed *G. tenuistipitata* in the rearing tanks, which absorbed nutrients for its growth [10, 13, 14]; and (2) The addition of molasses as a carbon source to stimulate the growth of heterotrophic bacteria in the biofloc. Ammonia levels could be reduced more rapidly via assimilation than by the nitrification process, which primarily controlled the increase in nitrogenous compound levels in the water [4, 5, 23].

**Table 1. Average parameters of water quality in the rearing tanks.**

| Density treatment | | 1,000 PL/$m^3$ (D1) | 1,500 PL/$m^3$ (D1.5) | 2,000 PL/$m^3$ (D2) | 2,500 PL/$m^3$ (D2.5) |
|---|---|---|---|---|---|
| Temperature (°C) | 7:00 h | 25.1±0.8 | 25.4±0.8 | 25.3±0.9 | 25.3±0.9 |
| | 14:00 h | 26.5±0.6 | 28.3±1.8 | 27.8±1.8 | 27.1±1.0 |
| pH | 7:00 h | 8.08±0.07 | 8.05±0.09 | 8.07±0.07 | 8.04±0.08 |
| | 14:00 h | 8.22±0.06 | 8.23±0.11 | 8.25±0.10 | 8.20±0.06 |
| Alkalinity ($CaCO_3$/l) | | 110.3±13.9 | 117.0±13.3 | 115.5±9.3 | 116.3±7.1 |
| TAN (mg/l) | | 0.09±0.01$^a$ | 0.16±0.05$^b$ | 0.19±0.02$^{bc}$ | 0.24±0.03$^c$ |
| $NO_2^-$ (mg/l) | | 0.57±0.08$^a$ | 0.86±0.16$^b$ | 0.99±0.05$^b$ | 1.33±0.06$^c$ |
| Biofloc volume (ml/l) | | 1.68±0.37$^a$ | 1.91±0.42$^b$ | 2.30±0.52$^c$ | 2.59±0.64$^d$ |
| Total heterotrophic bacteria (x$10^3$ CFU/ml) | | 1.98±0.73$^a$ | 2.63±0.29$^a$ | 3.23±0.62$^{ab}$ | 4.42±1.03$^b$ |
| *Vibrio* spp. (x$10^2$ CFU/ml) | | 3.60±0.5$^a$ | 5.13±0.35$^{ab}$ | 6,23±0.22$^b$ | 7.20±0.21$^b$ |

*: values are expressed as mean±SD (n=3). Mean values in with different superscripts within the same row are significantly different at $p<0.05$.

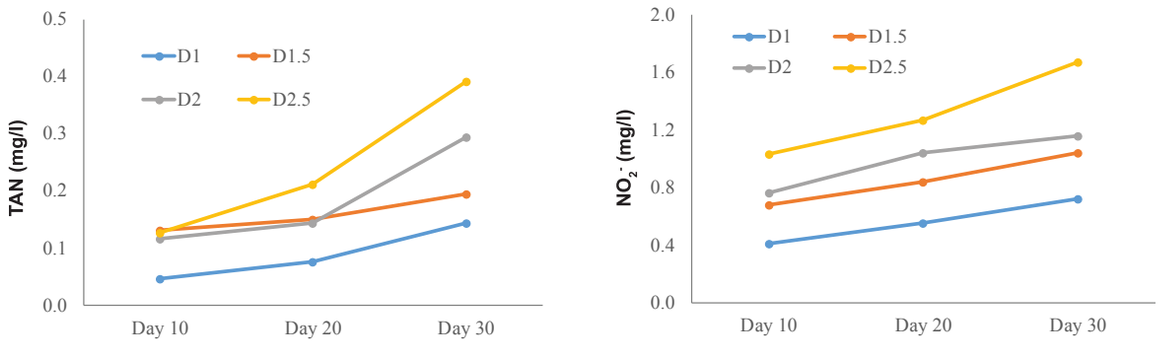


**Fig. 1. Variations in the contents of TAN and $NO_2^-$ during 30 days of nursery rearing.**

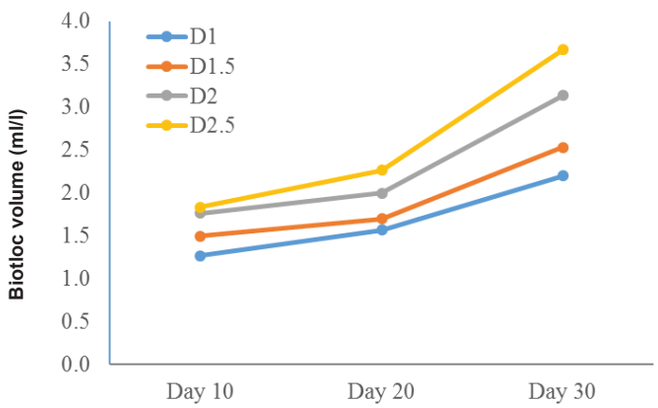


**Fig. 2. Variations in biofloc volume during 30 days of nursey rearing.**

At the termination of the experiment on day 30, biofloc volume ranged from 2.20 to 3.63 ml/l, with the lowest and highest values observed for the D1 and D2.5 treatments, respectively (Fig. 2). There was a statistically significant difference ($p<0.05$) in average biofloc volume among the four density treatments (see Table 1). Furthermore, biofloc volume increased with shrimp density and tended to rise with rearing time. This could be related to the addition of carbohydrates based on the amount of pellet feed fed to shrimp [4]. In this scenario, more commercial feed and molasses (carbonhydrate) were delivered at greater prawn densities, and with no water exchange during the rearing phase, resulting in the accumulation of shrimp excrement and inorganic suspended particles in the rearing tanks. This, in turn, stimulated the proliferation of heterotrophic bacteria, resulting in an increase in the overall bacterial population, which aggregated to form massive bioflocs, thereby increasing biofloc volume in the culture medium [4]. Previous researchers [5-9] have shown that bioflocs, comprising a variety of microbial organisms such as bacteria, algae, zooplankton, and protozoa, play a crucial role in maintaining good water quality and providing an additional food source for shrimp.

Similarly, total heterotrophic bacteria and *Vibrio* spp. counts increased with prawn density, reaching 1.98-4.41x$10^3$ CFU/ml and 0.36-0.72x$10^2$ CFU/ml, respectively, with the D2.5 group having significantly higher values than other treatments ($p<0.05$). In this study, the presence of low densities of total bacteria and *Vibrio* in the rearing tank was not detrimental to prawn performance [6, 7]. Previous research revealed that shrimp cultured in biofloc systems significantly reduced Vibrio density and boosted shrimp disease resistance [6, 9].

### *3.2. Biomass of red seaweed G. tenuistipitata*

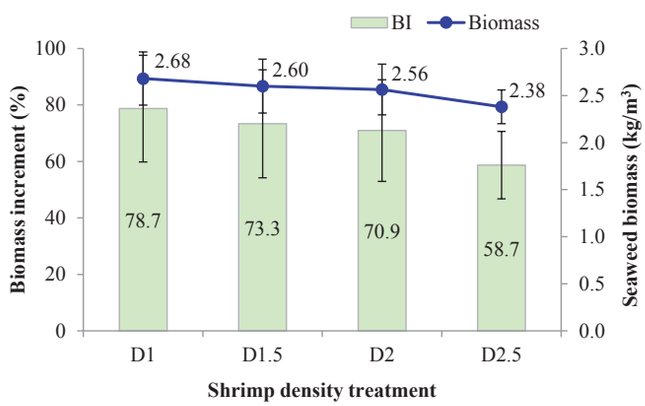


**Fig. 3. Growth rate of red seaweed *G. tenuistipitata* after 30 days of experiment.** *: values are expressed as mean ±SD (n=3).

Figure 3 shows that the average red seaweed biomass of *G. tenuistipitata* at the end of the experiment in all treatments ranged from 2.38 to 2.68 kg/$m^3$, which was

higher than the initial quantity (1.5 kg/m$^3$) and equivalent to a biomass increment (BI) of 58.7-78.7%. Although the D2.5 treatment had lower values than other treatments, no significant difference was observed among treatments ($p>0.05$). This indicates that red seaweed grows well in co-culture with prawns in the same tanks, which helps maintain good water quality in the culture medium. Analogous findings were found in recent investigations [13, 14, 24].

### *3.3. Prawn performance*

Prawn performance after 30 days of rearing is presented in Table 2. Results showed that the final length of the prawn ranged from 3.39 to 3.64 cm, and the final weight ranged from 0.25 to 0.32 g, corresponding to a specific growth rate in length ($SGR_L$) of 3.66-3.89%/day and in weight ($SGR_W$) of 9.93-10.89%/day. There was no statistical difference ($p>0.05$) between the D1 and D1.5 groups, both of which had significantly higher values than the D2 and D2.5 groups ($p<0.05$). This illustrates that high stocking densities (2,000 and 2,500 PL/m$^3$) resulted in significantly poorer growth rates than low stocking densities (1,000 and 1,500 PL/m$^3$).

The mean survival of prawns in D1 and D1.5 treatments was highest (91.67%), and it tended to decline at higher stocking density, with the D2.5 treatment having the lowest value (73.00%) and statistical difference ($p<0.05$) from other density treatments.

The average biomass and production of prawns ranged from 299.3 to 446.8 g/m$^3$ and 917 to 1,825 ind/m$^3$, respectively, and showed a tendency to increase with stocking density. Statistical analysis indicated that prawn biomass in the D1.5, D2, and D2.5 treatments was comparable ($p>0.05$), and all were significantly higher than the D1 treatment, while production (number of harvested prawn) was significantly different among rearing density treatments ($p<0.05$).

Feed conversion ratio (FCR) was 0.68-0.93, equivalent to feed efficiency (FE) of 108.6-146.0%, with higher stocking densities resulting in a higher FCR and lower FE. There was no statistical difference ($p>0.05$) between D1 and D1.5 groups or between D2 and D2.5 groups.

Stocking density is known to be one of the key technical parameters influencing growth, survival, and production of prawn and shrimp in the nursery phase, and the proper stocking density depends on the species, rearing method, duration, and stage of culture. When applying too high stocking density, living space is limited, cannibalism increases, and more feed is needed, which leads to poor water quality, crowding stress, delayed growth, high mortality, and pathogen outbreaks. low stocking density

**Table 2. Prawn postlarvae performance after 30 nursery rearing.**

| Treatment | D1 | D1.5 | D2 | D2.5 |
|---|---|---|---|---|
| Initial length (cm) | 1.13±0.12 | 1.13±0.12 | 1.13±0.12 | 1.13±0.12 |
| Final length (cm) | 3.64±0.07$^b$ | 3.63±0.08$^b$ | 3.46±0.09$^a$ | 3.39±0.11$^a$ |
| $SGR_L$ (%/day) | 3.89±0.06$^b$ | 3.88±0.07$^b$ | 3.72±0.09$^a$ | 3.66±0.10$^a$ |
| Initial weight (g) | 0.012±0.001 | 0.012±0.001 | 0.012±0.001 | 0.012±0.001 |
| Final weight (g) | 0.32±0.02$^b$ | 0.31±0.01$^b$ | 0.27±0.02$^a$ | 0.25±0.02$^a$ |
| $SGR_W$ (%/day) | 10.89±0.20$^b$ | 10.73±0.12$^b$ | 10.24±0.22$^a$ | 9.93±0.28$^a$ |
| Survival (%) | 91.67±0.84$^c$ | 91.67±4.45$^c$ | 81.67±1.91$^b$ | 73.00±2.34$^a$ |
| Biomass (g/m$^3$) | 299.3±16.1$^a$ | 427.2±17.5$^b$ | 437.9±25.8$^b$ | 446.8±25.5$^b$ |
| Production (ind/m$^3$) | 917±9$^a$ | 1.375±67$^b$ | 1.633±38$^c$ | 1.825±59$^d$ |
| FCR | 0.68±0.04$^a$ | 0.69±0.02$^a$ | 0.85±0.05$^b$ | 0.93±0.07$^b$ |

*: values are expressed as mean ±SD (n=3). Mean values in with different superscripts within the same row are significantly different at $p<0.05$.

gives high growth and survival but higher expenses and a lower production output per culture unit [16, 17, 25].

According to previous investigations, the co-culture of red seaweed with shrimp or prawn not only improved water quality but also functioned as natural food and a shelter, thereby increasing shrimp and prawn survival and production [16, 17, 25]. Additionally, biofloc formation in the rearing tanks had high nutrition content, which is a source of supplementation for the prawn diet [4, 7, 9].

Overall, the results showed that prawn performance in terms of growth rate, survival, and feed efficiency at a stocking density of 1,500 PL/$m^3$ was comparable to that of prawns reared at a density of 1,000 PL/$m^3$ and significantly higher than that of prawns reared at stocking densities of 2,000 and 2,500 PL/$m^3$.

## 4. Conclusions

The freshwater prawn *M. rosenbergii* cocultured with red seaweed *G. tenuistipitata* in a biofloc system maintained good water quality under no water exchange conditions, as shown by TAN and $NO_2^-$ levels as well as total bacteria and *Vibrio* spp. counts that were within the suitable range for prawn performance.

Freshwater prawn postlarvae co-cultured with red seaweed in a biofloc system at a stocking density of 1,500 ind/$m^3$ achieved optimal growth rates and feed efficiency at the nursery phase.

## CRediT author statement

Tien Hai Ly: Methodology, Formal analysis, Original draft preparation, Visualisation; Le Hoang Vu: Conceptualisation, Data curation, Investigation; Ly Van Khanh: Investigation, Visualisation, Formal analysis; Nguyen Thi Ngoc Anh: Supervision, Validation, Writing - Reviewing and Editing.

## ACKNOWLEDGEMENTS

This study was financed by Can Tho University and Bac Lieu University for scientific research activities. The authors would like to express their gratitude to Dinh Thi Kieu Ly for her assistance during the experiment.

## COMPETING INTERESTS

The authors declare that there is no conflict of interest regarding the publication of this article.

## REFERENCES

[1] M.B. New (2012), "Global scale of freshwater prawn farming", *Aquaculture Research*, **43(7)**, pp.960-969, DOI: 10.1111/j.1365-2109.2011.03008.x

[2] B.K. Chand, R.K. Trivedi, S.K. Dubey, et al. (2015), "Effect of salinity on survival and growth of giant freshwater prawn *Macrobrachium rosenbergii* (de Man)", *Aquaculture Reports*, **2**, pp.26-33, DOI: 10.1016/j.aqrep.2015.05.002.

[3] T.N. Hai, N.T. Phuong, L.Q. Viet, et al. (2020), "Promoting coastal aquaculture for adaptation to climate change and saltwater intrusion in the Mekong delta, Vietnam", *World Aquaculture*, **51(2)**, pp.19-26.

[4] Y. Avnimelech (2015), *Biofloc Technology, A Practical Guidebook*, 3rd Edition, Sorrento, lA: The World Aquaculture Society, 267pp.

[5] S. McCusker, M.B. Warberg, S.J. Davies, et al. (2023), "Biofloc technology as part of a sustainable aquaculture system: A review on the status and innovations for its expansion", *Aquaculture Fish and Fisheries*, **3**, pp.331-352, DOI:10.1002/aff2.108.

[6] R. Schweitzer, M.A.D. Lorenzo, F.V.D. Nescient, et al. (2017), "Nursery of young *Litopenaeus vannamei* post-larvae reared in biofloc-and microalgae-based systems", *Aquacultural Engineering*, **78**, pp.140-145, DOI: 10.1016/j.aquaeng.2017.07.001

[7] C. Negrini, C.S.D. Castro, A.T.B. Guimaraes, et al. (2017), "Stocking density for freshwater prawn *Macrobrachium rosenbergii* (Decapoda, Palaemonidae) in biofloc system", *Latin American Journal of Aquatic Research*, **45(5)**, pp.891-899, DOI: 10.3856/vol45-issue5-fulltext-3.

[8] M.E. Hosain, S.M.N. Amin, M.S. Kamarudin, et al. (2021), "Effect of salinity on growth, survival, and proximate composition of *Macrobrachium rosenbergii* post larvae as well as zooplankton composition reared in a maize starch based biofloc system", *Aquaculture*, **533**, DOI: 10.1016/j.aquaculture.2020.736235.

[9] C.M.A. Caipang, K.M.P. Trebol, M.J.S. Abeto, et al. (2022), "An innovative biofloc technology for the nursery production of Pacific whiteleg shrimp, *Penaeus vannamei* in tanks", *International Journal of Biosciences*, **21(4)**, pp.71-79, DOI: 10.12692/ijb/21.4.71-79.

[10] M.Y. Roleda, C.L. Hurd (2019), "Seaweed nutrient physiology: Application of concepts to aquaculture and bioremediation", *Phycologia*, **58**, pp.552-562, DOI: 10.1080/00318884.2019.1622920.

[11] M.N.P. Henares, M.V. Medeiros, A.F.M. Camargo (2020), "Overview of strategies that contribute to the environmental sustainability of pond aquaculture: Rearing systems, residue treatment, and environmental assessment tools", *Reviews in Aquaculture*, **12(1)**, pp.453-470, DOI: 10.1111/raq.12327.

[12] N.T.N. Anh (2019), "Integration of freshwater prawn *Macrobrachium rossenbergii* de Man, 1879 and red seaweed *Gracilaria tenuistipitata* under different feeding rates", *Livestock Research for Rural Development*, **31**, http://www.lrrd.org/lrrd31/6/ntnan31081.html, accessed 5 May 2020.

[13] N.T.N. Anh, B.N.T. An, L.M. Lan, et al. (2019), "Integrating different densities of white leg shrimp *Litopenaeus vannamei* and red seaweed *Gracilaria tenuistipitata* in the nursery phase: Effects on water quality and shrimp performance", *Journal of Applied Phycology*, **31**, pp.3223-3234, DOI: 10.1007/s10811-019-01824-7.

[14] N.T.N. Anh, N.H. Vinh, L.M. Lan, et al. (2020), "Polyculture culture of black tiger shrimp *Penaeus monodon* and red seaweed *Gracilaria tenuistipitata* under different densities: Effects on water quality, post-larvae performance and their resistance against *Vibrio parahaemolyticus*", *Journal of Applied Phycology*, **32**, pp.4333-4345, DOI: 10.1007/s10811-020-02253-7.

[15] H.T. Toi, N.T.N. Anh, P.T.T. Ngan, et al. (2023), "Effects of stocking densities and seaweed types as shelters on the survival, growth, and productivity of juvenile mud crabs (*Scylla paramamosain*)", *Egyptian Journal of Aquatic Research*, **49(3)**, pp.401-407, DOI: 10.1016/j.ejar.2023.01.005.

[16] D.R. Olague, J.T.P. Palafox, S.G.C. Vargasmachuca, et al. (2021), "Effect of nursery system and stocking density to produce juveniles of whiteleg shrimp *Litopenaeus vannamei*", *Aquaculture Reports*, **20**, DOI: 10.1016/j.aqrep.2021.100709.

[17] H.L.A. Marques, J.V. Lombardi (2011), "Compensatory growth of Malaysian prawns reared at high densities during the nursery phase", *Revista Brasileira De Zootecnia*, **40(4)**, pp.701-707, DOI: 10.1590/S1516-35982011000400001.

[18] American Public Health Association (1998), *Standard Methods For The Examination Of Water And Wastewater*, 1536pp.

[19] G.L. Barrow, R.K. Feltham (1993), *Covan And Steel's Manual For The Identification of Medical Bacteria*, 3rd Edition, Cambridge University Press, DOI: 10.1017/CBO9780511527104.

[20] G. Huys (2003), *Sampling and Sample Processing Procedures for The Isolation of Aquaculture-Associated Bacteria: Standard Operating Procedure*, Laboratory of Microbiology, Ghent University, Belgium, 15pp.

[21] H.L.A. Marques, M.B. New, M.V. Boock, et al. (2016), "Integrated freshwater prawn farming: State-of-the-art and future potential", *Reviews in Fisheries Science & Aquaculture*, **24(3)**, pp.264-293, DOI: 10.1080/23308249.2016.1169245

[22] C.C. Brazão, R.O. Kracizy, F.M. Dutra, et al. (2022), "Combined effect of ammonia and nitrite for *Macrobrachium amazonicum* (Heller, 1862) and *Macrobrachium rosenbergii* (De man, 1879) post-larvae", *Aquaculture*, **551**, DOI: 10.1016/j.aquaculture.2021.737880.

[23] G.S. Ferreira, V.F. Silva, M.A. Martins, et al. (2020), "Strategies for ammonium and nitrite control in *Litopenaeus vannamei* nursery systems with bioflocs", *Aquacultural Engineering*, **88**, DOI: 10.1016/j.aquaeng.2019.102040.

[24] H. Fourooghifard, A. Matinfar, M.S. Mortazavi, et al. (2018), "Nitrogen and phosphorous budgets for integrated culture of white leg shrimp *Litopenaeus vannamei* with red seaweed *Gracilaria corticata* in zero water exchange system", *Iranian Journal of Fisheries Sciences*, **17(3)**, pp.471-486, DOI: 10.22092/IJFS.2018.116382.

[25] S. Sun, H. Fu, Z. Gu, et al. (2016), "Effects of stocking density on the individual growth and differentiation of the oriental river prawn *Macrobrachium nipponense* (De Haan, 1849) (Caridea: Palaemonidae)", *Journal of Crustacean Biology*, **36(6)**, pp.769-775, DOI: 10.1163/1937240X-00002482.

DOI: 10.31276/VJSTE.66(1).84-89

# RNA isolation by two different methods in analysing adipose-biomarkers of mouse adipose tissues

**Dinh Toi Chu[1, 2], Hue Vu Thi[1, 2*], Ngoc Hoan Le[3]**

*[1]Faculty of Applied Sciences, International School, Vietnam National University - Hanoi, 79 Nguy Nhu Kon Tum Street, Nhan Chinh Ward, Thanh Xuan District, Hanoi, Vietnam*
*[2]Center for Biomedicine and Community Health, International School, Vietnam National University - Hanoi, 144 Xuan Thuy Street, Dich Vong Hau Ward, Cau Giay District, Hanoi, Vietnam*
*[3]Faculty of Biology, Hanoi National University of Education, Vietnam National University - Hanoi, 136 Xuan Thuy Street, Dich Vong Hau Ward, Cau Giay District, Hanoi, Vietnam*

Received 20 May 2023; revised 12 June 2023; accepted 5 September 2023

***Abstract:***

**The RNeasy Mini Kit and the TRI Reagent protocol are commonly employed techniques for extracting total RNA and are widely utilised in research pertaining to the expression of adipose biomarkers. This study was undertaken to establish and determine an appropriate method for isolating RNA from frozen adipose tissue, with the objective of analysing adipose biomarkers. Total RNA was extracted from frozen white adipose tissues of mice (-80$^{o}$C) using both the RNeasy Mini Kit and the TRI Reagent protocol. The concentration and purity of the RNA were assessed using NanoDrop. One-step RT-qPCR was employed to quantify the mRNA expression levels of three adipose biomarkers: MEST, SFRP5, and SCD1. The results of this investigation indicated that the RNeasy Mini Kit yielded a higher RNA concentration when compared to the TRI Reagent method. Furthermore, the RNeasy Mini Kit provided RNA samples with superior purity, as evidenced by a higher 260/230 ratio. Although RNA extracted using the TRI Reagent exhibited slightly elevated mRNA expression levels for the three biomarkers, these differences did not reach statistical significance. In summary, both methods are suitable for total RNA extraction, but the RNeasy Mini Kit is recommended for obtaining higher RNA concentration and purity. The choice of method should be contingent upon the intended downstream application of the RNA.**

***Keywords:*** **adipose biomarkers, adipose tissues, RNA isolation, RNeasy Mini Kit, TRI Reagent protocol.**

***Classification numbers:*** **3.4, 3.5**

## 1. Introduction

To assess the expression of a specific gene, reverse transcription polymerase chain reaction (RT-PCR) is employed to quantify its ribonucleic acid (RNA) concentration from total RNA. Therefore, isolating total RNA from adipose tissue represents one of the most critical steps that can significantly impact the outcomes of subsequent experiments. Given their acknowledged advantages, both the RNeasy Mini Kit and the TRI Reagent protocol are extensively employed in research concerning the expression of adipose biomarkers.

The RNeasy Mini Kit is a well-established commercial kit specifically designed for RNA extraction from adipose tissue [1]. While traditionally viewed as a passive energy storage organ, adipose tissue is now recognized as a complex and highly active metabolic and endocrine organ [2]. Consequently, adipose tissues play a pivotal role in the study of conditions such as diabetes, metabolic syndrome, and obesity, which have garnered substantial attention worldwide due to their epidemic prevalence [3]. Extracting RNA from adipose tissue presents more challenges compared to other tissues, primarily due to its elevated triglyceride levels and lower RNA concentration [4].

Isolating RNA from animal tissues with a high lipid content, such as adipose tissue, can prove to be a challenging task. Obtaining high-quality RNA with a satisfactory yield from adipose tissue is particularly

*Corresponding author: Email: huevt@vnuis.edu.vn

demanding. Although Pena et al. employed a modified version of the TRI Reagent approach, their RNA integrity values were considerably lower than those achieved using our combined protocol [5]. The TRI Reagent approach exhibited issues related to the purity of the isolated RNA in previous studies. It is widely recognized that all phenol-based procedures leave minimal residual organic solvents in the final separated sample, and these contaminants can potentially impact downstream applications [6-9]. The TRI Reagent approach yields samples that are contaminated with salts and solvents but exhibit better integrity.

Selecting an appropriate RNA extraction method is essential to cater to diverse research objectives, especially within the laboratory settings of Vietnam. Therefore, this study was conducted to establish and identify a suitable RNA isolation method for adipose tissue, with the specific aim of analysing adipose biomarkers.

## 2. Methods

### *2.1. Total RNA extraction*

In this study, inguinal white adipose tissue (iWAT) was collected from mice, with 10 mice per group. iWAT was collected from both sides of each mouse, and each side was cut and weighed to obtain 100 mg of tissue for each RNA extraction method. Following collection, the samples were promptly frozen in liquid nitrogen and stored in a deep freezer at -80$^{o}$C. Total RNA was extracted from the frozen mouse white fat using the QIAamp Viral RNA Mini Kit (QIAGEN, Germany) (Total RNA Kit) or the TRI Reagent protocol (TRI Reagent®, Sigma-Aldrich), as previously described [10, 11]. Briefly, each frozen sample was homogenized in 1000 µl of Buffer RLT or 1000 µl of TRI Reagent in a chilled tube using a Tissue Grinder. Subsequently, total RNA extraction was carried out following the procedures outlined in previous studies [10, 11]. During the RNA isolation using the kit, any contaminated DNA was removed using DNase I. Following isolation, total RNA from each sample was diluted to a final volume of 32 µl in RNase-free water, and in this study, we present the comparative concentrations, reflecting the yields of total RNA.

The RNeasy Mini Kit contains a selective binding silica membrane and a specialised buffer with a high salt content, enabling the purification of RNA molecules longer than 200 nucleotides. Consequently, total RNA from biological samples, which typically includes RNA fragments of approximately 18 nucleotides and longer, can be effectively purified using the RNeasy Mini Kit. Alternatively, a whole RNA (>200 nucleotides) fraction and a microRNA (miRNA)-enriched fraction can be extracted separately. Total RNA, inclusive of miRNA, is well-suited for miRNA quantification using real-time RT-PCR. In certain applications where messenger RNA (mRNA) and ribosomal RNA (rRNA) might introduce unwanted background noise, the enrichment of small RNA in a distinct fraction can be advantageous. While the RNeasy Mini Kit approach yields total RNA with excellent purity, quantity, and suitability for PCR applications from adipose tissue, it is somewhat more susceptible to degradation [12].

### *2.2. RNA measurement using NanoDrop*

The concentration and purity of RNA extracted using the RNeasy Mini Kit and the TRI Reagent were assessed using a NanoDrop spectrophotometer (Thermo Fisher Scientific, Wilmington, DE, USA). Measurements were taken for the absorbance ratios at 260-280 nm (260/280) and 260-230 nm (260/230), as well as the RNA concentration (ng/µl). The experimental procedure was previously outlined in publications [7, 8].

### *2.3. One-step RT-qPCR*

The mRNA levels of three genes, namely MEST, SFRP5, and SCD1, were determined using the one-step RT-qPCR method. The Rotor-Gene Q system (QIAGEN, Germany) was employed for the PCR reaction. Primers and Taqman probes for the target genes were obtained from previously published research [7, 9]. The mRNA expression of the target genes was normalized against Cyclophilin (Cyclo). The experimental procedure was described in prior publications [7, 9, 10].

### *2.4. Data analysis*

The data were managed and presented as mean ±SEM. Statistical analysis was conducted using Student's t-test for single comparisons with GraphPad Prism 8.0. Significance was established at $p<0.05$, with * indicating $p<0.05$, ** for $p<0.01$, and *** for $p<0.001$, while "n.s" represented not significant ($p\geq0.05$).

## 3. Results

### 3.1. The concentration of total RNA

**Table 1. Summary of the RNA isolation in the adipose biomarker analysis of mouse fat tissues.**

| | RNeasy Mini Kit | | | | | TRI Reagent | | | | |
|---|---|---|---|---|---|---|---|---|---|---|
| | *Mean* | *SEM* | *Max* | *Min* | *N* | *Mean* | *SEM* | *Max* | *Min* | *N* |
| RNA concentration (ng/µl) | 122.91 | 10.12 | 183.78 | 76.41 | 10 | 84.04 | 12.00 | 171.37 | 39.74 | 10 |
| Ratio 260/280 | 2.03 | 0.02 | 2.09 | 1.96 | 10 | 2.02 | 0.02 | 2.09 | 1.91 | 10 |
| Ratio 260/230 | 1.89 | 0.06 | 2.05 | 1.49 | 10 | 1.64 | 0.05 | 1.99 | 1.48 | 10 |
| MEST (mRNA level) | 0.10 | 0.04 | 0.38 | 0.01 | 10 | 0.17 | 0.03 | 0.33 | 0.06 | 10 |
| SFRP5 (mRNA level) | 0.10 | 0.04 | 0.33 | 0.01 | 10 | 0.14 | 0.03 | 0.31 | 0.03 | 10 |
| SCD1 (mRNA level) | 0.07 | 0.01 | 0.13 | 0.02 | 10 | 0.09 | 0.01 | 0.13 | 0.06 | 10 |

N indicates the number of samples/mice per group (each pair of samples were collected from 1 mouse).

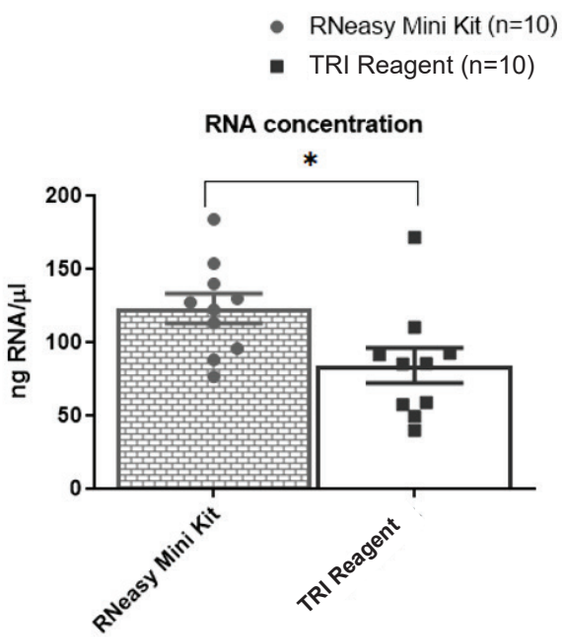


**Fig. 1. The concentration of total RNA extracted by two methods.** The mean RNA concentration can be described by using the RNeasy Mini Kit and the TRI Reagent method. Student's t-test for single comparisons was used. A significant difference between the two methods was accepted at $p<0.05$ (*).

Total RNA was extracted from frozen adipose tissue of mice, and its concentration (ng/µl) was compared between the RNeasy Mini Kit and the TRI Reagent (Table 1, Fig. 1). The results revealed a significantly higher mean RNA concentration with $p<0.05$ when using the RNeasy Mini Kit (122.91±10.12) compared to the TRI Reagent method (84.04±12.00). The maximum RNA concentration obtained was 183.78 ng/µl for the RNeasy Mini Kit and 171.37 ng/µl for the TRI Reagent, while the minimum RNA concentration was 76.41 ng/µl for the RNeasy Mini Kit and 39.74 ng/µl for the TRI Reagent. These findings suggest that the RNeasy Mini Kit is a more efficient method for RNA extraction, resulting in a higher RNA concentration with less variability in results.

### 3.2. The quality of total RNA

The quality of total RNA obtained from the two methods was assessed by determining the 260/280 and 260/230 absorbance ratios (Table 1, Fig. 2). There was no significant difference in the mean 260/280 ratio between the RNeasy Mini Kit (2.03±0.02) and the TRI Reagent (2.02±0.02). However, a significant difference was observed in the mean 260/230 ratio between the two methods ($p<0.01$). The mean ±SEM of the 260/230 ratio for the RNeasy Mini Kit was 1.89±0.06, indicating a pure RNA sample. In contrast, for the TRI Reagent, this ratio was 1.64±0.05, suggesting the presence of contaminants in the RNA sample. These results indicate that the RNeasy Mini Kit yields higher purity RNA samples compared to the TRI Reagent, as evidenced by the higher 260/230 ratio.

### 3.3. Analysis of mouse adipose-biomarkers

From the total RNA obtained from the two methods, the mRNA expression levels of three biomarkers (MEST,

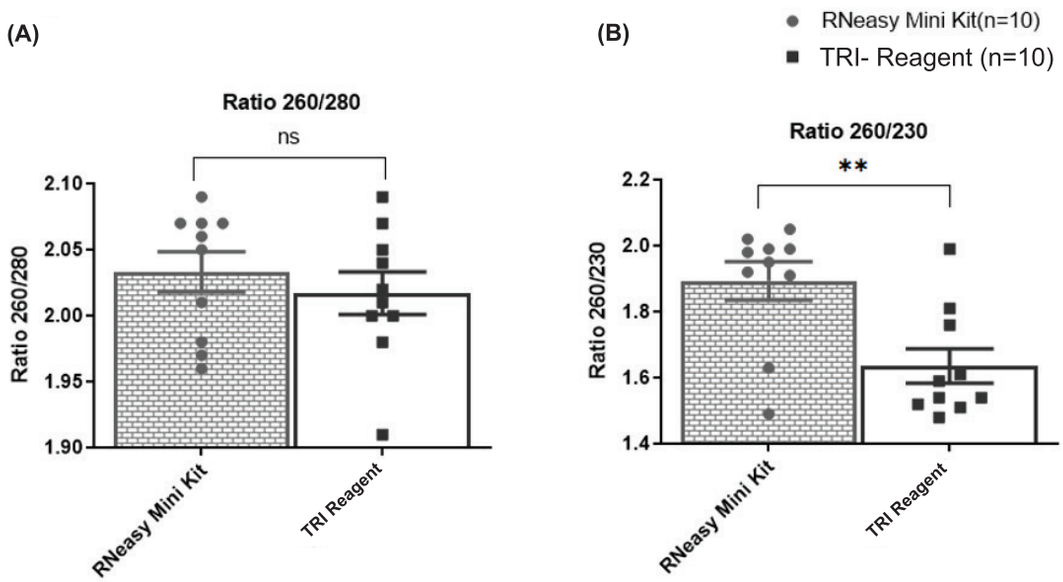


**Fig. 2. The quality of total RNA extracted by the two methods.** The quality of total RNA obtained from the two methods was compared by determining **(A)** the 260/280 ratio and **(B)** the 260/230 ratio. Student's t-test for single comparisons was used. "ns" indicates a non-significant difference and ** indicates p<0.01.

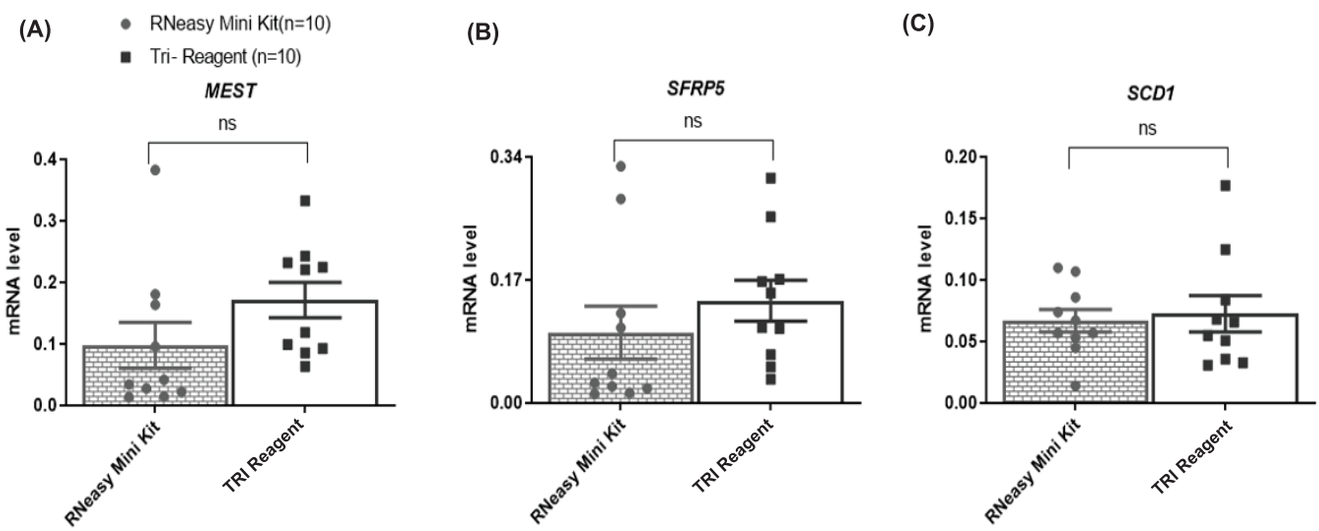


**Fig. 3. The RNA expression of some adipose biomarkers using total RNA extracted by the two methods.** mRNA expression levels of three biomarkers **(A)** MEST, **(B)** SFRP5, and **(C)** SCD1 using RT-PCR. Student's t-test for single comparisons was used. "ns" indicates a non-significant difference between the two methods.

SFRP5, SCD1) were measured using RT-PCR (Table 1, Fig. 3). The results indicated that the expression levels of MEST, SFRP5, and SCD1 appeared to be slightly higher when using RNA extracted with TRI Reagent compared to the RNeasy Mini Kit. Specifically, the MEST expression level was 0.17±0.03 with the TRI Reagent method, slightly higher than 0.10±0.04 with the RNeasy Mini Kit method. Similarly, the expression of SFRP5 was higher with RNA extracted using TRI Reagent (0.14±0.03) than with the RNeasy Mini Kit (0.10±0.04). Likewise, the SCD1 expression using TRI Reagent and RNeasy Mini Kit was 0.09±0.01 and 0.07±0.01, respectively. However, none of these differences reached statistical significance (p>0.05). These results indicate that the expression levels of critical biomarkers in adipose tissue remained consistent after RNA extraction using both methods.

## 4. Discussion

The isolation of high-quality RNA from adipose tissue presents challenges due to its high lipid content and relatively low cellular density. Researchers frequently turn to the RNeasy Mini Kit method and the TRI Reagent protocol as they are among the most commonly used techniques for total RNA isolation, with other methods often considered time-consuming and requiring larger input amounts [6]. The RNeasy Mini Kit, which employs phenol-chloroform (organic extraction), offers the advantage of isolating RNA from a single sample. However, it can be costly and yield lower quantities of samples, making the TRI Reagent protocol a viable alternative [3].

Researchers typically assess the quantity and quality of isolated RNA by examining absorbance ratios, specifically the 260/280 and 260/230 ratios, using a Nanodrop spectrometer. Ratios closer to 2.0 indicate better RNA quality. In line with Susanna Cirera's study, a combination of both methods yielded excellent isolate purity, with a 260/280 ratio of 2.00±0.049 and a 260/230 ratio of 1.73±0.189 [6]. Our study's results align with these findings. The RNeasy Mini Kit excels in terms of purity compared to the TRI Reagent protocol. This can be attributed to the RNeasy Mini Kit's use of silica film-based bonding technology, effectively removing contaminants such as proteins, genomic DNA, and polysaccharides. Consequently, researchers are more likely to obtain cleaner RNA samples for subsequent experiments. However, the TRI Reagent method yields a higher percentage of RNA samples compared to the RNeasy Mini Kit. Therefore, combining both methods can produce ample amounts of high-quality total RNA from adipose tissue, suitable for downstream applications such as RT-qPCR, microarrays, and high-throughput sequencing [6].

Despite their advantages, both methods have drawbacks, notably their cost. Commercial kits, although commonly used, tend to be expensive. However, the inherent automation capabilities of silica spin column extraction methods offer significant advantages. In the case of TRI reagents, RNA purity needs to be considered, as other substances like proteins and salts may still be present [6]. Hence, a flexible approach involving the combination of both methods can ensure efficient and cost-effective RNA isolation while maintaining high quality.

Previous research employing microarray analysis has identified several candidate genes as potential biomarkers for adipose tissue, including MEST, SFRP5, and SCD1 [10]. MEST and SFRP5-encoded proteins have been found to inhibit Wnt signalling, thereby suppressing mitochondrial respiration and promoting lipid accumulation in fat depots. In a mouse model of diet-induced obesity, higher expression levels of MEST and SFRP5 were significantly correlated with adiposity in both subcutaneous and visceral adipose tissues [10]. However, the mRNA and protein levels of MEST and SFRP5 were found to be sensitive to the age of adipose tissue, being severely suppressed in aging mice despite continued adipose expansion [11]. Although their expression levels decrease after reaching a plateau, MEST and SFRP5 have been identified as biomarkers for healthy adipocytes [10, 11]. SCD1 protein plays a crucial role in catalysing the biosynthesis of monounsaturated fatty acids, regulating lipogenesis. Due to its high expression during adipogenic differentiation, SCD1 is considered an adipogenesis biomarker. Like MEST and SFRP5, SCD1 did not exhibit significant changes in response to aging in mice with high adiposity [11].

D.T. Truong, et al. (2019) [11] conducted a study on C57BL/6J and 129S mouse models to investigate the impact of developmental phases on the function and expression of key adipose biomarkers. TRI reagent was used to extract total RNA from RP, EP, ING, and iBAT tissue, and RNA Mini Kit was employed in several independent experiments [11]. Another study established a positive correlation between SCD1, SFRP5, and MEST expression and the adiposity of mice subjected to a high-fat diet [10]. For cost-effectiveness reasons, a different study employed the TRI reagent protocol instead of the RNeasy Mini Kit for total RNA isolation. The authors reported similar results, with increased expression of SFRP5 and MEST in obese mice correlating with fat depot expansion, suggesting the use of SFRP5 and MEST as biomarkers for healthy adipocytes [10]. Concerns regarding the purity of products extracted by the TRI reagent led R.P.A. Koza, et al. (2016) [13] to use the RNeasy Mini Kit for RNA purification before measuring MEST and SFRP5 expression. They also observed significant correlations between MEST and SFRP5 expression and adiposity in inbred mice. Thus, the findings regarding the expression of these adipose biomarkers remain consistent irrespective of the RNA isolation methods. However, various modifications, such

as additional ethanol washes or reduced reagent volumes, can be applied to optimize the quality and quantity of total RNA isolated through standard protocols [14]. Our study's results indicate that the mRNA expression levels of MEST, SFRP5, and SCD1 in adipose tissue are not affected by the RNA isolation methods employed.

## 5. Conclusions

This study conducted a comparative analysis of total RNA extraction from frozen adipose tissue of mice using the RNeasy Mini Kit and the TRI Reagent method. The study assessed the concentration and quality of the extracted RNA and measured the mRNA expression levels of MEST, SFRP5, and SCD1 through RT-PCR. The findings indicated that the RNeasy Mini Kit yielded a higher RNA concentration with less variability in results when compared to the TRI Reagent method. Furthermore, the RNeasy Mini Kit provided RNA samples of superior purity, as evidenced by a higher 260/230 ratio. Despite slightly elevated mRNA expression levels of the three biomarkers observed in RNA extracted using the TRI Reagent method, these differences did not reach statistical significance. In summary, both the RNeasy Mini Kit and the TRI Reagent method are viable options for total RNA extraction. However, the RNeasy Mini Kit is recommended when aiming for higher RNA concentration and purity. The choice of method should be tailored to the specific downstream application of the RNA, taking into consideration the research objectives and priorities.

## CRediT author statement

Dinh Toi Chu: Conceptualisation, Methodology, Validation, Formal analysis, Data curation, Visualisation, Supervision, Writing - Reviewing and Editing; Hue Vu Thi: Methodology, Data curation, Writing - Original draft preparation; Ngoc Hoan Le: Data curation, Formal analysis, Writing - Reviewing and Editing.

## ACKNOWLEDGEMENTS

This research is funded by the Vietnam National Foundation for Science and Technology Development (NAFOSTED) under grant number 106.02-2019.314.

## COMPETING INTERESTS

The authors declare that there is no conflict of interest regarding the publication of this article.

## REFERENCES

[1] QIAGEN (2019), *RNeasy® Mini Handbook*, 101pp.

[2] E.E. Kershaw, J.S. Flier (2004), "Adipose tissue as an endocrine organ", *J. Clin. Endocrinol Metab.*, **89(6)**, pp.2548-2556, DOI: 10.1210/jc.2004-0395.

[3] P. Tan, E. Pepin, J.L. Lavoie (2018), "Mouse adipose tissue collection and processing for RNA analysis", *J. Vis. Exp.*, **131(31)**, DOI: 10.3791/57026.

[4] K. Hemmrich, B. Denecke, N.E. Paul, et al. (2010), "RNA isolation from adipose tissue: An optimised procedure for high RNA yield and integrity", *Laboratory Medicine*, **41(2)**, pp.104-106, DOI: 10.1309/LMFSBPUOA19MH5BV.

[5] R.N. Pena, A. Canovas, J. Estany (2010), "Technical note: Efficient protocol for isolation of total ribonucleic acid from lyophilised fat and muscle pig samples", *J. Anim. Sci.*, **88(2)**, pp.442-445, DOI: 10.2527/jas.2009-2298.

[6] S. Cirera (2013), "Highly efficient method for isolation of total RNA from adipose tissue", *BMC Research Notes*, **6**, DOI; 101186/1756-0500-6-472.

[7] M. Jura, J. Jarosławska, D.T. Chu, et al. (2016), "Mest and Sfrp5 are biomarkers for healthy adipose tissue", *Biochimie*, **124**, pp.124-133, DOI: 10.1016/j.biochi.2015.05.006.

[8] D.T. Chu, E. Malinowska, M. Jura, et al. (2017), "C57BL/6J mice as a polygenic developmental model of diet-induced obesity", *Physiological Reports*, **5(7)**, DOI: 10.14814/phy2.13093.

[9] Z. Lacinova, M. Dolinkova, D. Haluzikova, et al. (2008), "Comparison of manual and automatic (MagNA pure) isolation methods of total RNA from adipose tissue", *Molecular Biotechnology*, **38(3)**, pp.195-201, DOI: 10.1007/s12033-007-9016-5.

[10] D.T. Chu, E. Malinowska, B.G. Kozak, et al. (2014), "Expression of adipocyte biomarkers in a primary cell culture models reflects preweaning adipobiology", *J. Biol. Chem.*, **289(26)**, pp.18478-18488, DOI: 10.1074/jbc.M114.555821.

[11] D.T. Truong, N.V.N. Minh, D.P. Nhung, et al. (2019), "Short tandem repeats used in preimplantation genetic testing of β-thalassemia: Genetic polymorphisms for 15 linked loci in the Vietnamese population", *Open Access Maced. J. Med. Sci.*, **24(7)**, pp.4383-4388, DOI: 10.3889/oamjms.2019.840.

[12] L. Nikonova, R.A. Koza, T. Mendoza, et al. (2008), "Mesoderm-specific transcript is associated with fat mass expansion in response to a positive energy balance", *The FASEB Journal*, **22(11)**, pp.3925-3937, DOI: 10.1096/fj.08-108266.

[13] R.P.A. Koza, D.C. Higgins, R.A. Koza (2016), "Adipose tissue Mest and Sfrp5 are concomitant with variations of adiposity among inbred mouse strains fed a non-obesogenic diet", *Biochimie*, **124**, pp.134-140, DOI: 10.1016/j.biochi.2015.05.007.

[14] D. Roy, S. Tomo, A. Modi, et al. (2020), "Optimising total RNA quality and quantity by phenol-chloroform extraction method from human visceral adipose tissue: A standardisation study", *MethodsX*, **7**, DOI: 10.1016/j.mex.2020.101113.

DOI: 10.31276/VJSTE.66(1).90-95

# Expression of several deubiquitinase and tyrosine phosphatase genes involved in inflammatory response in lymphoma

**Nguyen Hoang Giang[1], Nguyen Trong Ha[2], Nguyen Thi Xuan[1*]**

*[1]Institute of Genome Research, Vietnam Academy of Science and Technology, 18 Hoang Quoc Viet Street, Nghia Do Ward, Cau Giay District, Hanoi, Vietnam*
*[2]103 Hospital, Vietnam Military Medical University, 261 Phung Hung Street, Phuc La Ward, Ha Dong District, Hanoi, Vietnam*

Received 30 January 2023; revised 24 April 2023; accepted 28 April 2023

***Abstract:***

**Lymphoma represents a heterogeneous group of cancers affecting the lymphatic system, encompassing non-Hodgkin lymphoma (NHL) and Hodgkin lymphoma (HL). The majority of NHL cases originate from B cells. HL is characterized by the presence of rare Hodgkin and Reed-Sternberg cells. Within the context of the inflammatory response, two SH2 domain-containing protein tyrosine phosphatases (SHPs), namely *SHP-1* and *SHP-2*, serve as negative regulators. Deubiquitinating enzymes (DUBs) play a crucial role in inhibiting NF-κB activation in response to various stimuli. This study focuses on the DUBs *OTUB1*, *OTUB2*, and *Cezanne*. Blood samples were collected from 50 NHL patients, 26 HL patients, and 50 healthy individuals. Quantitative RT-PCR was employed to assess the mRNA expression of *OTUB1, OTUB2*, *Cezanne, SHP-1*, and *SHP-2*, while ELISA was used to determine IL-6 and CA125 concentrations. The results revealed that the mRNA level of *OTUB1* was significantly downregulated in NHL patients but not in HL patients. Notably, Cezanne expression was downregulated in lymphoma patients, with significantly lower levels observed in HL compared to NHL patients. Furthermore, *SHP-1* mRNA expression was significantly lower in the NHL group compared to the HL group or healthy individuals. Conversely, *SHP-2* gene expression was upregulated in NHL patients but remained unchanged in HL patients. In conclusion, these findings highlight significant differences in the expressions of *DUB* and *SHP* genes and the inflammatory response in lymphoma patients. This study provides a foundation for further investigation into the roles of DUBs and tyrosine phosphatases in regulating the functional activation of lymphoma cells.**

***Keywords:*** **CA125, deubiquitinating enzymes, IL-6, lymphoma, tyrosine phosphatases.**

***Classification numbers:*** **3.4, 3.5**

## 1. Introduction

Lymphoma is a group of cancers affecting the lymphatic system, involving cells of the immune system. Lymphoma initiates when healthy B cells, T cells, or natural killer (NK) cells in the lymphatic system undergo alterations and uncontrolled growth, leading to the formation of tumours. It is comprised of two main subtypes: NHL and HL [1]. NHL is a lymphoproliferative disorder, with the majority originating from B cells, while the remainder arises from T lymphocytes or NK cells [2]. Approximately 90% of all lymphomas are NHL, with the remaining 10% classified as HL [3]. HL is a rare form of cancer characterized by the presence of rare Hodgkin and Reed-Sternberg cells (HRS) that originate from a subtype of B cells and are typically found in the bone marrow and peripheral blood [4, 5]. Several studies have indicated that lymphoma patients, particularly those with poor outcomes, exhibit elevated serum levels of carbohydrate antigen 125 (CA-125), a commonly used tumour biomarker, although it is more commonly associated with ovarian cancer [6, 7].

DUB genes, including OTU domain-containing ubiquitin aldehyde binding protein *OTUB1*, *OTUB2*, and *OTUD7B* (*Cezanne*), play pivotal roles in regulating the expression of various signal transduction pathways, such as NF-κB [8-10], by removing specific types

*Corresponding author: Email: xuannt@igr.ac.vn

of polyubiquitin chains from substrate proteins. This activity leads to the induction of various cellular biological processes. Recent research has demonstrated the involvement of *OTUB1* and *OTUB2* in modulating the development of solid cancers, including breast, liver, and lung cancers [9, 11, 12]. Mice lacking *OTUB1* exhibit abnormal responses in CD8 T cells and NK cells [13]. *Cezanne* inactivation has been associated with disease progression and poor prognosis in hepatocellular carcinoma [14]. Despite the well-established effects of DUBs on the activation of solid cancer cells, their impact on the biological activation of lymphoma cells remains largely unexplored.

Similar to DUBs, SH2 domain-containing protein tyrosine phosphatases (SHPs) are crucial for a wide range of cellular processes in response to external stimuli. Two protein tyrosine phosphatases (PTPs), *SHP-1* and *SHP-2*, are recognised as negative regulators of the inflammatory response, acting via NF-κB and STAT signalling pathways [15]. Mice lacking *SHP-1* display myelin deficiency due to increased inflammatory mediators [16]. In leukaemia and lymphoma, *SHP-1* expression is often inactivated as a result of DNA methylation of its promoter region [17]. Conversely, *SHP-2* levels are elevated in leukaemia and diffuse large B-cell lymphoma [18, 19]. In the context of solid cancers, *SHP-2* serves as a negative regulator of interferon production, diminishing cytotoxic effects in fibroblast cells [20].

This study aims to investigate the mRNA expressions of DUBs, SHPs, and the inflammatory response in Vietnamese lymphoma patients.

## 2. Materials and methods

### *2.1. Patients and control subjects*

Peripheral blood samples were collected from 76 untreated patients diagnosed with two types of lymphomas: 50 NHL and 26 HL, at the National Hospital of Haematology and Blood Transfusion and the 103 Military Hospital in Hanoi, Vietnam. The control group consisted of 50 healthy subjects. None of the individuals in the control group were on medication or had a known acute or chronic disease. All patients and volunteers provided written consent to participate in the study. Personal care and experimental procedures were conducted in accordance with Vietnamese laws governing human welfare and were approved by the Ethical Committee of the Institute of Genome Research, Vietnam Academy of Science and Technology. All experimental protocols involving human subjects adhered to the Helsinki Declaration of 1975, as revised in 2008.

### *2.2. RNA extraction and real-time RT-PCR*

Total mRNA was isolated using the Qiashredder and RNeasy Mini Kit from Qiagen, following the manufacturer's instructions. For first-strand cDNA synthesis, 1 µg of total RNA in 12.5 µl of DEPC-treated $H_2O$ was mixed with 1 µl of oligo-dT primer (500 µg/ml, Invitrogen) and heated for 2 min at 70°C. Quantitative real-time PCR using the LightCycler System (Roche Diagnostics) was employed to determine transcript levels of *SHP-1* and *SHP-2*, using the following primers (Table 1).

**Table 1. List of primers used for RT-PCR.**

| Genes | Direction | Primer sequence |
|---|---|---|
| *GAPDH* | Forward | 5'-GGAGCGAGATCCCTCCAAA-3' |
| *GAPDH* | Reverse | 5'-GGCTGTTGTCATACTTCTCAT-3' |
| *OTUD7B* | Forward | 5'-ACAATGTCCGATTGGCCAGT-3' |
| *OTUD7B* | Reverse | 5'-ACAGTGGGATCCACTTCACATTC-3' |
| *OTUB-1* | Forward | 5'-ACAGAAGATCAAGGACCTCCA-3' |
| *OTUB-1* | Reverse | 5'-CAACTCCTTGCTGTCATCCA-3' |
| *OTUB-2* | Forward | 5'-CTCACGTCGGCCTTCATCA-3' |
| *OTUB-2* | Reverse | 5'-GCCATGGGCTCTACTTCGT-3' |
| *SHP-1* | Forward | 5'-GCCCAGTTCATTGAAACCAC-3' |
| *SHP-1* | Reverse | 5'-GAGGGAACCCTTGCTCTTCT-3' |
| *SHP-2* | Forward | 5'GAGAGCAATGACGGCAAGTCT-3' |
| *SHP-2* | Reverse | 5'-CCTCCACCAACGTCGTATTTC-3' |

PCR reactions were conducted in a final volume of 20 µl, comprising 2 µl of cDNA, 2.4 µl of $MgCl_2$ (3 µM), 1 µl of primer mix (0.5 µM of both primers), 2 µl of cDNA Master SybrGreen I mix (Roche Molecular Biochemicals), and 12.6 µl of DEPC-treated water. Amplification of the target DNA involved 40 cycles of 95ºC for 10 s, 62ºC for 10 s, and 72ºC for 16 s, each with a temperature transition rate of 20ºC/s, a secondary target temperature of 50ºC, and a step size of 0.5ºC. Subsequently, melting curve analysis was conducted at 95ºC for 0 s, 60ºC for 10 s, and 95ºC for 0 s to ascertain the melting temperature of primer dimers and specific

PCR products. The ratio between the respective gene and corresponding GAPDH was calculated for each sample using the $2^{-\Delta CT}$ method.

### 2.3. Cytokine quantification

Serum samples were isolated from the blood samples of NHL and HL patients as well as healthy subjects, and these samples were stored at -20˚C until utilised for ELISA. IL-6 and CA-125 concentrations were determined using ELISA kits from Thermo Scientific, following the manufacturer's protocol.

### 2.4. Statistical analysis

Statistical analysis was performed using SPSS version 20 (IBM, USA). Differences between the control and patient groups were assessed for significance using a non-parametric Mann-Whitney U test. All statistical tests were two-sided, and the level of significance was set at $p<0.05$.

## 3. Results and discussion

### 3.1. Analysis of DUB gene expression in lymphoma patients

In terms of DUB gene expression, our findings revealed that the mRNA level of *OTUB1* was significantly lower in NHL patients compared to the control group, while no significant difference was observed in HL patients (Fig. 1A). In contrast, the expression of *OTUB2* remained unchanged in both NHL and HL groups (Fig. 1B). Importantly, we noted suppressed expression of *Cezanne* in both NHL and HL groups, with a notably more significant decrease in HL compared to NHL patients.

The downregulation of *Cezanne* in both NHL and HL groups and of *OTUB1* in NHL patients represents a novel discovery in this study. These findings suggest a pivotal role for *OTUB1* and *Cezanne* in influencing the development of lymphoma cells. Previous studies have primarily associated the effects of *OTUB1*, *OTUB2*, and *Cezanne* with the regulation of cellular processes in solid cancers [9, 11, 12, 14].

### 3.2. Expression level of SHP genes in lymphoma patients

To evaluate the activation of the SHP signalling pathway, we observed that mRNA expression of *SHP-1* was significantly reduced in the NHL group, while it remained unaltered in the HL group compared to healthy individuals (Fig. 2A). Intriguingly, the level of *SHP-1* was markedly lower in NHL compared to HL patients. This aligns with previous reports of reduced *SHP-1* expression in various cancers [17, 21], where *SHP-1* deficiency leads to impaired apoptosis and diminished treatment response [22]. In contrast, gene expression of *SHP-2* was elevated in NHL patients but exhibited no significant change in HL patients (Fig. 2B). Overexpression of *SHP-2* has also been detected in patients with leukaemia [19]. Consequently, the distinct roles of *SHP-1* and *SHP-2* in different cancer cell types, with their opposing effects, warrant further investigation into the molecular mechanisms governing the function of NHL cells.

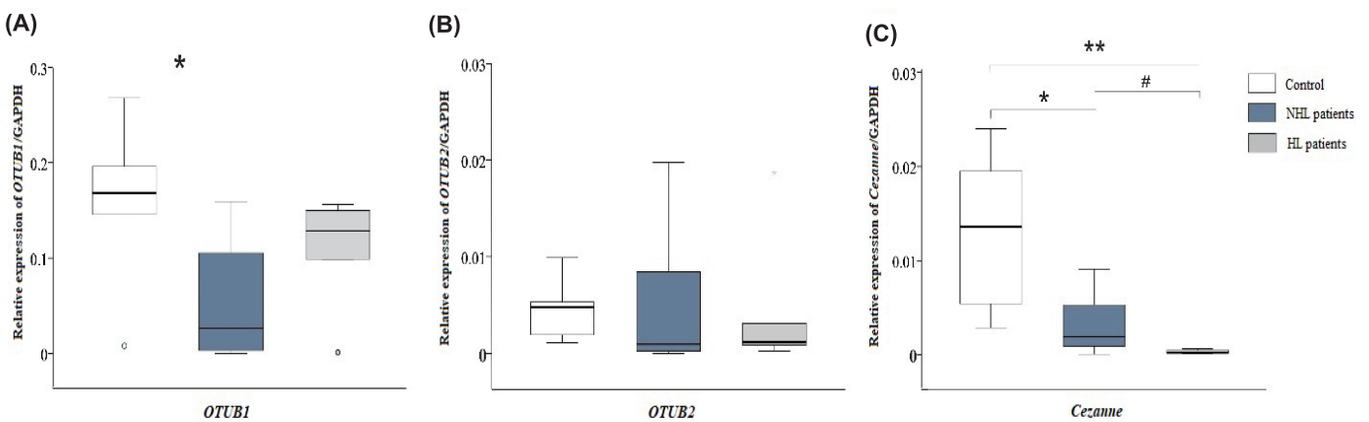


**Fig. 1. Box plot analysis of *OTUB1* (A), *OTUB2* (B), and *Cezanne* (C) gene expression in NHL (blue bar), HL (grey bars) patients, and the control group (white bar).** *($p<0.05$) and **($p<0.01$) indicate a significant difference between control and patient groups and #($p<0.05$) indicates a significant difference between NHL and HL groups (Mann-Whitney U test).

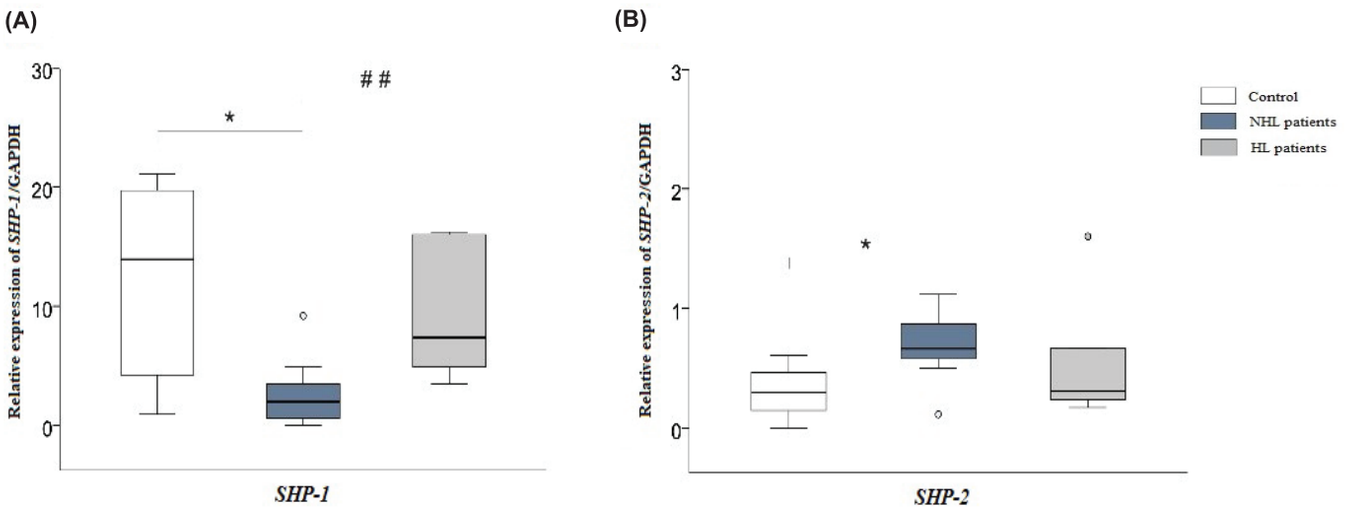


**Fig. 2. Box plot analysis of *SHP-1* (A) and *SHP-2* (B) gene expression in NHL (blue bar), HL (grey bars) patients, and the control group (white bar).** *(p<0.05) indicates a significant difference between control and patient groups and #(p<0.01) indicates a significant difference between NHL and HL groups (Mann-Whitney U test).

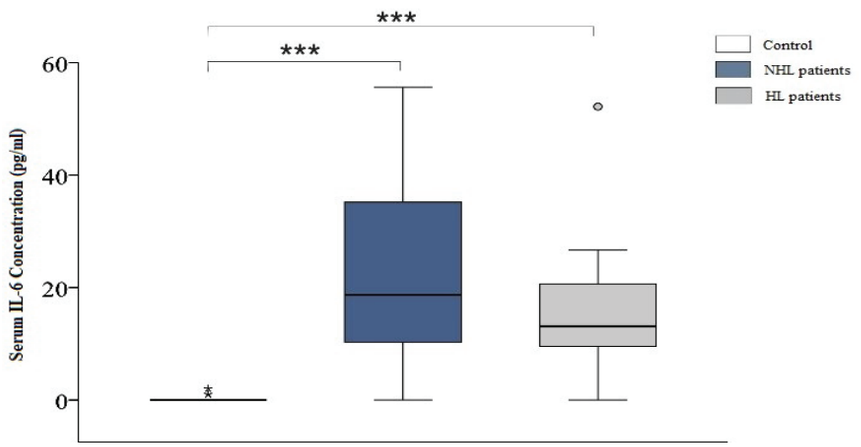


**Fig. 3. Box plot analysis of IL-6 serum level in NHL (grey bar), HL (blue bar), and the control group (white bar).** ***(p<0.001) indicates a significant difference between control and patient groups (Mann-Whitney U test).

### *3.3. Serum IL-6 level in lymphoma patients*

A recent study [23] has demonstrated the involvement of SHP molecules in the regulation of cytokine IL-6 in cancer cells, with higher levels of IL-6 reported in lymphoma patients [24]. The activation of *SHP-1* has also been associated with IL-6 release in prostate cancer cells [23]. Similarly, our findings indicate a significant increase in serum IL-6 concentration in both NHL and HL patient groups (Fig. 3).

### *3.4. Serum CA125 level in lymphoma patients*

The secretion of IL-6 has been linked to an elevated level of CA125 by cancer cells [25]. Consequently, we examined the serum CA125 levels in NHL, HL, and control groups using ELISA. The results revealed a significant increase in serum CA125 concentration in both NHL and HL groups, with a notably higher level in HL compared to NHL patients (Fig. 4). CA125 has previously been identified as a marker associated with the development and pathogenesis of lymphoma and ovarian cancer [6, 7]. In this study, we additionally observed that the frequency of lymphoma patients with CA125 levels exceeding the clinical cutoff of 35 UI/ml was higher in HL (48.14%) than in NHL (32%) patients. Notably, patients with CA125 levels ≥35 UI/ml tend to have lower survival rates than

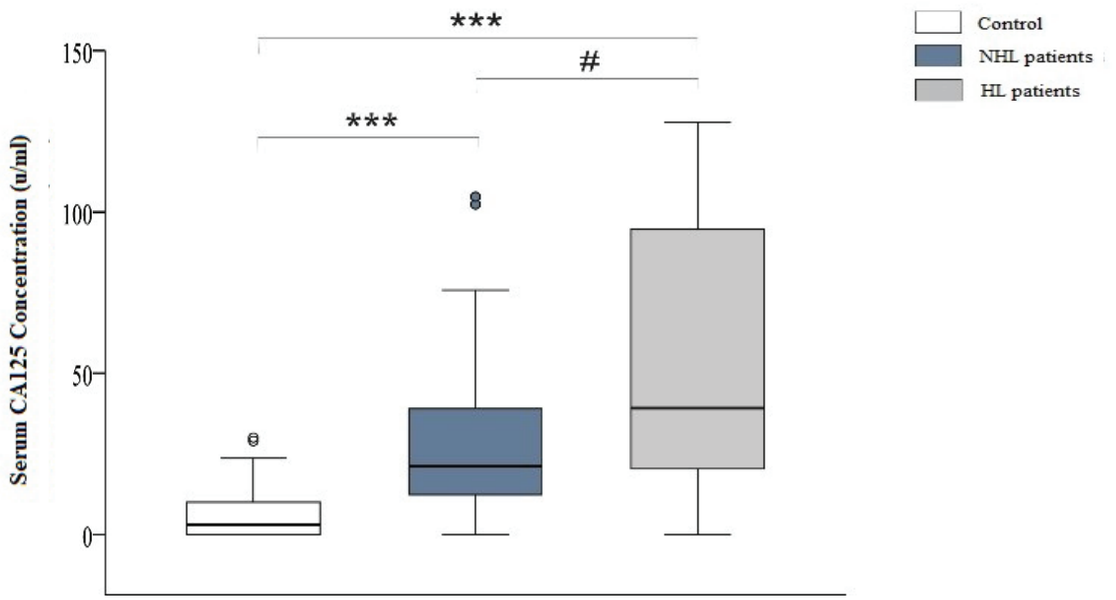


**Fig. 4. Box plot analysis of serum CA125 level in NHL (grey bar), HL (blue bar), and the control group (white bar).** ***(p<0.001) indicates a significant difference between control and patient groups and #(p<0.05) indicates a significant difference between NHL and HL groups (Mann-Whitney U test).

those with normal CA125 levels before any treatment [6]. These findings suggest a potential relationship between the level of CA125 and the modulatory activation of SHP pathways in lymphoma cells.

Additionally, we investigated the potential association between the expressions of *DUB* and *SHP* genes and the inflammatory response in lymphoma patients. However, no significant associations were observed.

## 4. Conclusions

Our results have revealed significant differences in the expressions of *DUB* and *SHP* genes and the inflammatory response in lymphoma patients. Specifically, the expressions of *SHP*, *OTUB1*, and *Cezanne* genes appear to be sensitive to the activation of NHL cells. Furthermore, the altered expressions of *Cezanne*, IL-6, and CA125 concentrations are dependent on the specific cell types of lymphoma. This study provides valuable insights and warrants further investigation into the roles of DUBs and tyrosine phosphatases in regulating the functional activation of lymphoma cells.

## CRediT author statement

Nguyen Hoang Giang, Nguyen Trong Ha: Conceptualisation and Design, Acquisition of data, Analysis and Interpretation of data; Nguyen Thi Xuan: Conceptualisation and Design, Acquisition of data, Analysis and Interpretation of data, Writing.

## ACKNOWLEDGEMENTS

This research is funded by the Vietnam Academy of Science and Technology (VAST) under grant number TDTBG0.05/21-23.

## COMPETING INTERESTS

The authors declare that there is no conflict of interest regarding the publication of this article.

## REFERENCES

[1] R.L. King, E.D. Hsi, W.C. Chan, et al. (2023), "Diagnostic approaches and future directions in Burkitt lymphoma and high-grade B-cell lymphoma", *Virchows Arch*, **482(1)**, pp.193-205, DOI: 10.1007/s00428-022-03404-6.

[2] C. Küçük, X. Hu, B. Jiang, et al. (2015), "Global promoter methylation analysis reveals novel candidate tumor suppressor genes in natural killer cell lymphoma", *Clin. Cancer Res.*, **21(7)**, pp.1699-1711, DOI: 10.1158/1078-0432.CCR-14-1216.

[3] E.N. Mugnaini, N. Ghosh (2016), "Lymphoma", *Prim. Care*, **43(4)**, pp.661-675, DOI: 10.1016/j.pop.2016.07.012.

[4] A.A. Ibraheem, F.M. Mottaghy, M.E. Juweid (2023), "PET/CT in Hodgkin lymphoma: An update", *Semin. Nucl. Med.*, **53(3)**, pp.303-319, DOI: 10.1053/j.semnuclmed.2022.10.006.

[5] S.M. Ansell (2015), "Hodgkin lymphoma: Diagnosis and treatment", *Mayo. Clin. Proc.*, **90(11)**, pp.1574-1583, DOI: 10.1016/j.mayocp.2015.07.005.

[6] F. Russo, S. Lastoria, G. Svanera, et al. (2007), "Long-term follow-up study on the role of serum CA-125 as a prognostic factor in 221 newly diagnosed patients with Hodgkin's lymphoma", *Leuk Lymphoma*, **48(4)**, pp.723-730, DOI: 10.1080/10428190601183710.

[7] G. Wei, Z. Yuping, W. Jun, et al. (2006), "CA125 expression in patients with non-hodgkin's lymphoma", *Leuk Lymphoma*, **47(7)**, pp.1322-1326, DOI: 10.1080/10428190600580882.

[8] K. Enesa, M. Zakkar, H. Chaudhury, et al. (2008), "NF-kappaB suppression by the deubiquitinating enzyme Cezanne: A novel negative feedback loop in pro-inflammatory signaling", *J. Biol. Chem.*, **283(11)**, pp.7036-7045, DOI: 10.1074/jbc.M708690200.

[9] Z.L. Gu, J. Huang, L.L. Zhen (2020), "Knockdown of otubain 2 inhibits liver cancer cell growth by suppressing NF-kappaB signaling", *Kaohsiung J. Med. Sci.*, **36(6)**, pp.399-404, DOI: 10.1002/kjm2.12187.

[10] F. Mulas, X. Wang, S. Song, et al. (2020), "The deubiquitinase OTUB1 augments NF-kappaB-dependent immune responses in dendritic cells in infection and inflammation by stabilizing UBC13", *Cell Mol. Immunol.*, **18(6)**, pp.1512-1527, DOI: 10.1038/s41423-020-0362-6.

[11] M.F. Baietti, M. Simicek, L.A. Asbagh, et al. (2016), "OTUB1 triggers lung cancer development by inhibiting RAS monoubiquitination", *EMBO Mol. Med.*, **8(3)**, pp.288-303, DOI: 10.15252/emmm.201505972.

[12] U. Karunarathna, M. Kongsema, S. Zona, et al. (2016), "OTUB1 inhibits the ubiquitination and degradation of FOXM1 in breast cancer and epirubicin resistance", *Oncogene*, **35(11)**, pp.1433-1444, DOI: 10.1038/onc.2015.208.

[13] X. Zhou, J. Yu, X. Cheng, et al. (2019), "The deubiquitinase OTUB1 controls the activation of $CD8^+$ T cells and NK cells by regulating IL-15-mediated priming", *Nat. Immunol.*, **20(7)**, pp.879-889, DOI: 10.1038/s41590-019-0405-2.

[14] J.H. Wang, W. Wei, Z.X. Guo, et al. (2015), "Decreased *Cezanne* expression is associated with the progression and poor prognosis in hepatocellular carcinoma", *J. Transl. Med.*, **13**, DOI: 10.1186/s12967-015-0396-1.

[15] J. Zhang, F. Zhang, R. Niu (2015), "Functions of SHP-2 in cancer", *J. Cell. Mol. Med.*, **19(9)**, pp.2075-2083, DOI: 10.1111/jcmm.12618.

[16] G.P. Christophi, M. Panos, C.A. Hudson, et al. (2009), "Macrophages of multiple sclerosis patients display deficient *SHP-1* expression and enhanced inflammatory phenotype", *Lab. Invest.*, **89(7)**, pp.742-759, DOI: 10.1038/labinvest.2009.32.

[17] Y. Li, L. Yang, Y. Pan, et al. (2014), "Methylation and decreased expression of *SHP-1* are related to disease progression in chronic myelogenous leukaemia", *Oncol. Rep.*, **31(5)**, pp.2438-2446, DOI: 10.3892/or.2014.3098.

[18] C. Voena, C. Conte, C. Ambrogio, et al. (2007), "The tyrosine phosphatase *SHP-2* interacts with NPM-ALK and regulates anaplastic lymphoma cell growth and migration", *Cancer Res.*, **67(9)**, pp.4278-4286, DOI: 10.1158/0008-5472.CAN-06-4350.

[19] R. Xu (2007), "*SHP-2*, a novel oncogenic tyrosine phosphatase and potential therapeutic target for human leukemia", *Cell Res.*, **17(4)**, pp.295-297, DOI: 10.1038/cr.2007.18.

[20] M. You, D.H. Yu, G.S. Feng (1999), "*SHP-2* tyrosine phosphatase functions as a negative regulator of the interferon-stimulated Jak/STAT pathway", *Mol. Cell Biol.*, **19(3)**, pp.2416-2424, DOI: 10.1128/MCB.19.3.2416.

[21] S. Takeuchi, M. Matsushita, M. Zimmermann, et al. (2011), "Clinical significance of aberrant DNA methylation in childhood acute lymphoblastic leukemia", *Leuk. Res.*, **35(10)**, pp.1345-1349, DOI: 10.1016/j.leukres.2011.04.015.

[22] K. Nakata, Y. Suzuki, T. Inoue, et al. (2011), "Deficiency of *SHP-1* leads to sustained and increased ERK activation in mast cells, thereby inhibiting IL-3-dependent proliferation and cell death", *Mol. Immunol.*, **48(4)**, pp.472-480, DOI: 10.1016/j.molimm.2010.10.001.

[23] H. Tassidis, Z. Culig, A.G. Wingren, et al. (2010), "Role of the protein tyrosine phosphatase *SHP-1* in Interleukin-6 regulation of prostate cancer cells", *Prostate*, **70(14)**, pp.1491-1500, DOI: 10.1002/pros.21184.

[24] I. Dlouhy, X. Filella, J. Rovira, et al. (2017), "High serum levels of soluble interleukin-2 receptor (sIL2-R), interleukin-6 (IL-6) and tumor necrosis factor alpha (TNF) are associated with adverse clinical features and predict poor outcome in diffuse large B-cell lymphoma", *Leuk. Res.*, **59**, pp.20-25, DOI: 10.1016/j.leukres.2017.05.014.

[25] K. Fan, C. Yang, Z. Fan, et al. (2018), "MUC16 C terminal-induced secretion of tumor-derived IL-6 contributes to tumor-associated Treg enrichment in pancreatic cancer", *Cancer Lett.*, **418**, pp.167-175, DOI: 10.1016/j.canlet.2018.01.017.

DOI: 10.31276/VJSTE.66(1).96-103

# Anti-inflammatory effect of gallic acid-conjugated chitooligosaccharides in lipopolysaccharide-stimulated RAW 264.7 macrophages

**Van-Hoai Bui[1, 2, 3], Hong-Tham N. Vo[1, 2, 3], Thanh-Tuan Duong[1, 2], Se-Kwon Kim[4], Dai-Nghiep Ngo[1, 2*]**

*[1]Deparment of Biochemistry, Faculty of Biology-Biotechnology, University of Science, Vietnam National University - Ho Chi Minh City, 227 Nguyen Van Cu Street, Ward 4, District 5, Ho Chi Minh City, Vietnam*
*[2]Vietnam National University - Ho Chi Minh City, Linh Trung Ward, Thu Duc City, Ho Chi Minh City, Vietnam*
*[3]Ho Chi Minh City University of Industry and Trade (HUIT), 140 Le Trong Tan Street, Tay Thanh Ward, Tan Phu District, Ho Chi Minh City, Vietnam*
*[4]Department of Marine Science and Convergence Engineering, College of Science and Technology, Hanyang University, 55 Hanyangdaehak-ro, Sangnok-gu, Ansan-si, Gyeonggi-do 11558, Korea*

Received 25 May 2023; revised 4 July 2023; accepted 5 September 2023

***Abstract:***

**The aim of the present study is to investigate the anti-inflammatory effect of gallic acid grafted onto COS chains (GA-COS), focusing on the reduction of nitric oxide production, downregulation of inflammatory signals such as inducible nitric oxide synthase (iNOS), gene expression of cytokines such as TNF-α, IL-1β, IL-6, and nuclear factor kappa B (NF-κB) signalling, including the p50 and p65 subunits. The anti-inflammatory effect is mediated through the reduction of nitric oxide production and downregulation of inflammatory proteins such as inducible nitric oxide synthase (iNOS), gene expression of cytokines like TNF-α, IL-1β, IL-6, and nuclear factor kappa B (NF-κB) signalling, including the p50 and p65 subunits. Target proteins were identified by western blot analysis with specific monoclonal antibodies. The levels of gene expression were determined by the RT-PCR method. The results demonstrate that GA-COS effectively reduces nitric oxide generation and downregulates iNOS protein and cytokine expression and NF-κB signalling in lipopolysaccharide (LPS) -induced RAW 264.7 cells. GA-COS exhibits significantly enhanced anti-inflammatory activity compared to the free chitooligosaccharide chain. This study lays the groundwork for future research to demonstrate that GA-COS holds significant potential as a novel compound for the prevention of inflammatory diseases.**

***Keywords:*** **anti-inflammatory activity, chitooligosaccharide, chitooligosaccharide conjugated gallic acid, nitric oxide, RAW 264.7 macrophage cells.**

***Classification numbers:*** **3.4, 3.5**

## 1. Introduction

In response to external agents such as pathogen invasion or exposure to toxic compounds, as well as internal factors such as cellular damage, the body's immune system initiates an inflammatory response [1]. Acute inflammation, characterized by rapid onset over minutes or hours and typically resolving within days, aims to heal intracellular damage. In contrast, chronic inflammation is a prolonged state of acute inflammation resulting from persistent infections that remain unresolved [2, 3]. Chronic inflammation is associated with various diseases, including stroke, chronic respiratory diseases, heart disorders, and cancer [4].

Macrophages, through the secretion of pro-inflammatory cytokines, play a crucial role in the regulation of inflammation [5]. Macrophages can be activated by stimuli such as bacterial LPS from gram-negative bacteria and pro-inflammatory cytokines [6]. In light of these observations, our study focuses on RAW 264.7 mouse macrophages stimulated with LPS as a model to investigate the anti-inflammatory activity of the synthesized compound. However, the regulation of inflammatory modulators involves complex feedback mechanisms [7]. In this study, we investigate the regulation of inflammatory modulators in LPS-stimulated RAW 264.7 cells through the NF-κB signalling pathways.

*[*]Corresponding author: Email: ndnghiep@hcmus.edu.vn*

In recent years, there has been growing interest in the use of bioactive compounds, particularly phenolic acids, for the treatment of chronic inflammation. Among phenolic acids, GA is a natural compound known for its various biological activities, including anti-inflammatory properties. Nevertheless, GA's limited solubility in water can affect its metabolism and absorption in the human body. Therefore, researchers have explored the grafting of GA onto chitooligosaccharide chains, non-toxic and water-soluble polysaccharides derived from chitin through a deacetylation process, to enhance the solubility of the synthesized compound and improve the bioactivity of the original COS chain [8, 9].

In previous research, GA-COS *via* the free radical-mediated conjugation method demonstrated enhanced antioxidant activities [10, 11]. However, there is currently no information available regarding the anti-inflammatory action of GA-COS against LPS-stimulated macrophages. The aim of the present study is to investigate the anti-inflammatory effect of GA-COS, focusing on the reduction of nitric oxide production, downregulation of inflammatory signals such as inducible iNOS, gene expression of cytokines such as TNF-α, IL-1β, IL-6, and NF-κB signalling, including the p50 and p65 subunits.

## 2. Materials and methods

### *2.1. Materials*

GA, lactic acid, sodium bicarbonate, ethanol, 3-(4,5-dimethylthiazol2-yl)-2,5-diphenyl tetrazolium bromide (MTT) were purchased from HiMedia (Mumbai, India). The Dimethyl sulfoxide (DMSO), hydrogen peroxide, Folin, TLC silica gel 60 F254, Triton X-100, sodium nitrite, Griess reagent, and agarose were from Merck (Darmstadt, Germany). Dulbecco's Modified Eagle Medium (DMEM), penicillin/streptomycin, foetal bovine serum (FBS), trypsin, 3,3',5,5'-Tetramethylbensidine solution (TMB), Tris hydrochloride (Tris-HCl), and the other materials required for culturing of cells were purchased from Sigma-Aldrich (St. Louis, MO, USA). Ascorbic acid (VWR, Leuven, Belgium), and all other chemicals were of analytical grade or the highest grade available commercially.

The GA-COS powder was prepared according to our previous research [10]. In brief, COSs (0.5 g) were dissolved in approximately 25 ml of water, and then 1 ml of 1.0 M $H_2O_2$ containing 0.054 g of ascorbic acid was added. After 30 minutes, gallic acid (0.25 g) was introduced into the mixture. The reaction was conducted at pH 5 and room temperature for 6 hours. After the reaction, the mixture was centrifuged through a 1 kDa filter membrane in a 50 ml centrifuge tube to remove any unreacted ingredients. Finally, the resulting solution was lyophilized using a freeze-dry system (FDU 2110, Eyela, Japan) to obtain solid GA-COS samples.

To confirm the successful grafting of gallic acid onto COS backbones, TLC analysis was performed. Gallic acid, ascorbic acid, and GA-COS were developed on a silica gel plate (TLC silica gel 60 F254, Merck, Germany) with a mobile phase consisting of chloroform - ethyl acetate - acetic acid (50:50:1) and heated at 100°C for 5 minutes. The developed TLC plate was observed under UV light.

The GA-COSs were characterised by proton nuclear magnetic resonance (1H-NMR) spectra. Samples were recorded using a NMR-500 MHz spectrometer (Bruker, Germany) under a static magnetic field of 500 MHz, and the samples were dissolved in $D_2O$.

### *2.2. Cell culture*

The RAW 264.7 mouse macrophage cells procured from ATCC were cultivated in DMEM medium supplemented with 10% FBS, 100 µg/ml penicillin-streptomycin, and maintained in a 5% $CO_2$ atmosphere at 37°C. Subsequently, RAW 264.7 cells were detached using a scraper [12].

### *2.3. Cytotoxicity determination of GA-COS*

The cytotoxicity of COS and GA-COS on RAW 264.7 cells was evaluated using the MTT method, as previously described [13]. Briefly, RAW 264.7 cells were seeded in 96-well plates at a concentration of $1x10^4$ cells/well and allowed to incubate for 24 hours. Following the 24-hour culture period, the medium in the wells was replaced with fresh medium containing various concentrations of COS and GA-COS. After an additional 24 hours of incubation, 100 µl of MTT solution was added to each well and further incubated for 4 hours at 37°C. Subsequently, 200 µl of DMSO was added to dissolve the formed formazan salt, and the absorbance of the samples was measured at

540 nm using a microplate reader (PerkinElmer, USA). The percentage of cell viability in untreated cells served as a control for calculating relative cell viability.

### *2.4. Nitric oxide (NO) assay*

RAW 264.7 cells were cultured in DMEM medium without phenol red at a density of $5x10^5$ cells per well for 24 hours. Subsequently, the RAW 264.7 cells were exposed to COS or GA-COS (at concentrations ranging from 10 to 100 µg/ ml)) and LPS (1 µg/ml) for 24 hours. The NO content in the culture medium was determined using the Griess method [14]. Specifically, 50 µl of Griess reagent (comprising 1% sulphanilamide and 0.1% naphthyl ethylenediamine dihydrochloride in 2.5% phosphoric acid) was mixed with 50 µl of the culture medium. After a 20-minute incubation period, absorbance was measured at 540 nm using the same microplate reader as previously mentioned. NO concentration was determined using a standard curve prepared with sodium nitrite.

### *2.5. Western blot assay*

RAW 264.7 cells were cultured in DMEM medium at a density of $5x10^5$ cells per well for 24 hours. After pretreatment with GA-COS or COS (at concentrations ranging from 10 to 100 µg/ml) for 1 hour, LPS (1 µg/ml) was introduced for 24 hours. The RAW 264.7 cells were lysed in RIPA buffer (comprising 150 mM NaCl, 0.5 mM EDTA pH 8.0, 50 mM Tris pH 8.0, 1% Triton X-100, 0.5% sodium deoxycholate, and 0.1% SDS). Protein concentration was determined using the bio-rad protein assay with bovine serum albumin as the standard. Subsequently, 50 µg of protein was denatured in a 4x sample buffer (3:1) at 90°C for 4 minutes, followed by cooling in water for 2 minutes, repeated twice. The protein samples were then subjected to electrophoresis on a 12.5% polyacrylamide gel using the miniVE electrophoresis and electrotransfer system (Amersham Bioscience, USA). Subsequently, the proteins were transferred onto nitrocellulose membranes using the miniVE system and blocked with 5% skim milk for a minimum of 1 hour at room temperature. The membrane was incubated overnight at 4°C with primary antibodies against iNOS, NF-**κ**B p50, and NF-**κ**B p65 (Proteintech, USA) and then washed three times with 1X PBS/0.2% Tween 20. Following this, the membrane was incubated with a peroxidase-conjugated secondary antibody (1:1000) (Proteintech Group, Inc.) for 1 hour at room temperature and washed three times with 1X PBS/0.2% Tween 20. Finally, the membrane was developed using a 3,3',5,5'-Tetramethylbenzidine solution to visualize the western blot bands [12].

### *2.6. RNA isolation and reverse transcription-polymerase chain reaction (RT-PCR) assay*

RAW 264.7 cells were cultured in a culture medium at a density of 5x105 cells in each dish. Subsequently, the RAW 264.7 cells were incubated with GA-COS or COS (at concentrations ranging from 10 to 100 µg/ml) for 1 hour and LPS (1 µg/ml) for 24 hours. Total RNA was then extracted using the All-In-One DNA/RNA Miniprep Kit (Bio Basic, USA) following the manufacturer's protocol. The factors of interest were determined using the RT-PCR method [15]. To initiate cDNA synthesis, 2 µg of total RNA was converted to cDNA using the primer reverse transcription system (Cole-Parmer, UK). The target cDNA was amplified using specific primers (Phusa Biochem, Vietnam) as follows: for TNF-α, forward 5'-AGC-CCC-CAG-TCT-GTA-TCC-TT-3' and reverse 5'-CAT-TCG-AGG-TCT-CAG-TGA-AT-3'; for IL-1β, forward 5'-GGG-CCT-CAA-AGG-AAA-GAA-TC-3' and reverse 5'-TCA-CAG-TTG-GGG-AAT-TCT-GC-3'; for IL-6, forward 5'-TTC-CAG-AAT-CCC-TGG-ACA-AG-3' and reverse 5'-TGG-TCA-AAC-TCT-TGG-GGT-TC-3'; for glyceraldehyde 3-phosphate dehydrogenase (GADPH), forward 5'-GTC-AAC-GGA-TTT-GGT-CGT-ATT-3' and reverse 5'-AGT-CTT-CTG-GGT-GGC-AGT-GAT-3'. The RT-PCR conditions, suitable for the MyTaq One-Step RT-PCR Kit (Meridian Bioscience, USA), included amplification cycles carried out at 45°C for 20 minutes (1 cycle), 95°C for 1 minute (1 cycle), and 95°C for 10 seconds - 60°C for 10 seconds - 72°C for 30 seconds (40 cycles). A 10 µl mixture was combined with 2 µl of GelRed and subjected to electrophoresis on a 1% agarose gel for 20 minutes at 100 V. Finally, the gels were visualized under UV light using gel documentation image analysis software, VisionCapt.

### 2.7. Statistical analysis

The data are presented as the mean±standard deviation (SD) of triplicate measurements. Multiple comparisons were conducted using the least significant difference (LSD), Duncan's multiple range test, and one-way analysis of variance (ANOVA) with Statgraphics Centurion software. Statistical significance was determined at $p<0.05$.

## 3. Results and discussion

### 3.1. Cell viability

In this study, RAW 264.7 cells were exposed to various concentrations of COS and GA-COS (ranging from 1 to 250 µg/ml) to assess non-cytotoxic concentrations for subsequent experiments. As illustrated in Fig. 1, the cell viability data unequivocally indicate that both COS and GA-COS did not exhibit any significant toxicity towards RAW 264.7 cells at the tested concentrations. GA-COS, in particular, demonstrated a cell viability exceeding 90% [9]. These results substantiate the non-toxic nature of COS and GA-COS at the concentrations assessed. It is noteworthy that previous reports have also established the non-toxicity of GA-conjugated COS in RAW 264.7 cells across all tested concentrations [9, 15].

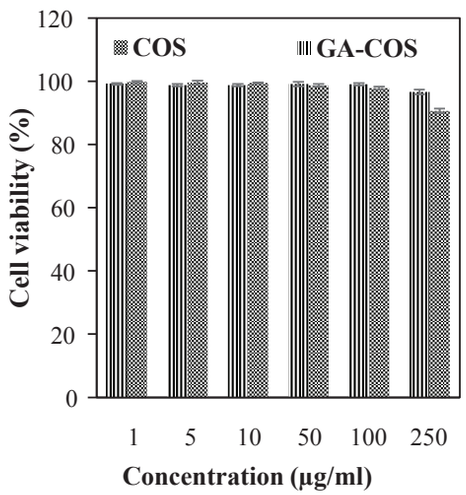


**Fig. 1. RAW 264.7 cell viability was determined by the MTT assay.**

The results of Fig. 1 shown are representative of separate experiments performed in triplicate. Error bars represent the standard error (SD).

### 3.2. Effects of GA-COS on nitric oxide production and protein expressions of iNOS in the LPS-induced RAW 264.7 cells

NO is a crucial mediator produced via the activity of the iNOS enzyme and plays a pivotal role in inflammation [6]. To elucidate the anti-inflammatory potential of GA-COS, an investigation was conducted to ascertain whether GA-COS influenced NO production in LPS-stimulated RAW 264.7 cells. The level of NO in the culture medium following LPS induction was assessed using the Griess reagent. As depicted in Fig. 2, GA-COS exhibited a significantly enhanced inhibitory effect on NO production, whereas COS demonstrated only a slight increase in inhibition at a concentration of 100 µg/ml. Specifically, GA-COS demonstrated an inhibition of NO production at 46.23±1.02%, whereas COS achieved an inhibition of 10.83±0.25%. This outcome underscores the capacity of GA grafted onto COS to improve the inhibition of NO production compared to the unmodified COS chain, thereby substantiating its potential for mitigating inflammation.

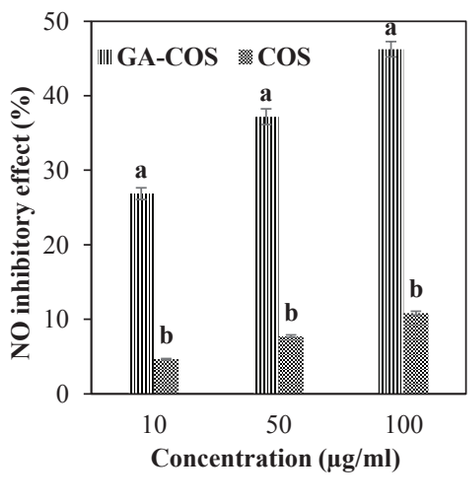


**Fig. 2. Effects of GA-COS on NO production inhibition in the LPS-stimulated RAW 264.7 cells.**

The results of Fig. 2 shown are representative of separate experiments performed in triplicate. Error bars represent the standard error (SD). Letters a, b indicate significant difference, $p<0.05$.

iNOS is an enzyme that plays a pivotal role in the inflammatory response. Increased expression levels of iNOS result in heightened NO production within cells, thereby contributing to inflammatory diseases. Western

blot analysis was conducted to assess the inhibitory effect of GA-COS on iNOS protein expression. Following a 1-hour pretreatment with GA-COS, RAW 264.7 macrophages were subsequently stimulated with LPS for 24 hours. GA-COS exhibited a concentration-dependent reduction in the expression of iNOS at the translational level (Fig. 3). Notably, a significant difference was observed compared to cells treated with COS, indicating the superior activity of GA-COS in suppressing iNOS expression in LPS-stimulated RAW 264.7 cells.

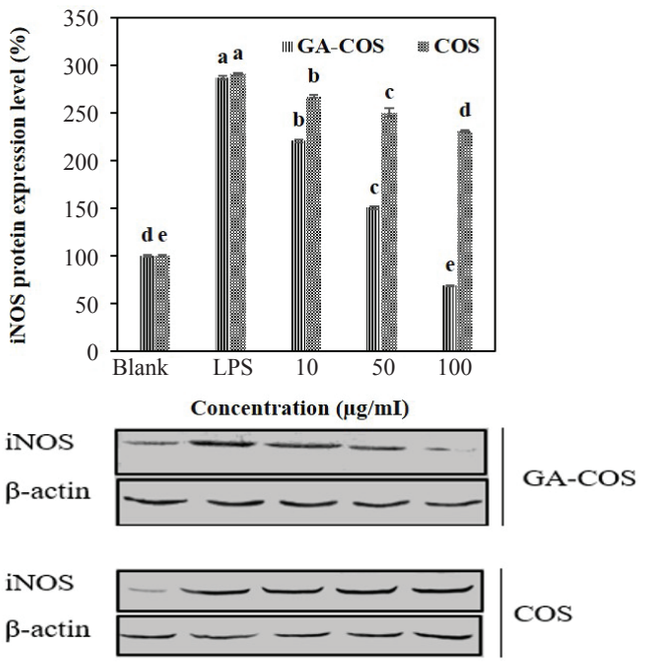


**Fig. 3. Effects of GA-COS and COS on protein expression of iNOS in LPS-induced RAW 264.7 cells.**

The results of Fig. 3 shown are representative of separate experiments performed in triplicate. Error bars represent the standard error (SD). Letters a-e indicate significant difference, $p<0.05$.

### *3.3. Effects of GA-COS on the mRNA expression of TNF-α, IL-1β, and IL-6 in the LPS-induced RAW264.7 cells*

To assess the impact of GA-COS on the production of pro-inflammatory cytokines, namely TNF-α, IL-1β, and IL-6, RAW264.7 cells were exposed to GA-COS for 1 hour and subsequently stimulated with LPS (1 µg/ml) for 24 hours. The results, as presented in Fig. 4, demonstrate that GA-COS led to a reduction in mRNA expression levels in LPS-induced RAW264.7 macrophages. At a concentration of 50 µg/ml, GA-COS exhibited inhibitory effects on the secretion of TNF-α, IL-1β, and IL-6 at levels of 92.44±2.99, 94.92±1.22, and 144.37±5.39%, respectively. It is noteworthy that, at equivalent concentrations, the influence of COS in reducing cytokine secretion was significantly lower than that of GA-COS.

The results shown are representative of separate experiments performed in triplicate. Error bars represent the standard error (SD). Letters a-e indicate significant difference, $p<0.05$.

### *3.4. Effects of GA-COS on NF-κB signalling activation*

NF-κB, comprising two subunits, p50 and p65, is a pivotal transcription factor responsible for regulating the expression of numerous proinflammatory mediators, including cytokines (IL-1α, IL-1β, IL-6, and TNF-α) and chemokines (IL-8, CCL2). In normal cells, NF-κB exists in an inactive complex state, sequestered in the cytoplasm by binding to an inhibitor known as I-κB. Stimulation of cells by inflammatory factors, such as UV radiation or bacterial agents, induces NF-κB activation. Following phosphorylation, NF-κB leads to the degradation of I-κB and translocates into the nucleus to initiate the transcription of target genes [16]. In our study, RAW 264.7 cells, stimulated by the extracellular agent LPS for 24 hours, exhibited increased expression of p50 and p65 proteins, with β-actin serving as a control. The inflammatory response was triggered by the interaction between LPS and toll-like receptor 4 (TLR4), culminating in the activation of the myeloid differentiation factor 88 (MyD88) signalling pathway. Subsequently, downstream signalling pathways, such as the NF-κB pathway, were activated, leading to nuclear translocation and the production of inflammatory cytokines and mediators [1]. As depicted in Fig. 5, the GA-COS derivative demonstrated a reduction in the expression levels of p50 and p65 proteins at concentrations ranging from 10 to 100 µg/ml, exhibiting a significant improvement compared to COS. Previous studies have also indicated that gallic acid-conjugated COS downregulates NF-κB

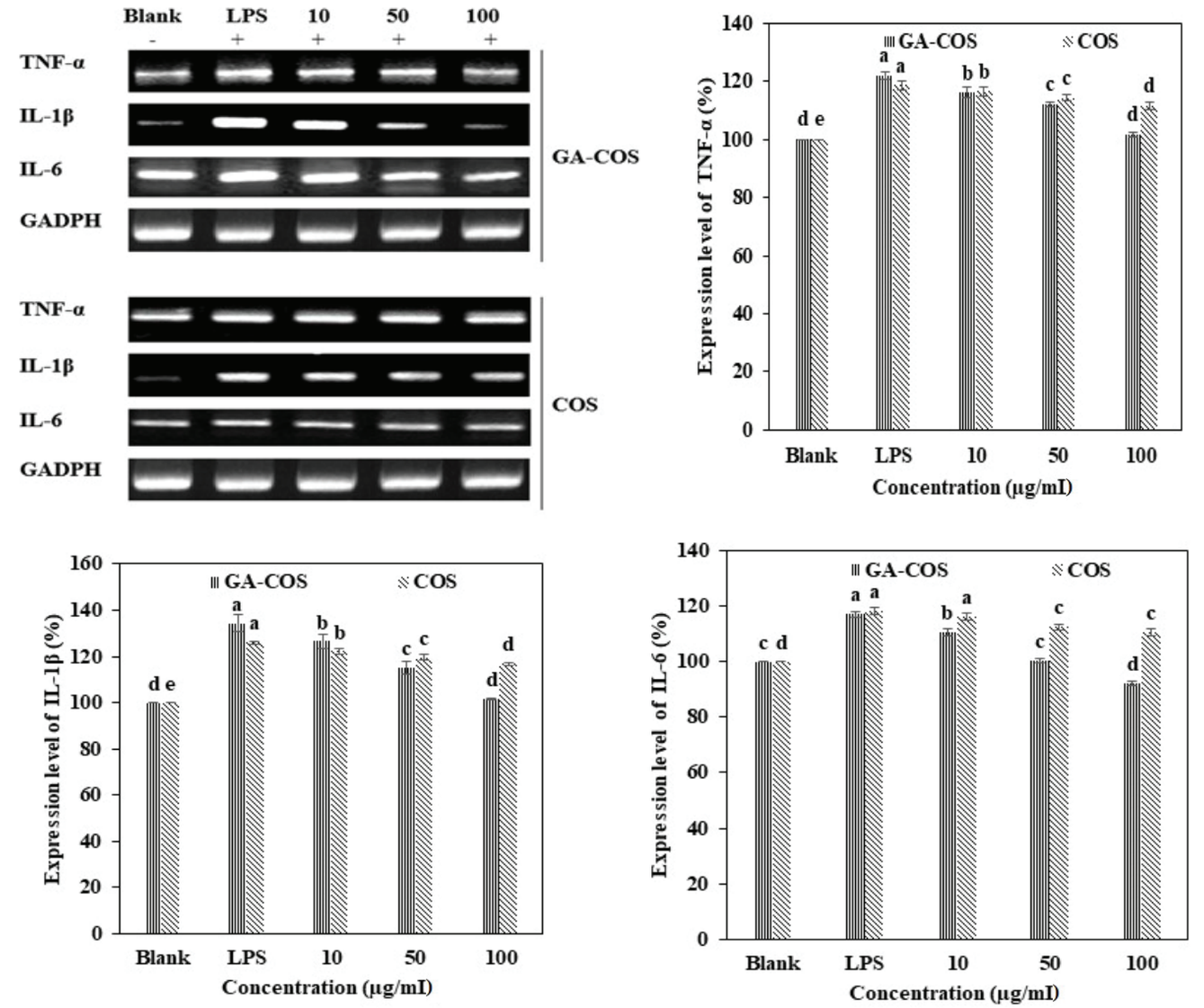


**Fig. 4. Effects of GA-COS on the mRNA expression of TNF-α, IL-1β, and IL-6 in the LPS-induced RAW264.7 cells.**

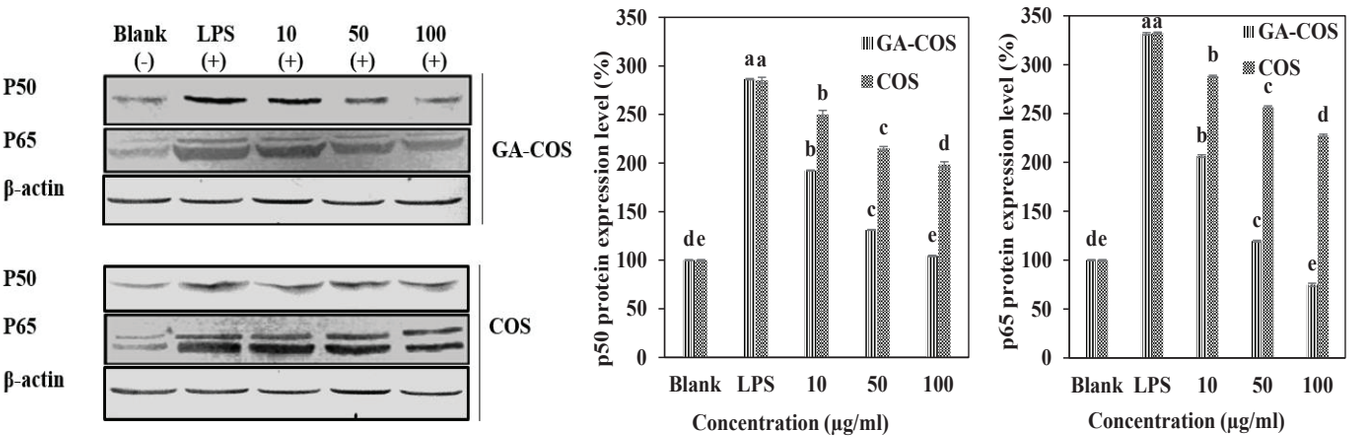


**Fig. 5. Effects of GA-COS and COS on p50 and p65 signal in LPS-stimulated RAW 264.7 cells.**

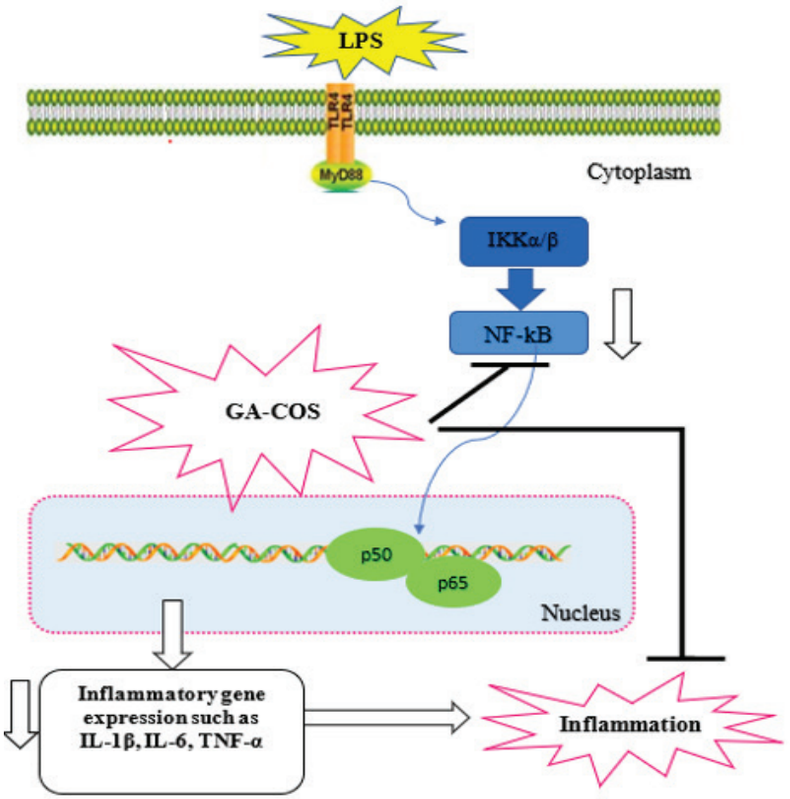


**Fig. 6. Diagram displaying the mechanism of NF-κB signal inhibition of GA-COS.**

protein signalling expression [12]. Fig. 6 provides an illustrative representation of the mechanism underlying the inhibition of NF-κB signalling by GA-COS.

The results of Fig. 5 shown are representative of separate experiments performed in triplicate. Error bars represent the standard error (SD). Letters a-e indicate significant difference, $p<0.05$.

## 4. Conclusions

GA-COS exhibited anti-inflammatory properties by suppressing NO formation, inhibiting iNOS protein expression, and downregulating the expression of p50 and p65 protein signals. Furthermore, it regulated the expression of pro-inflammatory cytokines such as TNF-α, IL-1β, and IL-6. This study lays the groundwork for future research to demonstrate that GA-COS holds significant potential as a novel compound for the prevention of inflammatory diseases.

## CRediT author statement

Van-Hoai Bui, Hong-Tham N. Vo, Thanh-Tuan Duong, Se-Kwon Kim: Conceptualisation, Methodology, Formal analysis, Software, Data curation, Validation, Visualisation, Investigation; Dai-Nghiep Ngo: Conceptualisation, Methodology, Formal analysis, Supervision, Original draft preparation, Writing - Reviewing and Editing, Project administration.

## ACKNOWLEDGEMENTS

This research is funded by the Vietnam National Foundation for Science and Technology Development (NAFOSTED) under grant number 106.02-2019.47.

## COMPETING INTERESTS

The authors declare that there is no conflict of interest regarding the publication of this article.

## REFERENCES

[1] L. Chen, H. Deng, H. Cui, et al. (2018), "Inflammatory responses and inflammation-associated diseases in organs", *Oncotarget*, **9(6)**, pp.7204-7218, DOI: 10.18632/oncotarget.23208.

[2] B. Kaminska (2005), "MAPK signalling pathways as molecular targets for anti-inflammatory therapy-from molecular mechanisms to therapeutic benefits", *Biochim. Biophys. Acta*, **1-2**, pp.253-262, DOI: 10.1016/j.bbapap.2005.08.017.

[3] T. Liu, L. Zhang, D. Joo, et al. (2017), "NF-κB signalling in inflammation", *Signal Transduction And Targeted Therapy*, **2(1)**, pp.1-9, DOI: 10.1038/sigtrans.2017.23.

[4] D. Furman, J. Campisi, E. Verdin, et al. (2019), "Chronic inflammation in the etiology of disease across the life span", *Nat. Med.*, **12**, pp.1822-1832, DOI: 10.1038/s41591-019-0675-0.

[5] Y.S. Cho, S.H. Lee, S.K. Kim, et al. (2011), "Aminoethyl-chitosan inhibit LPS-induced inflammatory mediator, iNOS and COX-2 expression in RAW264.7 mouse macrophage", *Process Biochemistry*, pp.465-470, DOI: 10.1016/j.procbio.2010.09.019.

[6] A. Cheng, H. Yan, C. Han, et al. (2014), "Polyphenols from blueberries modulate inflammation cytokines in LPS-induced RAW264. 7 macrophages", *International Journal of Biological Macromolecules*, **69**, pp.382-387, DOI: 10.1016/j.ijbiomac.2014.05.071.

[7] N. Fujiwara, K. Kobayashi (2005), "Macrophages in inflammation", *Current Drug Targets-Inflammation & Allergy*, **4(3)**, pp.281-286, DOI: 10.2174/1568010054022024.

[8] J. Liu, J. Lu, J. Kan, et al. (2013), "Synthesis of chitosan-gallic acid conjugate: Structure characterisation and *in vitro* anti-diabetic potential", *Int. J. Biol. Macromol.*, **62**, pp.321-329, DOI: 10.1016/j.ijbiomac.2013.09.032.

[9] H.H. Park, S.C. Ko, G.W. Oh, et al. (2018), "Characterisation and biological activity of PVA hydrogel containing chitooligosaccharides conjugated with gallic acid", *Carbohydr. Polyme*, **198**, pp.97-205, DOI: 10.1016/j.carbpol.2018.06.070.

[10] V.H. Bui, D.N. Ngo (2018), "Synthesis of gallic acid grafted chitooligosaccharides with an ascorbic acid/hydrogen peroxide redox pair to improve chitooligosaccharide activity", *Proceeding of The Biotechnology Conference*, Institute of Biotechnology, Vietnam Academy of Science and Technology, pp.159-164.

[11] V.H. Bui, D.N. Ngo, D.P. Chau, et al. (2020), *Antioxidant Effect Of Gallic Acid-Chitooligosacharides Derivatives In Raw264.7 Cell*, National Biotechnology Conference 2020, pp.960-964.

[12] D.N. Ngo, Z.J. Qian, T.S. Vo, et al. (2011), "Antioxidant activity of gallate-chitooligosaccharides in mouse macrophage RAW264. 7 cells", *Carbohydrate Polymers*, **4**, pp.1282-1288, DOI: 10.1016/j.carbpol.2011.01.022.

[13] D.N. Ngo. M.M. Kim, S.K. Kim (2012), "Protective effects of aminoethyl-chitooligosaccharides against oxidative stress in mouse macrophage RAW 264.7 cells", *International Journal of Biological Macromolecules*, **3**, pp.624-631, DOI: 10.1016/j.ijbiomac.2012.01.036.

[14] M.D.L. Trinh, M.H. Dinh, D.H. Ngo, et al. (2014), "Protection of 4-hydroxybenzyl-chitooligomers against inflammatory responses in Chang liver cells", *International Journal Of Biological Macromolecules*, **66**, pp.1-6, DOI: 10.1016/j.ijbiomac.2014.01.064.

[15] T.S. Vo, D.H. Ngo, L.G. Bach, et al. (2017), "The free radical scavenging and anti-inflammatory activities of gallate-chitooligosaccharides in human lung epithelial A549 cells", *Process Biochemistry*, **54**, pp.188-194, DOI: 10.1016/j.procbio.2017.01.001,

[16] P. Ma, H.T. Liu, P. Wei, et al. (2011), "Chitosan oligosaccharides inhibit LPS-induced over-expression of IL-6 and TNF-α in RAW264.7 macrophage cells through blockade of mitogen-activated protein kinase (MAPK) and PI3K/Akt signalling pathways", *Carbohydrate Polymers*, **4**, pp.1391-1398, DOI: 10.1016/j.carbpol.2011.01.045.

DOI: 10.31276/VJSTE.66(1).104-110

# Factors affecting the coagulation of milk protein during quark cheese processing in Vietnam

**Chinh Nghia Nguyen[1], Hang Ngan Dinh[1], Thu Trang Nguyen[1], Ha Trang Nguyen[1], Thi Trang Nguyen[1], Giang Hoang[2], Ky Son Chu[1], Thu Trang Vu[1*]**

*[1]School of Biotechnology and Food Technology, Hanoi University of Science and Technology, 1 Dai Co Viet Street, Bach Khoa Ward, Hai Ba Trung District, Hanoi, Vietnam*

*[2]High Command of Guard Police, Ministry of Public Security, 16 Tran Vu Street, Quan Thanh Ward, Ba Dinh District, Hanoi, Vietnam*

Received 20 October 2022; revised 29 October 2022; accepted 10 November 2022

***Abstract:***

**In recent years, cheese consumption in Vietnam is markedly rising, leading to the attention of local milk processors on cheese making. Quark-type cheese, a traditional food in Central Europe, is a type of well-known acid-coagulated cheese product. Milk coagulation properties (MCPs) play an important role to the success of the cheese-making process and are influenced by different parameters. In this study, the quality of raw milk for cheese making and the coagulation conditions in quark-type cheese processing were investigated. Raw milk collected from Phu Dong dairy farm met the requirement of Vietnamese standard for cheese making. The appropriate conditions for coagulation were identified: the heat treatment of milk at 60°C for 15 minutes, coagulation temperature at 40°C and pH 5.5, $CaCl_2$ concentration at 0.04g/l. Under these conditions, a short coagulation time (72.33 seconds) and high curd yields (50.70%) were obtained. These results suggested that quark-type cheese using raw milk in Vietnam could be successfully developed at larger scale.**

***Keywords:*** **coagulation conditions, curd yield, quark-type cheese, raw milk quality.**

***Classification numbers:*** **3.4, 3.5**

## 1. Introduction

In Vietnam, cheese has been considered a western dish and not a major focus of dairy manufacturers because of deficiencies in domestic raw milk. Indeed, nearly 86% of cheese products are imported in Vietnam [1]. However, an increase in cheese consumption has been recently recognized. Cheese consumption has risen by 8.3%/yr from 2016 to 2020, expanding to 9.3%/yr in 2023. Due to the increasing cheese demand, processing cheese products from local raw milk has recently gained a lot of attention from dairy manufacturers in Vietnam.

Quark-type cheese, a traditional food in the cuisines of Central Europe, is one of the most well-known acid-coagulated cheese types with a smooth texture and a mild, slightly sour flavour. Quark cheese technologies and manufacture have been thoroughly reviewed [2], and was modified until today. In quark-type cheese production, milk is pasteurized before cooling to 28-30°C, followed by acidic and rennet coagulation [3]. Compared with other cheese products, quark-type cheese could be produced faster.

Milk coagulation properties (MCPs) play an important role in the success of the cheese-making process and are influenced by different parameters such as raw milk quality, heat treatment of raw milk, concentration of $Ca^{2+}$, rennet addition, and pH for coagulation by rennet. Previously, Z. Miloradovic, et al. (2018) studied the effect of heat treatment on the characteristics of Quark cheese made from cow and goat milk [4]. The results showed a significant influence of heat treatment on the texture and relative protein proportions in cow quark cheese, while there was no influence on the texture of goat quark cheese. Recently, C.D. Thybo, et al. (2020) [5] reported a balance between micellar and free calcium in curd and serum phases during direct acidification of bovine milk by changing the organic acid type. Citric acid was

*Corresponding author: Email: trang.vuthu@hust.edu.vn

more efficient than lactic acid at lowering free calcium concentration, while the effect of temperature was larger for acidification with lactic acid. Moreover, acidification temperature had little effect on curd yield [5]. As those parameters influence cheese yield and quality at both laboratory and industry levels [6], it is important to investigate them for raw milk specific to each region.

Thus, the aim of this study is to evaluate Vietnamese raw milk quality for cheesemaking, and to discover the effect of factors in the coagulation of milk to apply to quark-type cheese processing.

## 2. Materials and methods

### *2.1. Materials*

Raw milk was collected from Phu Dong Dairy Farm, Gia Lam, Hanoi, Vietnam in the morning from March to September 2022. Raw milk was kept at 4°C immediately after milking and transported to the laboratory for analysis of dry matter, protein and fat content, acidity, and freshness. Before the preparation of cheese samples, the raw milk was stored for no longer than 24 h at 4°C.

The enzyme Marzyme® (Danisco, USA) was produced by fermentation of pure broth of the fungus *Rhizomucor miehei*. The optimal pH 5.5-6.0; optimal temperature is 36-40°C, and its enzyme activity is 703-738 IMCU/ml. The recommended dosage from the product manufacturer is 24-48 IMCU/l milk.

$CaCl_2$ salt was obtained from Solvay, Italy. Lactic acid solution was obtained from PURAC® FCC, Thailand.

### *2.2. Methods*

#### *2.2.1. Raw milk analysis*

Density, pH and total dry matter of raw milk were analysed according to TCVN 7405:2018 (ISO 6731:2010). Titratable acidity was measured according to AOAC 947.05. Protein and fat content were determined using the Kjeldahl method (ISO 8968-1:2014) and Gerber method (ISO 19662:2018), respectively.

#### *2.2.2. Heat treatment for cheesemaking milk*

500 ml of raw milk was prepared in a 1-l glass container and then heated indirectly in a water bath at 60°C for 15 min, 60°C for 30 min, and then 72°C for 15 min (Table 1).

**Table 1. Experimental design of heating treatment.**

| Sample | Temperature (°C) | Time (min) |
|---|---|---|
| Raw milk | - | - |
| Heated milk 1 | 60 | 15 |
| Heated milk 2 | 60 | 30 |
| Heated milk 3 | 72 | 15 |

Milk after heat treatment was analysed for total micro-organisms, *E. coli*, Coliform, *S. aureus*, mould, and yeast [7].

#### *2.2.3. Quark cheese processing*

500 ml of raw milk was prepared in a 1-l glass container. The raw milk was pasteurized as in Section 2.2.2 followed by a cool down to 25°C. Heated milk was adjusted to pH 5.5 using lactic acid and then the enzyme was added. After coagulation, the curd was cut into 1-$cm^3$ cubes and gently stirred at 38°C before draining. The curd was transferred to moulds with pressure of 0.03 kg/$cm^2$ and kept at room temperature for 1 h. Cheese was withdrawn from moulds, wrapped in plastic bags, and stored at 4°C.

#### *2.2.4. Coagulation time*

Coagulation time was determined according to IDF Standard 157: 2007/ISO 11815 and Z. Miloradovic, et al. with some modifications [4]. A spatula was inserted into the gel several times. Coagulation time was defined as the interval between the addition of the enzyme to the milk and the appearance of visible clusters of casein on the surface of the spatula.

#### *2.2.5. Coagulation conditions*

There are two main factors affecting coagulation for quark cheese processing: temperature and pH. A total of 16 samples were prepared with different temperature and pH conditions as shown in Table 2.

**Table 2. Experimental design of coagulation conditions.**

| Sample | 1 | 2 | 3 | 4 | 5 | 6 | 7 | 8 | 9 | 10 | 11 | 12 | 13 | 14 | 15 | 16 |
|---|---|---|---|---|---|---|---|---|---|---|---|---|---|---|---|---|
| Temperature (°C) | 30 | | | | 35 | | | | 40 | | | | 45 | | | |
| pH | 5.0 | 5.5 | 6.0 | 6.6 | 5.0 | 5.5 | 6.0 | 6.6 | 5.0 | 5.5 | 6.0 | 6.6 | 5.0 | 5.5 | 6.0 | 6.6 |

*2.2.6. Curd yield of Quark cheese*

Curd yield was calculated as follows:

$$\text{Curd yield} = \frac{\textit{Mass of cheese x Dry matter of cheese}}{\textit{Mass of milk x Dry matter of milk}}$$

*2.2.7. Textural property analysis of Quark cheese*

Textural properties were analysed by the texture analyser TA.XT plus (Stable Micro System, Godalming, UK) according to K. Szkolnicka, et al. (2021) [8] with some modification. Texture profile analysis (TPA) includes the assessment of the following characteristics: hardness (g.cm/s$^{-2}$) (the peak force during the penetration of the sample), springiness (the distance of the detected height during the second compression divided by the original compression distance), and cohesiveness (the area of work during the second compression divided by the area of work during the first compression). After 24 h of refrigerated storage (4°C), the samples underwent textural analysis. The cheese sample was taken out from 4°C and cut into 40x40 mm squares with 25 mm height. The samples were penetrated with a cylindrical 25-mm diameter aluminium probe. The test speed was at 2 mm/s and trigger force was at 5 g.

*2.2.8. Statistical analyses*

Physicochemical and textural analyses were performed in triplicate. The obtained results were statistically analysed at the significance level p=0.05 using Microsoft Excel. Mean values and standard deviations were calculated and the values were compared by ANOVA.

## 3. Results and discussion

### *3.1. Raw milk quality*

Raw milk was immediately kept at 4°C after collection. Physical and chemical properties of the raw milk are presented in Table 3.

**Table 3. Physicochemical parameters of raw milk.**

| Analytical parameters | Raw milk | Vietnamese standard TCVN 7405:2018 |
|---|---|---|
| Dry matter (%) | 12.9±0.5 | ≥11.5 |
| Fat (%) | 4.0±0.4 | ≥3.2 |
| Protein (%) | 3.1 ± 0.2 | ≥2.8 |
| Density (g/ml) | 1.027 | ≥1.026 |
| pH | 6.6 | - |
| Acidity (°T) | 15-17 | - |

The results show that raw milk collected from Phu Dong Dairy Farm met the requirements of Vietnamese standard TCVN 7405:2018. However, fat and protein content were significantly higher than that specified in TCVN 7405:2018, which were suitable for coagulation process during Quark cheese making.

### *3.2. Effect of heat treatment on the coagulation of milk*

Effect of heating treatment on the microbial quality of milk for cheese processing: Table 4 shows that raw milk only met the requirement of total number of aerobic microorganisms (3x10$^6$ CFU/ml), while other requirements were not met. "Heated milk 1" almost reached the microbiological criteria for pasteurized milk TCVN 5860:2019 (10$^4$ CFU/ml). However, the ability of coagulation of milk by rennin is known to decrease with heat treatment >70°C. Heat-treated milk has longer coagulation times and a gel structure softer than unheated milk [9]. The accessibility of k-casein bonds (Phe105-Met106) could be reduced by forming complexes with whey protein or precipitation of calcium phosphate by heating [10]. Although cheese made from unpasteurized milk is considered to have a better flavour, most producers pasteurize the milk to eliminate risks from microorganisms.

**Table 4. Effect of heating treatment on the microbial quality of milk for cheese processing.**

| CFU/ml | Raw milk | Heated milk 1 | Heated milk 2 | Heated milk 3 |
|---|---|---|---|---|
| Total micro-organisms | 2.6x10$^6$ | 6x10$^4$ | 7.5x10$^3$ | <10 |
| *E. coli* | 3.2x10$^3$ | N.D | N.D | N.D |
| *Coliform* | N.D | N.D | N.D | N.D |
| *S. aureus* | 8x10$^3$ | N.D | N.D | N.D |
| Yeast & Mould | 1.2x10$^3$ | N.D | N.D | N.D |

To study the effect of heat treatment on coagulation time and curd yield of fresh milk, the heat treatment was caried out as in Table 1 and the results are shown in Fig. 1. The results indicate that the curd yield of "Heated milk 2" was the highest and the coagulation time of "Heated milk 1" was the shortest. However, there are no significant differences compared to the raw milk (p>0.05). Heat-treated milk made protein recovery content in cheese increase due to denaturation of whey protein.


**Fig. 1. Effect of heat treatment on the coagulation time and curd yield in coagulation.**

The formation of whey protein/k-casein complexes at the surfaces of casein micelles or in the whey phase interferes with the contraction of curds and increase the moisture-holding capacity. However, excessive moisture is a common drawback of cheeses made from heated milk [9]. The recovery efficiency of the unpasteurized sample is like the others, but the quality of cheese drops significantly, especially in the texture aspect.

The effect of heat treatment on the texture of quark cheese is presented in Table 5. The longer the heating time and higher the temperature, the lower the quality of cheese. Especially with harsh pasteurizing temperatures, the hardness and cohesion of cheese made from "Heated milk 3" decreased from time to time. In general, the quality of cheese was negatively affected by heating. Cheeses produced from milk heated more than 70°C had lower hardness, fracture stress, fracture strain, surface hardness, and fracture hardness than milk cheeses with milder heating [2]. These trends are reflected in the interactive effects of altered composition (such as higher moisture content) and the effect of denatured whey/ protein/para-k-casein complexes on para-micelles. Casein forms the load-bearing protein network of cheese texture. Higher humidity also made the cheese softer and crumblier than cheese from milk with a mild heating setting [6].

For the "Heated milk 2" sample, hardness increased with storage time due to the loss of whey. The quality of cheese is not stable because the cohesion and flexibility decreased during storage. Overall, cheese from "Heated milk 1" had a similar structure to the unpasteurized sample.

### *3.3. Effect of coagulation conditions for quark cheese processing*

At pH 5.0, coagulation time was not determined for the four temperature ranges because milk at pH 5.0 reaches the isoelectric point of casein in milk medium (pH 4.6-4.7) wherein casein was coagulated by the $H^+$ ions of lactic acid that binds to the negatively charged casein micelle and reduces the charge, causing the casein micelles to clump together, causing agglomeration.

In contrast, coagulation did not occur at pH 6.6. After adding enzymes and holding the investigated temperature for 1 h, the milk remained liquid and the fat scum easily emerged. This was because pH 6.6 is outside the optimum

**Table 5. Effect of heat treatment on the structure of curd after storage.**

| Sample/storage time | Hardness (g.cm/s$^{-2}$) | | Cohesiveness | | Springiness | |
|---|---|---|---|---|---|---|
| | *24 h* | *72 h* | *24 h* | *72 h* | *24 h* | *72 h* |
| Raw milk | 3.60±0.09 | 3.94±0.52 | 0.57±0.05 | 0.50±0.04 | 2.32±0.09 | 2.40±0.26 |
| Heated milk 1 | 4.78±0.77 | 4.48±0.79 | 0.50±0.05 | 0.53±0.04 | 2.41±0.53 | 2.40±0.62 |
| Heated milk 2 | 3.85±0.43 | 4.10±0.93 | 0.48±0.05 | 0.41±0.07 | 1.97±0.39 | 1.62±0.14 |
| Heated milk 3 | 2.70±0.36 | 2.61±0.25 | 0.47±0.09 | 0.43±0.08 | 1.02±0.07 | 1.00±0.13 |

Values are expressed as mean ±SD (n=3). Values within a column not sharing a common superscript differ (p<0.05).

pH range of MARZYME®, which caused the enzyme to hydrolyse κ-casein very slowly making it difficult for the milk to coagulate to form a milky mass.

At 30 and 35°C, the coagulation time was higher than those at 40 and 45°C. At pH 6.0, the time until coagulation appeared was higher than at pH 5.5. In general, the lower the pH and the higher the temperature, the faster the coagulation time. When coagulating at pH 5.5 and 6.0, it gave a smooth and firm milky mass, and the coagulation time was short, especially at 40 and 45°C (Fig. 2).

The curd yield in samples with pH 5.0 was the lowest because the casein had coagulated immediately after lowering the pH. At a coagulation pH of 5.0, cheese products had the hardest texture, while the lowest hardness was achieved at a coagulation pH of 6.0. In fact, when storing cheese, for samples with pH 6.0, the whey in the cheese mass escaped the most, whereas samples at pH 5.0 and 5.5 were almost absent. This also affects product quality after storage (Fig. 3).

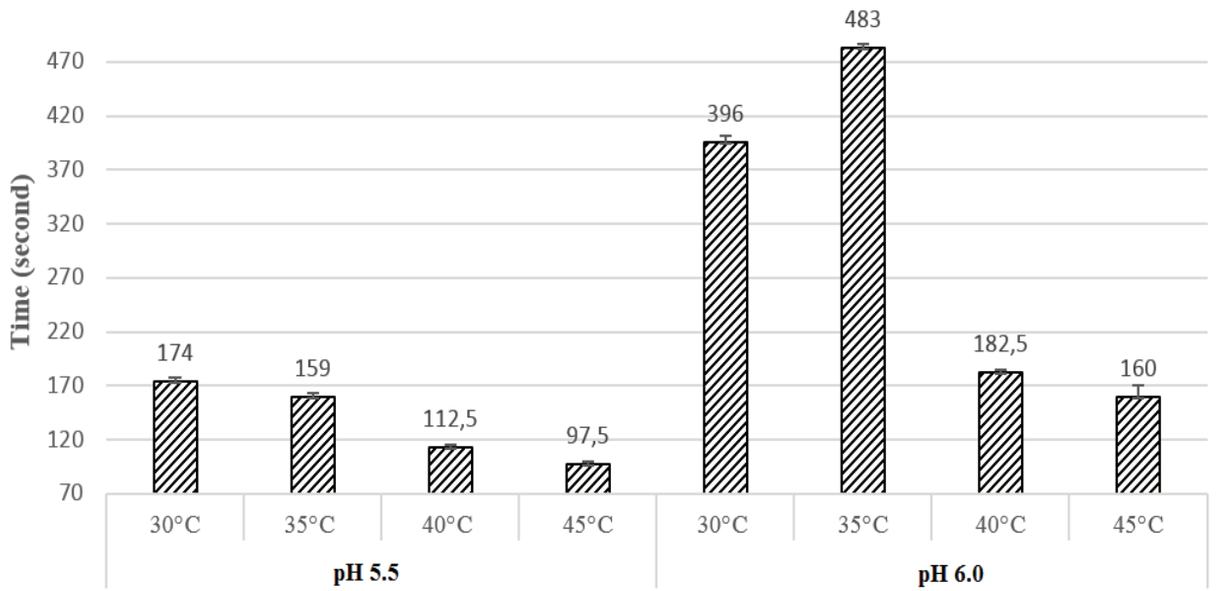


**Fig. 2. Time of coagulation appearance with different conditions of temperature and pH.**

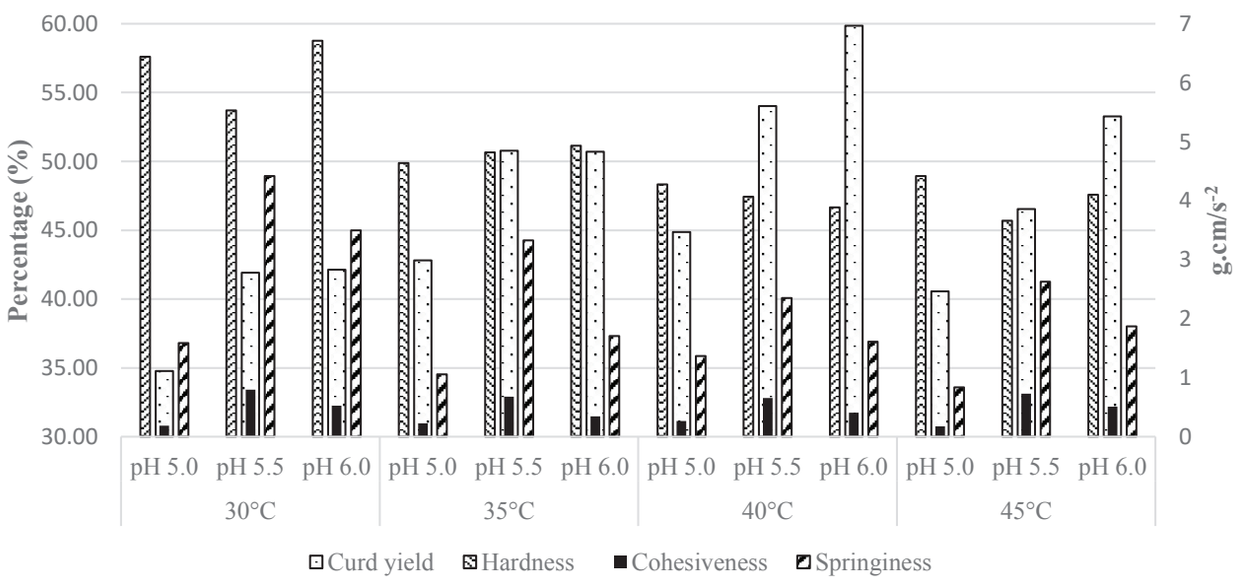


**Fig. 3. Curd yield and curd structure with different pH and temperature conditions.**

### *3.4. Effect of $Ca^{2+}$ on the coagulation of milk in cheese processing*

*3.4.1. Effect of $Ca^{2+}$ on the coagulation time*

Calcium addition contributes to the increase of bridging between casein micelles, further facilitating coagulant formation [11]. Through its effect on the milk-salt system, the addition of $Ca^{2+}$ also slightly lowers the pH of milk, promotes rennin activity, and reduces whey protein denaturation. The effect of calcium ions on the coagulation time of fresh milk is illustrated in Fig. 4.

From Fig. 4, it was clearly seen that there was a significant difference in the time of coagulation appearance between samples with different concentrations of $CaCl_2$ ($p<0.05$). The time until the appearance of coagulation decreased gradually when the concentration of $CaCl_2$ increased in the range from 0.4-0.8 g/l milk. At a concentration of $CaCl_2$ 0.8 g/l, the shortest coagulation time was found, which was not too different from the time at a concentration of 0.6 g/l milk ($p<0.05$).

*3.4.2. Effect of $Ca^{2+}$ on the curd yield and curd structure*

The concentration of $CaCl_2$ also affects the yield of cheese, but this difference was not too significant at the measured concentrations ($p>0.05$). The curd yield was described as the nutrients in the recovered cheese contained in the milk, so yield would be related to the ability to retain moisture and especially protein, fat, and calcium in the milk mass. The moisture content of the cheese was not significantly affected by the addition of calcium at different concentrations at any pH during milk coagulation [11].

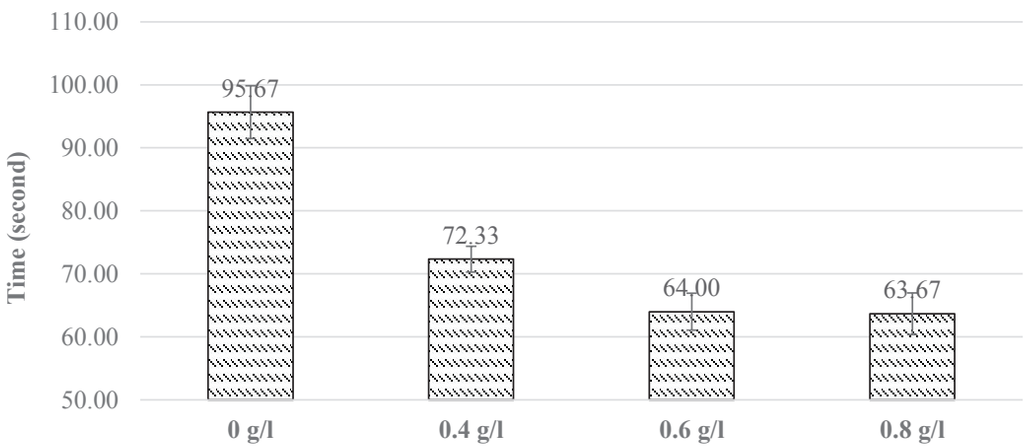


**Fig. 4. Time of coagulation appearance with different concentrations of $CaCl_2$.**

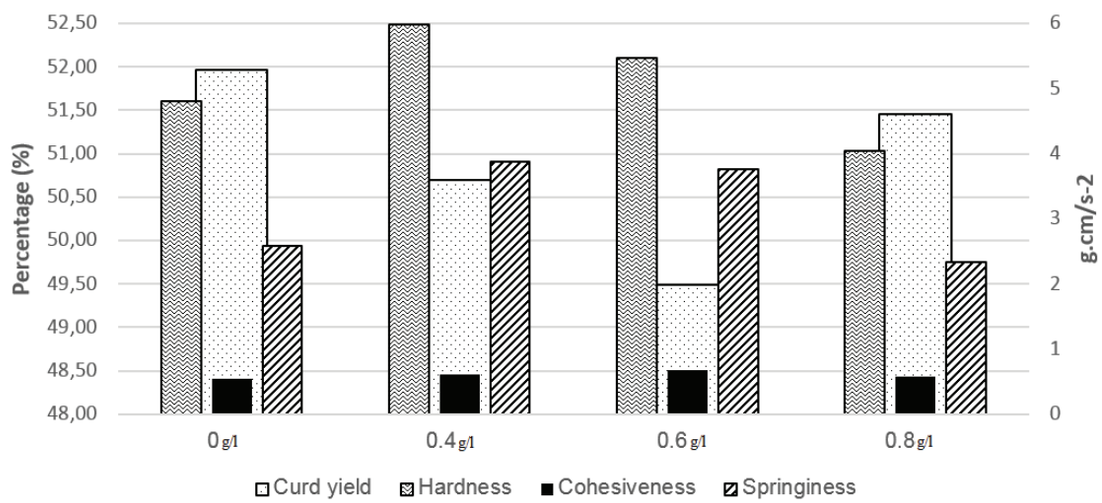


**Fig. 5. Effect of $CaCl_2$ concentration on curd yield and curd structure.**

At a concentration of 0.8 g/l, the best recovery efficiency was obtained, however, the difference was not large when compared with concentrations of 0.4 and 0.6 g/l ($p>0.05$). Regarding the dry matter content, although there was no significant difference, the results obtained at a concentration of 0.8 g/l were lower than that of the sample at 0.4 g/l. According to L. Ong, et al. (2013) [11], there was no significant difference ($p>0.05$) in the amount of fat retained in the final cheese. On the other hand, when tasting the cheese at concentrations of 0.6 and 0.8 g/l, we could feel the brackish taste of $CaCl_2$ salt in cheese the cheese [11].

The texture of raw curd increased gradually and was better than the sample without $CaCl_2$ at concentrations from 0 to 0.6 g/l, but the difference between concentrations was not significant ($p<0.05$). However, at a $CaCl_2$ concentration of 0.8 g/l, the structure was not only bad at concentrations of 0.4 and 0.6 g/l, but worse than the sample without $CaCl_2$. In addition, the product quality at a concentration of 0.8 g/l was also unstable when measuring the structure.

$CaCl_2$ with a concentration of 0.4 g/l in milk gave the best results in terms of coagulation time, product recovery efficiency, and product concentration as well as when the samples were tasted.

## 4. Conclusions

This study shows that raw milk from Phu Dong Dairy Farm, Gia Lam, Hanoi meets the standards for quark cheese processing. The optimal conditions for quark processing were determined: heat treatment of milk at 60°C for 15 min, coagulation temperature at 40°C, coagulation pH at 5.5, and concentration of $CaCl_2$ at 0.04 g/l milk. These results suggest that quark cheese processing could be further carried out on a pilot scale with high commercial potential to apply on larger scales.

## CRediT author statement

Chinh Nghia Nguyen: Writing - Reviewing and Editing; Hang Ngan Dinh: Methodology, Writing, Data analysis; Thu Trang Nguyen: Writing, Data analysis; Ha Trang Nguyen, Thi Trang Nguyen, Giang Hoang: Data analysis; Ky Son Chu: Reviewing, Editing; Thu Trang Vu: Methodology, Reviewing, Editing.

## ACKNOWLEDGEMENTS

This research is funded by the Vietnam - Czech Republic Bilateral under Project number NDT/CZ/22/04, Ministry of Science and Technology.

## COMPETING INTERESTS

The authors declare that there is no conflict of interest regarding the publication of this article.

## REFERENCES

[1] Invest & Export Brazil (2020), *Vietnam Market Study on Cheese and Dairy Products,* 201pp.

[2] T.P. Guinee (2021), "Effect of high-temperature treatment of milk and whey protein denaturation on the properties of rennet-curd cheese: A review", *International Dairy Journal*, **121**, DOI: 10.1016/j.idairyj.2021.105095.

[3] A.M. Cadavid, L. Bohigas, M. Toldra, et al. (2020), "Improving quark-type cheese yield and quality by treating semi-skimmed cow milk with microbial transglutaminase", *LWT*, **131**, DOI: 10.1016/j.lwt.2020.109756.

[4] Z. Miloradovic, J. Miocinovic, N. Kljajevic, et al. (2018), "The influence of milk heat treatment on composition, texture, colour and sensory characteristics of cows' and goats' Quark-type cheeses", *Small Ruminant Research*, **169**, pp.154-159, DOI: 10.1016/j.smallrumres.2018.09.012.

[5] C.D. Thybo, S.K. Lillevang, L.H. Skibsted, et al. (2020), "Calcium balance during direct acidification of milk for Mozzarella cheese production", *LWT*, **131**, DOI: 10.1016/j.lwt.2020.109677.

[6] T. Troch, E. Lefebure, V. Baeten, et al. (2017), "Cow milk coagulation: Process description, variation factors and evaluation methodologies: A review", *Base*, **21(4)**, pp.276-287, DOI: 10.25518/1780-4507.13692.

[7] L.T. Mai, N.T. Hien, P.T. Thuy (2005), *Analytical Methods in Fermentation Technology Field*, Science and Technics Publishing House, 336pp (in Vietnamese).

[8] K. Szkolnicka, I. Dmytrow, A.M. Malek (2021), "The characteristics of quark cheese made from buttermilk during refrigerated storage", *Foods*, **10(8)**, DOI: 10.3390/foods10081783.

[9] A.B. Hougaard, Y. Ardo, R.H. Ipsen (2010), "Cheese made from instant infusion pasteurized milk: Rennet coagulation, cheese composition, texture and ripening", *Int. Dairy J.*, **20(7)**, pp.449-458, DOI: 10.1016/j.idairyj.2010.01.005.

[10] M. Britten, H.J. Giroux (2022), "Rennet coagulation of heated milk: A review", *Int. Dairy J.*, **124**, DOI: 10.1016/j.idairyj.2021.105179.

[11] L. Ong, R.R. Dagastine, S.E. Kentish, et al. (2013), "The effect of calcium chloride addition on the microstructure and composition of Cheddar cheese", *Int. Dairy J.*, **33(2)**, pp.135-141, DOI: 10.1016/j.idairyj.2013.03.002.

# Development of a lateral flow immunoassay with HRP enhancement for spiked SARS-CoV-2 protein N detection in human saliva

**Minh Hieu Vu[1, 2], Doan Hong Ngoc Tran[2, 3], Minh-Anh Dang-Trinh[2], Huynh Chan Khon[3, 4, 5*]**

*[1]School of Biotechnology, International University, Vietnam National University - Ho Chi Minh City, Quarter 6, Linh Trung Ward, Thu Duc City, Ho Chi Minh City, Vietnam*
*[2]Institute of Malariology, Parasitology and Entomology, Ho Chi Minh City, 699 Tran Hung Dao Street, Ward 1, District 5, Ho Chi Minh City, Vietnam*
*[3]School of Biomedical Engineering, International University, Vietnam National University - Ho Chi Minh City, Quarter 6, Linh Trung Ward, Thu Duc City, Ho Chi Minh City, Vietnam*
*[4]Research Centre for Infectious Diseases, International University, Vietnam National University - Ho Chi Minh City, Quarter 6, Linh Trung Ward, Thu Duc City, Ho Chi Minh City, Vietnam*
*[5]Vietnam National University - Ho Chi Minh City, Linh Trung Ward, Thu Duc City, Ho Chi Minh City, Vietnam*

Received 22 March 2023; revised 26 May 2023; accepted 21 June 2023

***Abstract:***

**The Coronavirus (SARS-CoV-2) is an enveloped RNA virus that caused a dangerous COVID-19 pandemic following an outbreak in Wuhan, China in 2019. In response to the pandemic, the development of lateral flow assays (LFAs) has been crucial for the detection of viruses, commonly targeting the spike (S) or nucleocapsid (N) protein in nasopharyngeal swab (NS) specimens. COVID-19, caused by the SARS-CoV-2 virus, predominantly manifests as a respiratory tract infection-like illness, characterized by symptoms such as fever, dry cough, upper airway congestion, runny nose, sore throat, myalgia, headache, and exhaustion. This study presents the development of an LFA targeting the N protein to detect the coronavirus in saliva specimens, using a sandwich format. The use of 80 nm gold nanoparticles (AuNPs) has been investigated, and the application of horseradish peroxidase (HRP) and TMB substrate has been employed to enhance the limit of detection (LOD). The results demonstrate a significant 200-fold improvement in LOD, from 10 to 50 pg/ml, for N protein spiked in saliva samples after the application of HRP-TMB. This finding highlights an important advancement towards the utilization of saliva samples in diagnostic applications.**

***Keywords:*** **horseradish peroxidase, lateral flow assay, mixed-sized gold nanoparticles, SARS-CoV-2 nucleocapsid protein.**

***Classification numbers:*** **3.5, 3.6**

## 1. Introduction

The Coronavirus is an enveloped RNA virus belonging to the Coronaviridae family and primarily affects humans, as well as other species such as mammals and birds, causing various respiratory problems. Researchers have classified the Coronaviridae family into four genera, namely α, β, γ, and δ, based on the structure of the genome and phylogenetic analysis. The γ and δ genera mainly infect birds, while the α and β genera are commonly reported to infect mammals and humans [1]. Prior to the COVID-19 outbreak, two pandemics caused by β-CoV occurred: severe acute respiratory syndrome coronavirus (SARS-CoV, 2002-2003) and Middle East respiratory syndrome coronavirus [2]. COVID-19, caused by the SARS-CoV-2 virus, predominantly manifests as a respiratory tract infection-like illness, characterized by symptoms such as fever, dry cough, upper airway congestion, runny nose, sore throat, myalgia, headache, and exhaustion. While diarrhea has been recorded in a few patients, dyspnoea is a potential symptom in certain individuals. Severe cases of COVID-19 can rapidly

*Corresponding author: Email: hckhon@hcmiu.edu.vn

progress to septic shock, acute respiratory distress syndrome, and coagulation dysfunction [3].

Currently, there are two main groups of clinically and commercially available COVID-19 tests. The first category comprises molecular assays for detecting SARS-CoV-2 viral RNA using PCR-based or nucleic acid hybridization-related methods. The second group consists of immunological and serological tests that focus on identifying antibodies and antigens in infected individuals [3, 4]. However, these techniques require specialized equipment, are time-consuming, and labour-intensive, highlighting the urgent need for rapid, convenient, and affordable technologies. Consequently, there has been increased interest in immunogold labelling technology, which offers excellent sensitivity, a simple procedure, and rapid detection in immunoassays. LFA production has been developed to address these considerations. As of June 2021, 1,102,383 RT-qPCR tests had been performed, compared to 36,663,990 antigen quick tests (AQT) used by citizens in Europe [5].

Both the spike glycoprotein (S-protein) and the nucleocapsid (N-protein) can serve as primary immunoassay targets for SARS-CoV-2 [3]. The coronavirus spike protein, a trimeric single-pass membrane protein, plays a crucial role in the early stages of the virus infection cycle by facilitating the fusion of viral and host cell membranes. It consists of a long ectodomain, a single-pass transmembrane anchor, and a short intracellular tail. The ectodomain comprises the receptor-binding domain (RBD) subunit S1 and the membrane-fusion subunit S2. The S1 subunit attaches to a receptor on the host cell surface, while the S2 subunit merges the host and viral membranes to enable viral entry into host cells [6, 7]. The coronavirus nucleocapsid protein, which interacts with the viral membrane protein during virion assembly and forms complexes with genomic RNA, serves as a structural protein with multiple functions. It plays a crucial role in enhancing virus transcription, translation, and assembly [8]. Additionally, the nucleocapsid protein elicits a highly antigenic response and is frequently the primary target of the immune response, particularly with immunoglobulin G-dominated antibodies [9]. Moreover, the nucleocapsid protein employs strategies to evade the host's innate immune system by interfering with interferon production, which is essential for the viral pathogenesis response [10]. The detection of the SARS-CoV-2 antigen has predominantly focused on the receptor-binding domain of the S1 subunit and the nucleocapsid N protein, considering their significance in the pathophysiology and immunogenicity of the SARS-CoV-2 virion in the human body.

Since the onset of the pandemic, nasopharyngeal swabs (NS samples) have been widely used as the primary samples for SARS-CoV-2 diagnosis due to the high viral loads and early expression in the nasopharyngeal region, with viral loads ranging from approximately $9.9\times10^2$ to $1.2\times10^8$ copies/ml within the first 7 days [11]. However, the use of deep nasopharyngeal swabs has been reported as uncomfortable for both adults and children. As a result, based on user feedback and complaints, saliva specimens have been employed for COVID-19 LFAs throughout the United States, even though the reported viral load in saliva specimens is lower than that in nasopharyngeal swabs, ranging from $10^2$ to $10^3$ copies/ml [12]. Saliva samples have shown lower positivity rates (88%, 95% CI: 81 to 93%) compared to nasopharyngeal swabs [13]. Despite the challenges posed by saliva components, such as viscosity and enzyme activity, saliva remains a promising and comfortable sample type for SARS-CoV-2 LFAs.

Gold nanoparticle technology has been extensively utilized in LFA production. Various sizes of gold nanoparticles have been investigated for colorimetric analysis in LFAs. Larger gold nanoparticle sizes over 60 nm can lead to unstable outcomes in LFAs, although they exhibit a significant increase in colour [14, 15]. In recent years, with advancements in LFA development and the application of the enzyme-linked immunosorbent assay (ELISA) principle in LFAs, researchers have explored the

use of HRP enzymes as labels to build competitive LFAs for the multiplexed study of carbaryl and endosulfan, comparing the results obtained with different systems [16]. The application of the TMB substrate in HRP amplification involves a chemiluminescence reaction where HRP reduces hydrogen peroxide and oxidizes TMB, resulting in a colour change from colourless to blue, facilitating visual observation. Furthermore, HRP-TMB amplification has shown a 100-fold improvement in signal compared to conventional AuNP-based methods [17, 18].

Based on the information mentioned above, this study aims to investigate the use of 80 nm AuNPs in LFA production for the detection of SARS-CoV-2 N protein using human saliva samples. Additionally, the study explores the use of HRP as an enhancer to improve the LOD in AuNP-based LFAs and compares the results to a commercial LFA from China.

## 2. Materials and methods

### *2.1. Materials*

Gold Conjugation Kit (80 nm, 20 OD) and HRP Conjugation Kit - Lightning-Link® were purchased from Abcam (Cambridge, UK). Hi-FlowTM Plus 180 nitrocellulose membrane cards, C083 Cellulose Fiber Sample Pad Strips, and Glass Fiber Diagnostic Pad were purchased from Merck Millipore (Burlington, Massachusetts, USA). Saliva was collected from volunteers. SARS-CoV-2 Nucleocapsid Recombinant Protein (RP-87665, Invitrogen) was selected as the target antigen for all experiments. SARS-CoV-2 Nucleocapsid Recombinant Rabbit Monoclonal Antibody (3E8A5, Invitrogen) was used as the capture antibody, and Anti-SARS-CoV-2 Nucleocapsid antibody produced in mouse (7B3, Sigma-Aldrich) was used as the detection antibody, while Anti-Rabbit IgG (whole molecule) antibody produced in goat (R1131, Sigma Aldrich) was used as the control antibody. Healthy saliva samples were collected from volunteers.

### *2.2. Methods*

#### *2.2.1. Preparation of detection antibody-gold nanoparticle (Ab-AuNPs) conjugates*

The detection antibody (detection Ab) was conjugated to 80 nm AuNPs using the Gold Conjugation Kit (ab154876, Abcam) following the user manual. The UV-Vis spectra of bare AuNPs and detection Ab-AuNPs conjugates were analysed using a microplate reader (Synergy HT, Biotek). Absorbance spectra from 450-600 nm with 1 nm-step intervals were recorded for both solutions. A successful conjugation was expected to result in a right shift in the UV-Vis spectra due to the change in the local refractive index of the nanoparticles.

#### *2.2.2. Preparation of detection antibody-horseradish peroxidase (Ab-HRP) conjugates*

The detection antibody (detection Ab) was conjugated to HRP using HRP Conjugation Kit - Lightning Link ® (ab102890, AbCam) according to the user manual.

#### *2.2.3. Optimization of different lateral flow assay parameters*

Prior to the optimization process, the functionality of both capture and control antibodies, as well as the detection Ab-AuNPs conjugation, was tested on the half-strip model. The two antibodies (capture Ab and control Ab) were diluted in PBS pH 7.4 buffer and dotted on the nitrocellulose membrane to create a test line (T-line) and a control line (C-line). The membrane was then blocked with 1% (w/v) BSA for 15 minutes to minimize nonspecific binding, followed by complete air-drying before testing. Detection Ab-AuNPs conjugates were diluted in PBS pH 7.4 buffer containing 1% BSA. For testing the half-strip models, detection Ab-AuNPs conjugates were premixed with SARS-CoV-2 N protein at 500 ng/ml, which was further diluted in 1X PBS.

Three parameters of the LFA strips were optimized in this study: The concentration of capture antibody,

the concentration of Ab-AuNPs conjugate, and the concentration of Ab-HRP conjugate.

(1) Capture antibody concentration: Different dilution rates of capture antibody (0.5, 0.2, and 0.1 mg/ml) were prepared using 1X PBS pH 7.4 buffer and dotted on the membrane to create the T-line. The C-line was prepared at a concentration of 0.5 mg/ml, followed by dropping a mixture of detection Ab-AuNPs conjugates and diluted SARS-CoV-2 N protein onto the nitrocellulose membrane.

(2) Conjugate concentration: The intensity increased with higher conjugate concentrations. Detection Ab-AuNPs conjugate was prepared at different dilution rates of 1:2, 1:5, and 1:10, and then applied onto the nitrocellulose membrane after mixing with diluted SARS-CoV-2 N protein.

(3) Ab-HRP concentration: The Ab-HRP was serially diluted at different ratios ranging from 1:1 to 1:5000 by 1X PBS pH 7.4 buffer.

*2.2.4. Test-strip performance with HRP enhancement*

The full strip model of the LFA was assembled based on the established optimal conditions. SARS-CoV-2 N protein was resuspended and serially diluted in saliva samples, ranging from 500 ng/ml to 50 pg/ml. Each extracted sample (500 µl-1 ml) was added to the extraction buffer of the COVID-19 Antigen Rapid Test Kit (eDiagnosis). Subsequently, 100 µl of each extracted sample was applied to the developed test strips, and the signals were observed. To enhance the band intensity, all strips were washed with 1X PBS pH 7.4 buffer at least once. An optimal concentration of Ab-HRP (70 µl) was directly dropped onto the sample pad for absorbance. After 10 minutes in dark conditions, 5 µl of TMB substrate was added directly to the T-line and C-line of all strips for colour appearance. The reaction was stopped by washing the unbound Ab-HRP with 1X PBS.

*2.2.5. LOD and comparison with the commercial test kit*

Spiked saliva samples (100 µl) were dropped onto the Easy Diagnosis Antigen Kit Test to estimate the LOD. The results were compared with our developed test strip, which included HRP enhancement. Band intensities were observed visually and further analysed using ImageJ software. The LOD was determined as the lowest antigen concentration at which the test line was still visible.

## 3. Results

### *3.1. Establishment of a lateral flow assay for detecting SARS-CoV-2 nucleocapsid protein*

The working principle of our LFA design is illustrated in Fig. 1. Initially, the extracted sample is applied to the sample pad. The antigens present in the sample migrate towards the conjugation pad and bind with the detection Ab-AuNPs conjugates. The N protein-detection Ab-AuNPs complexes are captured by the immobilized capture antibody (capture Ab) at the T line, forming a sandwich structure. Any excess detection Ab-AuNP conjugates that do not bind to antigens are captured at the C line by anti-rabbit IgG, indicating a positive signal and confirming the proper functioning of the assay.

To evaluate the functionality of the assay, we first assembled a half-strip model, which consisted of only the nitrocellulose membrane and absorbent pad, and pre-mixed the sample with the detection Ab-AuNPs conjugates. The half-strip models were used to test samples containing N protein at a concentration of 1 µg/ml. A valid outcome of the strip should show the appearance of both the T line and C line in red colour (Fig. 1A), while the absence of the C line or the appearance of both lines indicates an invalid result (Fig. 1D). Subsequently, detection Ab-HRP was applied to the valid strips to enhance the signal (Fig. 1B). For signal examination, TMB substrate was directly added to the T line and C line, resulting in the appearance of blue colour in both lines for a positive result and only the C line appearance for a negative result (Fig. 1C).

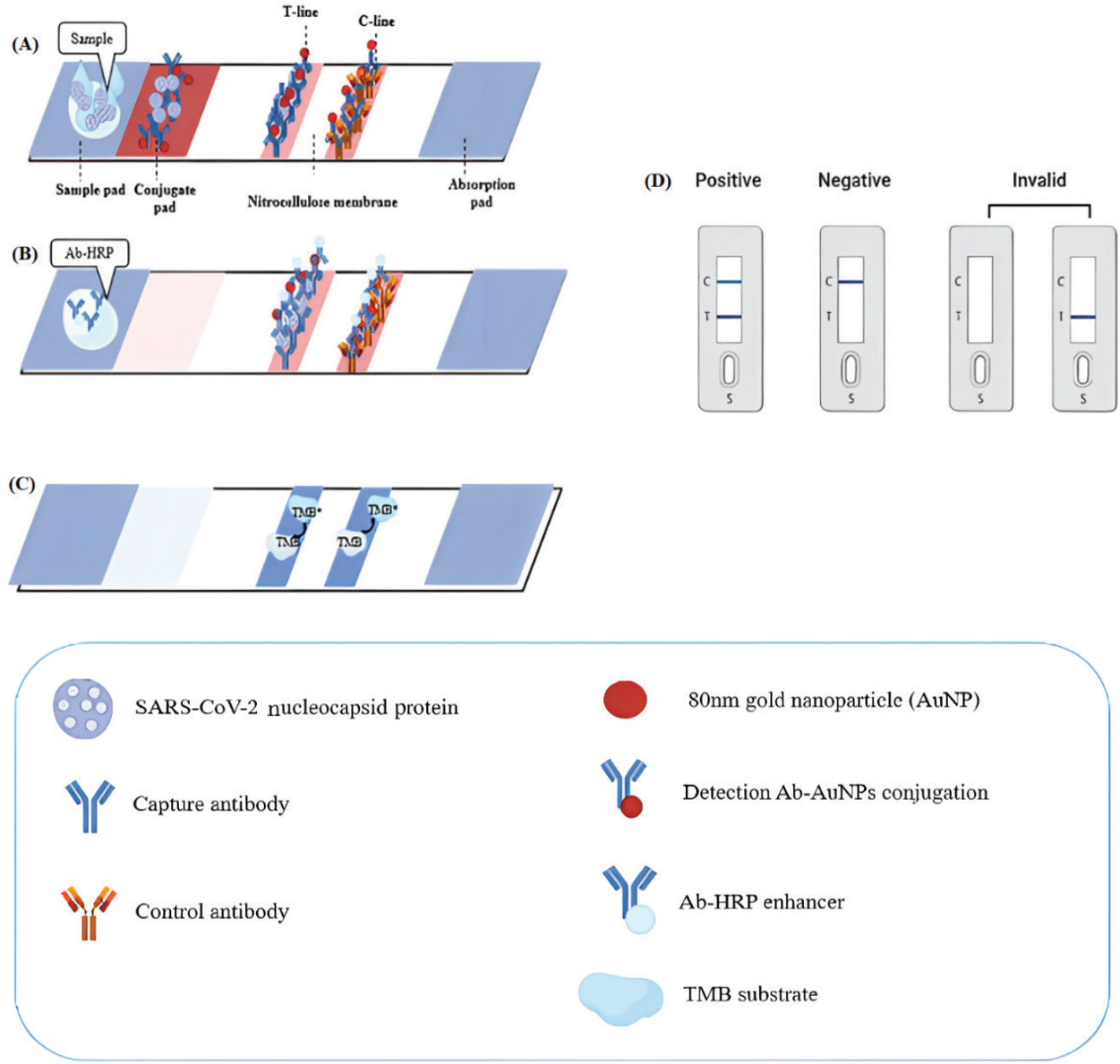


**Fig. 1. The designed LFA strips for SARS-CoV-2 detection and its principle. (A)** The principle of LFA using AuNP technology; **(B)** The binding of Ab-HRP into the based-AuNPs LFA strips; **(C)** The colour changes of HRP with TMB substrate reaction; **(D)** Interpreting results of LFA strips.

### *3.2. Full strip model*

After confirming the functionality of the assay using the half-strip models, we developed the full strip model of the LFA for SARS-CoV-2 N protein detection. Experiments were conducted to determine the optimal assembly conditions to achieve a good signal-to-noise ratio. A high level of background noise would hinder the subsequent HRP enhancement, as it would result in the entire strip turning blue, reducing the colour intensity observed visually. Through optimization experiments, we determined that the optimal dilution concentration of the capture Ab was 0.2 mg/ml, the dilution rate of the detection Ab-AuNPs conjugate was 1:5, and the dilution rate of the detection Ab-HRP conjugate was 1:1000. Fig. 2 illustrates the appearance of the developed full strip, including the sample pad, conjugate pad, nitrocellulose membrane, and absorption pad, after being tested with N protein at a concentration of 500 ng/ml.

**Fig. 2. The result of the developed full-strip, including the sample pad, conjugate pad, nitrocellulose membrane, and absorption pad, after being tested with 500 ng/ml SARS-CoV-2 N protein.**

### *3.3. Evaluation of LOD of LFA strip*

To determine the LOD of the LFA strips, SARS-CoV-2 N proteins were prepared at different concentrations ranging from 1 µg/ml to 50 pg/ml. After preparing complete LFA strips, samples with different concentrations were applied to the strips. Visual examination of the strips revealed the development of a positive signal at the T line for samples with concentrations ≥10 ng/ml (Fig. 3). For samples with concentrations lower than 10 ng/ml, the T line either showed a faint red line or no signal. Strong positive signals were observed at the C line in all test strips, indicating that they were functioning properly.

### *3.4. Enhancement of LFA strip sensitivity by HRP enhancement*

To enhance the LOD of the LFA strip for the N protein, the HRP enhancement method was applied after the strips showed certain signals. Specifically, LFA strips from the LOD experiments mentioned above were washed with 1X PBS buffer and treated with detection Ab-HRP, followed by 10 minutes of incubation in dark conditions. Visual examination of the signal intensities showed that the band intensities changed from the red colour of AuNPs to the blue colour due to the oxidation of the TMB substrate by HRP. As a result, the LOD was improved to 50 ng/ml through HRP enhancement, which represented a 200-fold increase compared to the AuNP method. The signal intensities before and after signal enhancement were further analysed using the ImageJ densitometry function (Figs. 4, 5).

### *3.5. Comparison of the LOD of the LFA strip with the commercial test kit*

Two types of tests were validated based on the appearance of the C line in the negative control strips. With the sample extracted using the commercial buffer provided in the eDiagnosis Antigen Test Kit, the commercial strip showed an LOD of 100 pg/ml (Fig. 6A) [19], while our developed LFA strip demonstrated an LOD of 50 pg/ml (Fig. 3B) after applying HRP enhancement. The ImageJ results confirmed the successful appearance of the T line in the LFA strip (Fig. 6B).

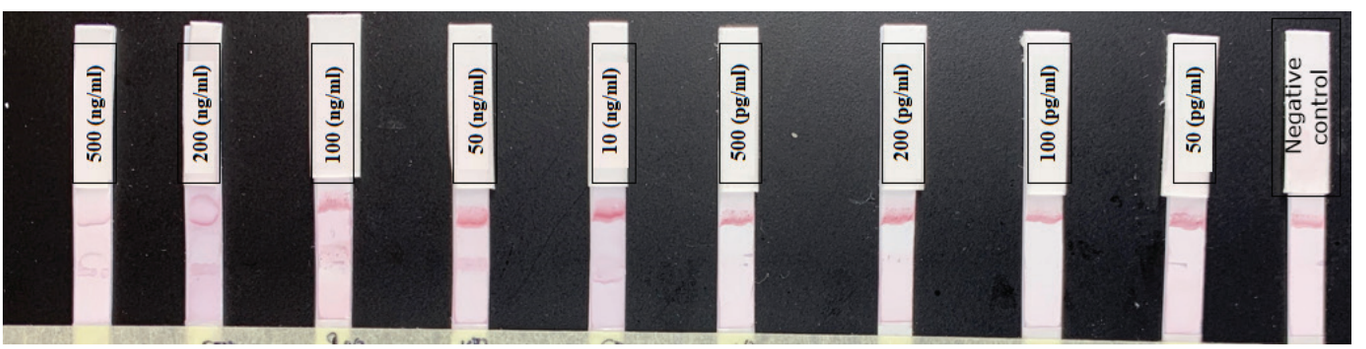


**Fig. 3. Visual examination of results from LFA strips with 80 nm AuNPs-Ab conjugates.**

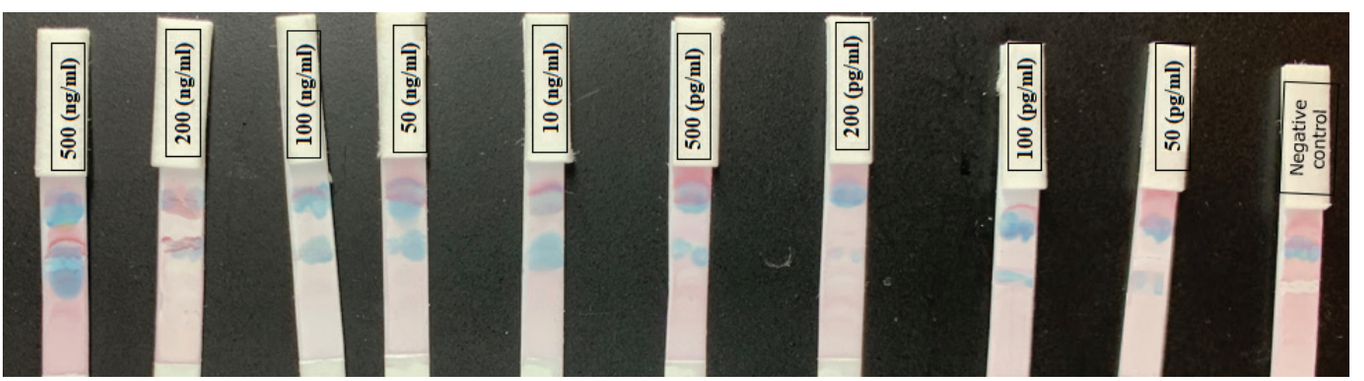


**Fig. 4. Visual examination of results from LFA strips after HRP signal enhancement.**

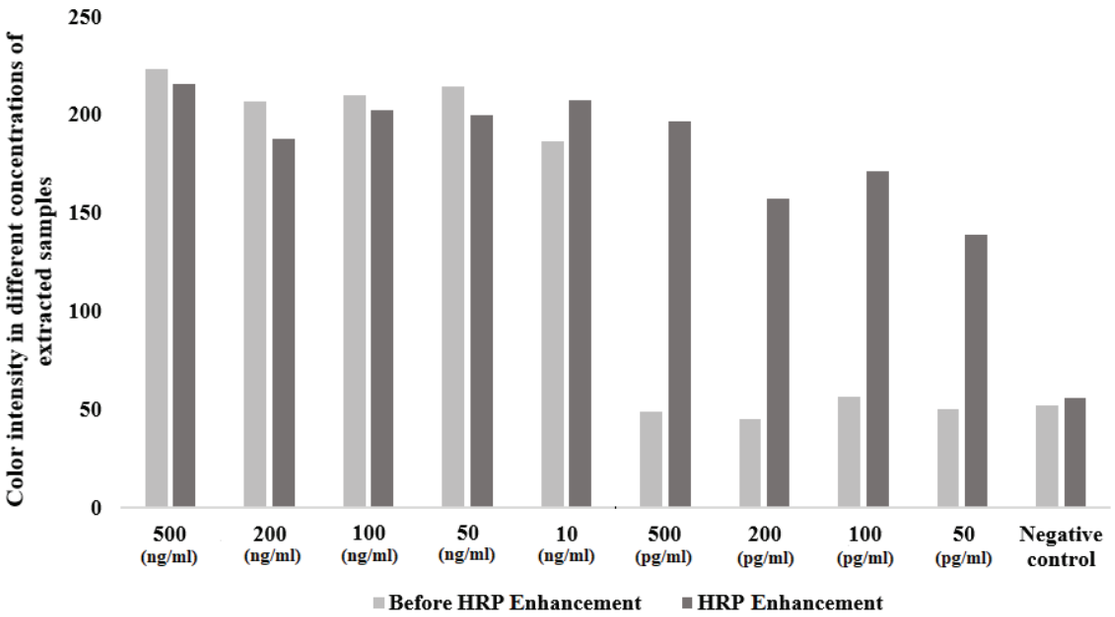


**Fig. 5. ImageJ analysis to compare band intensities of LFA strips before and after HRP signal enhancement.**

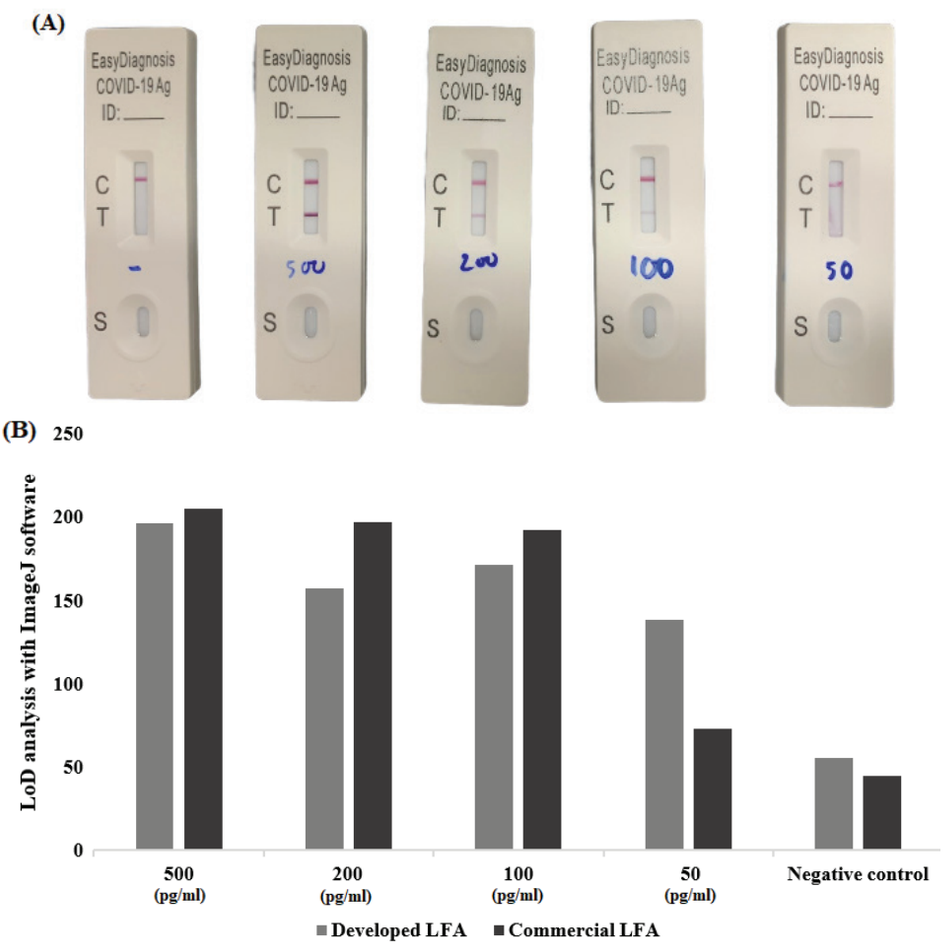


**Fig. 6. Commercial test kit analysis. (A)** LOD of the commercial test kit; **(B)** Data analysis of commercial test kit with the developed LFA strips using ImageJ software.

## 4. Discussion

LFAs are widely used for point-of-care diagnostics due to their simplicity, speed, and cost-effectiveness. In LFAs, AuNPs are commonly employed due to their unique optical properties, allowing for visual detection of target analytes. Typically, AuNPs with diameters ranging from 10 to 100 nm are used in LFAs, with sizes of 20, 30, and 40 nm being the most common. The size of the gold nanoparticles can affect the colour and intensity of the signal produced, as well as their stability and interaction with other components of the LFA. Previous studies have reported that the use of colloidal gold with a diameter ≥60 nm leads to unstable detection on the strip [20-24]. However, larger gold nanoparticles tend to produce stronger colour signals, which can impact assay sensitivity. In this study, we selected 80 nm AuNPs to enhance the colour signal in the LFA assays. The appearance of test lines on the LFA strips after sample loading indicated successful assay development, although the LOD was not yet optimal.

Various labelling approaches have been explored to enhance the sensitivity of LFAs, such as dual AuNPs, silver staining, enzyme amplification, surface-enhanced Raman scattering, and photothermal methods [25]. Each method has its own limitations, such as high cost, the need for additional signal readers, and dependence on dye stability. In this study, we employed HRP and its substrate TMB for signal enhancement in the LFA strips. HRP catalyses the conversion of TMB to a blue-coloured product, which is then converted to a yellow-coloured product by adding an acidic stop solution. In enzyme-linked immunosorbent assays, HRP is often conjugated to a detection antibody and used to detect the presence of specific antigens or antibodies in biological samples. HRP is widely available and relatively inexpensive compared to other enzymes used in assays. By applying HRP-antibody amplification and TMB substrate for signal enhancement, the sensitivity of the assay was significantly improved by 200-fold, with the LOD being enhanced from 10 ng/ml to 50 pg/ml. This improvement surpassed the sensitivity of the commercial test kit, which had a LOD at 100 pg/ml. These results demonstrate the potential of HRP enhancement as a means to increase signal intensity and develop novel LFAs.

## 5. Conclusions

This study highlights the promising role of HRP in enhancing LFAs. Through the application of HRP enhancement, there was a 200-fold improvement in the visual LOD, which increased from 10 ng/ml to 50 pg/ml of SARS-CoV-2 N protein in saliva when using the commercial buffer of the eDiagnosis COVID-19 Antigen Test Kit. Compared to other pathogen detection methods such as conventional culture, qRT-PCR, and ELISA, this assay demonstrated completion within approximately 15-20 minutes, with a simple procedure that can be visually interpreted and at a low cost. These characteristics position this assay as a significant step towards the development of future SARS-CoV-2 test kits targeting the N protein using HRP enhancement.

## CRediT author statement

Minh Hieu Vu: Algorithm, Experiment, Writing, and Editing; Doan Hong Ngoc Tran: Experiment, Writing - Original draft preparation; Minh-Anh Dang-Trinh: Reviewing and Editing; Huynh Chan Khon: Writing - Reviewing and Editing.

## COMPETING INTERESTS

The authors declare that there is no conflict of interest regarding the publication of this article.

## REFERENCES

[1] Coronaviridae Study Group of the International Committee on Taxonomy of Viruses (2020), "The species Severe acute respiratory syndrome-related Coronavirus: Classifying 2019-nCoV and naming it SARS-CoV-2", *Nature Microbiology*, **5(4)**, pp.536-544, DOI: 10.1038/s41564-020-0695-z.

[2] N. Zhu, D. Zhang, W. Wang, et al. (2020), "A novel Coronavirus from patients with Pneumonia in China, 2019", *New England Journal of Medicine*, **382(8)**, pp.727-733, DOI: 10.1056/nejmoa2001017.

[3] D. Liu, F. Wu, Y. Cen, et al. (2021), "Comparative research on nucleocapsid and spike glycoprotein as the rapid immunodetection targets of COVID-19 and establishment of immunoassay strips", *Molecular Immunology*, **131**, pp.6-12, DOI: 10.1016/j.molimm.2021.01.005.

[4] L.J. Carter, L.V. Garner, J.W. Smoot, et al. (2020), "Assay techniques and test development for COVID-19 diagnosis", *ACS Central Science*, **6(5)**, pp.591-605, DOI: 10.1021/acscentsci.0c00501.

[5] World Health Organization (2022), *Use of SARS-Cov-2 Antigen-Detection Rapid Diagnostic Tests for COVID-19 Self-Testing*, 16pp.

[6] F. Li (2016), "Structure, function, and evolution of Coronavirus spike proteins", *Annual Review of Virology*, **3**, pp.237-261, DOI: 10.1146/annurev-virology-110615-042301.

[7] A.H.M. Wong, A.C.A. Tomlinson, D. Zhou, et al. (2017), "Receptor-binding loops in alphacoronavirus adaptation and evolution", *Nature Communications*, **8(1)**, DOI: 10.1038/s41467-017-01706-x.

[8] R. McBride, M.V. Zyl, B.C. Fielding (2014), "The Coronavirus nucleocapsid is a multifunctional protein", *Viruses*, **6(8)**, pp.2991-3018, DOI: 10.3390/v6082991.

[9] H.K. Lee, B.H. Lee, N.K. Dutta, et al. (2008), "Detection of antibodies against SARS-Coronavirus using recombinant truncated nucleocapsid proteins by ELISA", *J. Microbiol. Biotechnol.*, **18(10)**, pp.1717-1721.

[10] M. Spiegel, A. Pichlmair, L.M. Sobrido, et al. (2005), "Inhibition of beta interferon induction by severe acute respiratory syndrome coronavirus suggests a two-step model for activation of interferon regulatory factor 3", *Journal of Virology*, **79(4)**, pp.2079-2086, DOI: 10.1128/jvi.79.4.2079-2086.2005.

[11] S.C.Y. Wong, H. Tse, H.K. Siu, et al. (2020), "Posterior oropharyngeal saliva for the detection of severe acute respiratory syndrome Coronavirus 2 (SARS-CoV-2)", *Clin. Infect. Dis.*, **71(11)**, pp.2939-2946, DOI: 10.1093/cid/ciaa797.

[12] L.L. Fernandes, V.B. Pacheco, L. Borges, et al. (2020), "Saliva in the diagnosis of COVID-19: A review and new research directions", *Journal of Dental Research*, **99(13)**, pp.1435-1443, DOI: 10.1177/0022034520960070.

[13] R.A. Lee, J.C. Herigon, A. Benedetti, et al. (2021), "Performance of saliva, oropharyngeal swabs, and nasal swabs for SARS-CoV-2 molecular detection: A systematic review and meta-analysis", **59(5)**, DOI: 10.1128/JCM.02881-20.

[14] B.N. Khlebtsov, R.S. Tumskiy, A.M. Burov, et al. (2019), "Quantifying the numbers of gold nanoparticles in the test zone of lateral flow immunoassay strips", *ACS Applied Nano Materials*, **2(8)**, pp.5020-5028, DOI: 10.1021/acsanm.9b00956.

[15] A. Momeni, M.R. Nejad, R. Salarian, et al. (2022), "Gold-based nanoplatform for a rapid lateral flow immunochromatographic test assay for gluten detection", *BMC Biomedical Engineering*, **4(1)**, DOI: 10.1186/s42490-022-00062-2.

[16] C. Zhang, Y. Zhang, S. Wang (2006), "Development of multianalyte flow-through and lateral-flow assays using gold particles and horseradish peroxidase as tracers for the rapid determination of carbaryl and endosulfan in agricultural products", *Journal of Agricultural and Food Chemistry*, **54(7)**, pp.2502-2507, DOI: 10.1021/jf0531407.

[17] D. Calabria, M.M. Calabretta, M. Zangheri, et al. (2021), "Recent advancements in enzyme-based lateral flow immunoassays", *Sensors*, **21(10)**, DOI: 10.3390/s21103358.

[18] C. Parolo, A.S. Torralba, J.F. Bergua, et al. (2020), "Tutorial: Design and fabrication of nanoparticle-based lateral-flow immunoassays", *Nature Protocols*, **15(12)**, pp.3788-3816, DOI: 10.1038/s41596-020-0357-x.

[19] A.I.C. Atienzar, K. Kontogianni, T. Edwards, et al. (2021), "Limit of detection in different matrices of 19 commercially available rapid antigen tests for the detection of SARS-CoV-2", *Scientific Reports*, **11(1)**, DOI: 10.1038/s41598-021-97489-9.

[20] F.M.M. Aldosari (2022), "Characterization of labeled gold nanoparticles for surface-enhanced Raman scattering", *Molecules*, **27(3)**, DOI: 10.3390/molecules27030892.

[21] A.M. Fales, W.C. Vogt, J. Pfefer, et al. (2017), "Quantitative evaluation of nanosecond pulsed laser-induced photomodification of plasmonic gold nanoparticles", *Scientific Reports*, **7(1)**, DOI: 10.1038/s41598-017-16052-7.

[22] D.S. Kim, Y.T. Kim, S.B. Hong, et al. (2016), "Development of lateral flow assay based on size-controlled gold nanoparticles for detection of hepatitis B surface antigen", *Sensors (Switzerland)*, **16(12)**, DOI: 10.3390/s16122154.

[23] C.M. Liu, C.M. Williams, N.M. Acuña, et al. (2022), "Development of a rapid gold nanoparticle-based lateral flow immunoassay for the detection of dengue virus", *Biosensors*, **12(7)**, DOI: 10.3390/bios12070495.

[24] A. Zuber, M. Purdey, E. Schartner, et al. (2016), "Detection of gold nanoparticles with different sizes using absorption and fluorescence based method", *Sensors and Actuators B: Chemical*, **227**, pp.117-127, DOI: 10.1016/j.snb.2015.12.044.

[25] Y. Deng, H. Jiang, X. Li, et al. (2021), "Recent advances in sensitivity enhancement for lateral flow assay", *Microchimica Acta*, **188(11)**, DOI: 10.1007/s00604-021-05037-z.

DOI: 10.31276/VJSTE.66(1).120-128
Review

# Environmental and health impacts of air pollution: A mini-review

**Linh-Thy Le[1, 2], Khanh-Bang V. Quang[1], Trieu-Vi Vo[1], Thanh-Mai T. Nguyen[1], Thi-Viet-Huong Dao[2], Xuan-Thanh Bui[2*]**

*[1]Faculty of Public Health, University of Medicine and Pharmacy at Ho Chi Minh City (UMP), 217 Hong Bang Street, Ward 11, District 5, Ho Chi Minh City, Vietnam*
*[2]Ho Chi Minh City University of Technology (HCMUT), 268 Ly Thuong Kiet Street, Ward 14, District 10, Ho Chi Minh City, Vietnam*

Received 5 September 2023; revised 5 January 2024; accepted 2 March 2024

***Abstract:***

**Air pollution is one of the leading risk factors for death but also a significant contributor to the global disease burden, affecting quality of life. According to a World Health Organisation (WHO) report, seven million people die from air pollution every year, and 9 out of 10 people worldwide breathe polluted air. Any person can be affected by exposure to polluted air, especially the elderly, children, pregnant women, and people with comorbidities. Some studies indicate that the diseases most affected by air pollution are respiratory infections, chronic obstructive pulmonary disease (COPD), lung cancer, and cardiovascular diseases. The degree of effect on the body depends on the pollutant composition, source and dose, level and duration of exposure to polluted air. Particulate matter ($PM_{10}$ and $PM_{2.5}$), carbon monoxide (CO), ozone ($O_3$), nitrogen dioxide ($NO_2$), and sulphur dioxide ($SO_2$) could lead to air pollution. Long-term exposure to air pollution can affect every organ in the body and worsen existing health conditions. Short-term exposure to contaminants can include unpleasant sensations such as coughing, wheezing, shortness of breath, eye, nose, and throat irritation, headache, dizziness, and fatigue. Community and individual solutions such as using clean fuel, wearing personal masks, filtering indoor air, and ventilating need to be taken to reduce the impact of air pollution.**

***Keywords:*** **air pollution, environment, health, impacts.**

***Classification number:*** **5.3**

## 1. Introduction

Air pollution is a global issue. According to World Health Organisation (WHO) statistics, over 92% of the population lives in polluted air [1]. This has significantly impacted human life and the natural environment. Notably, approximately 93% of children over 15 years old worldwide breathe polluted air, primarily due to indoor air pollution sources [2].

Air pollution entails a significant alteration in the composition of the air, caused by smoke, dust, vapours, or foreign gases being introduced into the atmosphere, leading to peculiar odours, reduced visibility, and climate change. These pollutants directly affect the health of humans, animals, and plants on Earth. PM, $O_3$, $NO_2$, and $SO_2$ are the main contributors to air pollution. In Vietnam, particulate matter (i.e. $PM_{2.5}$ and $PM_{10}$) was the most prominent concern among air pollutants from 2011 to 2020 [3]. Fine dust pollution remains a significant issue in major industrial centres of Vietnam such as Hanoi and Ho Chi Minh city. $PM_{2.5}$ and $PM_{10}$ levels at continuous automatic monitoring stations in Hanoi during the period 2018-2020 exceeded the QCVN 05:2013/BTNMT (National technical regulation on ambient air quality) threshold by 1.1 to 2.2 times [4]. Research by N.T.K. Oanh, et al. (2018) [5] estimated $PM_{2.5}$ emissions in 2018 from human activities and forest fires in Vietnam at approximately 600 thousand tons (excluding road dust and other sources). Among these, $PM_{2.5}$ emissions from agricultural waste incineration accounted for the highest proportion (40%), followed by residential cooking (17%), road traffic (13%), forest fires (12.7%), industrial activities (11%), and thermal power plants (3.3%). The remaining sectors collectively contributed about 3% of

*Corresponding author: Email: thanhait@yahoo.com

the country's total $PM_{2.5}$ emissions. Particularly, Hanoi and Ho Chi Minh city had the highest emissions, ranging from 9.01 to 10.25 tons/km$^2$/year. Provinces in other regions, such as the northern midlands, mountains, and the central region, had lower $PM_{2.5}$ emissions, ranging from 0.35 to 3.0 tons/km$^2$/year. The total amount of sulphur oxide ($SO_x$) emissions for the entire country in 2018 was about 750 thousand tons/year, with emissions from thermal power plants and industrial activities contributing over 91%.

The disease burden associated with exposure to indoor and outdoor air pollution is significant and increasing. It poses a major threat to human health, resulting in approximately 7 million deaths annually. Air pollution increases morbidity and mortality from non-communicable cardiovascular and respiratory diseases. Furthermore, deteriorating air quality is the leading cause of increased disease burden from lower respiratory tract infections, premature births, and other causes of death in children.

Moreover, air pollution remains a significant cause of disease burden in low- and middle-income countries [6]. In 2019, the impact of indoor and outdoor air pollution on mortality surpassed common factors such as obesity, low birth weight, or an unhealthy diet [7]. Additionally, based on European data, a 1 μg/m$^3$ increase in $PM_{2.5}$ concentration (or a sample mean increase of 10%) results in a 0.8% decrease in real GDP in the same year [8]. Besides the associated health burden, air pollution imposes additional economic costs, such as its impact on crops or damage to buildings and infrastructure. Furthermore, there are costs associated with climate change resulting from air pollution and environmental degradation [6].

Various reports have presented the air quality in Vietnam. According to Yale University's Environmental Performance Index (EPI) 2020, Vietnam's air pollution exposure ranks 115th out of 180 countries. On the IQir/AirVisual ranking, Vietnam's average $PM_{2.5}$ concentration in 2020 ranked 21$^{st}$ among 106 countries [5]. According to new data from the WHO, over 60,000 people died in 2016 from heart disease, stroke, lung cancer, chronic obstructive pulmonary disease, and pneumonia in Vietnam [9]. Therefore, this review aims to provide general information on air pollution, along with implementing some policies and measures to reduce the impact of air pollution on personal health and the community.

## 2. Air pollution

### *2.1. Classification of air pollution*

Air pollution can be defined as harmful chemicals or compounds, including those of biological origin, in the air at levels hazardous to health [10]. Additionally, air pollution refers to the presence of chemicals or compounds in the air that reduce air quality or cause harmful changes to the quality of life, such as destroying the ozone layer or causing global warming [11].

Air pollution is classified into outdoor and indoor air pollution. Outdoor air pollution mainly originates from vehicles and industrial plants such as thermal power plants, industrial boilers, garbage incinerators, and petrochemical plants. Indoor air can contain significant amounts of chemicals, irritants, carcinogenic chemicals, microbial agents, allergens, and fine indoor dust, termed indoor air pollution [12-15].

During the COVID-19 pandemic, governments imposed various restrictions to prevent the spread of the disease. People spent much of their time in indoor environments. Movement of people and transportation (road and air) was limited. Additionally, the suspension of international flights by airlines contributed to changes in air pollutant emissions. For example, $PM_{2.5}$ concentrations decreased by approximately 15% in the most polluted cities worldwide, with the most significant declines observed in capitals in the Americas, Asia, and Africa. Hence, it is considered that air pollution can directly result from economic growth and human activities. Various studies have shown that many indoor and outdoor pollutants are found in comparable concentrations. In some areas with limited ventilation, indoor pollution levels were higher. R. Xu, et al. (2020) [16] found that CO concentrations in indoor and outdoor environments were approximately the same at 396 and 386 ppb, respectively. Volatile organic compounds (VOC) and $PM_{10}$ concentrations in Portuguese and UK homes were several times higher than in outdoor environments [17].

### *2.2. Main source and causes of air pollution*

Air pollution consists of a mixture of dust, gases, fumes, particles, and biological materials in sufficient amounts to affect the environment and human health [11]. The primary sources of air pollution can be divided into natural and man-made sources. Natural activities

such as volcanoes (emitting toxic gases like sulphur, chlorine, and particulate matter such as ash) and forest fires generate large amounts of $CO_2$ or radioactive decay. The second source originates from human activities [18]. With rapid population growth and a constantly developing economy, energy demand has significantly increased. Human production activities generate products to meet essential needs but are also the primary source of toxic substances with harmful effects on humans. Emissions of exhaust gases, tobacco smoke, pesticides, solvents, detergents, particles, dust, moulds, fibres, and allergens are deposited daily [18, 19]. The consumption of more fossil fuels is also concerning as they cause harm affecting the sustainable development of the environment [20, 21]. Combustion sources and cooking activities also contribute to the emission of $CO_2$, $SO_2$, CO, $NO_2$, and PM into the indoor atmosphere [22].

Besides, outdoor and indoor air pollution are related [23, 24]. Several air pollutants have been recognised to exist indoors, including $NO_x$, $SO_2$, $O_3$, CO, volatile and semi-volatile organic compounds (VOCs), PM, radon, and microorganisms. Some pollutants (e.g., $NO_x$, $SO_2$, $O_3$, PM) are common indoors and outdoors, and some may originate outdoors [25]. As concentrations of outdoor pollutants increase, they are transported from the outdoors into the indoor environment, e.g., through ventilation systems [24].

### *2.3. Recommended standards of air pollutants*

**Table 1. Guidance on short-term, long-term air quality and short-term goals, updated in 2021.**

| Agent | Average time | Short-term goal | | | | AQG level |
|---|---|---|---|---|---|---|
| | | *1* | *2* | *3* | *4* | |
| $PM_{2.5}$ (µg/m³) | Yearly | 35 | 25 | 15 | 10 | 5 |
| | 24 hours[a] | 75 | 50 | 37,5 | 25 | 15 |
| $PM_{10}$ (µg/m³) | Yearly | 70 | 50 | 30 | 20 | 15 |
| | 24 hours[a] | 150 | 100 | 75 | 50 | 45 |
| $O_3$ (µg/m³) | Peak season[b] | 100 | 70 | - | - | 60 |
| | 8 hours[a] | 160 | 120 | - | - | 100 |
| $NO_2$ (µg/m³) | Yearly | 40 | 30 | 20 | - | 10 |
| | 24 hours[a] | 120 | 50 | - | - | 25 |
| $SO_2$ (µg/m³) | 24 hours[a] | 125 | 50 | - | - | 40 |
| CO (mg/m³) | 24 hours[a] | 7 | - | - | - | 4 |

[a]: 99th quartile range (e.g., exceeding 3-4 days/year); [b]: the highest average $O_3$ concentration over 8 hours daily for six consecutive months.

According to Table 1 and the WHO global air quality guidelines, compared to the 2005 AQG level, the updated 2021 version of the WHO has the following significant changes:

- The annual $PM_{2.5}$ AQG level has been lowered from 10 to 5 µg/m³. This reflects new evidence on the impact of $PM_{2.5}$ on mortality occurring at concentrations below 10 µg/m³. The 24-hour AQG level for $PM_{2.5}$ changed from 25 to 15 µg/m³.

- The annual $PM_{10}$ AQG level has been reduced from 20 g/m³ to 15 µg/m³. This reflects new evidence that the impact on mortality occurs at concentrations below 20 µg/m³. The 24-hour AQG for $PM_{10}$ has changed from 50 to 45 µg/m³.

- New peak season (long-term) ozone AQG level has been determined. This is based on new evidence on the long-term effects of ozone on total mortality and respiratory mortality. The short-term AQG level of 100 µg/m³ is the same as the 2005 short-term level.

- The annual AQG level for $NO_2$ has changed from 40 to 10 µg/m³. This is primarily because this update of air quality guidance is based on the long-term impact of $NO_2$ on all-cause mortality and respiratory mortality. A new 24-hour AQG level of 25 µg/m³ is recommended.

- A 24-hour AQG level for carbon monoxide of 4 µg/m³ is recommended. This is based on a new assessment of the impact of short-term carbon monoxide levels on hospitalisation for myocardial infarction[6].

## 3. Some studies on the relationship between air pollution and health

### *3.1. Individual level exposure*

When it comes to exposure to air pollution on an individual level, the level of exposure depends on the concentrations of pollutants in the air around them in which they reside, such as workplaces/schools or on the means of transport, etc., and the time people live/work in those spaces. Human activity time surveys show that people spend approximately 87% of their time in inadequately ventilated offices and 6% in closed vehicles. Thus, exposing themselves to air pollution on a personal level receives much attention [26, 27]. Several studies on individual monitors have found that indoor exposure to $PM_{2.5}$ contributes to 85.1% of the total exposure. The concentration of $PM_{2.5}$ inside the house increases the most at the entrance, followed by outdoor exposure (7.6%), bus (3.7%), subway (3.1%), and car (0.5%) [28].

Moreover, human activities within the home can increase an individual's exposure to $PM_{2.5}$. Three indoor practices that have been proven to raise the levels of fine dust within the home significantly are smoking cigarettes, burning incense, and cooking [29]. In 2020, WHO statistics revealed that approximately 2.4 billion individuals continue to cook using solid fuels, including wood, crop waste, charcoal, coal, and kerosene, in open-air furnaces and inefficient stoves [30]. This practice leads to an increase in the concentration of particles present in the household. In Vietnam, reports show an average individual $PM_{2.5}$ exposure of 64.28±33.18 µg/m$^3$. This exposure is higher than the concentration of $PM_{2.5}$ dust observed at two monitoring stations in district 2 and Zoo and Botanical Gardens, which is 38.49±18.45 µg/m$^3$ and 48.99±21.68 µg/m$^3$, respectively ($p<0.05$) [31]. Despite this, many remain unaware that indoor air pollution can increase exposure. The KAP Survey Model (Knowledge, Attitudes, and Practices) on indoor air pollution shows that most people do not have sufficient knowledge and correct behaviour about indoor air pollution [32-34].

### *3.2. Community level exposure*

Controlling individual exposure sources is essential for reducing health risks. However, when outdoor pollutant concentrations rise, they can infiltrate homes through ventilation systems or windows/doors [28]. Research by H.L. Chen, et al. (2020) [35] in Taiwan revealed that outdoor fine dust significantly contributes to individual exposure, accounting for approximately 44% (range 33-55%) of $PM_{2.5}$ and 74% (range 57-88%) of $NO_2$ .

Community-level exposure is associated with increased adverse health outcomes in humans [36-38]. According to a study by T.N. Dang, et al. (2022) [38] in Vietnam, monitoring $PM_{2.5}$ concentration at 31 locations in Ho Chi Minh city estimated an average $PM_{2.5}$ concentration of 27.8±7.7 µg/m$^3$. High environmental $PM_{2.5}$ concentration increases the risk of low-birth-weight babies at term during pregnancy [39]. The reports identify areas such as residential areas near main roads, factories, and chimneys as sources of air pollution for the community [36]. Vehicle transportation in urban areas is considered a source of air pollution and is linked to the development of asthma and other respiratory diseases in children [40]. Asian housing estates are often built along roads, leading to higher exposure levels in residents near significant roads than those measured in monitoring stations in the surrounding environment [41]. Accordingly, the exposure concentration of $PM_{2.5}$ for cyclists (105 µg/m$^3$) is higher than that for motorcyclists (95 µg/m$^3$), with $PM_{2.5}$ concentration in the surrounding air at 34 µg/m$^3$. Exposure to $PM_{2.5}$ was found to be highest in the morning and during peak traffic hours, especially in the inner city compared to the suburbs [42]. Studies conducted in central Manhattan (New York city, USA) revealed that the traffic system in alleyways significantly increases particulate pollution concentration in community air. Ultra-fine particles (UFP) increased by 11%, and $PM_{2.5}$ increased by 8% compared to the measured urban background index. Additionally, central parks showed a 40% higher particle density than the general background of the central area [43]. Moreover, vehicle emissions increased $PM_1$ and $PM_{2.5}$ levels at points such as bus stops and intersections by 5 µg/m$^3$ [41].

Additionally, public places such as restaurants, temples, and construction sites also contribute to increased airborne particle concentrations [36]. Incense burning in temple areas leads to a density increase of $PM_{2.5}$ particles by 2.72 µg/m$^3$, along with an elevation in the concentration of substances in incense smoke, such as VOC, carbonyl compounds, CO, $NO_x$, and $CH_4$ [20]. In Asia, the density of particles in temples is higher due to the practice of worshiping and burning incense in these countries. Research in Taiwan indicated that particle density in temples and pagodas increased by 13.2, 15.1, and 17.2 µg/m$^3$ for $PM_1$, $PM_{2.5}$, and $PM_{10}$ communities at all levels, respectively [17]. Another study by B. Wang found that particle density at two temples in Hong Kong increased from 4.2 to 18 in $PM_{2.5}$ [44].

## 4. Health effects of air pollution

Air pollution is considered a risk factor for several respiratory diseases. Most pollutants enter the body through the respiratory tract, making it the first gateway in the development and progression of air-polluted diseases [45]. Many pollutants are the leading cause of diseases in humans. In particular, particulate matter with tiny sizes, such as $PM_{10}$ and $PM_{2.5}$, can penetrate the lungs and cardiovascular system, causing cardiovascular disease, stroke, respiratory infections, COPD, asthma, and lung cancer [46].

Outdoor air pollution and urbanisation are associated with increased asthma incidence and severity. According to a study in ten European cities, the incidence of asthma

in children after exposure to pollutants from road vehicle exhaust was 14% and 15%, respectively. Those with asthma reported worsening conditions. Research has also shown a correlation between short-term exposure to $PM_{2.5}$ and $PM_{10}$ in the air with asthma symptoms, especially in children with atopy [47].

In 2023, a study showed that a combination of $PM_{2.5}$ and $O_3$ in the air caused asthma-related changes in children's airways [48]. $PM_{2.5}$, $PM_{10}$, and $O_3$ contribute to oxidative stress, facilitating pneumonia and may be the first step in carcinogenesis [49]. $NO_2$ exposure was reported to have a link with an increased risk of hospitalisation in patients with chronic obstructive pulmonary disease and asthma [50]. A systematic review and meta-analysis in China also demonstrated a positive correlation between $NO_2$ exposure and lung diseases. Specifically, an increase in $NO_2$ concentration to 10 µg/m$^3$ was associated with increased mortality from respiratory diseases and hospitalisation by 1.4 and 1%, respectively [51]. Additionally, according to many studies worldwide, exposure to fine dust particles ($PM_{2.5}$) combined with CO and $SO_2$ in the surrounding environment will increase the risk of death from respiratory diseases and lung cancer, with a 1.9% increase in total deaths when CO concentrations increased by 1 mg/m$^3$ [52].

Daily exposure to polluted air is linked to oxidation and cell inflammation, risk factors for chronic diseases and cancer. WHO classified air pollution as a human carcinogen in 2013. Several studies have provided evidence of a correlation between the diameter of $PM_{2.5}$ and lung cancer morbidity and mortality. The AHSMOG-2 study found that for every 10 µg/m$^3$ increase in $PM_{2.5}$ in the air, the risk of lung cancer also increased, and this rate was higher among people who lived in their area for five years or more and spent more than 1 hour/day outdoors [53]. The incidence of lung cancer is expected to increase due to daily exposure to air pollution associated with large-scale industrialisation and smoking habits [54].

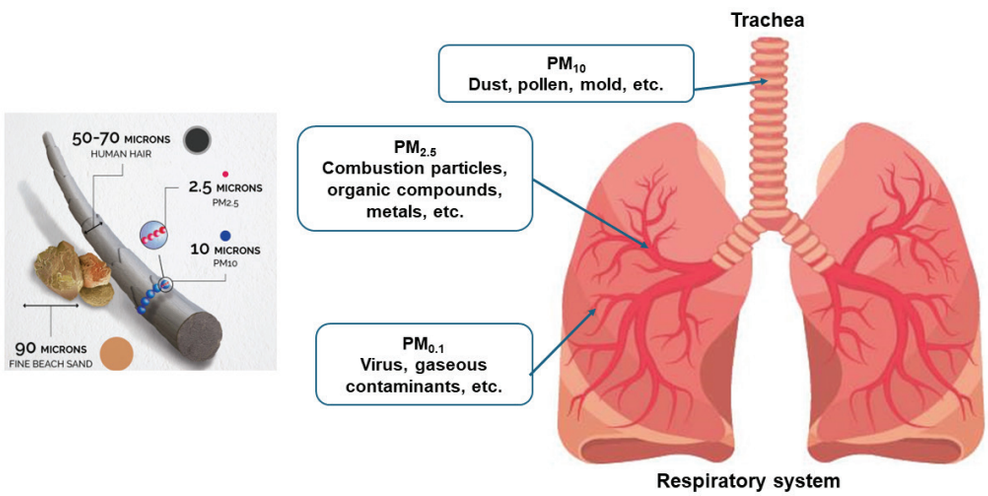


**Fig. 1. Size, main composition, and deposition site of PM in the lung.**

Many studies worldwide have identified a direct link between exposure to air pollution and cardiovascular diseases [55]. According to various studies, fine particulate matter can cause impaired blood vessel function and accelerate calcification in the arteries. In particular, the smaller the particles, the greater the ability to penetrate deep into the lower respiratory tract, thus having a more extraordinary ability to cause lung and heart diseases (Fig. 1) [45]. Together with particulate matter, CO is also known to be one of the most harmful substances to the central nervous system and cardiovascular systems. The affinity of CO for haemoglobin is 250 times greater than that of oxygen, leading to competition for the oxygen bond and the haeme nucleus of haemoglobin, resulting in oxygen loss and hypoxia [46]. Besides, high $NO_2$ exposure is thought to be associated with ventricular hypertrophy [56]. Additionally, scientific data from studies suggest an association between ambient air pollutants and blood pressure. To support this, a Korean study showed that exposure to pollutants such as $O_3$ and $NO_2$ in the short term increased systolic and diastolic blood pressure. Patients with hypertension are more susceptible to the effects of increased blood pressure than those with normal blood pressure. The mechanism by which $O_3$ exposure-induced hypertension is improved serotonin-induced vasoconstriction and decreased acetylcholine-induced vasodilation. Meanwhile, $SO_2$ and CO lower blood pressure within hours [57].

Besides the harmful effects of air pollution on the respiratory system, the impact on the eyes is also of great

concern. The extent of the damage is variable and can range from asymptomatic to dry eye syndrome. Long-term exposure to air pollution can increase the likelihood of eye diseases [45]. If the concentration of toxins in the air is high, it can cause clinical manifestations within the day. The major reported air pollution-related eye health problems are eye discomfort, eye irritation, conjunctivitis, dry eye syndrome (DES), meibomian gland dysfunction (MGB), and blepharitis [58]. High concentrations of airborne pollutants narrow the retinal vessels, leading to microcirculation disorders. A study was conducted in China on 9737 patients who came for an eye examination for conjunctivitis. The study results showed an association when the concentration of CO, $NO_2$, $SO_2$, $O_3$, $PM_{2.5}$, and $PM_{10}$ in the air increased to 10 μg/$m^3$ on the day of the visit and the previous day; the number of patients presenting for conjunctivitis also increased [59]. According to another study, $PM_{2.5}$ concentrations from 20 to 200 μg/ml were genotoxic, causing DNA damage and reducing the efficiency of corneal epithelial cells [60].

Air pollution not only affects adults but also has negative effects on children's health in their first years of life or exposure to air pollution by the mother during pregnancy. The cardiovascular, metabolic, respiratory, allergic, and neurodevelopmental systems have been reported to be affected by pollutants [61, 62]. Birth weight was reported to correlate with prenatal exposures to constituents sourced from industrial dust [63]. $PM_{2.5}$ and $PM_{10}$ particles, $SO_2$, $NO_2$, or $O_3$ have been reported to be associated with reduced or low birth weight in newborns or, more seriously, can lead to premature birth [64].

## 5. Some recommended solutions to reduce the impact of air pollution

According to WHO statistics, outdoor air pollution contributes to about four million deaths annually, mainly from cardiovascular and respiratory diseases. Essential policies supporting air quality standards, such as energy-efficient housing and sustainable land use, should be implemented to reduce outdoor air pollution. Some major cities have introduced policies to reduce urban air pollution, such as bike-sharing in Paris, congestion charging in London, and an environmental police force in Beijing [65]. Additionally, protecting the integrity of ecosystems helps improve the health of communities worldwide. Therefore, expanding green land is necessary to prevent biodiversity loss, especially in highly urbanised and polluted countries [66].

Healthcare professionals need to connect with patients through an automated air pollution alert network, including alerts via text, email, or phone [67, 68]. Individuals are encouraged to plan their activities through their news feed, website, or mobile application to reduce their exposure to air pollution.

Using a mask is one way to reduce exposure to air pollution at the individual level. Some standard masks used worldwide include N95 in the United States, KN95 in China, and FFP2 in European countries. Unlike ordinary masks, these masks are equipped with filters (can remove more than 95% of impurities in the air and prevent dust particles as small as 0.3 microns) and are designed to fit the face [69].

Since air pollution is usually diffusive from outside into buildings, indoor air pollution could contain contaminants from itself and outdoor sources [70]. Therefore, reducing $PM_{2.5}$ indoors can also minimise the impact of particles produced from outdoor sources on human health. PM can be removed by using an air purifier, ventilation, and air conditioning system. Most studies have focused on mechanical filtration with a highly efficient particulate containment/air filter (HEPA), which removes at least 99.97% of 0.3 μm particles. Besides, eliminating burning solid fuels is an effective way to reduce indoor air pollution. Access to cleaner fuels, such as liquefied petroleum gas, natural gas pipelines, and electric stoves, is critical to public health. Several studies have shown a positive association between replacing solid fuels with improved stoves and significant improvements in health outcomes [70, 71].

## 6. Conclusions

Among various factors causing air pollution, $PM_{2.5}$ is the leading cause of adverse health effects. The main contributors to air pollution are traffic (especially bus stops), markets, temples, restaurants, gas stations, etc. Personal $PM_{2.5}$ exposure contributions have been shown to be higher when people are at home. Many studies have shown air pollution as a risk factor for death related to heart disease, stroke, lower respiratory tract infections, lung cancer, diabetes, and COPD. Additionally, air pollution causes adverse health-related economic impacts. Therefore, reducing emissions and adapting to the impact of the climate are necessary activities to reduce air pollution. Furthermore, individual measures

to effectively reduce the health impact of air pollution include promoting personal mask-wearing, using air purifiers, ventilation, choosing low-exposure travel routes, and maintaining a proper diet.

## CRediT author statement

Linh-Thy Le: Investigation, Writing - Original draft preparation, Reviewing and Editing; Khanh-Bang V. Quang, Trieu-Vi Vo, Thanh-Mai T. Nguyen, Thi-Viet-Huong Dao: Reviewing and Editing; Xuan-Thanh Bui: Supervision, Conceptualisation, Writing - Reviewing.

## COMPETING INTERESTS

The authors declare that there is no conflict of interest regarding the publication of this article.

## REFERENCES

[1] J. Fairburn, S.A. Schüle, S. Dreger, et al. (2019), "Social inequalities in exposure to ambient air pollution: A systematic review in the WHO European region", *J. Environ. Res. Public Health*, **16(17)**, DOI: 10.3390/ijerph16173127.

[2] World Health Organisation (2022), "What are the WHO air quality guidelines?", www.who.int/news-room/feature-stories/detail/what-are-the-who-air-quality-guidelines, accessed 24 July 2023.

[3] Vietnam Ministry of Natural Resources and Environment (2020), *Report on National Environmental Status 2016-2020*, Dan Tri Publishing House, https://monre.gov.vn/Portal/Documents/2021/11/20211108_Bao%20cao%20HTMT%202016-2020_F.pdf, accessed 24 July 2023 (in Vietnamese).

[4] N.T.T. Nhung, V.T. Duc, V.D. Ngoc, et al. (2022), "Mortality benefits of reduction fine particulate matter in Vietnam, 2019", *Frontiers in Public Health*, **10**, DOI: 10.3389/fpubh.2022.1056370.

[5] N.T.K. Oanh, D.A. Permadi, P.K. Hopke, et al. (2018), "Annual emissions of air toxics emitted from crop residue open burning in Southeast Asia over the period of 2010-2015", *Atmospheric Environment*, **187**, pp.163-173, DOI: 10.1016/j.atmosenv.2018.05.061.

[6] World Health Organisation (2021), *WHO Global Air Quality Guidelines: Particulate Matter ($PM_{2.5}$ and $PM_{10}$), Ozone, Nitrogen Dioxide, Sulphur Dioxide and Carbon Monoxide*, https://apps.who.int/iris/handle/10665/345329, 273pp, accessed 25 June 2023.

[7] P. Kumar, A.B. Singh, T. Arora, et al. (2023), "Critical review on emerging health effects associated with the indoor air quality and its sustainable management", *Science of The Total Environment*, **872**, DOI: 10.1016/j.scitotenv.2023.162163.

[8] A. Dechezleprêtre, N. Rivers, B. Stadler (2019), "The economic cost of air pollution: Evidence from Europe", *OECD Economics Department Working Papers, No. 1584*, OECD Publishing, DOI: 10.1787/56119490-en.

[9] D.N. Huu, V.N. Ngoc (2021), "Analysis study of current transportation status in Vietnam's urban traffic and the transition to electric two-wheelers mobility", *Sustainability*, **13(10)**, DOI: 10.3390/su13105577.

[10] J.G. Martín, N.J.R. Kraakman, C. Pérez, et al. (2020), "A state-of-the-art review on indoor air pollution and strategies for indoor air pollution control", *Chemosphere*, **262**, DOI: 10.1016/j.chemosphere.2020.128376.

[11] P.O. Ukaogo, U. Ewuzie, C.V. Onwuka (2020, p.421), "Environmental pollution: Causes, effects, and the remedies", *Microorganisms for Sustainable Environment and Health*, pp.419-429, DOI: 10.1016/b978-0-12-819001-2.00021-8.

[12] D.Y.C. Leung (2015, p.1), "Outdoor-indoor air pollution in urban environment: Challenges and opportunity", *Frontiers in Environmental Science*, **2**, DOI: 10.3389/fenvs.2014.00069.

[13] B. Bera, S. Bhattacharjee, P.K. Shit, et al. (2020), "Significant impacts of COVID-19 lockdown on urban air pollution in Kolkata (India) and amelioration of environmental health", *Environment, Development and Sustainability*, DOI: 10.1007/s10668-020-00898-5.

[14] M.A.N. Martín, T.C. Vilches (2023), "Natural ventilation as a healthy habit during the first wave of the COVID-19 pandemic: An analysis of the frequency of window opening in Spanish homes", *Journal of Building Engineering*, **65**, DOI: 10.1016/j.jobe.2022.105649.

[15] V.V. Tran, D. Park, Y.C. Lee (2020), "Indoor air pollution, related human diseases, and recent trends in the control and improvement of indoor air quality", *International Journal of Environmental Research and Public Health*, **17(8)**, DOI: 10.3390/ijerph17082927.

[16] R. Xu, X. Qi, G. Dai, et al. (2020), "A comparison study of indoor and outdoor air quality in Nanjing, China", *Aerosol Air Qual. Res.*, **20(10)**, pp.2128-2141, DOI: 10.4209/aaqr.2019.10.0496.

[17] S. Vardoulakis, E. Giagloglou, S. Steinle, et al. (2020, p.5), "Indoor exposure to selected air pollutants in the home environment: A systematic review", *International Journal of Environmental Research and Public Health*, **17(23)**, DOI: 10.3390/ijerph17238972.

[18] M.C. Turner, Z.J. Andersen, A. Baccarelli, et al. (2020, p.9), "Outdoor air pollution and cancer: An overview of the current evidence and public health recommendations", *CA: A Cancer Journal for Clinicians*, **70(6)**, pp.460-479, DOI: 10.3322/caac.21632.

[19] P.O. Ukaogo, U. Ewuzie, C.V. Onwuka (2020, p.425), "Environmental pollution: Causes, effects, and the remedies", *Microorganisms for Sustainable Environment and Health*, pp.419-429, DOI: 10.1016/b978-0-12-819001-2.00021-8.

[20] L. Chunyu, S.Z.U. Abidin, W. Majeed, et al. (2021), "The non-linear relationship between carbon dioxide emissions, financial development and energy consumption in developing European and Central Asian economies", *Environ. Sci. Pollut. Res. Int.*, **28(44)**, pp.63330-63345, DOI: 10.1007/s11356-021-15225-2.

[21] Z. Lv, A.M.Y. Chu, M. McAleer, et al. (2019), "Modelling economic growth, carbon emissions, and fossil fuel consumption in China: Cointegration and multivariate causality", *Int. J. Environ. Res. Public Health*, **16(21)**, DOI: 10.3390/ijerph16214176.

[22] X. Wang, H. Firouzkouhi, J.C. Chow, et al. (2023), "Characterisation of gas and particle emissions from open burning of household solid waste from South Africa", *Atmos. Chem. Phys.*, **23(15)**, pp.8921-8937, DOI: 10.5194/acp-23-8921-2023.

[23] D.Y.C. Leung (2015, p.2), "Outdoor-indoor air pollution in urban environment: Challenges and opportunity", *Frontiers in Environmental Science*, **2**, DOI: 10.3389/fenvs.2014.00069.

[24] A. Mansouri, W. Wei, J.M. Alessandrini, et al. (2022), "Impact of climate change on indoor air quality: A review", *Int. J. Environ. Res. Public Health*, **19(23)**, DOI: 10.3390/ijerph192315616.

[25] P. Fermo, V. Comite (2022), "Indoor air quality in heritage and museum buildings", *Handbook of Cultural Heritage Analysis*, Springer, DOI: 10.1007/978-3-030-60016-7_34.

[26] M. Mannan, S.G.A. Ghamdi (2021), "Indoor air quality in buildings: A comprehensive review on the factors influencing air pollution in residential and commercial structure", *Int. J. Environ. Res. Public Health*, **18(6)**, DOI: 10.3390/ijerph18063276.

[27] Y. Ben, F. Ma, H. Wang, et al. (2019), "A spatio-temporally weighted hybrid model to improve estimates of personal $PM_{2.5}$ exposure: Incorporating big data from multiple data sources", *Environmental Pollution*, **253**, pp.403-411, DOI: 10.1016/j.envpol.2019.07.034.

[28] S.C. Lung, N. Chen, J.S. Hwang, et al. (2020), "Panel study using novel sensing devices to assess associations of $PM_{2.5}$ with heart rate variability and exposure sources", *Journal of Exposure Science & Environmental Epidemiology*, **30(6)**, pp.937-948, DOI: 10.1038/s41370-020-0254-y.

[29] S. Vardoulakis, E. Giagloglou, S. Steinle, et al. (2020, p.1), "Indoor exposure to selected air pollutants in the home environment: A systematic review", *Int. J. Environ. Res. Public Health*, **17(23)**, DOI: 10.3390/ijerph17238972.

[30] O.S. Idowu, L.B.D. Azevedo, F.V. Zohoori, et al. (2023), "Health risks associated with the production and usage of charcoal: A systematic review", *BMJ Open*, **13**, DOI: 10.1136/bmjopen-2022-065914.

[31] M.K.C. Sridhar, O.T. Okareh, M. Mustapha (2020), "Assessment of knowledge, attitudes, and practices on water, sanitation, and hygiene in some selected LGAs in Kaduna State, Northwestern Nigeria", *J. Environ. Public Health*, DOI: 10.1155/2020/6532512.

[32] K. Krupa, A. Piekut, R. Złotkowska (2012), "Assessment of risk perception connected with exposure to indoor air pollution in the group of inhabitants of Silesian Voivodeship", *Environmental Medicine*, **15(3)**, pp.46-54.

[33] B. Unni, N. Tang, Y.M. Cheng, et al. (2022), "Community knowledge, attitude and behaviour towards indoor air quality: A national cross-sectional study in Singapore", *Environmental Science & Policy*, **136**, pp.348-356, DOI: 10.1016/j.envsci.2022.06.021.

[34] United States Environmental Protection Agency (2022), *Introduction to Indoor Air Quality*, https://www.epa.gov/indoor-air-quality-iaq/indoor-air-pollution-introduction-health-professionals, accessed 28 October 2022.

[35] H.L. Chen, C.P. Li, C.S. Tang, et al. (2020), "Risk assessment for people exposed to $PM_{2.5}$ and constituents at different vertical heights in an urban area of Taiwan", *Atmosphere*, **11(11)**, DOI: 10.3390/atmos11111145.

[36] N. Hamatui, C. Beynon (2017), "Particulate matter and respiratory symptoms among adults living in Windhoek, Namibia: A cross sectional descriptive study", *Int. J. Environ. Res. Public Health*, **14(2)**, DOI: 10.3390/ijerph14020110.

[37] M. Brauer, G. Hoek, P.V. Vliet, et al. (2002), "Air pollution from traffic and the development of respiratory infections and asthmatic and allergic symptoms in children", *American Journal of Respiratory and Critical Care Medicine*, **166(8)**, pp.1092-1098, DOI: 10.1164/rccm.200108-007OC.

[38] T.N. Dang, L.T. Loi, L.T.V. Phuc (2022), "Relationship between $PM_{2.5}$ and low birth weight infant in Ho Chi Minh city: A spatial nested case control study", *ISEE Conference Abstracts*, **2022(1)**, DOI: 10.1289/isee.2022.P-1187.

[39] C.J. Matz, M. Egyed, R. Hocking, et al. (2019), "Human health effects of traffic-related air pollution (TRAP): A scoping review protocol", *Systematic Reviews*, **8(1)**, DOI: 10.1186/s13643-019-1106-5.

[40] S.C.C. Lung, P.K. Hsiao, T.Y. Wen, et al. (2014), "Variability of intra-urban exposure to particulate matter and CO from Asian-type community pollution sources", *Atmospheric Environment*, **83**, pp.6-13, DOI: 10.1016/j.atmosenv.2013.10.046.

[41] T.L.H. Vo, T.T. Truong, V.P. Dao, et al. (2021), "Personal exposure assessment of fine particulate matter for commuters in Hanoi", *TNU Journal of Science and Technology*, **226(06)**, pp.48-56, DOI: 10.34238/tnu-jst.3863.

[42] L.M. Zwack, C.J. Paciorek, J.D. Spengler, et al. (2011), "Characterizing local traffic contributions to particulate air pollution in street canyons using mobile monitoring techniques", *Atmospheric Environment*, **45(15)**, pp.2507-2514, DOI: 10.1016/j.atmosenv.2011.02.035.

[43] B. Wang, S. Lee, K. Ho, et al. (2007), "Characteristics of emissions of air pollutants from burning of incense in temples, Hong Kong", *Science of The Total Environment*, **377(1)**, pp.52-60, DOI: 10.1016/j.scitotenv.2007.01.099.

[44] A.G. Azam, B.R. Zanjani, M.B. Mood (2016), "Effects of air pollution on human health and practical measures for prevention in Iran", *Journal of Research in Medical Sciences: The Official Journal of Isfahan University of Medical Sciences*, **21**, DOI: 10.4103/1735-1995.189646.

[45] I. Manisalidis, E. Stavropoulou, A. Stavropoulos (2020), "Environmental and health impacts of air pollution: A review", *Front. Public Health*, **20(8)**, DOI: 10.3389/fpubh.2020.00014.

[46] P. Thangavel, D. Park, Y.C. Lee (2022), "Recent insights into particulate matter ($PM_{2.5}$)-mediated toxicity in humans: An overview", *Int. J. Environ. Res. Public Health*, **19(12)**, DOI: 10.3390/ijerph19127511.

[47] M.C. Altman, M. Kattan, G.T. O'Connor, et al. (2023), "Associations between outdoor air pollutants and non-viral asthma exacerbations and airway inflammatory responses in children and adolescents living in urban areas in the USA: A retrospective secondary analysis", *Lancet Planet Health*, **7(1)**, pp.e33-e44, DOI: 10.1016/S2542-5196(22)00302-3.

[48] D.F. Xing, C.D. Xu, X.Y. Liao, et al. (2019), "Spatial association between outdoor air pollution and lung cancer incidence in China", *BMC Public Health*, **19(1)**, DOI: 10.1186/s12889-019-7740-y.

[49] J. Kravchenko, H.K. Lyerly (2018), "The impact of coal-powered electrical plants and coal ash impoundments on the health of residential communities", *N.C. Med. J.*, **79(5)**, pp.289-300, DOI: 10.18043/ncm.79.5.289.

[50] J. Sun, A.J. Barnes, D. He, et al. (2017), "Systematic review and meta-analysis of the association between ambient nitrogen dioxide and respiratory disease in China", *Int. J. Environ. Res. Public Health*, **14(6)**, DOI: 10.3390/ijerph14060646.

[51] X. Xue, J. Chen, B. Sun, et al. (2018), "Temporal trends in respiratory mortality and short-term effects of air pollutants in Shenyang, China", *Environ.. Sci. Pollut. Res. Int.*, **25(12)**, pp.11468-11479, DOI: 10.1007/s11356-018-1270-5.

[52] L. Gharibvand, W.L. Beeson, D. Shavlik, et al. (2017), "The association between ambient fine particulate matter and incident adenocarcinoma subtype of lung cancer", *Environ. Health*, **16(1)**, DOI: 10.1186/s12940-017-0268-7.

[53] N. Wang, K. Mengersen, S. Tong, et al. (2019), "Short-term association between ambient air pollution and lung cancer mortality", *Environ. Res.*, **179**, Part A, DOI: 10.1016/j.envres.2019.108748.

[54] S.J. Snow, W. Cheng, A.S. Wolberg, et al. (2014), "Air pollution upregulates endothelial cell procoagulant activity via ultrafine particle-induced oxidant signaling and tissue factor expression", *Toxicol. Sci.*, **140(1)**, pp.83-93, DOI: 10.1093/toxsci/kfu071.

[55] P.J. Leary, J.D. Kaufman, R.G. Barr, et al. (2014), "Traffic-related air pollution and the right ventricle. The multi-ethnic study of atherosclerosis", *Am. J. Respir. Crit. Care Med.*, **189(9)**, pp.1093-1100, DOI: 10.1164/rccm.201312-2298OC.

[56] Y.J. Choi, S.H. Kim, S.H. Kang, et al. (2019), "Short-term effects of air pollution on blood pressure", *Sci. Rep.*, **9(1)**, DOI: 10.1038/s41598-019-56413-y.

[57] C.C. Lin, C.C. Chiu, P.Y. Lee, et al. (2022), "The adverse effects of air pollution on the eye: A review", *Int. J. Environ. Res. Public Health*, **19(3)**, DOI: 10.3390/ijerph19031186.

[58] Q. Fu, Z. Mo, D. Lyu, et al. (2017), "Air pollution and outpatient visits for conjunctivitis: A case-crossover study in Hangzhou, China", *Environ. Pollut.*, **231**, Part 2, pp.1344-1350, DOI: 10.1016/j.envpol.2017.08.109.

[59] Z.X. Gao, X.L. Song, S.S. Li, et al. (2016), "Assessment of DNA damage and cell senescence in corneal epithelial cells exposed to airborne particulate matter ($PM_{2.5}$) collected in Guangzhou, China", *Invest. Ophthalmol. Vis. Sci.*, **57(7)**, pp.3093-3102, DOI: 10.1167/iovs.15-18839.

[60] S. Basith, B. Manavalan, T.H. Shin, et al. (2022), "The impact of fine particulate matter 2.5 on the cardiovascular system: A review of the invisible killer", *Nanomaterials (Basel)*, **12(15)**, DOI: 10.3390/nano12152656.

[61] S. Li, L. Peng, X. Wu, et al. (2021), "Long-term impact of ambient air pollution on preterm birth in Xuzhou, China: A time series study", *Environ. Sci. Pollut. Res.*, **28(30)**, pp.41039-41050, DOI: 10.1007/s11356-021-13621-2

[62] R. Basu, M. Harris, L. Sie, et al. (2014), "Effects of fine particulate matter and its constituents on low birth weight among full-term infants in California", *Environ. Res.*, **128**, pp.42-51, DOI: 10.1016/j.envres.2013.10.008.

[63] A.D. Bergstra, B. Brunekreef, A. Burdorf (2021), "The influence of industry-related air pollution on birth outcomes in an industrialized area", *Environ. Pollut.*, **269**, DOI: 10.1016/j.envpol.2020.115741.

[64] M. Abdo, I. Ward, K. O'Dell, et al. (2019), "Impact of wildfire smoke on adverse pregnancy outcomes in Colorado, 2007-2015", *Int. J. Environ. Res. Public Health*, **16(19)**, DOI: 10.3390/ijerph16193720.

[65] M.S. Loop, L.A. McClure, E.B. Levitan, et al. (2018), "Fine particulate matter and incident coronary heart disease in the REGARDS cohort", *Am. Heart J.*, **197**, pp.94-102, DOI: 10.1016/j.ahj.2017.11.007

[66] P.L.S. Ljungman, N. Andersson, L. Stockfelt, et al. (2019), "Long-term exposure to particulate air pollution, black carbon, and their source components in relation to ischemic heart disease and stroke", *Environ. Health Perspect.*, **127(10)**, DOI: 10.1289/EHP4757.

[67] M.C. Turner, Z.J. Andersen, A. Baccarelli, et al. (2020, p.4), "Outdoor air pollution and cancer: An overview of the current evidence and public health recommendations", *CA: A Cancer Journal for Clinicians*, **70(6)**, pp.460-479, DOI: 10.3322/caac.21632.

[68] R.W. Allen, S.D. Adar, E. Avol, et al. (2012), "Modeling the residential infiltration of outdoor $PM_{2.5}$ in the multi-ethnic study of atherosclerosis and air pollution (MESA air)", *Environ. Health Perspect.*, **120(6)**, pp.824-830, DOI: 10.1289/ehp.1104447.

[69] J.P. McCracken, K.R. Smith, A. Díaz, et al. (2007), "Chimney stove intervention to reduce long-term wood smoke exposure lowers blood pressure among Guatemalan women", *Environ. Health Perspect.*, **115(7)**, pp.996-1001, DOI: 10.1289/ehp.9888.

[70] J. McCracken, K.R. Smith, P. Stone, et al. (2011), "Intervention to lower household wood smoke exposure in Guatemala reduces ST-segment depression on electrocardiograms", *Environ. Health Perspect.*, **119(11)**, pp.1562-1568, DOI: 10.1289/ehp.1002834.

[71] E.V. Bräuner, L. Forchhammer, P. Møller, et al. (2008), "Indoor particles affect vascular function in the aged: An air filtration-based intervention study", *Am. J. Respir. Crit. Care Med.*, **177(4)**, pp.419-425, DOI: 10.1164/rccm.200704-632OC.

**General Instructions on using this template and submitting a manuscript to VJSTE:** Thank you for preparing a manuscript for submission to VJSTE. Using this template, or following the guidelines below, will help us in processing your article.

The structure of different types of articles may vary according to the type of study, and the content of the article.

The following are the detailed main components of the original research and review articles submitted to the journal.

From 2023 onwards, you can submit your article at: https://mc04.manuscriptcentral.com/mostvjste

***Original research***

The original research should have three following parts:

**Preliminary section:** It includes title, list of all contributing authors with their institutional affiliation, and abstract (160-250 words) with at least 3 keywords.

**Title: How to format a science article (replace with your real title)**

**Author(s):** List the author name(s) separated by commas. Use superscript numbers to link affiliations, and symbols *†‡ for author notes. For example, Y. Obsie[1*], S.A. Adem[1, 2]

**Corresponding author(s):* Include the email addresses or telephone numbers of the corresponding author(s). Please use the asterisk (*) symbol for the corresponding author information. This information is at the bottom of the manuscript's first page.

*Author's affiliation addresses:*

*[1]Affiliations should be preceded by superscript numbers corresponding to the author list*

*[2]For any institutions, please provide the institution name, street, district, city, country*

Received ; revised ; accepted

***Abstract:***
**Start your abstract here…**
***Keywords:*** **keyword 1, keyword 2, keyword 3…**
***Classification number(s):*** **1.1, 3.4, 5.3, etc.**

**Abstract**: The abstract should range between 160 and 250 words and be structured in a single paragraph following keywords in a separate line. The abstract should represent the main part of the research manuscript. It should reflect a brief and comprehensive background following the aim of the study (main questions to be addressed), methods used for investigating the problem, a summary of significant findings, main conclusions, and implications of the results.

**Keywords:** They should come immediately after the abstract and contain 3-7 specific and relevant keywords. They should reflect the research study and the relevant field of research.

**Classification numbers:** Depend on the Journal's Classification Scheme.

Author(s) are encouraged to write a "Highlights" that summarises the most exciting, interesting points from your manuscript.

**Manuscript section:** It is the main body of the scientific manuscript including: 1) Introduction; 2) Material(s) and method(s); 3) Results and discussion (separation of these two sections is acceptable); 4) Conclusions; 5) Recommendations/Suggestions/Implications/Study limitations...(if any). These sections may slightly vary depending on the type of research approach and design used in the research. Each section should be numbered.

All of the Figures, Tables, and Equations should be cited in numerical order.

**Figures**

**Fig. #:** (Begin each figure caption with a label, "**Fig. 1.**" for example, as a new paragraph).

**Fig. 1.** The figure caption should begin with an overall descriptive statement of the figure followed by additional text. They should be immediately after each figure. Figure parts are indicated with capital letters **(A)**. If you prefer, you can place both the actual figures and captions logically through the text near where they are cited rather than at the end of the file (but not both). If a paragraph in the main text begins with the name of a figure, write out "Figure" in full (e.g., <para> "Figure 1 shows...").

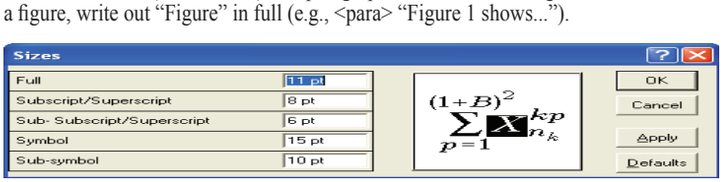


**Fig. 1. The figure caption.**

**Tables**

**Table #:** (Begin each table caption with a label "**Table 1.**", etc. as a new paragraph).

**Table 1.** Start this caption with a short description of your table. Format tables using the Word Table commands and structures. Do not create tables using spaces or tabs characters.

**Table 1. Caption.**

| a | b | c | d | e |
|---|---|---|---|---|
| f | | | | |
| g | | | | |
| h | | | | |

**Equations**

$$\int_a^b xdx \tag{1}$$

**Equations** can be included. We do not recommend using the native Word 2007, 2008, 2010 or 2011 equation editor. This can in some cases produce less reliable MathML, the online markup language we use, which may result in display errors. Instead, use the legacy equation editor in Word (Insert menu; select insert object; select word equation) or use MathType (recommended). If you enter equations in simple LaTeX, check that they will convert accurately (Word 2007 and higher can convert simple LaTeX equations).

**Closing section:** It includes appendices/supplementary materials/data availability statement (if applicable), CRediT author statement (for multiple authors), acknowledgements (if applicable), competing interests, ethics (if any) and a complete list of references corresponding to all the citations given in the text of the manuscript. The appendices/supplementary materials may include data files and other material relevant to the research that should be submitted in separate files if required.

**APPENDICES (if any)**

The appendices should ideally be under 1000 words (approximately 2 A4 pages) for printing version. With longer appendices, they are only accepted for online publication.

**CRediT author statement (for multiple authors)**

CRediT offers authors the opportunity to share an accurate and detailed description of their diverse contributions to the published work.

**ACKNOWLEDGEMENTS (if applicable)**

This section is for the researchers who were funded for the research projects, and it should enclose all sources of financial support.

**COMPETING INTERESTS**

The author(s) declare(s) that there is no conflict of interest regarding the publication of this article.

**REFERENCES**

For in-text citation: References should be cited in the bracket with a number [1]. Multiple reference citations are separated by commas [2, 3] or if a series, dashes [4-6]. When citing sources with the author(s) and the year, they should be shortened to the first author's name, followed by et al. (with more than one author) and the year.

For reference list: With less than or equal to three authors, list all the author(s). With more than three authors, the first three should be listed and followed by et al.

References are listed in numerical order, and in the same order in which they are cited in text. The reference list should include all and only those references you have cited in the text. The reference list appears at the end of the article.

The reference consists of: Initial(s) and first/last name of the author(s), author' names separated by commas (Year of publication), "Titles of journal articles or chapter of book", *Title of Journal, Book or Other Publication*, **Volume(Number)** (if any), page numbers (if any), DOI (if any), URL and accessed date (if any) (in its original language if not English).

To cite a website and online/electronic resources, please include the accessed date (day month year).

Example of a reference list:

[1] T. Binzoni, T.S. Leung, D. Boggett, et al. (2003), "Non-invasive laser Doppler perfusion measurements of large tissue volumes and human skeletal muscle blood RMS velocity", *Phys. Med. Biol.*, **48(1)**, pp.2527-2549, DOI: 10.1088/0031-9155-48-15-318.

[2] H.W. Bischoff, H.C. Bold (1963), *Some Soil Algae from Enchanted Rock and Related Algal Species*, University of Texas Publications, 95pp.

[3] R. Busi (2016), "Weedy rice in the Philippines and Vietnam", https://www.aciar.gov.au/publication/technical-publications/weedy-rice-philippines-and-vietnam-final-report, accessed 15 July 2018.

***Review articles***

They should be different from the original research as they would contain different sections on the literature review. Authors may structure this part as per nature, background, and available literature on the issue argued in the manuscript.

**For more detailed instructions, please visit our website: vietnamscience.vn or vietnamscience.vjst.vn**

This manuscript template has been used from 2021 onwards.

P-ISSN 2525-2461 • E-ISSN 2615-9937

# Vietnam Journal of Science, Technology and Engineering

MARCH 2024 • VOLUME 66 NUMBER 1

## EDITORIAL BOARD



### EDITORIAL OFFICE

113 Tran Duy Hung Str., Cau Giay Dist., Hanoi, Vietnam
Tel: (84.24) 39436793; Fax: (84.24) 39436794
Email: vjste@most.gov.vn
Website: vietnamscience.vn or vietnamscience.vjst.vn

### PUBLICATION LICENCE

No. 459/GP-BTTTT 20th July 2021
No. 50/GP-BTTTT 1st February 2023